

Title	Reaction dynamics of strange and charm hadron productions
Author(s)	Kim, Sangho
Citation	大阪大学, 2015, 博士論文
Version Type	VoR
URL	<a href="https://doi.org/10.18910/54028">https://doi.org/10.18910/54028</a>
rights	
Note	

***Osaka University Knowledge Archive : OUKA***

<https://ir.library.osaka-u.ac.jp/>

Osaka University

OSAKA UNIVERSITY

DOCTORAL THESIS

---

# Reaction dynamics of strange and charm hadron productions

---

*Author:*

Sang-Ho KIM

*Supervisor:*

Prof. Atsushi HOSAKA

*A thesis submitted in fulfilment of the requirements  
for the degree of Doctor of Physics*

*in the*

Research Center for Nuclear Physics  
Department of Physics

August 2015

# Declaration of Authorship

I, Sang-Ho KIM, declare that this thesis titled, 'Reaction dynamics of strange and charm hadron productions' and the work presented in it are my own. I confirm that:

- This work was done wholly or mainly while in candidature for a research degree at this University.
- Where any part of this thesis has previously been submitted for a degree or any other qualification at this University or any other institution, this has been clearly stated.
- Where I have consulted the published work of others, this is always clearly attributed.
- Where I have quoted from the work of others, the source is always given. With the exception of such quotations, this thesis is entirely my own work.
- I have acknowledged all main sources of help.
- Where the thesis is based on work done by myself jointly with others, I have made clear exactly what was done by others and what I have contributed myself.

Signed:

---

Date:

---

OSAKA UNIVERSITY

# *Abstract*

Theory Group  
Department of Physics

Doctor of Physics

## **Reaction dynamics of strange and charm hadron productions**

by Sang-Ho KIM

Open strange and charm productions are considered to play a central role in unraveling the features of hadrons which include not only the ground states but also various excited states, so called exotic hadrons as well. These reactions give insights into the dynamics of quarks and gluons. To make a close link with the underlying QCD, we need microscopic descriptions for the reactions. In this thesis, we study the reaction mechanism of the photon- and pion-induced strange and charm productions.

In the first part, we investigate the photoproductions of  $K^*\Sigma$  and  $K^*\Lambda$  off the nucleon targets focusing on the role of  $N^*$  and  $\Delta^*$  resonances. An effective Lagrangian model is employed with hadronic degrees of freedom. Some PDG resonances are taken into account in the  $s$ -channel diagram process in addition to other mesons and baryons of ground states. The resonance parameters are determined by the PDG data if available, otherwise by using the SU(6) quark model. We find that the role of resonances is different from each other. In the  $K^*\Sigma$  process, higher resonances scarcely affect the total and differential cross sections. Instead, certain higher resonances play a crucial role in the  $K^*\Lambda$  process. However, in both cases, spin observables are more affected by resonances rather than other background contributions, in general.

The structure and the interaction of charmed baryons are also important topics in hadron physics. They have become even more interesting by the recent observation of the pentaquark  $P_c^+$  containing  $c\bar{c}$ . In the second part, therefore, we study the production of the most fundamental process,  $\pi^-p \rightarrow D^{*-}Y_c$ , where  $Y_c$  denotes a charmed baryon. Pion-induced  $K^*\Lambda$  and  $D^*\Lambda_c$  productions off the nucleon targets are also investigated with the effective Lagrangian and Regge models. Relying on the experimental data of the  $K^*\Lambda$  process, the production rate of the  $D^*\Lambda_c$  one is estimated. This study gives an important clue to the upcoming J-PARC experimental project.

# *Acknowledgements*

First of all, I would like to express my gratitude to supervisor, Professor Atsushi Hosaka. He gave me invaluable teaching and advice to improve the knowledge of physics. It made me gain an insight into the nature of hadron physics. Professor Hyun-Chul Kim was a great mentor. We had fruit discussions many times and he encouraged me to become a good scientist. Other collaborators, Prof. Seung-il Nam, Prof. Hiroyuki Noumi, Prof. Kotaro Shirotori, and Prof. Hideko Nagahiro helped me to achieve the thesis. Their aid will be a priceless asset to me. I gratefully acknowledge other RCNP members, Prof. Kazuyuki Ogata, Prof. Noriyoshi Ishii, Prof. Hiroyuki Kamano, secretary of RCNP Ms. Mika Tambara, and so on, with the help of staying in Osaka. I also would like to thank “the Ministry of Education, Culture, Science and Technology of Japan” for supporting the MEXT scholarship and the theory group of RCNP for the financial support of local expenses.

Finally I express my sincere thanks to my parents and wife Insun Choi. The gratitude towards her presence can scarcely be exaggerated. I appreciate her support and understanding of my life in Japan.

# Contents

<b>Declaration of Authorship</b>	<b>i</b>
<b>Abstract</b>	<b>ii</b>
<b>Acknowledgements</b>	<b>iii</b>
<b>Contents</b>	<b>iv</b>
<b>List of Figures</b>	<b>viii</b>
<b>List of Tables</b>	<b>xii</b>
<b>1 Introduction</b>	<b>1</b>
1.1 Hadron production reaction . . . . .	1
1.2 Strangeness productions . . . . .	1
1.2.1 Nucleon resonances . . . . .	1
1.2.2 Models of strangeness productions . . . . .	2
1.2.3 Reactions studied in this thesis . . . . .	4
1.3 Charmed productions . . . . .	4
1.3.1 Background . . . . .	4
1.3.2 Planned experiments . . . . .	5
1.3.3 Reactions studied in this thesis . . . . .	6
<b>2 Formalism</b>	<b>7</b>
2.1 Effective Lagrangians . . . . .	7
2.2 Regge model . . . . .	9
2.2.1 Motivation . . . . .	9
2.2.2 Formula . . . . .	11
2.2.3 Unitarity . . . . .	13
2.2.4 Regge trajectories . . . . .	13
2.2.5 General features . . . . .	15
<b>3 <math>K^*\Sigma</math> photoproduction</b>	<b>17</b>
3.1 Motivation . . . . .	17
3.2 Formalism . . . . .	18
3.2.1 $K^*$ , $K$ , and $\kappa$ exchanges in the $t$ channel . . . . .	19

3.2.2	$N$ and $\Delta$ exchanges in the $s$ channel	21
3.2.3	$\Lambda$ , $\Sigma$ , and $\Sigma^*$ exchanges in the $u$ channel	22
3.2.4	Contact term	23
3.2.5	Baryon resonances in the $s$ channel	23
3.2.6	Form factors	26
3.3	Results	27
3.3.1	Total cross sections	27
3.3.2	Differential cross sections	29
3.3.3	Spin observables	30
3.4	Summary	34
<b>4</b>	<b><math>K^*\Lambda</math> photoproduction</b>	<b>36</b>
4.1	Particle data group	36
4.2	Motivation	37
4.3	Formalism	38
4.3.1	Nonresonant terms	39
4.3.2	Nucleon resonances in the $s$ channel	41
4.3.3	Form factors	42
4.4	Results	43
4.4.1	Total cross sections	44
4.4.2	Differential cross sections	45
4.4.3	Spin observables	46
4.5	Summary	52
<b>5</b>	<b>Production rates of charmed baryons</b>	<b>53</b>
5.1	Motivation	53
5.2	Quark-diquark model	54
5.3	Amplitudes	56
5.4	Production rates	57
5.5	Summary	59
<b>6</b>	<b>Pion-induced <math>K^{*0}\Lambda</math> and <math>D^{*-}\Lambda_c^+</math> productions</b>	<b>60</b>
6.1	Motivation	60
6.2	Formalism (Effective Lagrangian method)	62
6.2.1	Effective Lagrangians	62
6.2.2	Scattering amplitudes	64
6.2.3	Form factors	64
6.2.4	Charm production	65
6.3	Results (Effective Lagrangian method)	65
6.3.1	Total cross sections	66
6.3.2	Differential cross sections $d\sigma/d\Omega$	67
6.3.3	Differential cross sections $d\sigma/dt$	69
6.3.4	Charm production	70
6.4	Formalism (Regge approach)	71
6.4.1	Regge propagators and trajectories	71
6.4.2	Regge amplitudes and form factors	74
6.4.3	Charm production	75

6.5	Results (Regge approach)	75
6.5.1	Form factors and phases	76
6.5.2	Total cross sections	77
6.5.3	Differential cross sections $d\sigma/d\Omega$	78
6.5.4	Differential cross sections $d\sigma/dt$	79
6.5.5	Charm production	79
6.5.6	Comparison with another model	81
6.6	Normalization factor	82
6.6.1	Formalism	82
6.6.2	Results	83
6.7	Summary	84
<b>7</b>	<b>Summary</b>	<b>86</b>
<b>A</b>	<b>Notation and kinematics</b>	<b>89</b>
A.1	Notation	89
A.1.1	Metric	89
A.1.2	Pauli and Dirac matrices	90
A.1.3	Spinors	91
A.1.3.1	Bjorken-Drell representation	91
A.1.3.2	Helicity based representation	91
A.2	Kinematics	92
A.2.1	Mandelstam variables	92
A.2.2	Energy and momentum in two-body process	92
<b>B</b>	<b>Propagators and helicity amplitudes</b>	<b>95</b>
B.1	Resonance propagators	95
B.2	Photon helicity amplitudes	96
<b>C</b>	<b>Spin observables</b>	<b>98</b>
C.1	Single polarization observables	99
C.2	Double polarization observables	100
<b>D</b>	<b>Baryon wave functions</b>	<b>103</b>
D.1	Three quark system	103
D.1.1	Spin ( $2^3 = 8 = 4(S) + 2(\rho) + 2(\lambda)$ )	103
D.1.2	Flavor ( $3^3 = 27 = 10(S) + 8(\rho) + 8(\lambda) + 1(A)$ )	104
D.1.3	Spin $\times$ Flavor wave functions ( $2^3 \times 3^3 = 6^3 = 216$ )	104
D.2	Two body system	105
D.3	Matrix elements	105
D.3.1	$N(1/2^+) \rightarrow$ ground state baryons	106
D.3.2	$N(1/2^+) \rightarrow p$ -wave baryons	107
D.3.3	$N(1/2^+) \rightarrow d$ -wave baryons	108
D.4	Baryon wave functions	109
D.5	Harmonic oscillator wave functions	110



---

<b>E</b>	<b>Regge parameters</b>	<b>112</b>
E.1	Regge trajectories . . . . .	112
E.2	Regge energy scale parameters . . . . .	114
<b>F</b>	<b>Isospin Factors</b>	<b>115</b>
F.1	$\Delta$ vertex . . . . .	115
F.2	VVP vertex . . . . .	116
<b>G</b>	<b>Structures of Feynman Amplitudes</b>	<b>117</b>
G.1	$K$ amplitude . . . . .	117
G.2	$K^*$ amplitude . . . . .	118
G.3	$\Sigma$ amplitude . . . . .	119
<b>H</b>	<b>Size of a charmed baryon</b>	<b>121</b>
	<b>Bibliography</b>	<b>123</b>

# List of Figures

1.1	RPR model for the $\pi^- p \rightarrow K^0 \Lambda$ . . . . .	3
2.1	diagrams for the $\pi N \rightarrow \pi N$ . . . . .	8
2.2	$t$ -channel diagrams for the (a) $\pi^- p \rightarrow K \Sigma$ . . . . .	9
2.3	Differential cross sections for the $\pi^- p \rightarrow K^0 \Sigma^0$ and $\pi^- p \rightarrow K^+ \Sigma^-$ at $P_{\text{lab}} = 2.20 \text{ GeV}/c$ (left panel). Total cross sections for the same channels (right panel). The data are from Ref. [64]. . . . .	9
2.4	$t$ -channel diagrams for the (b) $\pi^+ n \rightarrow K \Sigma$ . . . . .	10
2.5	$t$ -channel diagrams for the (c) $\pi^- n \rightarrow K^0 \Sigma^-$ (left panel) and the (d) $\pi^+ p \rightarrow K^+ \Sigma^+$ (right panel). . . . .	10
2.6	Integration Contour. . . . .	12
2.7	$\pi$ , $\omega$ , and $\rho$ Regge trajectories (left panel) and $K$ and $K^*$ trajectories (right panel). . . . .	14
2.8	$\Sigma$ and $\Sigma^*$ Regge trajectories. . . . .	15
3.1	Tree-level Feynman diagrams for the $\gamma p \rightarrow K^* \Sigma$ . . . . .	18
3.2	Total cross sections for the $\gamma p \rightarrow K^{*0} \Sigma^+$ (left panel) and the $\gamma p \rightarrow K^{*+} \Sigma^0$ (right panel). The data are from Ref. [70] (black circles), Ref. [72] (open squares), and Ref. [68] (black triangles). . . . .	28
3.3	Resonance contributions to the total cross sections for the $\gamma p \rightarrow K^{*0} \Sigma^+$ (left panel) and the $\gamma p \rightarrow K^{*+} \Sigma^0$ (right panel). . . . .	29
3.4	Differential cross sections for the $\gamma p \rightarrow K^{*0} \Sigma^+$ in the range of $E_\gamma = (1.925 - 2.9125) \text{ GeV}$ . The data are from Ref. [70] (black circles) and Ref. [72] (open squares). . . . .	29
3.5	Differential cross sections for the $\gamma p \rightarrow K^{*+} \Sigma^0$ in the range of $E_\gamma = (1.85 - 3.75) \text{ GeV}$ . The data are from Ref. [68]. . . . .	30
3.6	Photon-beam asymmetries $\Sigma_\gamma$ for the $\gamma p \rightarrow K^{*0} \Sigma^+$ (upper panel) and the $\gamma p \rightarrow K^{*+} \Sigma^0$ (lower panel) as functions of $\cos \theta$ in the range of $E_\gamma = (2.075 - 2.9125) \text{ GeV}$ . . . . .	31
3.7	Recoil asymmetries $P_y$ for the $\gamma p \rightarrow K^{*0} \Sigma^+$ (upper panel) and the $\gamma p \rightarrow K^{*+} \Sigma^0$ (lower panel) as functions of $\cos \theta$ in the range of $E_\gamma = (2.075 - 2.9125) \text{ GeV}$ . . . . .	32
3.8	Target asymmetries $T_y$ for the $\gamma p \rightarrow K^{*0} \Sigma^+$ (upper panel) and the $\gamma p \rightarrow K^{*+} \Sigma^0$ (lower panel) as functions of $\cos \theta$ in the range of $E_\gamma = (2.075 - 2.9125) \text{ GeV}$ . . . . .	32
3.9	Photon-beam asymmetries $\Sigma_\gamma$ for the $\gamma p \rightarrow K^{*0} \Sigma^+$ (upper panel) and the $\gamma p \rightarrow K^{*+} \Sigma^0$ (lower panel) as functions of $E_\gamma$ , the scattering angle being changed from $0^\circ$ to $180^\circ$ . . . . .	33

3.10	Recoil asymmetries $P_y$ for the $\gamma p \rightarrow K^{*0}\Sigma^+$ (upper panel) and the $\gamma p \rightarrow K^{*+}\Sigma^0$ (lower panel) as functions of $E_\gamma$ , the scattering angle being changed from $0^\circ$ to $180^\circ$ .	33
3.11	Target asymmetries $T_y$ for the $\gamma p \rightarrow K^{*0}\Sigma^+$ (upper panel) and the $\gamma p \rightarrow K^{*+}\Sigma^0$ (lower panel) as functions of $E_\gamma$ , the scattering angle being changed from $0^\circ$ to $180^\circ$ .	34
4.1	Spectrum of nucleon resonances.	37
4.2	Total cross sections for the $\gamma p \rightarrow K^{*+}\Lambda$ with various theoretical results.	38
4.3	Tree-level Feynman diagrams for the $\gamma N \rightarrow K^*\Lambda$ .	39
4.4	Total cross sections for the $\gamma p \rightarrow K^{*+}\Lambda$ (left panel) and the $\gamma n \rightarrow K^{*0}\Lambda$ (right panel). The data are from Ref. [68].	44
4.5	Resonance contributions to the total cross sections for the $\gamma p \rightarrow K^{*+}\Lambda$ (left panel) and the $\gamma n \rightarrow K^{*0}\Lambda$ (right panel).	44
4.6	Differential cross sections for the $\gamma p \rightarrow K^{*+}\Lambda$ in the range of $E_\gamma = 1.7\text{--}3.9$ GeV. The data are from Ref. [68].	45
4.7	Differential cross sections for the $\gamma n \rightarrow K^{*0}\Lambda$ in the range of $E_\gamma = 1.9\text{--}2.7$ GeV.	46
4.8	Photon-beam asymmetries $\Sigma_\gamma$ for the $\gamma p \rightarrow K^{*+}\Lambda$ (upper panel) and the $\gamma n \rightarrow K^{*0}\Lambda$ (lower panel) as functions of $\cos\theta$ at $E_\gamma = 2.15$ and $2.65$ GeV.	47
4.9	Recoil asymmetries $P_y$ for the $\gamma p \rightarrow K^{*+}\Lambda$ (upper panel) and the $\gamma n \rightarrow K^{*0}\Lambda$ (lower panel) as functions of $\cos\theta$ at $E_\gamma = 2.15$ and $2.65$ GeV.	48
4.10	Target asymmetries $T_y$ for the $\gamma p \rightarrow K^{*+}\Lambda$ (upper panel) and the $\gamma n \rightarrow K^{*0}\Lambda$ (lower panel) as functions of $\cos\theta$ at $E_\gamma = 2.15$ and $2.65$ GeV.	48
4.11	Beam-target asymmetries $C_{zz}^{BT}$ for the $\gamma p \rightarrow K^{*+}\Lambda$ (upper panel) and the $\gamma n \rightarrow K^{*0}\Lambda$ (lower panel) as functions of $\cos\theta$ at $E_\gamma = 2.15$ and $2.65$ GeV.	49
4.12	Beam-recoil asymmetries $C_{zz}^{BR}$ for the $\gamma p \rightarrow K^{*+}\Lambda$ (upper panel) and the $\gamma n \rightarrow K^{*0}\Lambda$ (lower panel) as functions of $\cos\theta$ at $E_\gamma = 2.15$ and $2.65$ GeV.	50
4.13	Target-recoil asymmetries $C_{zz}^{TR}$ for the $\gamma p \rightarrow K^{*+}\Lambda$ (upper panel) and the $\gamma n \rightarrow K^{*0}\Lambda$ (lower panel) as functions of $\cos\theta$ at $E_\gamma = 2.15$ and $2.65$ GeV.	50
4.14	Target-vector-meson asymmetries $C_{zz}^{TV}$ for the $\gamma p \rightarrow K^{*+}\Lambda$ (upper panel) and the $\gamma n \rightarrow K^{*0}\Lambda$ (lower panel) as functions of $\cos\theta$ at $E_\gamma = 2.15$ and $2.65$ GeV.	51
4.15	Recoil-vector-meson asymmetries $C_{zz}^{RV}$ for the $\gamma p \rightarrow K^{*+}\Lambda$ (upper panel) and the $\gamma n \rightarrow K^{*0}\Lambda$ (lower panel) as functions of $\cos\theta$ at $E_\gamma = 2.15$ and $2.65$ GeV.	51
5.1	$t$ -channel process for the $\pi N \rightarrow VB$ , where $V = K^*, D^*$ (left panel). Quark-diquark structure (right panel).	54
5.2	Jacobi coordinates (left panel). $\lambda$ and $\rho$ coordinates of a three-quark system (right panel).	55
6.1	Forward differential cross sections $d\sigma/dt(\theta = 0)$ as a function of $s/s_{\text{th}}$ Ref. [62].	61
6.2	Tree-level diagrams for the $\pi^- p \rightarrow K^{*0}\Lambda$ .	62
6.3	Tree-level diagrams for the $\pi^- p \rightarrow D^{*-}\Lambda_c^+$ .	65

6.4	Total cross section for the $\pi^-p \rightarrow K^{*0}\Lambda$ based on the effective Lagrangian method with the PS Lagrangian. The data are taken from Ref. [129] (triangles) and Ref. [130] (circles).	66
6.5	Total cross section for the $\pi^-p \rightarrow K^{*0}\Lambda$ based on the effective Lagrangian method with the PV Lagrangian. The data are taken from Ref. [129] (triangles) and Ref. [130] (circles).	67
6.6	Differential cross sections $d\sigma/d\Omega$ for the $\pi^-p \rightarrow K^{*0}\Lambda$ as functions of $\cos\theta$ based on the effective Lagrangian method with the PS Lagrangian. The data are taken from Ref. [130].	68
6.7	Differential cross sections $d\sigma/d\Omega$ for the $\pi^-p \rightarrow K^{*0}\Lambda$ as functions of $\cos\theta$ based on the effective Lagrangian method with the PV Lagrangian. The data are taken from Ref. [130].	68
6.8	Differential cross sections $d\sigma/dt$ for the $\pi^-p \rightarrow K^{*0}\Lambda$ as functions of $t'$ based on the effective Lagrangian method with the PV Lagrangian. The data are taken from Ref. [132] (squares), Ref. [133] (stars), and Ref. [130] (circles).	69
6.9	Total cross section for the $\pi^-p \rightarrow D^{*-}\Lambda_c^+$ based on the effective Lagrangian method using PV Lagrangian (left panel). Comparison of the total cross section for the $\pi^-p \rightarrow D^{*-}\Lambda_c^+$ with that for the $\pi^-p \rightarrow K^{*0}\Lambda$ (right panel). The data are taken from Ref. [129] (triangles) and Ref. [130] (circles).	70
6.10	Comparison of the differential cross section for the $\pi^-p \rightarrow D^{*-}\Lambda_c^+$ with that for the $\pi^-p \rightarrow K^{*0}\Lambda$ based on the effective Lagrangian method using PV Lagrangian. The data are taken from Ref. [130].	71
6.11	(a) Planar and (b) non-planar diagrams for the $\pi^-p \rightarrow K^{*0}\Lambda$ .	71
6.12	$K$ and $K^*$ meson trajectories.	72
6.13	$\Sigma$ trajectory [67].	73
6.14	Planar and non-planar diagrams for the $\pi^-p \rightarrow D^{*-}\Lambda_c^+$ in the left and right panels, respectively.	75
6.15	Total cross sections for the $\pi^-p \rightarrow K^{*0}\Lambda$ based on the Regge approach without form factors. The data are taken from Ref. [129] (triangles) and Ref. [130] (circles).	76
6.16	Total cross sections for the $\pi^-p \rightarrow K^{*0}\Lambda$ based on the Regge approach according to the phases for each channel. The data are taken from Ref. [129] (triangles) and Ref. [130] (circles).	77
6.17	Total cross sections for the $\pi^-p \rightarrow K^{*0}\Lambda$ based on the Regge approach. The data are taken from Ref. [129] (triangles) and Ref. [130] (circles).	78
6.18	Differential cross sections $d\sigma/d\Omega$ for the $\pi^-p \rightarrow K^{*0}\Lambda$ as functions of $\cos\theta$ based on the Regge approach. The data are taken from Ref. [130].	78
6.19	Differential cross sections $d\sigma/dt$ for the $\pi^-p \rightarrow K^{*0}\Lambda$ as functions of $t'$ based on the Regge approach. The data are taken from Ref. [132] (squares), Ref. [133] (stars), and Ref. [130] (circles).	79
6.20	Total cross section for the $\pi^-p \rightarrow D^{*-}\Lambda_c^+$ based on the Regge approach (left panel). Comparison of the the total cross section for the $\pi^-p \rightarrow D^{*-}\Lambda_c^+$ with that for the $\pi^-p \rightarrow K^{*0}\Lambda$ (right panel). The data are taken from Ref. [129] (triangles) and Ref. [130] (circles).	80
6.21	Comparison of the differential cross section for the $\pi^-p \rightarrow D^{*-}\Lambda_c^+$ with that for the $\pi^-p \rightarrow K^{*0}\Lambda$ based on the Regge approach. The data are taken from Ref. [130].	80

6.22	Total cross section for the $\pi^- p \rightarrow D^{*-} \Lambda_c^+$ (thicker curve) is compared with that for the $\pi^- p \rightarrow K^{*0} \Lambda$ (thinner one). . . . .	81
6.23	Total cross sections for the $\pi^- p \rightarrow K^{*0} \Lambda$ (left panel) and for the $\pi^- p \rightarrow D^{*-} \Lambda_c^+$ (right panel) based on the Regge approach using the Titov's prescription. The data are taken from Ref. [129] (triangles) and Ref. [130] (circles). . . . .	84
6.24	Comparison of the total cross section for the $\pi^- p \rightarrow D^{*-} \Lambda_c^+$ with that for the $\pi^- p \rightarrow K^{*0} \Lambda$ using the Titov's prescription. The data are taken from Ref. [129] (triangles) and Ref. [130] (circles). . . . .	84
A.1	Mandelstam variables in the two-body process. . . . .	92
A.2	center of mass frame. . . . .	93
A.3	laboratory frame. . . . .	93
H.1	Relative coordinates for a three-body system. . . . .	121

# List of Tables

1.1	Strangeness reaction channels and their thresholds [GeV]. . . . .	2
3.1	Transition magnetic moments $h_{1,2}$ in Eqs. (3.24) extracted from the helicity amplitudes $A_{1,3}$ [GeV $^{-\frac{1}{2}}$ ] [3, 76]. . . . .	24
3.2	Strong coupling constants $g_1$ in Eqs. (3.26) extracted from the decay amplitudes $G_{s,l}$ [ $\sqrt{\text{MeV}}$ ] [5]. . . . .	25
3.3	Isospin factors to each channel for the $\gamma p \rightarrow K^* \Sigma$ . . . . .	27
3.4	Cutoff masses [GeV] to each channel for the $\gamma p \rightarrow K^* \Sigma$ . . . . .	27
4.1	Transition magnetic moments $h_{1,2}$ in Eqs. (4.6) extracted from the helicity amplitudes $A_{1,3}$ [GeV $^{-\frac{1}{2}}$ ] [3, 104, 114] for the (I) $K^{*+} \Lambda$ ((II) $K^{*0} \Lambda$ ) channel. . . . .	41
4.2	The masses, the decay widths, and the strong coupling constants $g_1$ in Eqs. (4.7) extracted from the decay amplitudes $G_{s,l}$ [ $\sqrt{\text{MeV}}$ ] [5]. . . . .	42
4.3	Isospin factors to each channel for the $\gamma N \rightarrow K^* \Lambda$ . . . . .	43
4.4	Cutoff masses [GeV] to each channel for the $\gamma N \rightarrow K^* \Lambda$ . . . . .	43
5.1	Baryon masses $M$ [MeV], spin-dependent coefficients $C$ and the ratios of production rates $\mathcal{R}$ given in Eq. (5.19). The second and third rows are the ratios $\mathcal{R}$ for the strange and charmed baryons, respectively, which are normalized to the ground state $\Lambda$ . They are computed at $k_\pi^{Lab} = 4.2$ GeV for the strange, and at $k_\pi^{Lab} = 20$ GeV for the charmed baryons. . . . .	58
6.1	The relevant coupling constants used in the $\pi^- p \rightarrow K^{*0} \Lambda$ . . . . .	63
6.2	Cutoff masses [GeV] to each channel for the $\pi^- p \rightarrow K^{*0} \Lambda$ and the $\pi^- p \rightarrow D^{*-} \Lambda_c^+$ . . . . .	66
6.3	Free parameters in form factors to each channel for the $\pi^- p \rightarrow K^{*0} \Lambda$ and the $\pi^- p \rightarrow D^{*-} \Lambda_c^+$ . . . . .	76
D.1	Spin-flavor wave functions of a baryon. . . . .	104
E.1	Mason trajectories from Ref. [134]. . . . .	113
E.2	Baryon trajectories. . . . .	113
E.3	The energy scale parameters . . . . .	114

# Chapter 1

## Introduction

### 1.1 Hadron production reaction

Understanding various reaction mechanisms is very useful for investigating hadron properties. Many experimental facilities are becoming more sophisticated and refined and the electromagnetic- or hadron-beam energies are also increasing. Consequently, reactions are gradually extended to the strange and charm hadron productions which are the main issues of hadron physics nowadays. A theoretical description of reaction dynamics is very important. Quantum Chromodynamics (QCD) is known to be the fundamental theory of strong interactions in the standard model. But the analysis in the low-energy regime has difficulty because of its nonperturbative property, despite the success at high energies. Thus various effective models are essentially needed to gain a clear insight into the structures and features of hadrons with hadronic degrees of freedom instead of quarks and gluons.

### 1.2 Strangeness productions

#### 1.2.1 Nucleon resonances

Most of the evidence and features of nucleon resonances are derived from the partial-wave analyses of pion-induced meson productions ( $\pi N \rightarrow \pi N, \eta N$  etc) and photon-induced pion production ( $\gamma N \rightarrow \pi N$ ) [1]. The information about the nucleon resonances which lie below 1.8 GeV is well organized since there have been a lot of studies both theoretically and experimentally. In comparison with this low energy region, relatively higher energy regions still need a tremendous task. Examining the resonance properties mostly with the  $\pi N$  channel meets a limitation. Recently, two nucleon resonances  $N(2300)$  and

$N(2570)$  are found in the decay of  $\psi(3686) \rightarrow p\bar{p}\pi_0$  [2]. Although such an experiment from the charm sector helps us to confirm some resonances, it rarely happens. Therefore, studying alternative reactions is attracting a lot of interest.

	channel	threshold		channel	threshold
(a) $KY$	$K\Lambda(1116)$	1.61	(c) $K^*Y$	$K^*\Lambda(1116)$	2.01
	$K\Sigma(1193)$	1.69		$K^*\Sigma(1193)$	2.08
(b) $KY^*$	$K\Lambda^*(1405)$	1.90	(d) $K^*Y^*$	$K^*\Lambda^*(1405)$	2.30
	$K\Lambda^*(1520)$	2.01		$K^*\Lambda^*(1520)$	2.41
	$K\Sigma^*(1385)$	1.88		$K^*\Sigma^*(1385)$	2.28

TABLE 1.1: Strangeness reaction channels and their thresholds [GeV].

Open strangeness meson and baryon productions have been playing an important role in resolving this problem. In Table. 1.1, the relevant channels and the corresponding threshold energies are listed together. All these channels can be suitable candidates for identifying the nucleon resonances higher than 1.8 GeV since their thresholds lie around 1.8 GeV or even larger than that energy.

To predict the resonance spectrum from the theoretical point of view, quark models are employed. The constituent-quark model (CQM) [3–7] is mostly developed and widely used. But in addition to the resonances confirmed in experiment, unobserved resonances are anticipated and they are expected to couple weakly to the  $\pi N$  channel but strongly to the kaon one. This so-called “missing resonances” problem is another important motivation for investigating strangeness hadron productions. Existence of these missing resonances remains to be proved and these processes will promote the validity of the constituent-quark model.

The strangeness degree of freedom is added besides the light quark ones, which leads one to use SU(3) symmetry rather than SU(2) as done in the pion production process. In strangeness channels, the partial-wave analyses method could not be as powerful as before since the background contribution begins to come into play more than the  $\pi N$  channels.

### 1.2.2 Models of strangeness productions

Besides the abundant  $\pi N$  scattering data, many experimental data have been produced from the strange sector recently, especially in the photon-induced reactions of meson-baryon final states. Correspondingly, remarkable progress in theoretical analyses is made also. The most studied among them is the  $KY$  channel. Based on the experimental



data [8–14], a lot of theoretical works have been carried out in the framework of tree-level effective Lagrangians [15–19], Regge model [20–22], RPR (Regge-plus-Resonance) model [23–25], and coupled-channel method [26–28].

An effective Lagrangian method considers a few single particle exchanges which are mostly chosen to be ground state particles and thus describes the low energy regions quite well. On the other hand, a Regge approach takes account of the exchange of whole families of hadrons with all spins  $J$ . It leads one to extend the domain of energies of applicability to high energies from the effective Lagrangian method. An RPR model develops the standard Regge model since it incorporates  $N^*$  or  $\Delta^*$  resonances in the  $s$  channel in addition to the background contribution. In other words, because high energies are mostly described by the  $t$ -channel Regge background, the Regge parameters are constrained by this region. Then low energy regions are supplemented by constructing  $s$ -channel resonance exchanges. Because the background plays a crucial role in strangeness production processes contrary to nonstrange ones, this model can be widely applied to various reaction mechanisms.

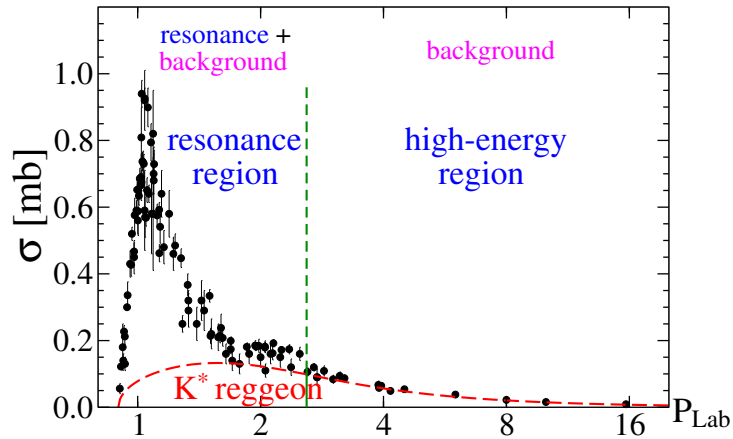


FIGURE 1.1: RPR model for the  $\pi^- p \rightarrow K^0 \Lambda$ .

Figure 1.1 explains schematically how the RPR model can be applied. When considering the  $\pi^- p \rightarrow K^0 \Lambda$  reaction, only  $K^*$ -reggeon exchange is allowed in the  $t$  channel. We first fix the  $K^*$ -reggeon coupling to the high-energy data ( $P_{\text{Lab}} \gtrsim 3 \text{ GeV}/c$ ). Then the low energy region is filled with resonance terms besides the background contribution. To understand a certain reaction process completely, we eventually need to reach a full coupled-channel method. It incorporates the effect of all possible initial and final state interactions.

The  $KY^*$  channel is also studied extensively. This channel is even more interesting since the threshold is larger than that of the  $KY$  channel, which lies near the 2 GeV. Thus examining this channel would be a good opportunity to extract the resonance properties with a wider spectrum. One specific example is the  $K\Lambda^*(1520)$  reaction. Based on

the effective Lagrangian method [29–33] and the Regge model [34–37], the experimental data [38–42] are analyzed in great detail.

### 1.2.3 Reactions studied in this thesis

In this thesis, we mainly focus on the  $K^*Y$  channel. In contrast to the well studied reactions ( $KY$  and  $KY^*$  channels), the  $K^*Y$  and  $K^*Y^*$  channels are still far from a clear understanding. Both the effective Lagrangian method and the Regge approach are utilized. In chapter 2, we explain the general framework of these two models. The photoproductions  $\gamma N \rightarrow K^*\Sigma$  [43] and  $\gamma N \rightarrow K^*\Lambda$  [44] are investigated in chapters 3 and 4, respectively. We concentrate on studying which baryon resonances near the threshold come into play significantly as for the intermediate states. Not only the contribution of backgrounds but also that of  $N^*$  and  $\Delta^*$  resonances of spins up to  $7/2$  are taken into account.

Photoproduction of the strange vector-meson ( $K^*$ ) provides richer physics compared with the  $K$  photoproduction. It is a vector meson with quantum number  $I(J^P) = 1/2(1^-)$ , thus the exchange of the scalar meson  $\kappa$  is allowed in the  $t$  channel, which is forbidden in the  $KY$  channel. Furthermore, the polarization of the  $K^*$ -meson can be taken as an important subject to be examined together with other polarization observables in terms of the spin-density matrices.

## 1.3 Charmed productions

### 1.3.1 Background

Charm- and bottom-quark physics becomes one of the most important issues in hadron physics, as experimental facilities report new hadrons containing one or two heavy quarks, either charm quarks or bottom ones, with unprecedented precision. Quarkonium-like states called  $X$ ,  $Y$ ,  $Z$  are the main issues among them. For example,  $X(3872)$  and  $Z_c(3900)$  are found in the charm sector, and  $Z_b(10610)$  and  $Z_b(10650)$  in the bottom sector. The Belle Collaboration, Babar Collaboration, and BESIII Collaboration have announced new mesons [45–52], some of which were also confirmed by the LHCb Collaboration [53, 54] (see Refs. [55, 56] for reviews). These  $X$ ,  $Y$ ,  $Z$  states contain  $c$ ,  $\bar{c}$  (or  $b$ ,  $\bar{b}$ ), and light quarks, which is different from the quark-antiquark states ( $q\bar{q}$ ) as the standard quark model describes. Thus quark dynamics become more complicated than the case where only light  $u$ ,  $d$ , and  $s$  quarks are considered. Moreover, these  $X$ ,  $Y$ ,  $Z$  are resonances, not ground states. Many of them above decay channel thresholds are

not sufficiently confirmed. Therefore, it seems that investigating the combination of heavy and light quarks is important. We need a more basis of the system of heavy and light quarks and one suitable opportunity is a charmed baryon and its excited states.

While the mesons with charm have been extensively studied theoretically as well as experimentally, charmed baryons have been less investigated. However, the charmed baryons are equally or even more important, since they provide a good opportunity to examine the role of both chiral symmetry and heavy quark symmetry in heavy-light quark systems. Moreover, the structure and the production mechanisms of the charmed baryons are much less known than those of light-quark baryons.

Meanwhile, the exotic states were a highly debatable topic in the baryon sector. Particularly, the pentaquark  $\Theta^+$ , whose quark content is  $uudd\bar{s}$ , was of great interest in the 2000's whether it exists in nature. This issue firstly occurred by the predictions of the mass of about 1530 MeV and the narrow decay width of less than 15 MeV in 1997 [57]. Then the observation of the  $\Theta^+$  in the LEPS Collaboration [58] triggered off a wave of controversy. On the other hand, in the charm sector, the first evidence for the exotic states was found at HERA by the H1 Collaboration in 2004 [59]. The mass of such a baryon is about 3099 MeV and the minimal constituent quark composition is expected to be  $uudd\bar{c}$ . It can be a candidate for a charmed pentaquark state. Interestingly enough, very recently, the so-called pentaquark charmonium state  $P_c^+$ , made of  $uudc\bar{c}$  quarks, is observed in  $\Lambda_b^0 \rightarrow J/\Psi K^- p$  decays [60]. This proves more obviously that exotic baryons exist in nature in the heavy quark sector. It indicates that the heavy baryon sector can give us a clue to unraveling the mystery of such multiquark states by analogy with (or even better than) the light baryon sector.

### 1.3.2 Planned experiments

Having mentioned the background above, we explain the status of recent experiments regarding charmed baryon productions. In 2012, the J-PARC (Japan Proton Accelerator Research Complex) facility submitted a new proposal for the study of charmed baryons via the pion-induced reactions at a high-momentum beam line [61]. The high pion beam of up to 20 GeV/c will be made for the production of charmed baryons. This energy is suited for producing charmed baryons with a fixed target and is able to produce excited states of energy up to around 1 GeV excitation from the ground state. Once we have a chance to observe various charmed baryons, it will provide very useful information about the underlying quark dynamics inherent in them.

One of the general features of charmed baryons is the distinction of different excitation modes of a three-quark system, the so-called  $\rho$  and  $\lambda$  modes. For the equal quark mass

system as in the case of light flavor baryons, they are degenerate. However, if one of the three quarks is replaced by the charm quark which is heavier than the  $u$ ,  $d$ , and  $s$  quarks, the  $\rho$  and  $\lambda$  modes split. This must be shown in the excited states of charmed baryons and is known as an isotope shift caused by a kinematical effect. The separation of the two modes makes us to understand the dynamics of the two light quarks, that is, the diquark. Therefore, charmed baryons will provide a good opportunity for the study of diquarks which is not well understood while is expected to play an important role in various hadron physics.

### 1.3.3 Reactions studied in this thesis

In this thesis, we aim to examine the production rates of various charmed baryons with the aid of a quark-diquark model in chapter 5 [62]. We focus on the  $\pi p \rightarrow D^{*-} Y_c$  process, where  $Y_c$  is the ground or various excited charmed baryons. Then in chapter 6, the production rate of the  $\pi p \rightarrow D^{*-} \Lambda_c^+$  reaction is estimated in comparison with the  $\pi p \rightarrow K^{*0} \Lambda$ . Two theoretical methods, effective Lagrangians and Regge model, are employed. The charmed reaction is not yet established both in theory and experiment. The production rate of the total and differential cross sections for the  $\pi p \rightarrow D^{*-} \Lambda_c^+$  can be useful for the future J-PARC experiments.

## Chapter 2

# Formalism

### 2.1 Effective Lagrangians

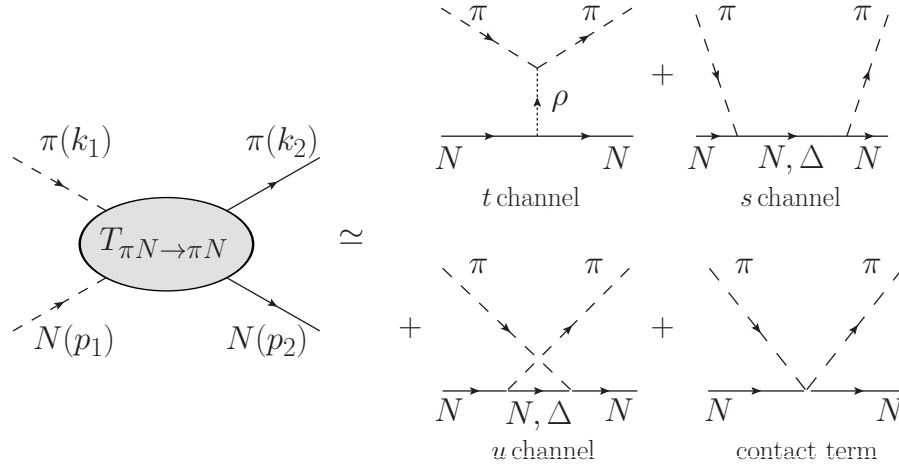
The most basic and common model when describing the hadron reactions is the tree-level effective Lagrangians. It is known to describe the low energy region well. In this model, there are two main ingredients: coupling constants and form factors. The coupling constants can be determined by using SU(3) flavor symmetry or well-known baryon-baryon potentials such as the Nijmegen potential together with the experimental data of hadron scatterings and decays. However, the cutoff masses for the form factors cause ambiguity in describing reactions.

For the description of hadron interaction amplitudes, we need to draw pictures for each scattering process. According to Gribov [63],

*The Feynman diagrams can be considered as a ‘laboratory of theoretical physics’.*

Thus we construct tree-level diagrams classified as follows; so-called  $t$ -channel,  $s$ -channel,  $u$ -channel, and contact terms. One simple example is the  $\pi N \rightarrow \pi N$  reaction which is expressed by diagrams in Fig. 2.2. In the effective Lagrangian method, interaction vertices are given by “effective Lagrangians” and intermediate lines express propagators of virtual particles which are contained in the Lagrangians. The corresponding Lagrangians read

$$\begin{aligned}\mathcal{L}_{\rho\pi\pi} &= -ig_{\rho\pi\pi}\rho_\mu(\boldsymbol{\pi} \cdot \partial^\mu \boldsymbol{\pi} - \partial^\mu \boldsymbol{\pi} \cdot \boldsymbol{\pi}), \\ \mathcal{L}_{\rho NN} &= -g_{\rho NN}\bar{N}\left[\rho^\mu\gamma_\mu - \frac{\kappa_{\rho NN}}{2M_N}\partial^\nu\rho^\mu\sigma_{\mu\nu}\right]N + \text{H.c.},\end{aligned}\tag{2.1}$$

FIGURE 2.1: diagrams for the  $\pi N \rightarrow \pi N$ .

for the  $t$ -channel exchange. Then we can compute the scattering amplitude in this channel as

$$\mathcal{M}_\rho = I_\rho \frac{g_{\rho\pi\pi} g_{\rho NN}}{t - M_\rho^2} k_1^\mu \left[ -g_{\mu\nu} + \frac{(k_2 - k_1)_\mu (k_2 - k_1)_\nu}{M_\rho^2} \right] \left[ \gamma^\nu - \frac{i k_{\rho NN}}{2M_N} \sigma^{\nu\lambda} (k_2 - k_1)_\lambda \right], \quad (2.2)$$

Other diagrams are calculated in a similar way.

As shown here, once we define the most general Lagrangians which satisfy symmetry principles, we can calculate the scattering amplitudes. The causality makes sure that the scattering amplitudes are analytic functions of momenta. An analytic function is identified by its singularities [63]. The structure of these is proceeded with the help of Feynman diagrams. To be clear, we make the main hypothesis [63]:

*Analytic properties of the exact amplitude coincide with those of the corresponding perturbation-theory diagrams.*

The only important point is to have the input objects - bare particles - to be point-like, which is interpreted with some quantum field theory (QFT) scheme [63].

In this thesis, we apply this method to various reactions, and the concrete expressions for the relevant effective Lagrangians and scattering amplitudes will be discussed in detail from next chapters.

## 2.2 Regge model

### 2.2.1 Motivation

Most reaction processes have a tendency for a forward peak. This becomes more obvious as the production energy increases. Regge formalism is designed to fit this high energy region where  $s$  is large and  $t$  small. It is also applicable to the backward angle region which corresponds to that of at large  $s$  and small  $u$ . When we measure the cross section for a certain reaction process, the magnitude is usually governed by whether it contains a  $t$ -channel process or not. This is due to the fact that there is a correlation between the forward peak behavior in a  $s$ -channel process and the exchange of particles in the  $t$  channel.

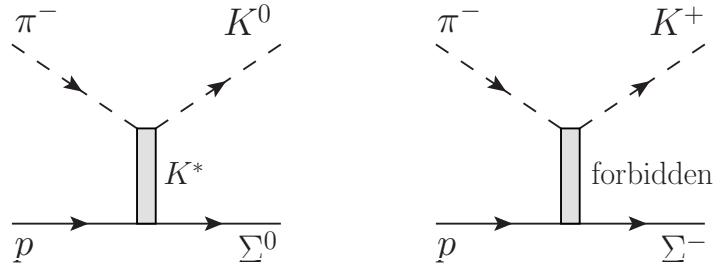


FIGURE 2.2:  $t$ -channel diagrams for the (a)  $\pi^- p \rightarrow K\Sigma$ .

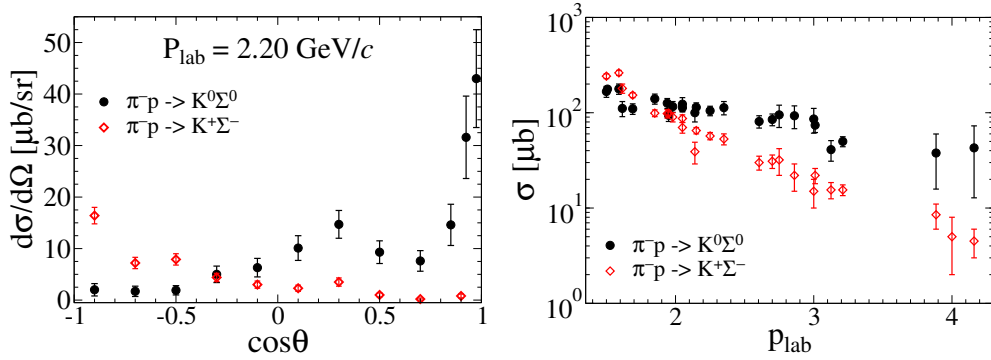


FIGURE 2.3: Differential cross sections for the  $\pi^- p \rightarrow K^0 \Sigma^0$  and  $\pi^- p \rightarrow K^+ \Sigma^-$  at  $P_{\text{lab}} = 2.20 \text{ GeV}/c$  (left panel). Total cross sections for the same channels (right panel). The data are from Ref. [64].

Pion-induced  $K$ -meson production can be a proper example to confirm this. It is classified according to the charge sums of the initial or final particles as (a)  $Q = 0$ :  $\pi^- p \rightarrow K^0 \Sigma^0$  and  $\pi^- p \rightarrow K^+ \Sigma^-$ , (b)  $Q = 1$ :  $\pi^+ n \rightarrow K^+ \Sigma^0$  and  $\pi^+ n \rightarrow K^0 \Sigma^+$ , (c)  $Q = -1$ :  $\pi^- n \rightarrow K^0 \Sigma^-$ , (d)  $Q = 2$ :  $\pi^+ p \rightarrow K^+ \Sigma^+$ . Figure 2.2 depicts the  $t$ -channel tree-level diagrams for the (a)  $\pi^- p \rightarrow K\Sigma$  process. After taking a careful look at the Clebsch-Gordan coefficients for the  $(\frac{1}{2} \times \frac{1}{2})$  and  $(\frac{3}{2} \times \frac{1}{2})$  tables, we can find that there is single charge exchange and isospin  $\frac{1}{2}$  or  $\frac{3}{2}$  for the  $\pi^- p \rightarrow K^0 \Sigma^0$ , which indicates that

$K\pi$  resonances such as the  $K^*(892)$  and  $K^*(1420)$  can be possible as for the intermediate states. Meanwhile, for the  $\pi^-p \rightarrow K^+\Sigma^-$ , double charge exchange and isospin  $\frac{3}{2}$  is allowed, none of which exists.

This fact is proved by the experimental data for the differential cross sections as shown in the left panel of Fig. 2.3. Since the  $t$ -channel exchange turns out to be applicable only for the  $\pi^-p \rightarrow K^0\Sigma^0$  channel, it reveals a very forward peak and the backward effects are relatively much suppressed. On the other hand, the  $\pi^-p \rightarrow K^+\Sigma^-$  has larger backward contribution rather than other angle regions. The relevant total cross sections in the right panel of Fig. 2.3 also support the effect of the existence of  $t$ -channel exchange. Except for the threshold region, it is found that  $\sigma(\pi^-p \rightarrow K^0\Sigma^0) \gg \sigma(\pi^-p \rightarrow K^+\Sigma^-)$ . It indicates that including  $t$ -channel resonances may be an essential part for the description of high energy regions.

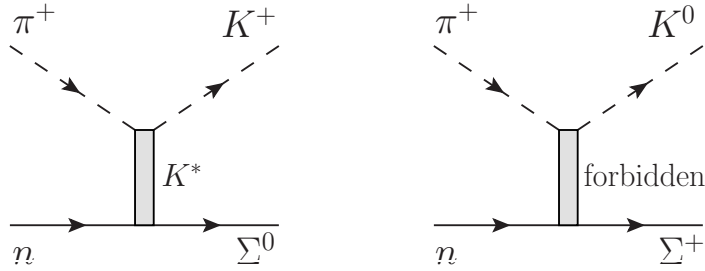


FIGURE 2.4:  $t$ -channel diagrams for the (b)  $\pi^+n \rightarrow K\Sigma$ .

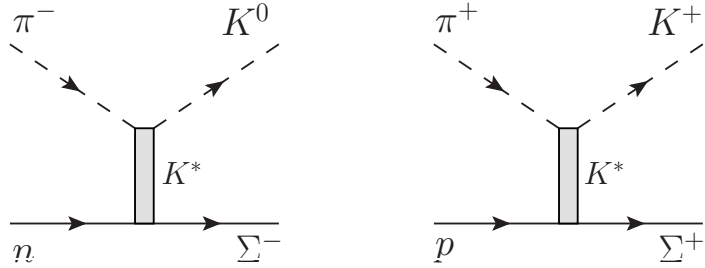


FIGURE 2.5:  $t$ -channel diagrams for the (c)  $\pi^-n \rightarrow K^0\Sigma^-$  (left panel) and the (d)  $\pi^+p \rightarrow K^+\Sigma^+$  (right panel).

Concerning the (b)  $\pi^+n \rightarrow K\Sigma$  channel, we can reach a similar conclusion as displayed in Fig. 2.4,  $\sigma(\pi^+n \rightarrow K^+\Sigma^0) \gg \sigma(\pi^+n \rightarrow K^0\Sigma^+)$ . But when the charge sums are  $Q = -1$  and  $2$ , only the (c)  $\pi^-n \rightarrow K^0\Sigma^-$  and the (d)  $\pi^+p \rightarrow K^+\Sigma^+$  channels are possible, respectively, and  $t$ -channel exchange is also allowed for each of them, as shown in Fig. 2.5.



### 2.2.2 Formula

For a two-body scattering process,  $A + B \rightarrow C + D$ , we can express the scattering amplitude  $\mathcal{M}$  as a function of Lorentz invariant kinematic variables such as the Mandelstam variables  $s$ ,  $t$ , and  $u$ . From the following relation

$$s + t + u = \sum_i^4 M_i^2, \quad (2.3)$$

where  $M_i$  is the rest mass of initial and final particle  $i$ , it is possible to reduce to two independent values; for example,  $\mathcal{M}(s, t)$  or  $\mathcal{M}(s, u)$ .

To derive the Regge theory [65], we start with the partial-wave expansion for the amplitude  $A(s, t)$  in the physical region of the  $t$ -channel ( $s < 0$ ,  $t > 4M^2$ )

$$A(s, t) = 16\pi \sum_{l=0}^{\infty} (2l+1) A_l(t) P_l(z_t), \quad (2.4)$$

where

$$z_t = \cos \theta_t = 1 + \frac{2s}{t - 4M^2}, \quad (2.5)$$

in the equal-mass case. When  $s$  is large enough, the Legendre polynomials approximate to

$$\begin{aligned} P_l(z) &= \frac{1}{2^l l!} \frac{d^l}{dz^l} (z^2 - 1)^l \\ &\simeq \frac{1}{2^l l!} \frac{d^l}{dz^l} z^{2l} \\ &= \frac{1}{2^l l!} \frac{(2l)!}{l!} z^l, \end{aligned} \quad (2.6)$$

that is,  $P_l(z) \sim z^l$  and  $A(s, t) \sim s^l$ . After truncating the sum over the angular momentum  $l$  at a certain maximum value  $l_{\max}$ , we would like to perform an analytical continuation of Eq. (2.4) to the physical region of  $s$ -channel scattering ( $t < 0$  and  $s$  is large).

To achieve it, we first divide the amplitude  $A(s, t)$  in Eq. (2.4) into  $A_l^\pm(t)$ ,

$$A_l^\pm(t) = \begin{cases} A_l(t) & l \text{ even} \\ A_l(t) & l \text{ odd} \end{cases}, \quad (2.7)$$

then it is organized as

$$A^\pm(s, t) = 8\pi \sum_{l=0}^{\infty} (2l+1) A_l^\pm(t) (P_l(z_t) \pm P_l(-z_t)), \quad (2.8)$$

because of  $P_l(-z) = (-1)^l P_l(z)$ . The amplitudes  $A^\pm$  are referred to as even- and odd-signatured amplitudes.

Cauchy's theorem is employed to rewrite the partial-wave expansions as integrals. Together with Residue theorem defined by

$$\oint_C f dz = 2\pi i \sum_{n=1}^N \text{Res} f(z_n), \quad \text{Res} f(a) = \text{Res} \frac{g(a)}{h(a)} = \lim_{z \rightarrow a} \frac{g(z)}{h'(z)}, \quad (2.9)$$

Eq. (2.8) is rewritten as

$$A^\pm(s, t) = 4\pi i \int_C dl (2l+1) A^\pm(l, t) \frac{P_l(-z_t) \pm P_l(z_t)}{\sin(\pi l)}. \quad (2.10)$$

Here the contour  $C$  is chosen as Fig. 2.6.

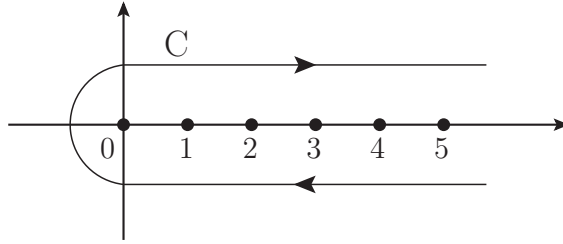


FIGURE 2.6: Integration Contour.

The crucial point of Regge theory is that the poles of the amplitude in the complex  $l$ -plane are closely related to bound or resonance states. The poles are known as Regge poles, or reggeons, and are identified as 'Regge trajectories'  $\alpha(t)$ . These trajectories connect hadrons with their families which have the same internal quantum numbers (isospin, strangeness, charm, baryon number, etc.):  $\alpha(M^2) = J$ , where  $M$  and  $J$  are the mass and the spin of a related hadron, respectively.

We can continue this partial-wave expansion from the physical  $t$ -channel region ( $s < 0, t > 4M^2$ ) analytically to the physical region of high-energy  $s$ -channel scattering ( $t < 0$ ). We finally obtain

$$A^\pm(s, t) \sim \sum_i \beta_i^\pm(t) \Gamma(-\alpha_i^\pm(t)) (1 \pm e^{-i\pi\alpha_i^\pm(t)}) \left(\frac{s}{s_0}\right)^{\alpha_i^\pm(t)}, \quad (2.11)$$

which is the Regge representation for  $A^\pm(s, t)$ . The factors

$$\xi_\alpha^\pm = 1 \pm e^{-i\pi\alpha_i^\pm(t)} \quad (2.12)$$

are called signature factors and  $s_0$  is a scale parameter with the dimensions of squared mass. The phase of the amplitude is determined by this signature factor since other terms are known to be real in the  $s$ -channel physical region. Now, we are able to describe high energy regions for the scattering process  $A + B \rightarrow C + D$ , which has a strong link with the collection of resonances of low-energy process in another crossing channel,  $A + \bar{C} \rightarrow \bar{B} + D$ .

### 2.2.3 Unitarity

It is also interesting to examine only a single term of the amplitude written in Eq. (2.4). Then the problem of series convergence is temporarily avoided and the following is obtained

$$\begin{aligned} A(s, t) &= 16\pi(2J+1)A_J(t)P_J\left(1 + \frac{2s}{t-4m^2}\right) \\ &\sim f(t)s^J. \end{aligned} \quad (2.13)$$

Using the optical theorem

$$\sigma_{12}^{\text{Tot}} = \frac{1}{2|p_1|\sqrt{s}} \text{Im}A(s, t=0), \quad (2.14)$$

$A(s, t=0)$  being the elastic scattering amplitude, we can derive

$$\sigma^{\text{Tot}} \sim s^{J-1}, \quad (2.15)$$

at large  $s$ . However, it violates the unitarity when resonances of higher spins are exchanged ( $J \geq 2$ ). The Froissart bound [66] tells us that

$$\sigma^{\text{Tot}}(s) \leq \text{constant} \times \log^2(s/s_0). \quad (2.16)$$

Thus, it is indeed natural to include all the possible hadrons which lie on the same trajectory to conserve the unitarity.

### 2.2.4 Regge trajectories

In numerical calculations, we need to know the actual value of the Regge trajectory,  $\alpha(t)$ . As mentioned already, it is a collection of hadrons of the squared mass  $M^2(t > 0)$

with the spin  $J$ .

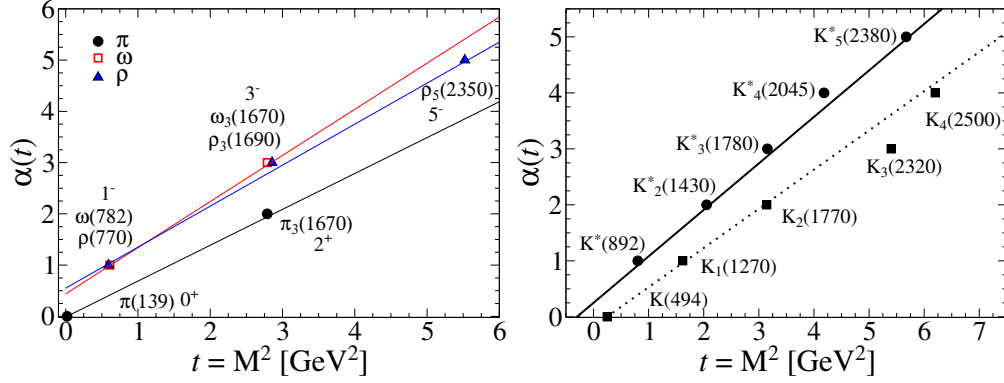


FIGURE 2.7:  $\pi$ ,  $\omega$ , and  $\rho$  Regge trajectories (left panel) and  $K$  and  $K^*$  trajectories (right panel).

Figure 2.7 displays the meson trajectories for the nonstrange (strange) sector in the left (right) panel. For the nonstrange sector, the  $\omega$  and  $\rho$  trajectories overlap each other and the  $\pi$  trajectory is located below them. The trajectory lines are determined from the Chew-Frautschi plots [20]. The values are given by

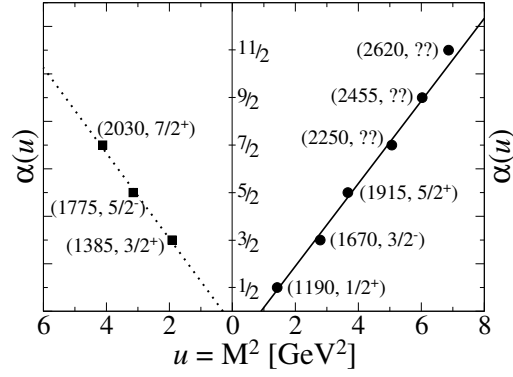
$$\begin{aligned}\alpha_\pi(t) &= 0.7(t - M_\pi^2), \\ \alpha_\rho(t) &= 0.55 + 0.8t, \\ \alpha_\omega(t) &= 0.44 + 0.9t.\end{aligned}\tag{2.17}$$

For the strange sector, the resonances are richer than the nonstrange one. The  $K$  and  $K^*$  Regge trajectories are chosen as

$$\begin{aligned}\alpha_K(t) &= 0.7(t - M_K^2) \\ \alpha_{K^*}(t) &= 0.25 + 0.83t.\end{aligned}\tag{2.18}$$

Usually, Regge trajectories have two signatures. One contains only odd spins of hadrons. The other does only even spins. It is notable that the odd ( $K_1(1270)$ ,  $K_3(2320)$ ) and even ( $K(494)$ ,  $K_2(1770)$ ,  $K_4(2500)$ ) trajectories are almost degenerated each other for the  $K$  trajectory. The  $K^*$  trajectory exhibits this behavior too.

The baryon trajectories are also need to be examined since the Regge approach is applicable to the backward regions in the  $u$  channel. For example, for the  $\Sigma$  trajectory, the higher spins of some resonances are unknown. Thus assuming that the quantum numbers of those resonances are fixed, we are able to depict the  $\Sigma(1190)$  and  $\Sigma^*(1385)$  Regge trajectories in Fig 2.8.

FIGURE 2.8:  $\Sigma$  and  $\Sigma^*$  Regge trajectories.

The Regge lines are determined from Ref [67] and given by

$$\begin{aligned}\alpha_{\Sigma(1190)}(u) &= -0.79 + 0.87u, \\ \alpha_{\Sigma^*(1385)}(u) &= -0.27 + 0.9u.\end{aligned}\tag{2.19}$$

The nucleon trajectories are classified as

$$\begin{aligned}\alpha_{N(938)}(u) &= -0.34 + 0.99u, \\ \alpha_{N^*(1520)}(u) &= 0.63 + 0.89u, \\ \alpha_{N^*(1675)}(u) &= 0 + 0.9u.\end{aligned}\tag{2.20}$$

Other baryon trajectories read

$$\begin{aligned}\alpha_{\Delta}(u) &= 0.07 + 0.92u, \\ \alpha_{\Lambda}(u) &= -0.65 + 0.94u, \\ \alpha_{\Xi}(u) &= -0.95 + 0.84u.\end{aligned}\tag{2.21}$$

The duality ideas, supported by this amazing linearity of Regge trajectories, via the Veneziano amplitude, brought about the concept of hadronic strings and the advance on string theories [63].

### 2.2.5 General features

The Regge theory has the advantage that it determines the asymptotic behavior of the cross section,

$$\frac{d\sigma}{dt}(s \rightarrow \infty, t \rightarrow 0) \propto s^{2\alpha(t)-2},\tag{2.22}$$

at high energies. Among various contributions of Regge trajectories (reggeons), the dominance is governed by the magnitude of the intercept,  $\alpha(0)$ . For example, the vector reggeon is more prominent than the pseudoscalar reggeon.

The gamma function contained in Eq. 2.11 has a relation to the Feynman propagator  $1/(t - M^2)$ . Using the definition of the gamma function

$$\begin{aligned}\Gamma(x) &= (x-1)\Gamma(x-1) \quad (x > 1), \\ \Gamma(-x) &= \frac{\Gamma(1-x)}{-x} \quad (x < 0),\end{aligned}\tag{2.23}$$

we can derive that

$$\Gamma[-\alpha(t)] = \frac{\Gamma[1-\alpha(t)]}{-\alpha(t)} = \frac{\Gamma[1-(t-M_{\text{ps}}^2)\alpha']}{(t-M_{\text{ps}}^2)\alpha'} \simeq \frac{1}{(t-M_{\text{ps}}^2)} \frac{-1}{\alpha'},\tag{2.24}$$

with  $\alpha(t) = (t-M_{\text{ps}}^2)\alpha'$ . It implies that the closer we go to the pole, the more the results of the Regge model will become similar to those of the tree-level Feynman diagram model.

## Chapter 3

# $K^*\Sigma$ photoproduction

In chapter 1, we have mentioned that the  $K^*Y$  channel can be a good opportunity for investigating the nucleon resonances which lie near their thresholds, 2.08 GeV for the  $K^*\Sigma$  channel and 2.01 GeV for the  $K^*\Lambda$  one. First of all, in this section, the  $K^*\Sigma$  photoproduction off the nucleon target is studied in a fully relativistic manner [43].

### 3.1 Motivation

Recently, new experimental data for the total and differential cross sections for the reaction  $\gamma p \rightarrow K^{*+}\Sigma^0$  were announced by the CLAS Collaboration at the Thomas Jefferson National Accelerator Facility (TJNAF) with high precision [68]. The Collaboration at the Super Photon Ring-8 GeV (SPRING-8) also reported new data for the spin-density matrix elements for the reaction  $\gamma p \rightarrow K^{*0}\Sigma^+$  [69]. As regards the  $K^{*0}\Sigma^+$  production channel, earlier experiments already exist, one is from the CBELSA/TAPS Collaboration at the Electron Stretcher and Accelerator (ELSA) [70] and the other is from the CLAS Collaboration [71, 72]. Considering all these data accumulated so far, we are nearer than ever to gaining an insight into both the  $\gamma p \rightarrow K^{*0}\Sigma^+$  and the  $\gamma p \rightarrow K^{*+}\Sigma^0$  reaction mechanisms together.

These two reaction processes have been studied theoretically using an effective Lagrangian method [73] as well as a chiral quark model [74].  $K^*$  photoproduction enables us to study the  $\kappa$  exchange contribution, which is forbidden to  $K$  photoproduction because angular momentum and parity are violated in the  $\gamma K\kappa$  interaction. It turned out that  $\kappa$  exchange should play an important role in the  $\gamma p \rightarrow K^{*0}\Sigma^+$  reaction mechanism [73]. Subsequently, the experimental data from the LEPS Collaboration supported

the importance of scalar-meson exchange indeed [69]. Nevertheless, those previous theoretical results are still far from the new CLAS data [68]. Thus, we think it is worthwhile to investigate these mechanisms again more systematically.

We employ a tree-level effective Lagrangian method as done in Ref. [73], in which several lowest-order Feynman diagrams are considered to construct scattering amplitudes. They are the  $t$ -channel contribution ( $K^*$ -,  $K$ -, and  $\kappa$ - exchanges), the  $s$ -channel diagrams ( $N(938)$ - and  $\Delta(1232)$ -pole exchanges), and the  $u$ -channel diagrams ( $\Lambda(1116)$ -,  $\Sigma(1190)$ -pole, and  $\Sigma^*(1385, 3/2^+)$  exchanges). In the present work [43, 75], besides those background terms, various baryon resonances are taken into account such as  $D_{13}(2080)$ ,  $S_{11}(2090)$ ,  $G_{17}(2190)$ ,  $D_{15}(2200)$ ,  $S_{31}(2150)$ ,  $G_{37}(2200)$ , and  $F_{37}(2390)$  in the  $s$  channel [76]. Note that  $\Delta$  resonances are also allowed here because of isospin conservation in addition to nucleon resonances. These resonances have not been considered in the previous theoretical work [73] and thus lead us to a more challenging area.

### 3.2 Formalism

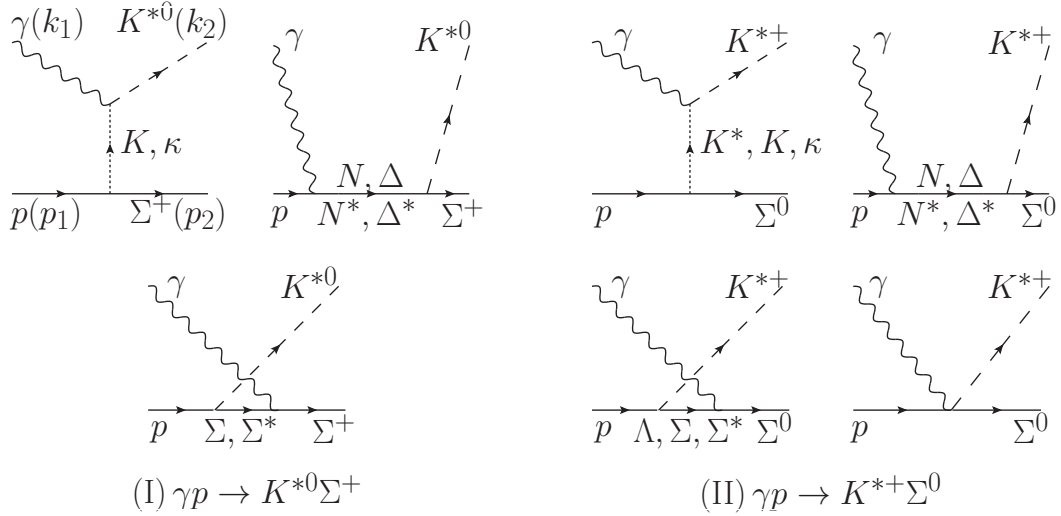


FIGURE 3.1: Tree-level Feynman diagrams for the  $\gamma p \rightarrow K^* \Sigma$ .

We first define the effective Lagrangians for each vertex from the Feynman diagrams. The relevant and generic tree-level diagrams for the reaction  $\gamma p \rightarrow K^* \Sigma$  are depicted in Fig. 3.1.  $k_1$  and  $p_1$  are the momenta of the initial photon and nucleon, respectively, while  $k_2$  and  $p_2$  denote those of the final  $K^*$  and  $\Sigma$ , respectively. For convenience, we classify this process as  $K^{*0} \Sigma^+$  and  $K^{*+} \Sigma^0$  channels, respectively, from now on,

$$(I) \gamma p \rightarrow K^{*0} \Sigma^+, \quad (II) \gamma p \rightarrow K^{*+} \Sigma^0. \quad (3.1)$$



Commonly included for both channels are  $K$  and  $\kappa$  meson exchanges in the  $t$  channel,  $N$ ,  $\Delta$ ,  $N^*$ , and  $\Delta^*$  baryon exchanges in the  $s$  channel, and  $\Sigma$  and  $\Sigma^*(1385)$  hyperons in the  $u$  channel.  $K^*$  exchange is allowed only for the (II)  $K^{*+}\Sigma^0$  channel but not for the (I)  $K^{*0}\Sigma^+$  one due to its electrically neutral vertex of  $\gamma K^* \bar{K}^*$  provided we ignore the magnetic and quadratic moments of  $K^*$ .  $\Lambda$  exchange is also absent from the (I)  $K^{*0}\Sigma^+$  channel because of charge conservation. Consequently, contact term is required only for the (II)  $K^{*+}\Sigma^0$  channel to satisfy the Ward-Takahashi (WT) identity.

The scattering amplitude to each channel can be written as

$$\mathcal{M} = \varepsilon_\nu^* \bar{u}_\Sigma \mathcal{M}^{\mu\nu} u_N \epsilon_\mu, \quad (3.2)$$

where the Dirac spinors of the nucleon and  $\Sigma$  are represented by  $u_N$  and  $u_\Sigma$ , respectively, and  $\epsilon_\mu$  and  $\varepsilon_\mu$  denote the polarization vectors of the photon and  $K^*$ , respectively:

$$\epsilon_\mu = \begin{cases} \epsilon_\parallel = (0, 1, 0, 0) \\ \epsilon_\perp = (0, 0, 1, 0) \end{cases}, \quad \varepsilon_\mu = \begin{cases} \varepsilon_1 = (0, \cos \theta, 0, -\sin \theta) \\ \varepsilon_2 = (0, 0, 1, 0) \\ \varepsilon_3 = \frac{1}{M_{K^*}} (k_{K^*}, E_{K^*} \sin \theta, 0, E_{K^*} \cos \theta) \end{cases}, \quad (3.3)$$

satisfying  $\epsilon^2 = \varepsilon^2 = -1$ , and otherwise zero.  $\theta$  is the scattering angle between the incoming photon and the outgoing  $K^*$  meson in the center-of-mass (COM) frame.

### 3.2.1 $K^*$ , $K$ , and $\kappa$ exchanges in the $t$ channel

The effective Lagrangians are constructed to satisfy symmetry principles. The  $t$ -channel scattering amplitudes are obtained from the following Lagrangians:

$$\begin{aligned} \mathcal{L}_{\gamma K^* K^*} &= -ie_{K^*} A^\mu (K^{*- \nu} K_{\mu\nu}^{*+} - K_{\mu\nu}^{*-} K^{*+ \nu}), \\ \mathcal{L}_{\gamma K^* K} &= g_{\gamma K K^*} \varepsilon^{\mu\nu\alpha\beta} (\partial_\mu A_\nu) (\partial_\alpha \bar{K}_\beta^*) K + \text{H.c.}, \\ \mathcal{L}_{\gamma K^* \kappa} &= g_{\gamma K^* \kappa} F^{\mu\nu} \bar{\kappa} K_{\mu\nu}^* + \text{H.c.}, \end{aligned} \quad (3.4)$$

for the electromagnetic interactions. Here  $A_\mu$ ,  $K_\mu^*$ ,  $K$ , and  $\kappa$  stand for the photon, the fields of  $K^*(892, 1^-)$ ,  $K(494, 0^-)$ , and  $\kappa(800, 0^+)$  mesons, respectively [1]. The field tensors for the photon and the  $K^*$  meson are defined by  $F_{\mu\nu} = \partial_\mu A_\nu - \partial_\nu A_\mu$  and  $K_{\mu\nu}^* = \partial_\mu K_\nu^* - \partial_\nu K_\mu^*$ , respectively.  $e_{K^*}$  denotes the unit electric charge  $e = \sqrt{4\pi\alpha_E}$  with the fine-structure constant  $\alpha_E = 1/137.04$ .

The coupling constants  $g_{\gamma K^* K}$  are determined from the experimental data of the  $K^*$  decay width and the corresponding decay modes of  $\Gamma(K^* \rightarrow K\gamma)$  [1]. The decay width

is expressed in terms of the coupling constant  $g_{\gamma K^* K}$

$$\Gamma(K^* \rightarrow K\gamma) = g_{\gamma K^* K}^2 \frac{k_\gamma^3}{12\pi}, \quad (3.5)$$

where  $k_\gamma$  is the three-momentum of the decaying particle

$$k_\gamma = \frac{M_{K^*}^2 - M_K^2}{2M_{K^*}}. \quad (3.6)$$

After calculating each decay width as [1]

$$\begin{aligned} \Gamma(K^{*\pm} \rightarrow K^\pm \gamma) &\approx 50.8 \text{ MeV} (9.9 \cdot 10^{-4}) = 50 \text{ KeV}, \\ \Gamma(K^{*0} \rightarrow K^0 \gamma) &\approx 47.4 \text{ MeV} (2.39 \cdot 10^{-3}) = 113 \text{ KeV}, \end{aligned} \quad (3.7)$$

we can easily obtain

$$g_{\gamma K^* K}^{\text{charged}} = 0.254 \text{ GeV}^{-1}, \quad g_{\gamma K^* K}^{\text{neutral}} = -0.388 \text{ GeV}^{-1}, \quad (3.8)$$

using Eq. (3.5).

The vector-meson dominance model is employed to determine the coupling constants  $g_{\gamma K^* \kappa}$  [77]:

$$g_{\gamma K^* \kappa}^{\text{charged}} = -0.119 e \text{ GeV}^{-1}, \quad g_{\gamma K^* \kappa}^{\text{neutral}} = -2g_{\gamma K^* \kappa}^{\text{charged}}. \quad (3.9)$$

There remains some uncertainty for the  $\kappa$  meson's parameters since it is poorly established. In the present work, they are chosen as  $M_\kappa = 800 \text{ MeV}$  for the mass and  $\Gamma_\kappa = 550 \text{ MeV}$  for the decay width.

The strong interactions are described by the following Lagrangians:

$$\begin{aligned} \mathcal{L}_{K^* NY} &= -g_{K^* NY} \left[ \bar{K}^{*\mu} \bar{Y} \gamma_\mu - \frac{\kappa_{K^* NY}}{2M_N} \partial^\nu \bar{K}^{*\mu} \bar{Y} \sigma_{\mu\nu} \right] N + \text{H.c.}, \\ \mathcal{L}_{KN\Sigma} &= -ig_{KN\Sigma} \bar{K} \bar{\Sigma} \gamma_5 N + \text{H.c.}, \\ \mathcal{L}_{\kappa N\Sigma} &= -g_{\kappa N\Sigma} \bar{\kappa} \bar{\Sigma} N + \text{H.c.}, \end{aligned} \quad (3.10)$$

where  $Y$  designates  $\Lambda$  or  $\Sigma$  fields in which  $\Sigma = \boldsymbol{\tau} \cdot \boldsymbol{\Sigma}$  and  $\boldsymbol{\tau}$  are the Pauli matrices.  $N$ ,  $\Lambda$ , and  $\Sigma$  stand for the nucleon,  $\Lambda(1116, 1/2^+)$ , and  $\Sigma(1190, 1/2^+)$  baryon fields, respectively [1]. The corresponding coupling constants for the  $K^*$ - and  $\kappa$ - interactions are taken from the Nijmegen soft-core model (NSC97a) [78]:

$$g_{K^* N\Lambda} = -4.26, \quad \kappa_{K^* N\Lambda} = 2.66, \quad g_{K^* N\Sigma} = -2.46, \quad \kappa_{K^* N\Sigma} = -0.47, \quad g_{\kappa N\Sigma} = -5.32. \quad (3.11)$$

The value of  $g_{KN\Sigma}$  is calculated by using the SU(3) flavor-symmetry relation, which gives  $g_{KN\Sigma} = 3.58$ .

The scattering amplitudes for  $t$ -channel exchanges are summarized as

$$\begin{aligned}
\mathcal{M}_{K^*}^{\mu\nu} &= I_{K^*} \frac{e_{K^*} g_{K^*N\Sigma}}{t - (M_{K^*} - i\Gamma_{K^*}/2)^2} (2k_2^\mu g^{\nu\alpha} - k_2^\alpha g^{\mu\nu} + k_1^\nu g^{\mu\alpha}) \\
&\quad \times \left[ g_{\alpha\beta} - \frac{(k_1 - k_2)_\alpha (k_1 - k_2)_\beta}{M_{K^*}^2} \right] \left[ \gamma^\beta - \frac{i\kappa_{K^*N\Sigma}}{2M_N} \sigma^{\beta\delta} (k_1 - k_2)_\delta \right], \\
\mathcal{M}_K^{\mu\nu} &= I_K \frac{ig_{\gamma KK^*} g_{KN\Sigma}}{t - M_K^2} \epsilon^{\mu\nu\alpha\beta} k_{1\alpha} k_{2\beta} \gamma_5, \\
\mathcal{M}_\kappa^{\mu\nu} &= I_\kappa \frac{-2g_{\gamma K^*\kappa} g_{\kappa N\Sigma}}{t - (M_\kappa - i\Gamma_\kappa/2)^2} (k_1 \cdot k_2 g^{\mu\nu} - k_1^\nu k_2^\mu). \tag{3.12}
\end{aligned}$$

Note that each decay width is included by replacing  $M$  in the propagator by  $M - i\Gamma/2$  in the  $K^*$  and  $\kappa$  amplitudes. The  $K^*$  decay width is chosen as  $\Gamma_{K^*} = 50.8 \text{ MeV}$  [1].

### 3.2.2 $N$ and $\Delta$ exchanges in the $s$ channel

The effective Lagrangians corresponding to  $s$ -channel exchanges are expressed by

$$\begin{aligned}
\mathcal{L}_{\gamma NN} &= -\bar{N} \left[ e_N \not{A} - \frac{e\kappa_N}{2M_N} \sigma_{\mu\nu} \partial^\nu A^\mu \right] N, \\
\mathcal{L}_{\gamma N\Delta} &= e\bar{\Delta}_\mu \left[ \frac{ig_1}{2M_N} \gamma_\nu \gamma_5 + \frac{g_2}{(2M_N)^2} \gamma_5 \partial_\nu \right] N F^{\mu\nu} + \text{H.c.}, \\
\mathcal{L}_{K^*\Delta\Sigma} &= -\frac{if_{K^*\Delta\Sigma}}{2M_{K^*}} \bar{\Delta}^\mu \gamma^\nu \gamma_5 \Sigma K_{\mu\nu}^* + \text{H.c.}, \tag{3.13}
\end{aligned}$$

and by  $\mathcal{L}_{K^*N\Lambda}$  written in Eq. (3.10). Here  $e_N$  corresponds to the unit electric charge  $e$  for proton and 0 for neutron interactions, respectively. The anomalous magnetic moments of the nucleon are given by [1]

$$\kappa_n = -1.91, \quad \kappa_p = +1.79. \tag{3.14}$$

The  $\Delta$  field,  $\Delta(1232, 3/2^+)$ , is described by the Rarita-Schwinger formalism [79, 80]. The electric and magnetic couplings are chosen as  $g_1 = 4.13$  and  $g_2 = 4.74$  using the experimental data for the helicity amplitudes [81, 82]. The coupling  $f_{K^*\Delta\Sigma}$  is estimated using the SU(3) flavor-symmetry relation and the quark-model prediction:

$$f_{K^*\Delta\Sigma} = -\frac{2M_{K^*}}{M_\rho} f_{\rho N\Delta} = -12.8, \tag{3.15}$$

with  $f_{\rho N\Delta} = 5.5$  [83].

The scattering amplitudes for  $N$  and  $\Delta$  exchanges are organized as follows:

$$\begin{aligned}
\mathcal{M}_N^{\mu\nu} &= I_N \frac{g_{K^*N\Sigma}}{s - M_N^2} \left[ \gamma^\nu - \frac{i\kappa_{K^*N\Sigma}}{2M_N} \sigma^{\nu\alpha} k_{2\alpha} \right] \\
&\quad \times (k_1 + p_1 + M_N) \left[ e_N \gamma^\mu + \frac{ie\kappa_N}{2M_N} \sigma^{\mu\beta} k_{1\beta} \right],
\end{aligned}$$

$$\begin{aligned} \mathcal{M}_\Delta^{\mu\nu} &= I_\Delta \frac{f_{K^*\Delta\Sigma}}{s - (M_\Delta - i\Gamma_\Delta/2)^2} \frac{e}{2M_{K^*}} \gamma_\rho \gamma_5 (k_2^\beta g^{\nu\rho} - k_2^\rho g^{\nu\beta}) \\ &\times \Delta_{\beta\alpha} \left[ \frac{g_1}{2M_N} \gamma_\delta - \frac{g_2}{(2M_N)^2} p_{1\delta} \right] \gamma_5 (k_1^\alpha g^{\mu\delta} - k_1^\delta g^{\mu\alpha}), \end{aligned} \quad (3.16)$$

where  $\Gamma_\Delta \sim 116 \text{ MeV}$  [1]. The detailed form of the Rarita-Schwinger spin projection  $\Delta_{\beta\alpha}$  is referred to the Appendix B.

### 3.2.3 $\Lambda$ , $\Sigma$ , and $\Sigma^*$ exchanges in the $u$ channel

The electromagnetic effective Lagrangians for the hyperon vertices are defined by

$$\begin{aligned} \mathcal{L}_{\gamma\Sigma\Lambda} &= \frac{e\mu_{\Sigma\Lambda}}{2M_N} \bar{\Sigma} \sigma_{\mu\nu} \partial^\nu A^\mu \Lambda, \\ \mathcal{L}_{\gamma\Sigma\Sigma} &= -\bar{\Sigma} \left[ e_\Sigma \not{A} - \frac{e\kappa_\Sigma}{2M_N} \sigma_{\mu\nu} \partial^\nu A^\mu \right] \Sigma, \\ \mathcal{L}_{\gamma\Sigma\Sigma^*} &= e\bar{\Sigma}_\mu^* \left[ \frac{ig_{\gamma\Sigma\Sigma^*}^V}{2M_N} \gamma_\nu \gamma_5 + \frac{g_{\gamma\Sigma\Sigma^*}^T}{(2M_N)^2} \gamma_5 \partial_\nu \right] \Sigma F^{\mu\nu} + \text{H.c.}, \end{aligned} \quad (3.17)$$

and the strong interactions for the hyperon ones by

$$\begin{aligned} \mathcal{L}_{K^*N\Sigma^*} &= i \frac{f_{K^*N\Sigma^*}^{(1)}}{2M_{K^*}} \bar{N} \gamma^\nu \gamma_5 \Sigma^{*\mu} K_{\mu\nu}^* + \frac{f_{K^*N\Sigma^*}^{(2)}}{(2M_{K^*})^2} \partial^\nu \bar{N} \gamma_5 \Sigma^{*\mu} K_{\mu\nu}^* \\ &\quad - \frac{f_{K^*N\Sigma^*}^{(3)}}{(2M_{K^*})^2} \bar{N} \gamma_5 \Sigma^{*\mu} \partial^\nu K_{\mu\nu}^* + \text{H.c.}, \end{aligned} \quad (3.18)$$

and  $\mathcal{L}_{K^*N\Lambda}$  written in Eq. (3.10). Here the transition magnetic moment between the fields of  $\Sigma$  and  $\Lambda$  is known as  $\mu_{\Sigma\Lambda} = 1.61 \pm 0.08$  [1] and the  $(e_{\Sigma^+}, e_{\Sigma^0}, e_{\Sigma^-})$  correspond to  $(1, 0, -1)$ , respectively. The anomalous magnetic moments of the  $\Sigma$  are [1]

$$\kappa_{\Sigma^+} = +1.46, \quad \kappa_{\Sigma^0} = +0.65, \quad \kappa_{\Sigma^-} = -0.16. \quad (3.19)$$

In order to determine the coupling constants  $g_{\gamma\Sigma\Sigma^*}^{V,T}$ , the experimental data for the  $\Sigma^* \rightarrow \Sigma\gamma$  radiative decay is needed. But only the upper limits of the hyperon decay rates are known [84]. Moreover,  $\Sigma^{*-} \rightarrow \Sigma^-\gamma$  is known to be  $U$ -spin forbidden, which means that its decay rate vanishes in the exact  $SU(3)$  symmetry. Instead, these decay rates were estimated within several different theoretical predictions [85–90]. Since Ref. [89] has computed the  $E2/M1$  ratio as well as the hyperon radiative decay rates, we apply the results of Ref. [89], so that  $g_{\gamma\Sigma\Sigma^*}^{V,T}$  are calculated as follows:

$$\begin{aligned} g_{\gamma\Sigma\Sigma^*}^{V+} &= +2.66, & g_{\gamma\Sigma\Sigma^*}^{T+} &= +0.74, \\ g_{\gamma\Sigma\Sigma^*}^{V0} &= +1.10, & g_{\gamma\Sigma\Sigma^*}^{T0} &= +0.55, \\ g_{\gamma\Sigma\Sigma^*}^{V-} &= +0.49, & g_{\gamma\Sigma\Sigma^*}^{T-} &= -0.39. \end{aligned} \quad (3.20)$$

The coupling constant  $f_{K^*N\Sigma^*}^{(1)}$  is chosen as  $-5.21$  by SU(3) flavor symmetry. Considering the possible Lorentz structure for the  $\Sigma^*$  to the vector-meson and the nucleon, we can construct the interaction Lagrangian in terms of three terms. The experimental and theoretical information on  $f_{K^*N\Sigma^*}^{(2,3)}$  are not well known thus these terms are excluded in the present work, which seems to be reasonable, since these two coupling constants are smaller than  $f_{K^*N\Sigma^*}^{(1)}$ .

The scattering amplitudes for hyperon exchanges are summarized as follows:

$$\begin{aligned}
\mathcal{M}_\Lambda^{\mu\nu} &= I_\Lambda \frac{g_{K^*N\Lambda}}{u - M_\Lambda^2} \frac{ie\mu_{\Sigma\Lambda}}{2M_N} \sigma^{\mu\alpha} k_{1\alpha} \\
&\quad \times (\not{p}_2 - \not{k}_1 + M_\Lambda) \left[ \gamma^\nu - \frac{i\kappa_{K^*N\Lambda}}{2M_N} \sigma^{\nu\beta} k_{2\beta} \right], \\
\mathcal{M}_\Sigma^{\mu\nu} &= I_\Sigma \frac{g_{K^*N\Sigma}}{u - M_\Sigma^2} \left[ e_\Sigma \gamma^\mu + \frac{ie\kappa_\Sigma}{2M_N} \sigma^{\mu\alpha} k_{1\alpha} \right] \\
&\quad \times (\not{p}_2 - \not{k}_1 + M_\Sigma) \left[ \gamma^\nu - \frac{i\kappa_{K^*N\Sigma}}{2M_N} \sigma^{\nu\beta} k_{2\beta} \right], \\
\mathcal{M}_{\Sigma^*}^{\mu\nu} &= I_{\Sigma^*} \frac{f_{K^*N\Sigma^*}^{(1)}}{u - (M_{\Sigma^*} - i\Gamma_{\Sigma^*}/2)^2} \frac{e}{2M_{K^*}} \left[ \frac{g_1}{2M_N} \gamma_\rho + \frac{g_2}{(2M_N)^2} p_{2\rho} \right] \\
&\quad \times (k_1^\beta g^{\rho\mu} - k_1^\rho g^{\beta\mu}) \gamma_5 \Delta_{\beta\alpha} \gamma_\delta \gamma_5 (k_2^\alpha g^{\nu\delta} - k_2^\delta g^{\alpha\nu}), \tag{3.21}
\end{aligned}$$

where  $\Gamma_{\Sigma^*} = 36$  MeV [1]. Similarly to the case of  $\Delta$  exchange, the form of the Rarita-Schwinger spin projection  $\Delta_{\beta\alpha}$  is referred to the Appendix B.

### 3.2.4 Contact term

In the case of the (II)  $K^{*+}\Sigma^0$  channel, contact term is included by the minimal gauge substitution  $\partial^\mu \rightarrow ieA^\mu$  to the  $K^*N\Sigma$  interaction

$$\mathcal{L}_{\gamma K^*N\Sigma} = -\frac{ieg_{K^*N\Sigma}\kappa_{K^*N\Sigma}}{2M_N} A^\nu \bar{K}^{*\mu} \bar{\Sigma} \sigma_{\mu\nu} N + \text{H.c.}, \tag{3.22}$$

to conserve the U(1) gauge invariance. The corresponding scattering amplitude reads

$$\mathcal{M}_c^{\mu\nu} = -\frac{ieg_{K^*N\Sigma}\kappa_{K^*N\Sigma}}{2M_N} \sigma^{\mu\nu}. \tag{3.23}$$

### 3.2.5 Baryon resonances in the $s$ channel

We now switch to the  $s$ -channel baryon resonances besides the basic background terms discussed above. They are referred to as PDG resonances and included are  $D_{13}(2080)$ ,  $S_{11}(2090)$ ,  $G_{17}(2190)$ , and  $D_{15}(2200)$  for the nucleon resonances and  $S_{31}(2150)$ ,  $G_{37}(2200)$ , and  $F_{37}(2390)$  for the delta ones [76], which lie near the threshold of the  $K^*\Sigma$  photoproduction process.

The relevant electromagnetic Lagrangians for those resonances read

$$\begin{aligned}
\mathcal{L}_{\gamma NR_{1/2\pm}} &= \frac{eh_1}{2M_N} \bar{N}\Gamma^{(\mp)} \sigma_{\mu\nu} \partial^\nu A^\mu R + \text{H.c.}, \\
\mathcal{L}_{\gamma NR_{3/2\pm}} &= -ie \left[ \frac{h_1}{2M_N} \bar{N}\Gamma_\nu^{(\pm)} - \frac{ih_2}{(2M_N)^2} \partial_\nu \bar{N}\Gamma^{(\pm)} \right] F^{\mu\nu} R_\mu + \text{H.c.}, \\
\mathcal{L}_{\gamma NR_{5/2\pm}} &= e \left[ \frac{h_1}{(2M_N)^2} \bar{N}\Gamma_\nu^{(\mp)} - \frac{ih_2}{(2M_N)^3} \partial_\nu \bar{N}\Gamma^{(\mp)} \right] \partial^\alpha F^{\mu\nu} R_{\mu\alpha} + \text{H.c.}, \\
\mathcal{L}_{\gamma NR_{7/2\pm}} &= ie \left[ \frac{h_1}{(2M_N)^3} \bar{N}\Gamma_\nu^{(\pm)} - \frac{ih_2}{(2M_N)^4} \partial_\nu \bar{N}\Gamma^{(\pm)} \right] \partial^\alpha \partial^\beta F^{\mu\nu} R_{\mu\alpha\beta} + \text{H.c.} \quad (3.24)
\end{aligned}$$

according to the spin and parity chosen.  $R$ ,  $R_\mu$ ,  $R_{\mu\alpha}$ , and  $R_{\mu\alpha\beta}$  designate the spin-1/2, spin-3/2, spin-5/2, and spin-7/2 nucleon or delta resonance fields.  $\Gamma^{(\pm)}$  and  $\Gamma_\mu^{(\pm)}$  are defined by

$$\Gamma^{(\pm)} = \begin{pmatrix} \gamma_5 \\ \mathbf{1} \end{pmatrix}, \quad \Gamma_\mu^{(\pm)} = \begin{pmatrix} \gamma_\mu \gamma_5 \\ \gamma_\mu \end{pmatrix}. \quad (3.25)$$

We use the experimental data for the helicity amplitudes  $A_{1,3}$  [76] if possible, otherwise apply the quark-model predictions of Ref. [3] to extract the transition magnetic moments  $h_{1,3}$ . They are related linearly each other. The detailed relations are referred to the Appendix B. In Table 3.1, all the relevant parameters are listed.

	Resonance	$A_1$	$A_3$	$h_1$	$h_2$
$N^*$	$D_{13}(2080)$	-0.020	+0.017	+0.608	-0.620
	$S_{11}(2090)$	+0.012	...	+0.055	...
	$G_{17}(2190)$	-0.034	+0.028	+7.69	-7.17
	$D_{15}(2200)$	-0.002	-0.006	+0.123	+0.011
$\Delta^*$	$S_{31}(2150)$	+0.004	...	+0.018	...
	$G_{37}(2200)$	+0.014	-0.004	-2.31	+2.47
	$F_{37}(2390)$	+0.024	+0.030	-1.89	-1.54

TABLE 3.1: Transition magnetic moments  $h_{1,2}$  in Eqs. (3.24) extracted from the helicity amplitudes  $A_{1,3}$  [ $\text{GeV}^{-\frac{1}{2}}$ ] [3, 76].

The strong interactions are expressed by the following Lagrangians:

$$\begin{aligned}
\mathcal{L}_{K^*\Sigma R_{1/2\pm}} &= \\
&- \frac{1}{2M_N} \bar{R} \left[ g_1 \left( \pm \frac{\Gamma_\mu^{(\mp)} \Sigma \partial^2}{M_R \mp M_N} - i\Gamma^{(\mp)} \partial_\mu \right) - g_2 \Gamma^{(\mp)} \sigma_{\mu\nu} \Sigma \partial^\nu \right] K^{*\mu} + \text{H.c.}, \\
\mathcal{L}_{K^*\Sigma R_{3/2\pm}} &= \\
&i\bar{R}_\mu \left[ \frac{g_1}{2M_N} \Sigma \Gamma_\nu^{(\pm)} \mp \frac{ig_2}{(2M_N)^2} \partial_\nu \Sigma \Gamma^{(\pm)} \pm \frac{ig_3}{(2M_N)^2} \Sigma \Gamma^{(\pm)} \partial_\nu \right] K^{*\mu\nu} + \text{H.c.}, \\
\mathcal{L}_{K^*\Sigma R_{5/2\pm}} &= \bar{R}_{\mu\alpha} \times \\
&\left[ \frac{g_1}{(2M_N)^2} \Sigma \Gamma_\nu^{(\mp)} \pm \frac{ig_2}{(2M_N)^3} \partial_\nu \Sigma \Gamma^{(\mp)} \mp \frac{ig_3}{(2M_N)^3} \Sigma \Gamma^{(\mp)} \partial_\nu \right] \partial^\alpha K^{*\mu\nu} + \text{H.c.}, \\
\mathcal{L}_{K^*\Sigma R_{7/2\pm}} &= -i\bar{R}_{\mu\alpha\beta} \times
\end{aligned}$$

$$\left[ \frac{g_1}{(2M_N)^3} \Sigma \Gamma_\nu^{(\pm)} \mp \frac{ig_2}{(2M_N)^4} \partial_\nu \Sigma \Gamma^{(\pm)} \pm \frac{ig_3}{(2M_N)^4} \Sigma \Gamma^{(\pm)} \partial_\nu \right] \partial^\alpha \partial^\beta K^{*\mu\nu} + \text{H.c.} \quad (3.26)$$

according to the types of spin and parity.

The strong coupling constants  $g_1$ ,  $g_2$ , and  $g_3$  in Eqs. (3.26) can be extracted from the partial-wave decay amplitudes  $G_{s,l}$  predicted by a relativized quark pair creation model [5]:

$$\Gamma_{R \rightarrow K^*\Sigma} = \sum_{s,l} |G_{s,l}|^2, \quad (3.27)$$

where  $\Gamma_{R \rightarrow K^*\Sigma}$  is the decay width of a certain resonance  $R$  into the  $K^*\Sigma$  channel. In Ref [5], the strong decays of nonstrange resonances into the strange final states, such as  $\Lambda(1405)K$ ,  $\Lambda(1520)K$ ,  $\Sigma(1385)K$ ,  $\Lambda K^*$ , and  $\Sigma K^*$ , are organized systematically. In the present work, we aim at studying the role of resonances near the threshold regions. Thus it seems to be fair to take account of the contribution of the lower partial waves. Correspondingly, only the leading terms,  $g_1$ , are considered. The signs of these strong coupling constants are determined phenomenologically. Concerning the values of the decay widths, we use  $\Gamma_R = 300 \text{ MeV}$  in common to reduce the free parameters. We tabulate the relevant parameters in Table 3.2.

	Resonance	$G_{s,l}$	$g_1$
$N^*$	$D_{13}(2080)$	-0.5	-0.238
	$S_{11}(2090)$	-0.9	$\mp 0.909$
	$G_{17}(2190)$	-0.3	+5.63
	$D_{15}(2200)$	+0.2	+1.11
$\Delta^*$	$S_{31}(2150)$	-4.8	+2.54
	$G_{37}(2200)$	+0.5	$\pm 8.32$
	$F_{37}(2390)$	+0.6	+5.02

TABLE 3.2: Strong coupling constants  $g_1$  in Eqs. (3.26) extracted from the decay amplitudes  $G_{s,l}$  [ $\sqrt{\text{MeV}}$ ] [5].

The scattering amplitudes for the resonance terms for each spin and parity finally read

$$\begin{aligned} \mathcal{M}_{R(1/2^\pm)}^{\mu\nu} &= I_R \frac{-ie}{s - M_R^2} \frac{h_{1R_1}}{(2M_N)^2} \left[ g_1 \frac{M_{K^*}^2}{M_R \mp M_N} \Gamma^{\nu(\mp)} \mp ig_2 \Gamma^{(\mp)} \sigma^{\nu\beta} k_{2\beta} \right] \\ &\quad \times (\not{k}_1 + \not{p}_1 + M_R) \Gamma^{(\mp)} \sigma^{\mu\alpha} k_{1\alpha}, \\ \mathcal{M}_{R(3/2^\pm)}^{\mu\nu} &= I_R \frac{e}{s - M_R^2} \left[ \frac{g_1}{2M_N} \Gamma_\rho^{(\pm)} + \frac{g_2}{(2M_N)^2} p_{2\rho} \Gamma^{(\pm)} - \frac{g_3}{(2M_N)^2} k_{2\rho} \Gamma^{(\pm)} \right] \\ &\quad \times \Delta_{\beta\alpha}(R, k_1 + p_1) \left[ \frac{\mu_{R_3}}{2M_N} \Gamma_\delta^{(\pm)} \mp \frac{\bar{\mu}_{R_3}}{(2M_N)^2} \Gamma^{(\pm)} p_{1\delta} \right] \\ &\quad \times (k_2^\beta g^{\nu\rho} - k_2^\rho g^{\nu\beta}) (k_1^\alpha g^{\mu\delta} - k_1^\delta g^{\alpha\mu}), \\ \mathcal{M}_{R(5/2^\pm)}^{\mu\nu} &= I_R \frac{e}{s - M_R^2} \left[ \frac{g_1}{(2M_N)^2} \Gamma_\rho^{(\mp)} + \frac{g_2}{(2M_N)^3} p_{2\rho} \Gamma^{(\mp)} - \frac{g_3}{(2M_N)^3} k_{2\rho} \Gamma^{(\mp)} \right] \\ &\quad \times \Delta_{\beta_1\beta_2;\alpha_1\alpha_2}(R, k_1 + p_1) \left[ \frac{\mu_{R_5}}{(2M_N)^2} \Gamma_\delta^{(\mp)} \pm \frac{\bar{\mu}_{R_5}}{(2M_N)^3} \Gamma^{(\mp)} p_{1\delta} \right] \end{aligned}$$

$$\begin{aligned}
& \times k_2^{\beta_2} (k_2^{\beta_1} g^{\nu\rho} - k_2^\rho g^{\nu\beta_1}) k_1^{\alpha_2} (k_1^{\alpha_1} g^{\mu\delta} - k_1^\delta g^{\alpha_1\mu}), \\
\mathcal{M}_{R(7/2^\pm)}^{\mu\nu} = & I_R \frac{e}{s - M_R^2} \left[ \frac{g_1}{(2M_N)^3} \Gamma_\rho^{(\pm)} + \frac{g_2}{(2M_N)^4} p_{2\rho} \Gamma^{(\pm)} - \frac{g_3}{(2M_N)^4} k_{2\rho} \Gamma^{(\pm)} \right] \\
& \times \Delta_{\beta_1\beta_2\beta_3;\alpha_1\alpha_2\alpha_3}(R, k_1 + p_1) \left[ \frac{\mu_{R7}}{(2M_N)^3} \Gamma_\delta^{(\pm)} \mp \frac{\bar{\mu}_{R7}}{(2M_N)^4} \Gamma^{(\pm)} p_{1\delta} \right] \\
& \times k_2^{\beta_2} k_2^{\beta_3} (k_2^{\beta_1} g^{\nu\rho} - k_2^\rho g^{\nu\beta_1}) k_1^{\alpha_2} k_1^{\alpha_3} (k_1^{\alpha_1} g^{\mu\delta} - k_1^\delta g^{\alpha_1\mu}). \tag{3.28}
\end{aligned}$$

Here the decay widths should be included in the Feynman propagators by replacing  $M_R$  by  $M_R - i\Gamma_R/2$ . The details of the propagators of resonance fields up to spin-7/2 are referred to the Appendix B [91–94].

### 3.2.6 Form factors

The relevant hadrons are not simply pointlike objects. To take account of the finite size effect of hadrons, a phenomenological form factor is included at each vertex. It should be chosen so as to conserve the gauge invariance, if necessary which is supplemented by the inclusion of a contact term. Various efforts have been devoted not to violate the gauge invariance [95–99]. We follow the prescription suggested by Ref. [98].

In the present work, two different types of form factors are taken into account, one is for the mesonic ( $\Phi = K^*, K, \kappa$ ) and the other is for the baryonic ( $B = N, \Delta, \Lambda, \Sigma, \Sigma^*, R$ ) vertices,

$$F_\Phi(q, M_\Phi) = \frac{\Lambda_\Phi^2 - M_\Phi^2}{\Lambda_\Phi^2 - q^2}, \quad F_B(q, M_B) = \frac{\Lambda_B^4}{\Lambda_B^4 + (q^2 - M_B^2)^2}. \tag{3.29}$$

Here  $q$  denotes the off-shell transfer momentum of the relevant hadron in each channel. The cutoff masses,  $\Lambda_\Phi$  and  $\Lambda_B$ , are determined by fitting to the experimental data.

The problem happens when the amplitude itself breaks the gauge invariance. For example, in the process of the (I)  $K^{*0}\Sigma^+$  channel, the electric term of  $N$  exchange and  $\Sigma$  exchange term do not satisfy the gauge invariance, but the sum does. In this case the common form factor is introduced. The form is given by

$$F_{\text{com}} = F_N F_{\Sigma(K^*)} - F_N - F_{\Sigma(K^*)}. \tag{3.30}$$

for the (I)  $K^{*0}\Sigma^+$  and (II)  $K^{*+}\Sigma^0$  channels, respectively. In the process of the (II)  $K^{*+}\Sigma^0$  channel, a contact term is included additionally.

Finally, the scattering amplitudes can be written as

$$\begin{aligned}
\mathcal{M}(\gamma p \rightarrow K^{*0}\Sigma^+) = & [\mathcal{M}_N^{\text{elec}} + \mathcal{M}_\Sigma] F_{\text{com}}^2 + \mathcal{M}_N^{\text{mag}} F_N^2 \\
& + \mathcal{M}_K F_K^2 + \mathcal{M}_\kappa F_\kappa^2 + \mathcal{M}_\Delta F_\Delta^2 + \mathcal{M}_{\Sigma^*} F_{\Sigma^*}^2
\end{aligned}$$



$$+\mathcal{M}_{N^*}F_{N^*}^2 + \mathcal{M}_{\Delta^*}F_{\Delta^*}^2 \quad (3.31)$$

for the (I)  $K^{*0}\Sigma^+$  channel and

$$\begin{aligned} \mathcal{M}(\gamma p \rightarrow K^{*+}\Sigma^0) = & [\mathcal{M}_{K^*} + \mathcal{M}_N^{\text{elec}} + \mathcal{M}_c]F_{\text{com}}^2 + \mathcal{M}_N^{\text{mag}}F_N^2 \\ & + \mathcal{M}_K F_K^2 + \mathcal{M}_\kappa F_\kappa^2 \\ & + \mathcal{M}_\Delta F_\Delta^2 + \mathcal{M}_\Lambda F_\Lambda^2 + \mathcal{M}_\Sigma F_\Sigma^2 + \mathcal{M}_{\Sigma^*} F_{\Sigma^*}^2 \\ & + \mathcal{M}_{N^*} F_{N^*}^2 + \mathcal{M}_{\Delta^*} F_{\Delta^*}^2 \end{aligned} \quad (3.32)$$

for (II)  $K^{*+}\Sigma^0$  channel, respectively.

Each amplitude also has an isospin factor which is summarized in Table 3.3.

channels	$I_{K^*}$	$I_K$	$I_\kappa$	$I_N, I_{N^*}$	$I_\Delta, I_{\Delta^*}$	$I_\Lambda$	$I_\Sigma$	$I_{\Sigma^*}$
(I) $\gamma p \rightarrow K^{*0}\Sigma^+$	$\times$	$\sqrt{2}$	$\sqrt{2}$	$\sqrt{2}$	$-\sqrt{2}/3$	$\times$	$\sqrt{2}$	$\sqrt{2}$
(II) $\gamma p \rightarrow K^{*+}\Sigma^0$	1	1	1	1	$2/3$	1	1	1

TABLE 3.3: Isospin factors to each channel for the  $\gamma p \rightarrow K^*\Sigma$ .

### 3.3 Results

In this section, our numerical results are presented and discussed. Based on the experimental data for the total and differential cross sections [68, 70, 72], the free parameters, cutoff masses, are determined. Subsequently, a few spin observables are predicted, which are expected to be measured at various experimental facilities. To optimize the free parameters to the data, the  $t$ -channel cutoff masses are primarily determined, and then those corresponding to baryon exchanges are fixed. They are listed in Table 3.4.

$\Lambda_{K^*}$	$\Lambda_K$	$\Lambda_\kappa$	$\Lambda_N$	$\Lambda_\Delta$	$\Lambda_\Lambda$	$\Lambda_\Sigma$	$\Lambda_{\Sigma^*}$	$\Lambda_{N^*}$	$\Lambda_{\Delta^*}$
0.80	1.15	1.15	1.50	1.50	0.70	0.95	0.95	1.00	1.00

TABLE 3.4: Cutoff masses [GeV] to each channel for the  $\gamma p \rightarrow K^*\Sigma$ .

#### 3.3.1 Total cross sections

In the left panel of Fig. 3.2, each contribution to the total cross sections is drawn as a function of the photon energy  $E_\gamma$  for the the (I)  $K^{*0}\Sigma^+$  channel. Note that the data of open squares are estimated ones, based on the interpolating polynomial method to the fourth order. In general, the total result fits the estimation from the CLAS

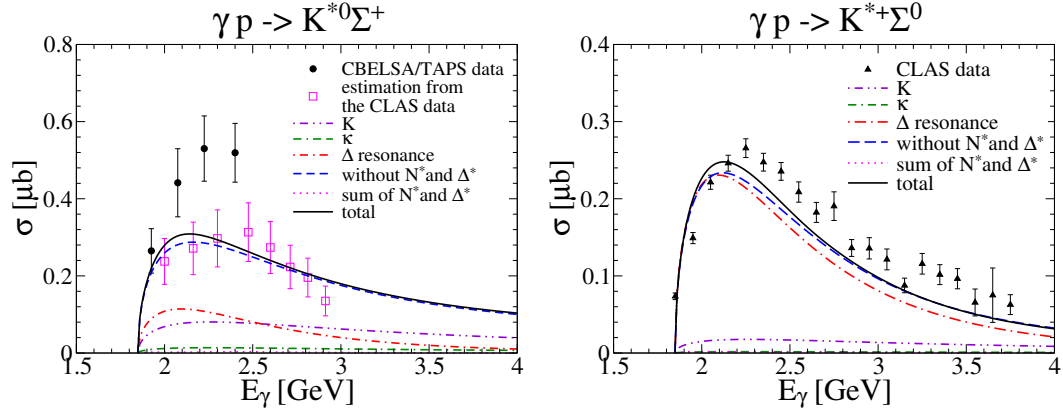


FIGURE 3.2: Total cross sections for the  $\gamma p \rightarrow K^{*0}\Sigma^+$  (left panel) and the  $\gamma p \rightarrow K^{*+}\Sigma^0$  (right panel). The data are from Ref. [70] (black circles), Ref. [72] (open squares), and Ref. [68] (black triangles).

data [72] pretty well, while it seems to be underestimated compared to the CBELSA/-TAPS data [70].  $K$  and  $\Delta(1232)$ -pole exchanges play the most important role, while the  $N^*$  and  $\Delta^*$  resonance contributions are almost marginal over the whole energy region.

In the right panel of Fig. 3.2, the total cross section for the (II)  $K^{*+}\Sigma^-$  channel is presented. Since we have used the same coupling constants for the corresponding vertices, isospin factors chiefly control the relative strength between the two channels. It turns out that the total result of this channel is a little smaller than that of the (I)  $K^{*0}\Sigma^+$  one. Though the isospin factor of the  $K^{*+}\Sigma^0\Delta^+$  vertex is larger than that of the  $K^{*0}\Sigma^+\Delta^+$  one, i.e.  $I_{K^{*+}\Sigma^0\Delta^+}/I_{K^{*0}\Sigma^+\Delta^+} = \sqrt{2}$ , the  $t$ -channel contribution is prominent in the (I)  $K^{*0}\Sigma^+$  channel rather than in the (II)  $K^{*+}\Sigma^-$  one. At any rate, with the dominant effects of  $\Delta(1232)$ -pole exchange on the total result, we can reproduce the CLAS data [68] quite well. On the other hand, the  $N^*$ ,  $\Delta^*$  resonances and  $u$ -channel hyperons have minute effects on the (II)  $K^{*+}\Sigma^-$  channel, which is similar to the (I)  $K^{*0}\Sigma^+$  one. However, although resonance contributions are almost tiny, they can play a certain role in describing the polarization observables. They are expected to exhibit more sensitive angular dependence than other contributions. Since there is also some ambiguity in choosing the coupling constants, we tried to use other values from the Nijmegen potential (NSC97f) [78]. But we reached the same conclusion.

In Fig. 3.3, each resonance contributions to the total cross sections are shown for both channels. As will be checked in the next subsection, the  $N^*$  and  $\Delta^*$  resonances have some effects on the polarization observables, thus we need to scrutinize them. Although  $G_{17}(2190)$  has a large effect among the resonances, it is too small compared to the total result. The magnitude of the resonance contributions is approximately 100 times smaller than that of the background ones. The  $D_{15}(2200)$  and  $G_{37}(2200)$  are not shown in Fig. 3.3, because they are almost negligible.

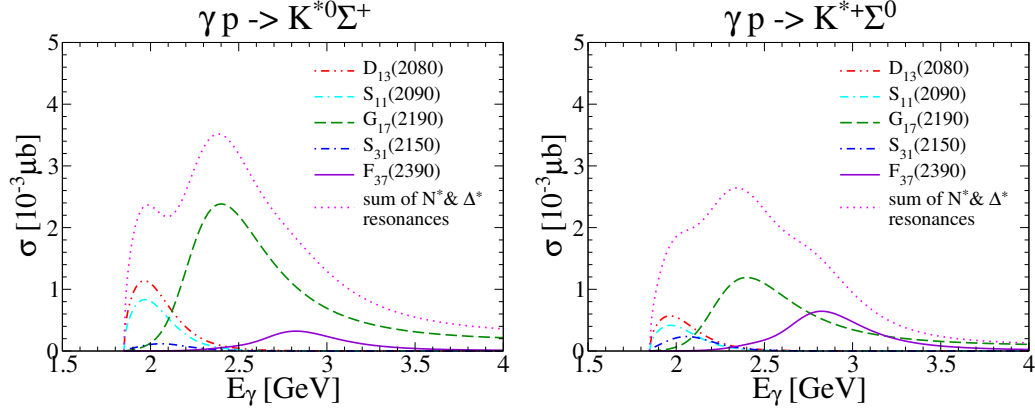


FIGURE 3.3: Resonance contributions to the total cross sections for the  $\gamma p \rightarrow K^{*0}\Sigma^+$  (left panel) and the  $\gamma p \rightarrow K^{*+}\Sigma^0$  (right panel).

### 3.3.2 Differential cross sections

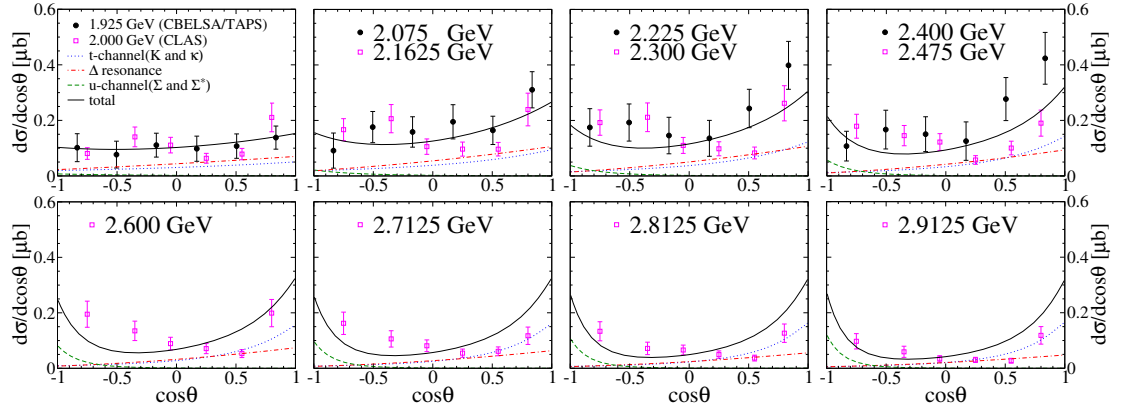


FIGURE 3.4: Differential cross sections for the  $\gamma p \rightarrow K^{*0}\Sigma^+$  in the range of  $E_\gamma = (1.925 - 2.9125)$  GeV. The data are from Ref. [70] (black circles) and Ref. [72] (open squares).

Figure 3.4 draws the numerical results of the differential cross sections  $d\sigma/d\cos\theta$  for the (I)  $K^{*0}\Sigma^+$  channel as functions of  $\cos\theta$ . As expected from the results of total cross sections, there is almost no effect from  $N^*$  and  $\Delta^*$  resonances. Near threshold regions, the angular dependence of  $\Delta$ -pole and  $t$ -channel ( $K$  and  $\kappa$ ) exchanges looks similar, but as the energy increases, the  $t$ -channel contribution becomes large in the forward direction. On the other hand, the  $u$ -channel exchanges ( $\Sigma$  and  $\Sigma^*$ ) come into play in the backward direction.

We depict the differential cross sections for the (II)  $K^{*+}\Sigma^0$  channel in Fig. 3.5. Unlike the (I)  $K^{*0}\Sigma^+$  channel,  $K^*$  exchange,  $\Lambda$  exchange, and the contact term are taken into account besides other diagrams so as to satisfy the WT identity. Thus the angular dependence looks different each other. There are some contributions of  $t$ -channel exchanges at the forward angles, but in general the  $\Delta$  exchange governs its behavior over

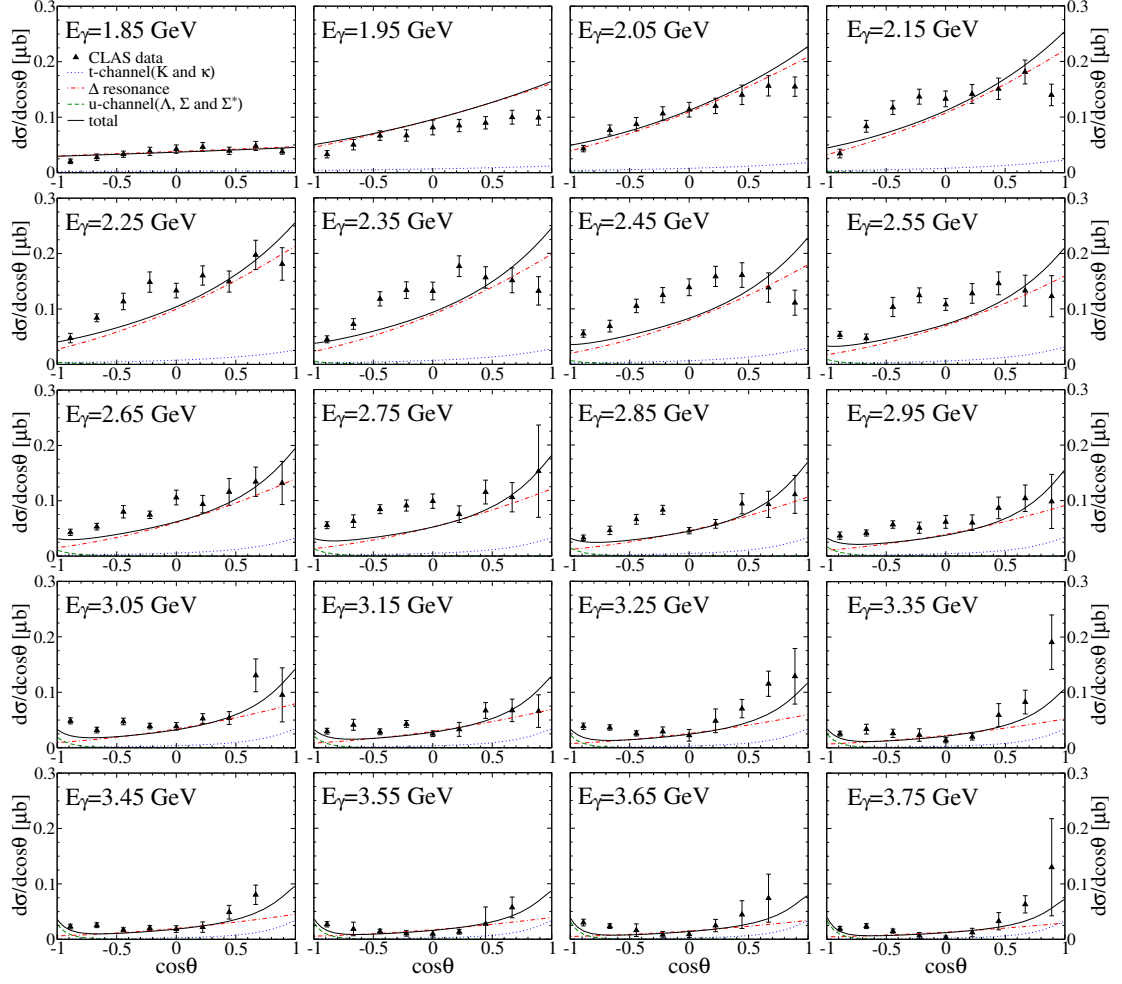


FIGURE 3.5: Differential cross sections for the  $\gamma p \rightarrow K^{*+}\Sigma^0$  in the range of  $E_\gamma = (1.85 - 3.75)$  GeV. The data are from Ref. [68].

the whole angular region. Except for the bump structure of the CLAS data [68] near the threshold regions, our result is in good agreement with the data.

### 3.3.3 Spin observables

Having fixed the free parameters to the total and differential experimental data given above, we are ready to display the predictions of the single-polarization observables. The definitions of the photon-beam  $\Sigma_\gamma$ , recoil  $P_y$ , and target  $T_y$  asymmetries are followed from Ref. [100]:

$$\begin{aligned}
 \Sigma_\gamma &\equiv \frac{d\sigma(\epsilon_\perp) - d\sigma(\epsilon_\parallel)}{d\sigma(\epsilon_\perp) + d\sigma(\epsilon_\parallel)}, \\
 P_y &\equiv \frac{d\sigma(s_y^\Sigma = \frac{1}{2}) - d\sigma(s_y^\Sigma = -\frac{1}{2})}{d\sigma(s_y^\Sigma = \frac{1}{2}) + d\sigma(s_y^\Sigma = -\frac{1}{2})}, \\
 T_y &\equiv \frac{d\sigma(s_y^N = \frac{1}{2}) - d\sigma(s_y^N = -\frac{1}{2})}{d\sigma(s_y^N = \frac{1}{2}) + d\sigma(s_y^N = -\frac{1}{2})}.
 \end{aligned} \tag{3.33}$$

Here all the denominators are equivalent to the  $d\sigma_{\text{unpol.}}$ , that is, the unpolarized differential cross section. These polarization observables satisfy the following conditions in the collinear limit

$$\Sigma_\gamma = P_y = T_y = 0 \text{ at } \cos\theta = \pm 1. \quad (3.34)$$

In the present work, we define the reaction plane by the  $x$ - $z$  axes. Thus the  $y$  axis is perpendicular to the reaction plane.  $\epsilon_\perp$  and  $\epsilon_\parallel$  are the photon polarization vectors defined in Eq. (3.3) in detail.  $s_y^B$  indicates the spin of a baryon  $B$  along the  $y$  direction.

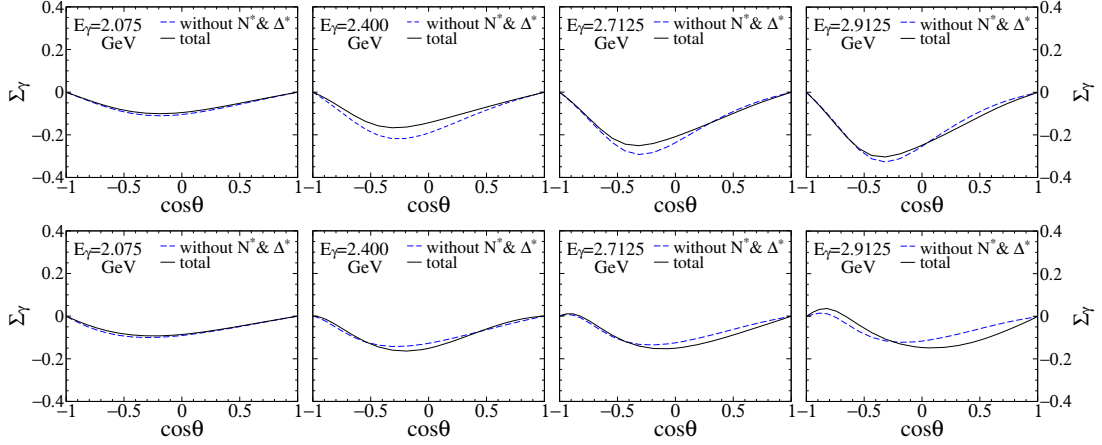


FIGURE 3.6: Photon-beam asymmetries  $\Sigma_\gamma$  for the  $\gamma p \rightarrow K^{*0}\Sigma^+$  (upper panel) and the  $\gamma p \rightarrow K^{*+}\Sigma^0$  (lower panel) as functions of  $\cos\theta$  in the range of  $E_\gamma = (2.075 - 2.9125)$  GeV.

We draw the numerical results of the photon-beam asymmetries  $\Sigma_\gamma$  in Fig. 3.6. It turns out that the  $N^*$  and  $\Delta^*$  resonances do not much come into play the  $\Sigma_\gamma$  for both the (I)  $K^{*0}\Sigma^+$  and (II)  $K^{*+}\Sigma^0$  channels. While  $t$ -channel exchange governs the  $K^*\Sigma$  channel mechanisms because of their large magnetic couplings, the  $\Delta$ -pole contribution pulls down  $\Sigma_\gamma$  to the negative direction. The effect of the  $\Delta$ -pole contribution becomes important with  $E_\gamma$  increasing.

In contrary to the  $\Sigma_\gamma$ , the resonances have some effects on the recoil asymmetries  $P_y$  as depicted in Fig. 3.7. Since we have taken into account rather large spins for resonances, their effects on recoil and target asymmetries, defined as the subtraction between the opposite spin directions of the polarized differential cross sections of the baryons, are expected to be natural. But the absolute values of the total results are less than 0.15 over the whole energy region. Thus their effects are not so impressive. We present the numerical results of the target asymmetries  $T_y$  in Fig. 3.8. The effects of the resonances on  $T_y$  tend to be very similar to those on  $P_y$ . But the phases of the  $T_y$  and  $P_y$  curves for the corresponding channels are opposite to each other.

Let us switch to the description of the same observables as functions of  $E_\gamma$ , fixing the angles  $\theta$  between  $\theta = 0^\circ$  and  $\theta = 180^\circ$ . In Fig. 3.9, we can find that, though the  $N^*$  and

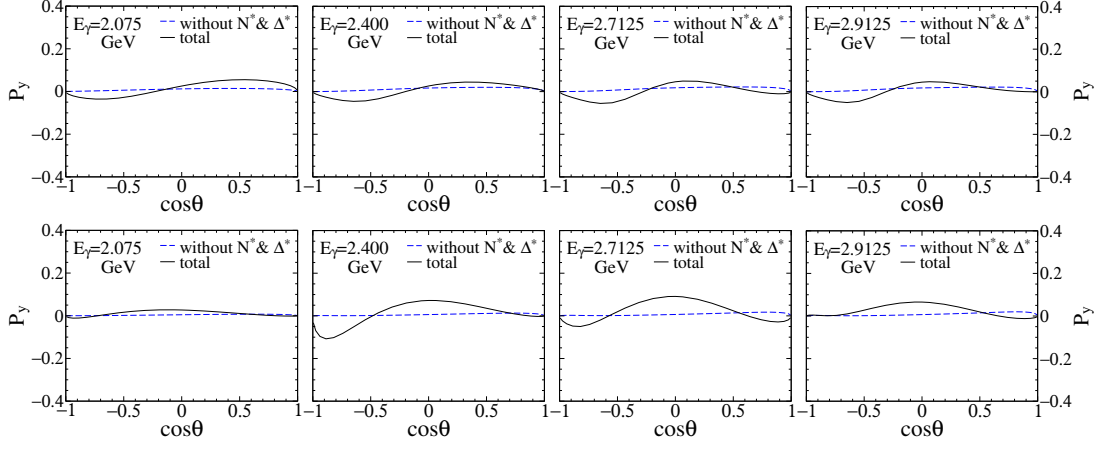


FIGURE 3.7: Recoil asymmetries  $P_y$  for the  $\gamma p \rightarrow K^{*0}\Sigma^+$  (upper panel) and the  $\gamma p \rightarrow K^{*+}\Sigma^0$  (lower panel) as functions of  $\cos\theta$  in the range of  $E_\gamma = (2.075 - 2.9125)$  GeV.

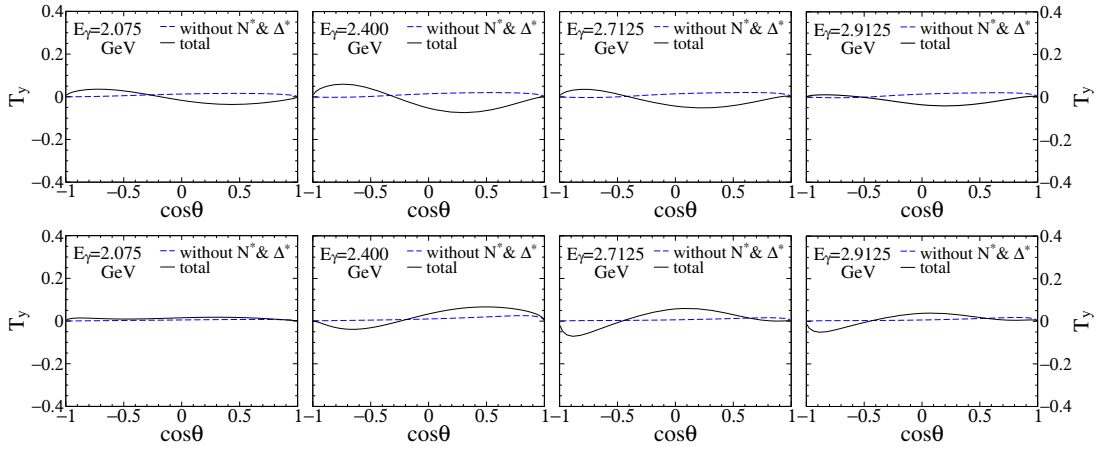


FIGURE 3.8: Target asymmetries  $T_y$  for the  $\gamma p \rightarrow K^{*0}\Sigma^+$  (upper panel) and the  $\gamma p \rightarrow K^{*+}\Sigma^0$  (lower panel) as functions of  $\cos\theta$  in the range of  $E_\gamma = (2.075 - 2.9125)$  GeV.

$\Delta^*$  resonances seem to exhibit small effects, one can see a slight change of  $\Sigma_\gamma$  with  $E_\gamma$  increasing. In particular, in the intermediate angles ( $60^\circ \lesssim \theta \lesssim 120^\circ$ ), the influence of the resonances is more clearly revealed.

Figures 3.10 and 3.11 draw the  $P_y$  and  $T_y$ , respectively. When the resonances are turned off, both the  $P_y$  and  $T_y$  have almost zero, independent of  $E_\gamma$ . When the resonances are included, it turns out that both the  $P_y$  and  $T_y$  in the intermediate angles start to rise until certain regions and then falls off slowly, as  $E_\gamma$  increases. This tendency is more obvious especially for the (I)  $K^{*0}\Sigma^+$  channel.

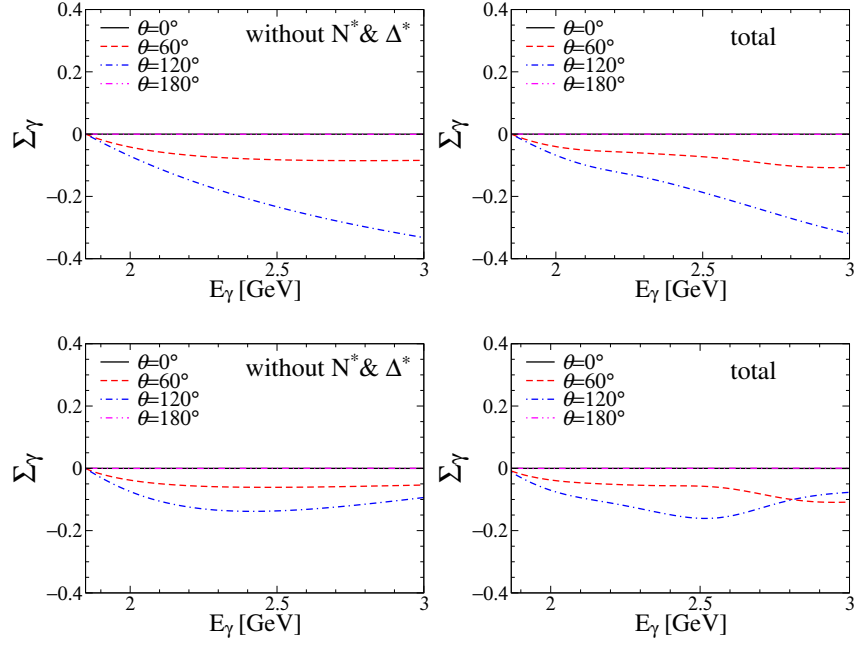


FIGURE 3.9: Photon-beam asymmetries  $\Sigma_\gamma$  for the  $\gamma p \rightarrow K^{*0}\Sigma^+$  (upper panel) and the  $\gamma p \rightarrow K^{*+}\Sigma^0$  (lower panel) as functions of  $E_\gamma$ , the scattering angle being changed from  $0^\circ$  to  $180^\circ$ .

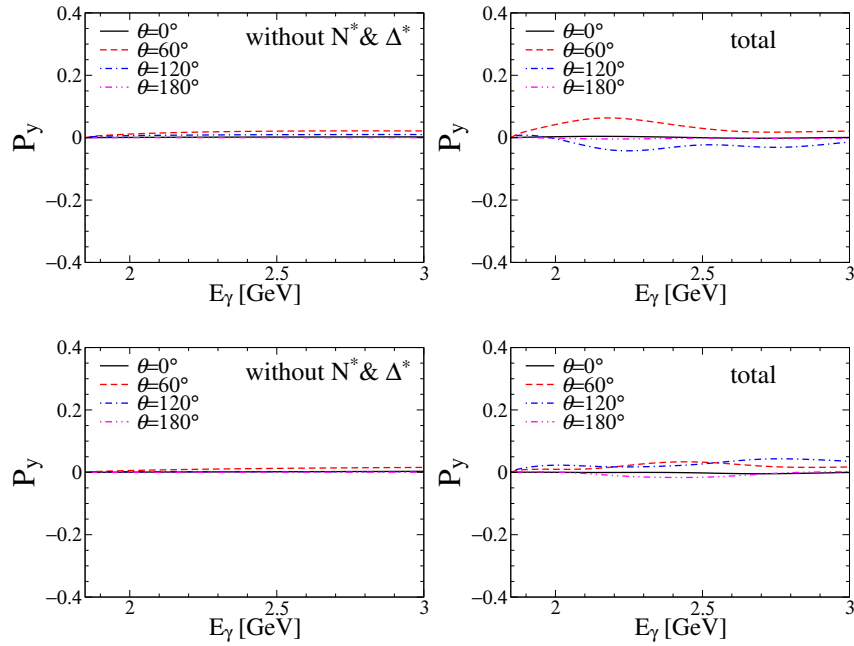


FIGURE 3.10: Recoil asymmetries  $P_y$  for the  $\gamma p \rightarrow K^{*0}\Sigma^+$  (upper panel) and the  $\gamma p \rightarrow K^{*+}\Sigma^0$  (lower panel) as functions of  $E_\gamma$ , the scattering angle being changed from  $0^\circ$  to  $180^\circ$ .

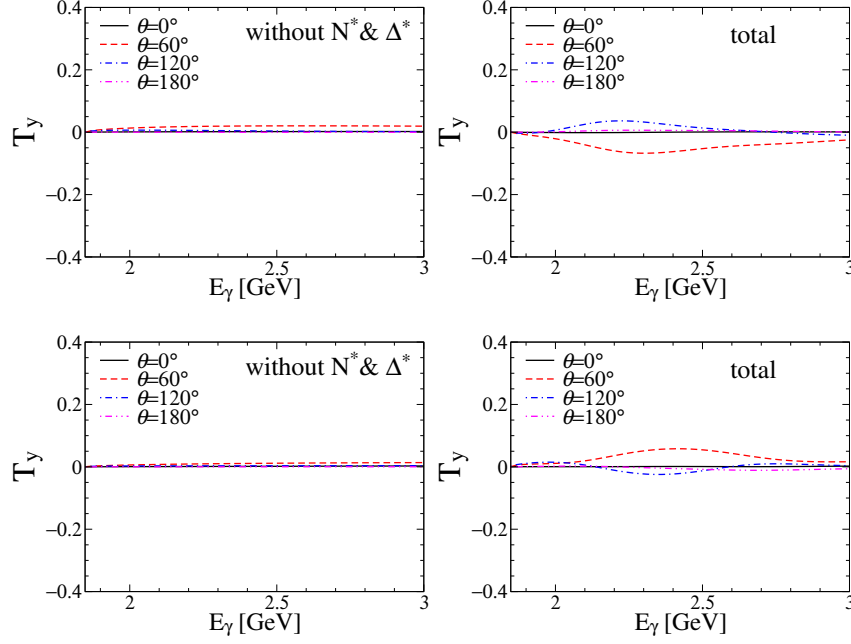


FIGURE 3.11: Target asymmetries  $T_y$  for the  $\gamma p \rightarrow K^{*0}\Sigma^+$  (upper panel) and the  $\gamma p \rightarrow K^{*+}\Sigma^0$  (lower panel) as functions of  $E_\gamma$ , the scattering angle being changed from  $0^\circ$  to  $180^\circ$ .

### 3.4 Summary

We have studied  $K^*\Sigma(1190)$  photoproduction, employing the effective Lagrangian method at the tree-level Born approximation. We mainly took account of the  $N^*$  and  $\Delta^*$  resonance contributions besides the nonresonant background ones. The form factors are chosen so as to satisfy the WT identity.

It turned out that the total cross sections for both the (I)  $K^{*0}\Sigma^+$  and (II)  $K^{*+}\Sigma^0$  photoproductions are negligibly affected by the resonance contributions. Instead, they are dominated by the Born diagrams such as the  $\Delta$ -pole and  $K$  exchanges. The total cross section for the (II)  $K^{*+}\Sigma^0$  channel turns out to be a little smaller than that for the (I)  $K^{*0}\Sigma^+$  one because of the differences in the coupling constants and isospin factors. This tendency is obviously distinguished from the case of  $K\Sigma(1190)$  photoproduction [15]. The differential cross sections for the (I)  $K^{*0}\Sigma^+$  channel are reproduced quite well compared with the CLAS data [72], showing that the main dependence is due to the  $\Delta$ -pole and  $K$  exchanges. As for the (II)  $K^{*+}\Sigma^0$  channel, the  $\Delta$ -pole occupies almost entire regions, exhibiting rather flat curves.

The photon-beam asymmetry  $\Sigma_\gamma$  is marginally affected by the resonance contributions, but because of the Born terms it has a negative value especially in the range of  $-0.5 \leq \cos\theta \leq 0$ . The recoil and target asymmetries  $P_y$  and  $T_y$  reveal some structures due to the  $N^*$  and  $\Delta^*$  resonances in comparison with the Born terms, though their



effects are almost invisible in the cross sections. The predictions of those polarization observables will bring us useful guides for future experiments in understanding the role of resonances in photoproductions, together with the double polarization observables such as the polarization transport coefficients  $C_{x,y}$  [101, 102]. They are expected to be measured by the CLAS, LEPS, and CBELSA/TAPS Collaborations.

## Chapter 4

# $K^*\Lambda$ photoproduction

We investigate the  $\gamma N \rightarrow K^*\Lambda$  process focusing on the role of nucleon resonances in a similar way as done in chapter 3. An effective Lagrangian method is employed at the tree-level Born approximation. After determining the background parameters, we extract the resonance couplings based on the experimental data and the SU(6) quark model. It turns out that the relevant resonances play a different role compared with the  $\gamma N \rightarrow K^*\Sigma$  process.

### 4.1 Particle data group

The 2012 edition of Review of Particle Physics [103] were much improved from those in the 2010 edition [76], especially for the information about the  $N^*$  resonances. This revision is mainly based on a new multi-channel partial wave analysis [104]. So far the existence and properties of  $N^*$  resonances were determined by the partial wave analyses of  $\pi N$  scattering data [105] but more investigation is needed for a complete understanding. Anisovich *et al.* performed a multichannel partial wave analysis taking both the pion- and photon-induced reactions off proton targets [104].

According to this analysis, a few new  $N^*$  resonances were either newly found or rearranged in the  $N^*$  spectrum [103, 106, 107]. The former ones are  $N(1880)1/2^+$  and  $N(2040)3/2^+$  even though they are not well established. The latter ones correspond to  $S_{11}(2090)$  and  $D_{15}(2200)$ , which were moved down to  $N(1895)1/2^-$  and  $N(2060)5/2^-$ , respectively, with their photon decay amplitudes added. As for the  $N(2190)7/2^-$ , its photon decay amplitudes were renewed. Whereas there has been only a two-star  $N(2000)$  concerning the evidence for a  $J^P = 5/2^+$  state with a mass above 1800 MeV, it was split (according to mass) into two two-star states, the  $N(1860)5/2^+$  and  $N(2000)5/2^+$ . A

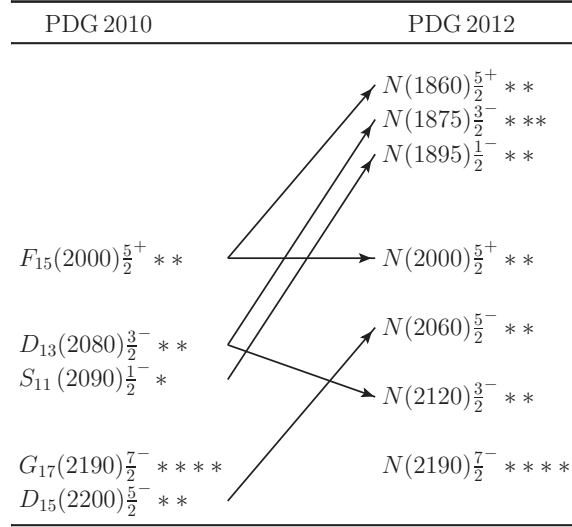


FIGURE 4.1: Spectrum of nucleon resonances.

noticeable thing is that the  $D_{13}(2080)$  has disappeared in the PDG 2012 edition. Instead, two new resonances with  $J^P = 3/2^-$  are included:  $N(1875)3/2^-$  and  $N(2120)3/2^-$ . The old  $D_{13}(2080)$  seems to correspond to  $N(1875)3/2^-$  below the  $K^*\Lambda$  threshold, though the new data for the photon decay helicity amplitudes [103, 104] are very different from the old ones [76, 108, 109]. A diagrammatic expression is shown in Fig. 4.1.

## 4.2 Motivation

Before the Review of Particle Physics was changed in 2012, a few theoretical works were performed concerning the  $\gamma p \rightarrow K^{*+}\Lambda$  process. Ref. [82] employed an effective Lagrangian approach considering only Born term tree diagrams, the  $t$ -channel mesons ( $K$ ,  $K^*$ , and  $\kappa$ ),  $s$ -channel nucleon, and  $u$ -channel hyperon ( $\Lambda$ ,  $\Sigma$ , and  $\Sigma^*$ ) contributions. In addition to those, nucleon resonances were included in Ref. [110],  $D_{13}(2080)$  and  $D_{15}(2200)$ , which lie close to the threshold energy of  $K^*\Lambda$  photoproduction. Others such as  $S_{11}(2090)$  and  $P_{11}(2100)$  were excluded since they are poorly confirmed experimentally. Because of the complexity stemming from their higher spins,  $G_{17}(2190)$  and  $H_{19}(2220)$  are not included too. It was found that the  $D_{13}(2080)$  resonance played an important role in describing the experimental data near the threshold region. A Reggeized meson exchange model is also attempted to describe the behavior of the total cross section [111]. However, they are all based on the preliminary experimental data for the total and differential cross sections [112, 113].

The first high-statistics experimental data for both the total and differential cross sections for the reaction  $\gamma p \rightarrow K^{*+}\Lambda$  has been reported recently by the CLAS Collaboration

at the Thomas Jefferson National Accelerator Facility (TJNAF) [68]. As for the total cross section data, the threshold region was enhanced compared to the previous preliminary data depicted in the conference proceeding [112]. Though the original motivation of Ref. [68] was to study the role of  $\kappa(800)$  meson in the  $t$ -channel process, the new CLAS data near the threshold gives us a clue in understanding the role of higher nucleon resonances. The new data indicates that there are still missing parts in the previous analyses.

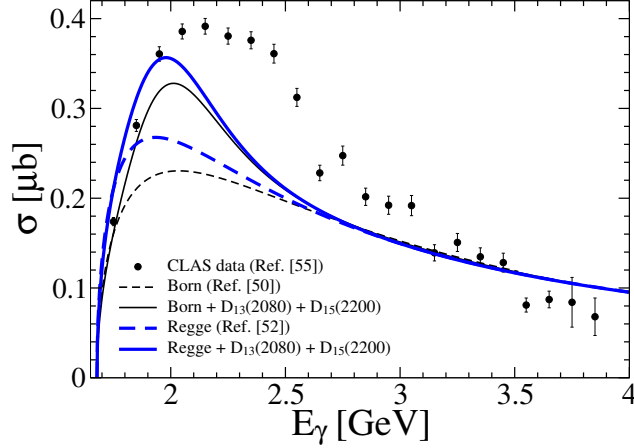
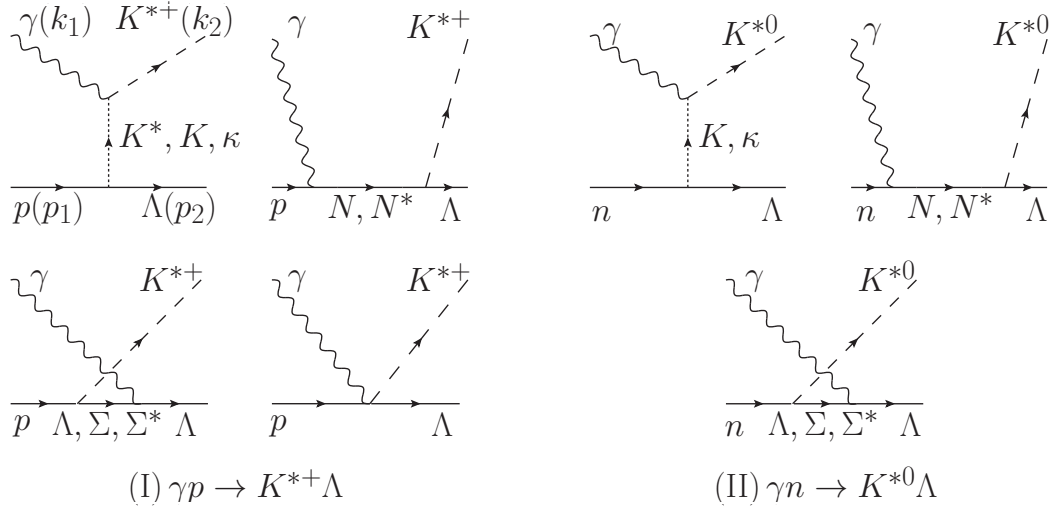


FIGURE 4.2: Total cross sections for the  $\gamma p \rightarrow K^* \Lambda$  with various theoretical results.

As discussed in Ref. [68] in detail, all theoretical results [73, 82, 110, 111] look different from the new CLAS data. The explicit results are displayed in Fig. 4.2 with various contributions. The thin- and thick-dashed curves are drawn from the effective Lagrangian approach (O-K model) [82] and Reggeized model (O-N-H model) [111], respectively. The thin-solid curve represents our model (K-N-O-K model) [110], which includes two resonances ( $D_{13}(2080)$  and  $D_{15}(2200)$ ) besides the Born term contributions. To match the Born term parameters with the O-K model, some cutoff masses in form factors are changed from  $\Lambda_{K,\kappa} = 1.25$  GeV to  $\Lambda_{K,\kappa} = 1.1$  GeV. The modified O-N-H model, which is based on the O-N-H model but additionally includes extra resonances used in the K-N-O-K model, are represented in the thick-solid curve. If one takes this situation seriously, the production mechanism of the  $\gamma N \rightarrow K^* \Lambda$  should be reanalyzed with the new  $N^*$  data employed.

### 4.3 Formalism

In this subsection, we account for the general formalism of an effective Lagrangian approach. The tree-level Feynman diagrams relevant to the  $\gamma N \rightarrow K^* \Lambda$  reaction are

FIGURE 4.3: Tree-level Feynman diagrams for the  $\gamma N \rightarrow K^* \Lambda$ .

displayed in Fig. 4.3. We classify this process as

$$(I) \gamma p \rightarrow K^{*+} \Lambda, \quad (II) \gamma n \rightarrow K^{*0} \Lambda. \quad (4.1)$$

The  $t$ -channel process includes  $K^*$ ,  $K$ , and  $\kappa$  exchanges. The nucleon and  $N^*$  resonance exchanges are taken into account in the  $s$  channel, and the  $u$ -channel process corresponds to  $\Lambda$ ,  $\Sigma$ , and  $\Sigma^*$  exchanges. The contact term is included to preserve gauge invariance only in the (I)  $K^{*+} \Lambda$  channel.  $K^*$  exchange is also considered only in this channel because of charge conservation.

### 4.3.1 Nonresonant terms

The photon-meson interactions are described by the following effective Lagrangians:

$$\begin{aligned}
 \mathcal{L}_{\gamma K^* K^*} &= -ie_{K^*} A^\mu \left( K^{*\nu} K_{\mu\nu}^\dagger - K_{\mu\nu}^* K^{*\dagger\nu} \right), \\
 \mathcal{L}_{\gamma K^* K} &= g_{\gamma K^* K} \varepsilon^{\mu\nu\alpha\beta} (\partial_\mu A_\nu) (\partial_\alpha \bar{K}_\beta^*) K + \text{H.c.}, \\
 \mathcal{L}_{\gamma K^* \kappa} &= g_{\gamma K^* \kappa} A^{\mu\nu} \bar{\kappa} K_{\mu\nu}^* + \text{H.c.},
 \end{aligned} \quad (4.2)$$

and the electromagnetic (EM) interactions for the baryons are

$$\begin{aligned}
\mathcal{L}_{\gamma NN} &= -\bar{N} \left[ e_N \gamma_\mu - \frac{e\kappa_N}{2M_N} \sigma_{\mu\nu} \partial^\nu \right] A^\mu N, \\
\mathcal{L}_{\gamma \Lambda \Lambda} &= \frac{e\kappa_\Lambda}{2M_N} \bar{\Lambda} \sigma_{\mu\nu} \partial^\nu A^\mu \Lambda, \\
\mathcal{L}_{\gamma \Lambda \Sigma} &= \frac{e\mu_{\Sigma\Lambda}}{2M_N} \bar{\Sigma} \sigma_{\mu\nu} \partial^\nu A^\mu \Lambda + \text{H.c.}, \\
\mathcal{L}_{\gamma \Lambda \Sigma^*} &= -\frac{ie}{2M_N} \left[ g_{\gamma \Lambda \Sigma^*}^V \bar{\Lambda} \gamma_\nu - \frac{ig_{\gamma \Lambda \Sigma^*}^T}{2M_N} \partial_\nu \bar{\Lambda} \right] \gamma_5 \Sigma_\mu^* F^{\mu\nu} + \text{H.c.} \quad (4.3)
\end{aligned}$$

The EM couplings for the spin-3/2 hyperon  $\Sigma^*$  are related to the well-known magnetic dipole ( $M1$ ) and electric quadrupole ( $E2$ ) moments. These coupling constants are determined by the experimental data for the radiative decay width  $\Gamma_{\Sigma^* \rightarrow \gamma \Lambda}$  [1], which leads to  $(g_{\gamma \Lambda \Sigma^*}^V, g_{\gamma \Lambda \Sigma^*}^T) = (3.78, 3.18)$ .

Finally, the effective Lagrangians for the meson-baryon interactions are given by

$$\begin{aligned}
\mathcal{L}_{K N \Lambda} &= -ig_{KN\Lambda} \bar{N} \gamma_5 \Lambda K + \text{H.c.}, \\
\mathcal{L}_{\kappa N \Lambda} &= -g_{\kappa N \Lambda} \bar{N} \Lambda \kappa + \text{H.c.}, \\
\mathcal{L}_{K^* N Y} &= -g_{K^* N Y} \bar{N} \left[ \gamma_\mu Y - \frac{\kappa_{K^* N Y}}{2M_N} \sigma_{\mu\nu} Y \partial^\nu \right] K^{*\mu} + \text{H.c.}, \\
\mathcal{L}_{K^* N \Sigma^*} &= -\frac{if_{K^* N \Sigma^*}^{(1)}}{2M_{K^*}} \bar{K}_{\mu\nu}^* \bar{\Sigma}^{*\mu} \gamma^\nu \gamma_5 N - \frac{f_{K^* N \Sigma^*}^{(2)}}{(2M_{K^*})^2} \bar{K}_{\mu\nu}^* \bar{\Sigma}^{*\mu} \gamma_5 \partial^\nu N \\
&\quad + \frac{f_{K^* N \Sigma^*}^{(3)}}{(2M_{K^*})^2} \partial^\nu \bar{K}_{\mu\nu}^* \bar{\Sigma}^{*\mu} \gamma_5 N + \text{H.c.} \quad (4.4)
\end{aligned}$$

Here  $A_\mu$ ,  $K_\mu^*$ ,  $K$ , and  $\kappa$  denote the photon,  $K^*(892, 1^-)$  vector meson,  $K(494, 0^-)$  pseudoscalar meson, and  $\kappa(800, 0^+)$  scalar meson, respectively.  $N$ ,  $\Lambda$ ,  $\Sigma$ , and  $\Sigma^*$  stand for the nucleon,  $\Lambda(1116, 1/2^+)$ ,  $\Sigma(1190, 1/2^*)$ , and  $\Sigma^*(1385, 3/2^+)$  hyperon fields, respectively [1]. The  $F_{\mu\nu}$  and  $K_{\mu\nu}^*$  represent the field tensor for the photon and  $K^*$  vector meson, defined by  $F_{\mu\nu} = \partial_\mu A_\nu - \partial_\nu A_\mu$  and  $K_{\mu\nu}^* = \partial_\mu K_\nu^* - \partial_\nu K_\mu^*$ , respectively.  $Y$  denote  $\Lambda$  or  $\Sigma$  fields, and  $\Sigma = \boldsymbol{\tau} \cdot \boldsymbol{\Sigma}$  and  $\Sigma_\mu^* = \boldsymbol{\tau} \cdot \boldsymbol{\Sigma}_\mu^*$ . The baryon fields with spin  $s = 3/2$  are described by the Rarita-Schwinger field [79, 80].

Finally, the contact term is considered only for the charged  $K^*$  production to conserve the  $U(1)$  gauge invariance. The corresponding Lagrangian is given by

$$\mathcal{L}_{\gamma K^* N \Lambda} = -\frac{ie_{K^*} g_{K^* N \Lambda} \kappa_{K^* N \Lambda}}{2M_N} \bar{\Lambda} \sigma^{\mu\nu} A_\nu K_\mu^* N + \text{H.c.} \quad (4.5)$$

As for the details of the coupling constants and the structures of scattering amplitudes, we refer to chapter 3.

### 4.3.2 Nucleon resonances in the $s$ channel

We use the PDG 2012 edition [103] as for the information about the  $N^*$  resonances. We consider, in this work, the  $N(2000) 5/2^+$ ,  $N(2060) 5/2^-$ ,  $N(2120) 3/2^-$ , and  $N(2190) 7/2^-$  resonances near the threshold region. The values of the masses and decay widths are taken from the Breit-Wigner ones [104, 114].

The EM Lagrangians are written as

$$\begin{aligned}\mathcal{L}_{\gamma NR_{3/2^\pm}} &= -ie \left[ \frac{h_1}{2M_N} \bar{N} \Gamma_\nu^{(\pm)} - \frac{ih_2}{(2M_N)^2} \partial_\nu \bar{N} \Gamma^{(\pm)} \right] F^{\mu\nu} R_\mu + \text{H.c.}, \\ \mathcal{L}_{\gamma NR_{5/2^\pm}} &= e \left[ \frac{h_1}{(2M_N)^2} \bar{N} \Gamma_\nu^{(\mp)} - \frac{ih_2}{(2M_N)^3} \partial_\nu \bar{N} \Gamma^{(\mp)} \right] \partial^\alpha F^{\mu\nu} R_{\mu\alpha} + \text{H.c.}, \\ \mathcal{L}_{\gamma NR_{7/2^\pm}} &= ie \left[ \frac{h_1}{(2M_N)^3} \bar{N} \Gamma_\nu^{(\pm)} - \frac{ih_2}{(2M_N)^4} \partial_\nu \bar{N} \Gamma^{(\pm)} \right] \partial^\alpha \partial^\beta F^{\mu\nu} R_{\mu\alpha\beta} + \text{H.c.} \quad (4.6)\end{aligned}$$

The transition magnetic moments  $h_{1,2}$  given in Eq. (4.6) are determined by the Breit-Wigner helicity amplitudes from Refs. [104, 114] or by the predictions from the relativistic quark model [3]: the parameters for  $N(2000) 5/2^+$ ,  $N(2060) 5/2^-$ , and  $N(2120) 3/2^-$  are taken from Refs. [104, 114], whereas those for  $N(2190) 7/2^-$  are from Ref. [3]. All the relevant parameters are organized in Table 4.1.

Resonances	$A_1$	$A_3$	$h_1$	$h_2$
$N(2000) 5/2^+$	+32 (-18)	+48 (-35)	+0.114(-0.395)	+1.22(-0.500)
$N(2060) 5/2^-$	+67 (+25)	+55 (-37)	-2.45(+0.027)	-3.81(-2.85)
$N(2120) 3/2^-$	+130 (+110)	+150 (+40)	-0.827(-1.66)	+2.14(+2.31)
$N(2190) 7/2^-$	-34 (+10)	+28 (-14)	+7.87(-2.94)	-7.36(+2.49)

TABLE 4.1: Transition magnetic moments  $h_{1,2}$  in Eqs. (4.6) extracted from the helicity amplitudes  $A_{1,3}$  [ $\text{GeV}^{-\frac{1}{2}}$ ] [3, 104, 114] for the (I)  $K^{*+}\Lambda$  ((II)  $K^{*0}\Lambda$ ) channel.

The effective Lagrangians for the strong vertices read

$$\begin{aligned}\mathcal{L}_{K^*\Lambda R_{3/2^\pm}} &= \\ i\bar{R}_\mu &\left[ \frac{g_1}{2M_N} \Lambda \Gamma_\nu^{(\pm)} \mp \frac{ig_2}{(2M_N)^2} \partial_\nu \Lambda \Gamma^{(\pm)} \pm \frac{ig_3}{(2M_N)^2} \Lambda \Gamma^{(\pm)} \partial_\nu \right] K^{*\mu\nu} + \text{H.c.}, \\ \mathcal{L}_{K^*\Lambda R_{5/2^\pm}} &= \bar{R}_{\mu\alpha} \times \\ &\left[ \frac{g_1}{(2M_N)^2} \Lambda \Gamma_\nu^{(\mp)} \pm \frac{ig_2}{(2M_N)^3} \partial_\nu \Lambda \Gamma^{(\mp)} \mp \frac{ig_3}{(2M_N)^3} \Lambda \Gamma^{(\mp)} \partial_\nu \right] \partial^\alpha K^{*\mu\nu} + \text{H.c.}, \\ \mathcal{L}_{K^*\Lambda R_{7/2^\pm}} &= -i\bar{R}_{\mu\alpha\beta} \times \\ &\left[ \frac{g_1}{(2M_N)^3} \Lambda \Gamma_\nu^{(\pm)} \mp \frac{ig_2}{(2M_N)^4} \partial_\nu \Lambda \Gamma^{(\pm)} \pm \frac{ig_3}{(2M_N)^4} \Lambda \Gamma^{(\pm)} \partial_\nu \right] \partial^\alpha \partial^\beta K^{*\mu\nu} + \text{H.c.} \quad (4.7)\end{aligned}$$

The strong coupling constants in Eq. (4.7),  $g_i$ , are obtained from the following relation,

$$\Gamma_{N^* \rightarrow K^* \Lambda} = \sum_{s,l} |G_{s,l}|^2, \quad (4.8)$$

where the explicit form of the decay amplitudes  $G_{s,l}$  is given in Ref. [5]. Here, we take account of the lowest partial-wave contribution for  $G_{s,l}$  and thus only the lowest multipole, i.e., the first term of Eq. (4.7), is considered as in Ref. [110]. The signs of these strong coupling constants are determined phenomenologically. Because of lack of information, we also assume that  $N(2000) 5/2^+$ ,  $N(2060) 5/2^-$ ,  $N(2120) 3/2^-$ , and  $N(2190) 7/2^-$  may correspond to  $F_{15}(2000)$ ,  $D_{15}(2200)$ ,  $D_{13}(2080)$ , and  $G_{17}(2190)$  in the PDG 2010 edition [76], respectively. However, as will be shown in the next section, the  $N(2120) 3/2^-$  turns out to be distinguished from the old  $D_{13}(2080)$  that played an important role in the previous work [110]. In fact, the  $D_{13}(2080)$  more or less corresponds to the lower-lying 3-star  $N^*$  resonance  $N(1875) 3/2^-$ . Therefore, we have to fit the parameters of the  $N(2120) 3/2^-$  to the CLAS data. Table 4.2 list the relevant parameters.

PDG	$M_{BW}$	$\Gamma_{BW}$	$G_{s,l}$	$g_1$	$g_1(\text{final})$
$N(2000) 5/2^+$	2090	460	+0.3	+1.37	+1.37
$N(2060) 5/2^-$	2060	375	+0.2	+5.42	+5.42
$N(2120) 3/2^-$	2150	330	+3.8	+1.29	+0.30
$N(2190) 7/2^-$	2180	335	+2.5	-44.3	-44.3

TABLE 4.2: The masses, the decay widths, and the strong coupling constants  $g_1$  in Eqs. (4.7) extracted from the decay amplitudes  $G_{s,l}$  [ $\sqrt{\text{MeV}}$ ] [5].

### 4.3.3 Form factors

In an effective Lagrangian approach, a form factor should be considered at each vertex, since it parameterizes the structure of the hadron. However, it is in fact rather difficult to handle the form factors at an EM vertex, since it breaks the gauge invariance due to its nonlocality [115]. To circumvent this problem, the prescription explained in Refs. [97–99] is used. Though it is phenomenological, it provides a convenient way of dealing with the form factors for an EM vertex. The form factors for off-shell mesons and baryons are given by

$$F_\Phi = \frac{\Lambda_\Phi^2 - M_\Phi^2}{\Lambda_\Phi^2 - p^2}, \quad F_B = \frac{\Lambda_B^4}{\Lambda_B^4 + (p^2 - M_B^2)^2}, \quad (4.9)$$

respectively, where  $M_{(\Phi,B)}$ , and  $p$  denote the the mass and the momentum of the off-shell hadron, respectively. For the charged  $K^*$  production, to conserve the gauge invariance,



we consider a common form factor for the  $K^*$  and  $N$  exchanges as

$$F_{\text{com}} = F_{K^*}F_N - F_{K^*} - F_N, \quad (4.10)$$

which is excluded for the neutral  $K^*$  production since all the particle exchanges satisfy the gauge invariance by themselves. The cutoff parameters are determined phenomenologically. However, to reduce theoretical ambiguities due to the wide range of the cutoff masses, we limit their values around 1 GeV.

Considering all the ingredients so far, the scattering amplitudes have the following forms:

$$\begin{aligned} \mathcal{M}(\gamma p \rightarrow K^{*+}\Lambda) = & (\mathcal{M}_{K^*} + \mathcal{M}_N + \mathcal{M}_c)F_{\text{com}}^2 + \mathcal{M}_K F_K^2 + \mathcal{M}_\kappa F_\kappa^2 \\ & + \mathcal{M}_\Lambda F_\Lambda^2 + \mathcal{M}_\Sigma F_\Sigma^2 + \mathcal{M}_{\Sigma^*} F_{\Sigma^*}^2 + \mathcal{M}_{N^*} F_{N^*}^2 \end{aligned} \quad (4.11)$$

for the (I)  $K^{*+}\Lambda$  channel and

$$\begin{aligned} \mathcal{M}(\gamma n \rightarrow K^{*0}\Lambda) = & \mathcal{M}_K F_K^2 + \mathcal{M}_\kappa F_\kappa^2 + \mathcal{M}_N F_N^2 \\ & + \mathcal{M}_\Lambda F_\Lambda^2 + \mathcal{M}_\Sigma F_\Sigma^2 + \mathcal{M}_{\Sigma^*} F_{\Sigma^*}^2 + \mathcal{M}_{N^*} F_{N^*}^2 \end{aligned} \quad (4.12)$$

for the (II)  $K^{*0}\Lambda$  channel.

Each amplitude also has an isospin factor. In Table 4.3, we list them.

channels	$I_{K^*}$	$I_K$	$I_\kappa$	$I_N, I_{N^*}$	$I_\Lambda$	$I_\Sigma$	$I_{\Sigma^*}$
(I) $\gamma p \rightarrow K^{*+}\Lambda$	1	1	1	1	1	1	1
(II) $\gamma n \rightarrow K^{*0}\Lambda$	$\times$	1	1	1	1	-1	-1

TABLE 4.3: Isospin factors to each channel for the  $\gamma N \rightarrow K^*\Lambda$ .

## 4.4 Results

In this section, we first present the results of the total and differential cross sections after determining the cutoff masses by fitting them to the available experimental data [68]. Then various spin observables are predicted and discussed. The cutoff masses chosen are given in Table 4.4.

$\Lambda_{K^*}$	$\Lambda_K$	$\Lambda_\kappa$	$\Lambda_N$	$\Lambda_\Lambda$	$\Lambda_\Sigma$	$\Lambda_{\Sigma^*}$	$\Lambda_{N^*}$
0.90	1.10	1.10	0.90	0.90	0.90	0.90	0.90

TABLE 4.4: Cutoff masses [GeV] to each channel for the  $\gamma N \rightarrow K^*\Lambda$ .

### 4.4.1 Total cross sections

In Fig. 4.4, we depict the total cross sections for the (I)  $K^{*+}\Lambda$  and (II)  $K^{*0}\Lambda$  channels in the left and right panels, respectively. In the case of the (I)  $K^{*+}\Lambda$  process, resonances play a decisive role in describing the CLAS data [68] in that the total result is in good agreement with the experimental data. On the other hand, in the case of the (II)  $K^{*0}\Lambda$  process, resonances are not as important as the  $K^{*+}\Lambda$  one. The  $K^*$  exchange and the contact term are forbidden because of the neutral charge of the  $K^{*0}$ . Nevertheless, the total cross section is quite larger than that of the (I)  $K^{*+}\Lambda$  process, since the neutral coupling constant of the  $\gamma K K^*$  vertex is larger than the charged one by a factor of about  $\sqrt{2}$  (Eq. (3.8)), which gives rise to a twofold difference in the total cross section (see the dashed curves in Fig 4.4 for comparison). Thus the main contribution to the total cross section for the (II)  $K^{*0}\Lambda$  channel comes from the  $K$  exchange.

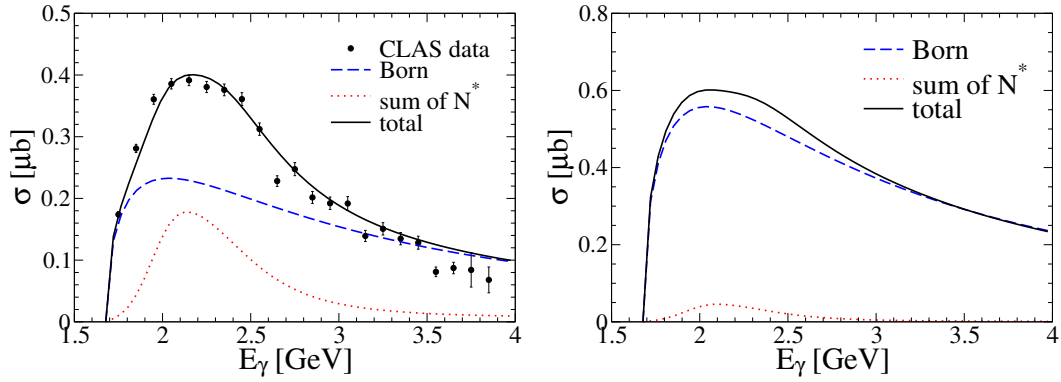


FIGURE 4.4: Total cross sections for the  $\gamma p \rightarrow K^{*+}\Lambda$  (left panel) and the  $\gamma n \rightarrow K^{*0}\Lambda$  (right panel). The data are from Ref. [68].

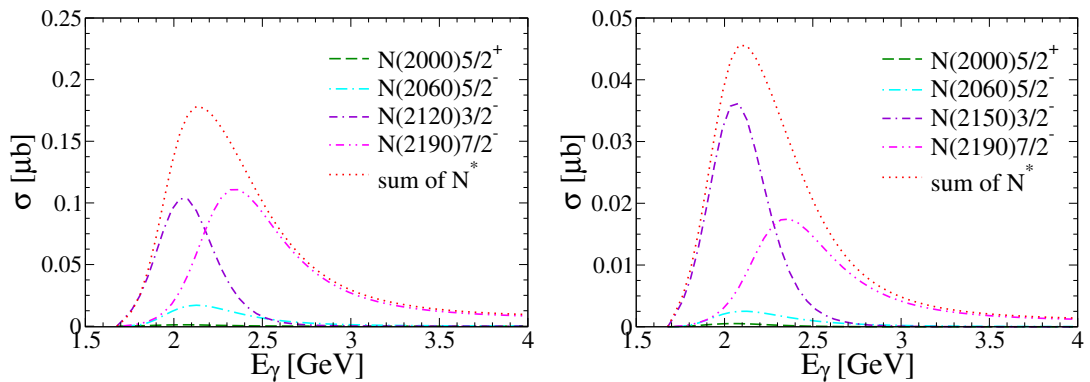


FIGURE 4.5: Resonance contributions to the total cross sections for the  $\gamma p \rightarrow K^{*+}\Lambda$  (left panel) and the  $\gamma n \rightarrow K^{*0}\Lambda$  (right panel).

The details of resonance contributions are drawn in Fig. 4.5. In the case of the (I)  $K^{*+}\Lambda$  channel, it is found that the  $N(2000)5/2^+$  is almost negligible and the  $N(2060)5/2^-$  gives a small contribution to the total cross section. Concerning  $N(2120)3/2^-$ , we first assume that it corresponds to the old  $D_{13}(2080)$  (see Fig. 4.1). Then the effect of the

$N(2120) 3/2^-$  turns out to be overestimated in comparison with the experimental data, namely approximately  $\sim 1.9 \mu\text{b}$  for the total cross section. Thus we put the strong coupling constant of  $N(2120) 3/2^-$  as a free parameter and fit it to the experimental data. The coupling constant  $g_1$  is changed from  $+1.29$  to  $+0.30$ , as shown in Table 4.2. Consequently, the  $N(2120) 3/2^-$  is found to be as equally important as  $N(2190) 7/2^-$ . With these two  $N^*$  resonances considered, the CLAS data of the total cross section is well reproduced. In the case of the (II)  $K^{*0}\Lambda$  channel, the resonance contribution is approximately four times smaller than that of the (I)  $K^{*+}\Lambda$  channel.

#### 4.4.2 Differential cross sections

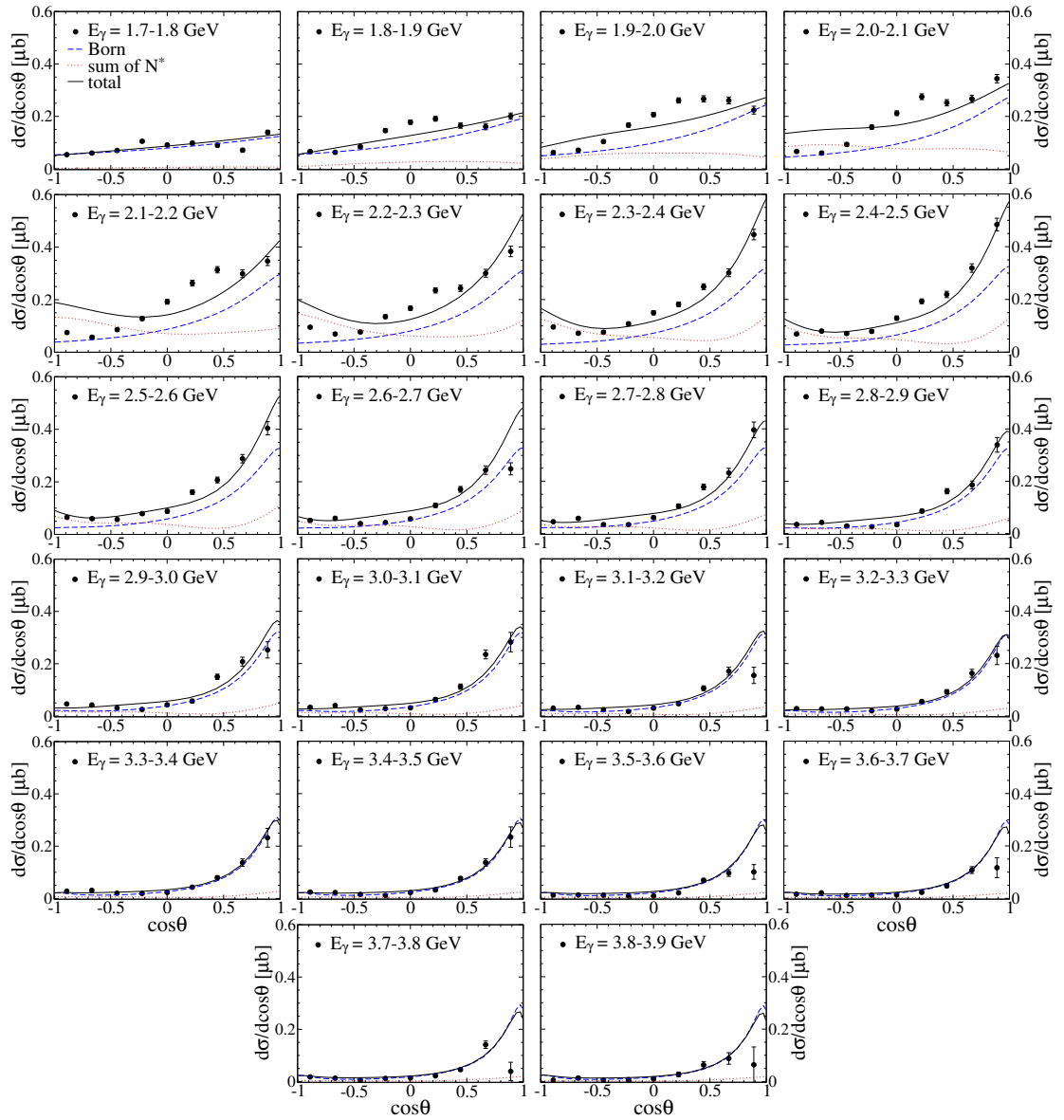


FIGURE 4.6: Differential cross sections for the  $\gamma p \rightarrow K^{*+}\Lambda$  in the range of  $E_\gamma = 1.7 - 3.9$  GeV. The data are from Ref. [68].

Figure 4.6 shows the differential cross sections for the (I)  $K^{*+}\Lambda$  channel as a function of  $\cos\theta$ . There exist broad bump structures in the range of  $1.8 \text{ GeV} \leq E_\gamma \leq 2.3 \text{ GeV}$ , which are not sufficient to be described by our model. But as  $E_\gamma$  increases our results begin to match the CLAS data pretty well. Together with the Born terms,  $N^*$  resonances improve on the cross sections. At high energies, we again find discrepancy in forward angle regions. This is the limitation of the effective Lagrangian method. More sophisticated theoretical models may enhance the present results.

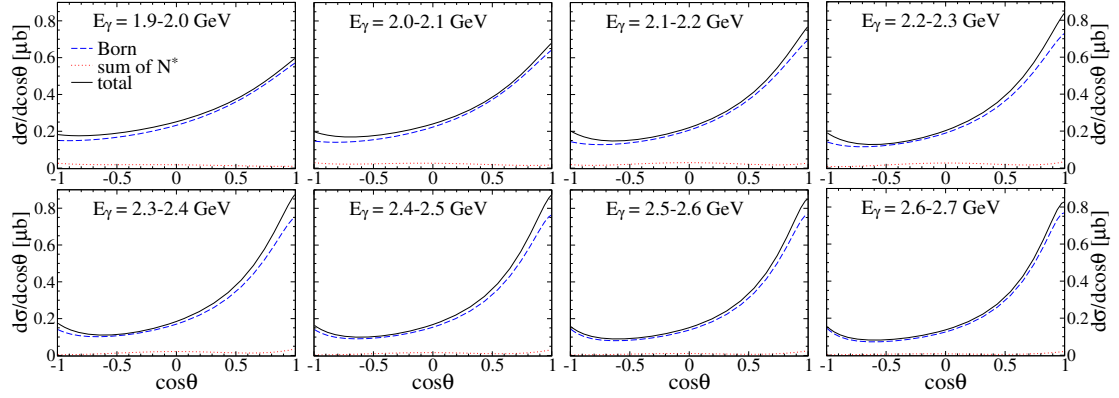


FIGURE 4.7: Differential cross sections for the  $\gamma n \rightarrow K^{*0}\Lambda$  in the range of  $E_\gamma = 1.9 - 2.7 \text{ GeV}$ .

Figure 4.7 predicts the differential cross sections for the (II)  $K^{*0}\Lambda$  channel. The corresponding experimental data will be announced soon [116, 117].

#### 4.4.3 Spin observables

Let us turn to the discussion of the polarization observables [118–120], which provide important information on the helicity amplitudes and spin structure of a process. In Appendix C, they are expressed in terms of the helicity amplitudes. The reaction takes place in the  $x - z$  plane. The notation for the polarized differential cross sections are given by [120]

$$d\sigma(B, T; R, V) = \frac{d\sigma}{d\Omega}(B, T; R, V), \quad (4.13)$$

where  $B$ ,  $T$ ,  $R$ ,  $V$  stand for the polarizations of the photon beam ( $B$ ), the target nucleon ( $T$ ), the recoil  $\Lambda$  ( $R$ ), and the produced  $K^*$  vector meson ( $V$ ), respectively, for the  $\gamma N \rightarrow K^*\Lambda$  process.

We begin with the single polarization observables. The definitions of the photon-beam asymmetry ( $\Sigma_x$ ), the target asymmetry ( $T_y$ ), and the recoil asymmetry ( $P_y$ ) are defined by

$$\Sigma_x = \frac{d\sigma(\perp, U; U, U) - d\sigma(\parallel, U; U, U)}{d\sigma(\perp, U; U, U) + d\sigma(\parallel, U; U, U)},$$

$$\begin{aligned}
T_y &= \frac{d\sigma(U, y; U, U) - d\sigma(U, -y; U, U)}{d\sigma(U, y; U, U) + d\sigma(U, -y; U, U)}, \\
P_y &= \frac{d\sigma(U, U; y, U) - d\sigma(U, U; -y, U)}{d\sigma(U, U; y, U) + d\sigma(U, U; -y, U)},
\end{aligned} \tag{4.14}$$

where  $\parallel$  and  $\perp$  stand for the linear polarizations of the photon along the direction of the  $\mathbf{x}$  and  $\mathbf{y}$  axes, respectively (Eq. (3.3)).  $y$  and  $-y$  represent the polarization states of the baryons in the direction of the  $\mathbf{y}$  and  $-\mathbf{y}$  axes, respectively. The  $U$  means that the corresponding particle state is unpolarized.

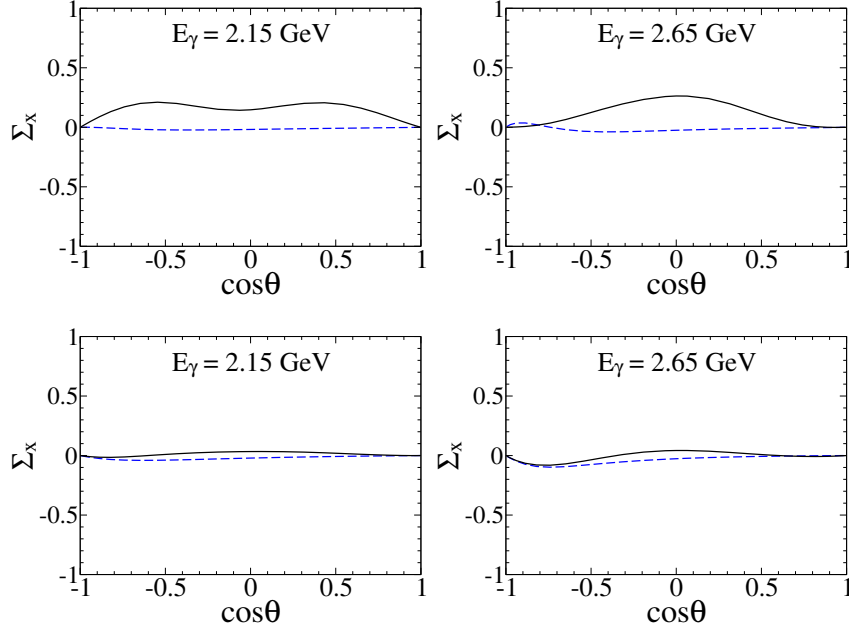


FIGURE 4.8: Photon-beam asymmetries  $\Sigma_\gamma$  for the  $\gamma p \rightarrow K^{*+}\Lambda$  (upper panel) and the  $\gamma n \rightarrow K^{*0}\Lambda$  (lower panel) as functions of  $\cos \theta$  at  $E_\gamma = 2.15$  and  $2.65$  GeV.

In the upper panel of Fig. 4.8, the photon-beam asymmetries  $\Sigma_x$  for the (I)  $K^{*+}\Lambda$  channel are displayed. Similarly to the  $\gamma N \rightarrow K^*\Sigma$  process as done in the previous chapter, the beam asymmetry is close to with zero without the  $N^*$  resonances. But when included, it is found that  $\Sigma_x$  becomes positive and has broad bump structures. The lower panel of Fig. 4.8 shows the  $\Sigma_x$  for the (II)  $K^{*0}\Lambda$  channel. We can see that including the  $N^*$  resonances does not exhibit a notable feature, since  $K$  exchange governs the total and differential cross sections.

Figures 4.9 and 4.10 correspond to the results of the target and recoil asymmetries, respectively. It is interesting that the shape the  $P_y$  is clearly distinguished from that of the beam asymmetry. The  $P_y$  keeps its netegative value from the forward angle, and turn positive around  $\cos \theta = -0.5$  until the backward angle. In the case of the recoil asymmetries, the results are just opposite to those of the target asymmetries.

Next, we examine the results of the double polarization asymmetries. Among the many different polarization observables in the vector meson photoproduction, only some of the

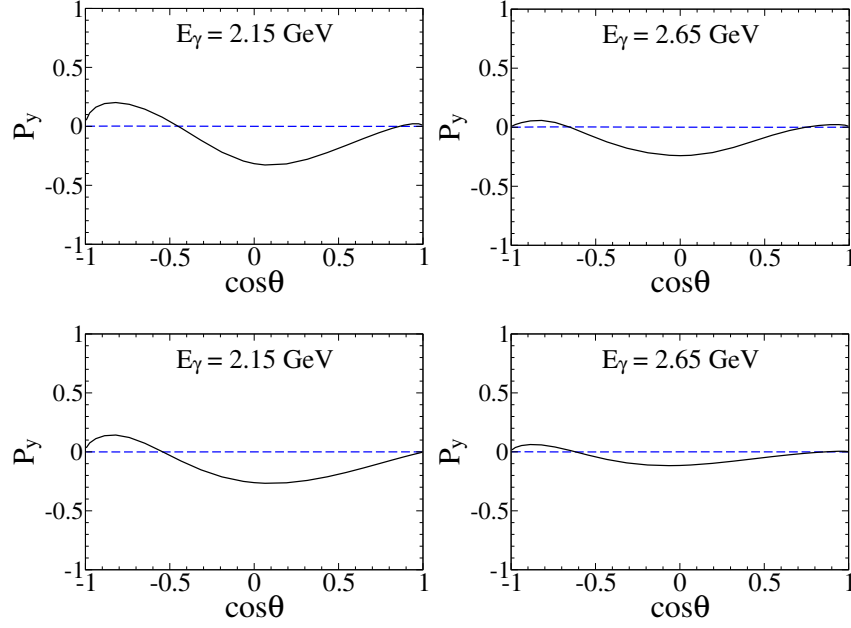


FIGURE 4.9: Recoil asymmetries  $P_y$  for the  $\gamma p \rightarrow K^{*+}\Lambda$  (upper panel) and the  $\gamma n \rightarrow K^{*0}\Lambda$  (lower panel) as functions of  $\cos\theta$  at  $E_\gamma = 2.15$  and  $2.65$  GeV.

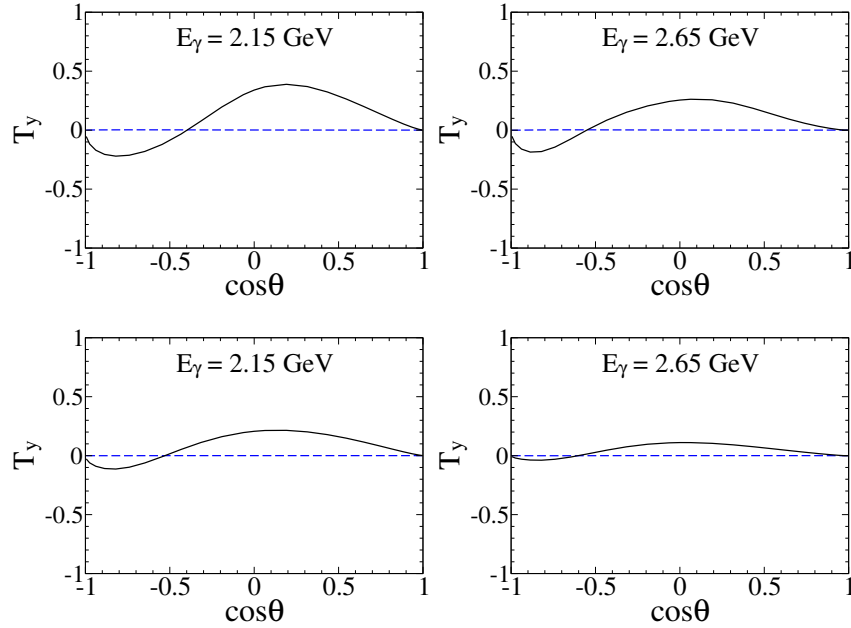


FIGURE 4.10: Target asymmetries  $T_y$  for the  $\gamma p \rightarrow K^{*+}\Lambda$  (upper panel) and the  $\gamma n \rightarrow K^{*0}\Lambda$  (lower panel) as functions of  $\cos\theta$  at  $E_\gamma = 2.15$  and  $2.65$  GeV.

double polarization asymmetries will be investigated, which are defined as follows:

$$\begin{aligned}
C_{zz}^{BT} &= \frac{d\sigma(r, z; U, U) - d\sigma(r, -z; U, U)}{d\sigma(r, z; U, U) + d\sigma(r, -z; U, U)}, \\
C_{zz}^{BR} &= \frac{d\sigma(r, U; z, U) - d\sigma(r, U; -z, U)}{d\sigma(r, U; z, U) + d\sigma(r, U; -z, U)}, \\
C_{zz}^{TR} &= \frac{d\sigma(U, z; z, U) - d\sigma(U, z; -z, U)}{d\sigma(U, z; z, U) + d\sigma(U, z; -z, U)}, \\
C_{zz}^{TV} &= \frac{d\sigma(U, z; U, r) - d\sigma(U, -z; U, r)}{d\sigma(U, z; U, r) + d\sigma(U, -z; U, r)}, \\
C_{zz}^{RV} &= \frac{d\sigma(U, U; z, r) - d\sigma(U, U; -z, r)}{d\sigma(U, U; z, r) + d\sigma(U, U; -z, r)},
\end{aligned} \tag{4.15}$$

where  $r$  designates the circularly polarized photon beam (or produced vector meson) with helicity  $+1$ . The  $C_{zz}^{BT}$ ,  $C_{zz}^{BR}$ ,  $C_{zz}^{TR}$ ,  $C_{zz}^{TV}$ , and  $C_{zz}^{RV}$  are called the beam-target (BT) asymmetry, the beam-recoil (BR) asymmetry, the target-recoil (TR) asymmetry, the target-vector-meson (TV) asymmetry, and the recoil-vector-meson (RV) asymmetry. The  $N^*$  resonances reveal even more dramatic effects, in particular, in the case of the (I)  $K^{*+}\Lambda$  channel.

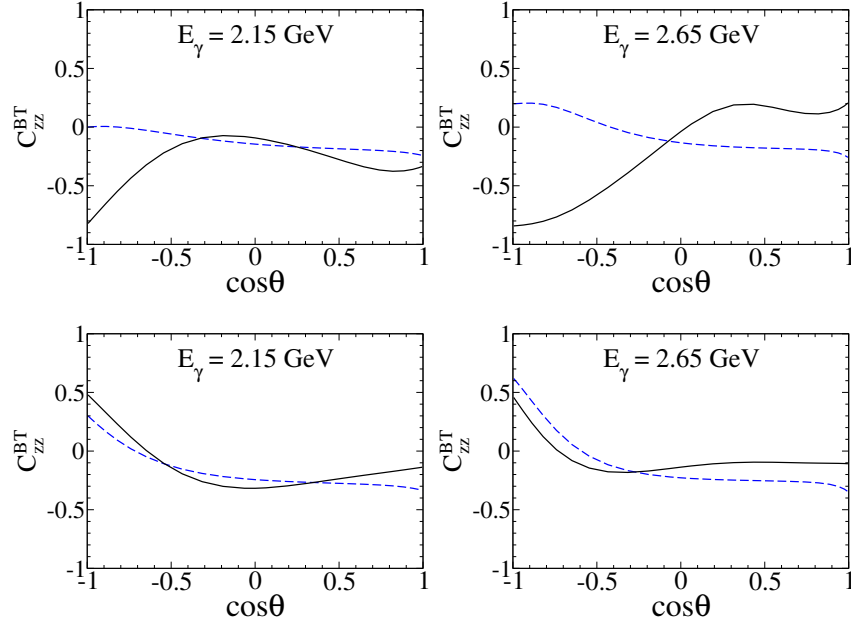


FIGURE 4.11: Beam-target asymmetries  $C_{zz}^{BT}$  for the  $\gamma p \rightarrow K^{*+}\Lambda$  (upper panel) and the  $\gamma n \rightarrow K^{*0}\Lambda$  (lower panel) as functions of  $\cos\theta$  at  $E_\gamma = 2.15$  and  $2.65$  GeV.

In the upper panel of Fig. 4.11, the effects of the  $N^*$  resonances on the BT asymmetry for the (I)  $K^{*+}\Lambda$  channel are shown in comparison with the results without the  $N^*$ . While the  $C_{zz}^{BT}$  vanishes in the very backward direction ( $\cos\theta = -1$ ) without the  $N^*$  resonances, the inclusion of them brings its value down to be negative ( $\approx 0.8$ ). It implies that the polarization of the proton chiefly depends on the  $N^*$  resonances. Interestingly, the effects of the  $N^*$  resonances are not at all lessened even at a higher  $E_\gamma$ . The value of the  $C_{zz}^{BT}$  turns positive at the forward angle, as  $E_\gamma$  increases. The effects of the  $N^*$

resonances on the (II)  $K^{*0}\Lambda$  channel are different from those on the (I)  $K^{*+}\Lambda$  one, as depicted in the lower panel of Fig. 4.11. However, in this case, the BT asymmetry is positive in the very backward direction and then turns negative as  $\cos\theta$  increases.

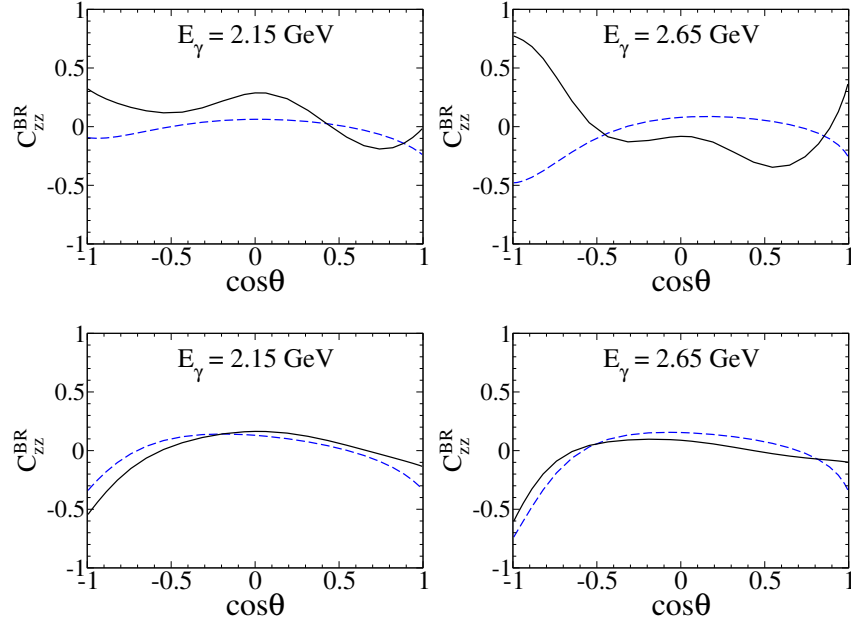


FIGURE 4.12: Beam-recoil asymmetries  $C_{zz}^{BR}$  for the  $\gamma p \rightarrow K^{*+}\Lambda$  (upper panel) and the  $\gamma n \rightarrow K^{*0}\Lambda$  (lower panel) as functions of  $\cos\theta$  at  $E_\gamma = 2.15$  and  $2.65$  GeV.

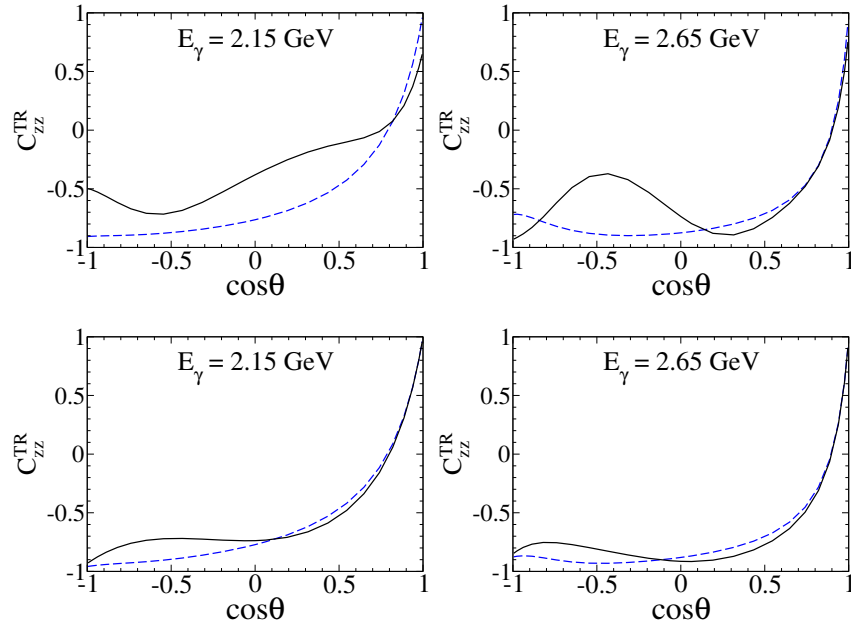


FIGURE 4.13: Target-recoil asymmetries  $C_{zz}^{TR}$  for the  $\gamma p \rightarrow K^{*+}\Lambda$  (upper panel) and the  $\gamma n \rightarrow K^{*0}\Lambda$  (lower panel) as functions of  $\cos\theta$  at  $E_\gamma = 2.15$  and  $2.65$  GeV.

The upper and lower panels of Fig. 4.12 depict the BR asymmetries for the (I)  $K^{*+}\Lambda$  and (II)  $K^{*0}\Lambda$  channels, respectively. Again, the effects of the  $N^*$  resonances on  $C_{zz}^{BR}$  are clearly seen in the case of the charged reaction. On the other hand, the  $N^*$  effects are tiny for the neutral channel. We come to the same conclusion for the TR, TV,



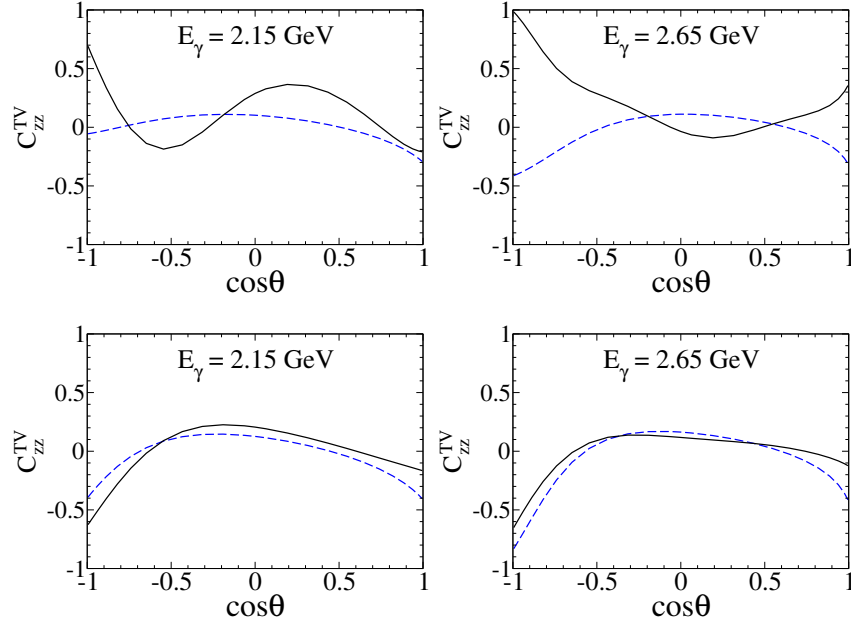


FIGURE 4.14: Target-vector-meson asymmetries  $C_{zz}^{TV}$  for the  $\gamma p \rightarrow K^{*+}\Lambda$  (upper panel) and the  $\gamma n \rightarrow K^{*0}\Lambda$  (lower panel) as functions of  $\cos\theta$  at  $E_\gamma = 2.15$  and  $2.65$  GeV.

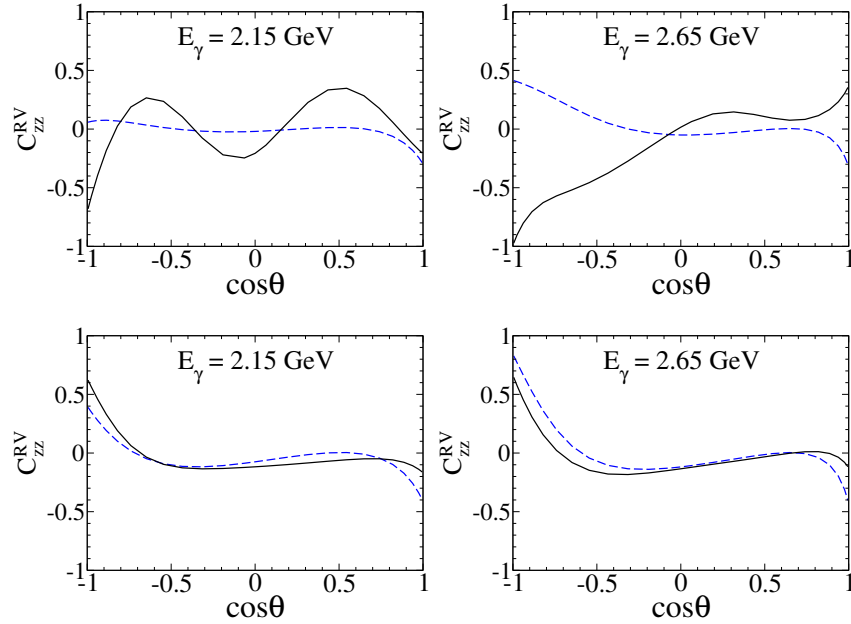


FIGURE 4.15: Recoil-vector-meson asymmetries  $C_{zz}^{RV}$  for the  $\gamma p \rightarrow K^{*+}\Lambda$  (upper panel) and the  $\gamma n \rightarrow K^{*0}\Lambda$  (lower panel) as functions of  $\cos\theta$  at  $E_\gamma = 2.15$  and  $2.65$  GeV.

and RV asymmetries, as shown in Figs. 4.13–4.15, respectively. Future measurements of the double polarization observables will be essential to scrutinizing the role of the  $N^*$  resonances in the  $\gamma N \rightarrow K^*\Lambda$  reactions.

## 4.5 Summary

The aim of this chapter was to study the role of the  $N^*$  resonances in describing the reaction mechanism of  $\gamma N \rightarrow K^*\Lambda$ . We took account of four  $N^*$  resonances,  $N(2000) 5/2^+$ ,  $N(2060) 5/2^-$ ,  $N(2120) 3/2^-$ , and  $N(2190) 7/2^-$  located near the threshold, based on the PDG 2012 edition.

The  $N(2120) 3/2^-$  and  $N(2190) 7/2^-$  played a decisive role in explaining the experimental data for the  $\gamma p \rightarrow K^{*+}\Lambda$ . The total cross sections are in excellent agreement with the CLAS data. The differential cross sections were also well described in the range of  $2.3 \text{ GeV} \leq E_\gamma \leq 3.5 \text{ GeV}$ , except for the bump structures near the threshold and the forward angle data at higher energies. This feature of the  $N^*$  resonances is totally different from the case of  $K^*\Sigma$  photoproduction [43] studied in chapter 3. The extracted resonance coupling constants based on the SU(6) quark model [5] indicate this conclusion. Directly comparing Table 4.2 in this work with Table 3.2 in chapter 3, one can verify the large difference, for example,  $g_{K^*\Sigma_{G_{17}}}/g_{K^*\Lambda_{G_{17}}} \sim 1/8$  due to the different isospin factors.

We calculated the total and differential cross sections for the  $\gamma n \rightarrow K^{*0}\Lambda$ . It turned out that the effects of the  $N^*$  resonances on the neutral channel are marginal. We also predicted the single and double spin observables for both channels. The contribution of the  $N^*$  resonances to them is prominent in the  $\gamma p \rightarrow K^{*+}\Lambda$  reaction, while it is less noticeable for  $K^{*0}\Lambda$  photoproduction.

The  $\gamma N \rightarrow K^*\Lambda$  can be regarded as a subprocess of the  $\gamma N \rightarrow K\pi\Lambda$  reaction. It indicates that  $K^*\Lambda$  photoproduction may be strongly coupled to another subprocess such as the  $\gamma N \rightarrow K\Sigma^*(1385)$  reaction. Therefore it is also interesting to study both the  $\gamma N \rightarrow K^*\Lambda$  and  $\gamma N \rightarrow K\Sigma^*(1385)$  processes within a coupled-channel formalism.

## Chapter 5

# Production rates of charmed baryons

Having examined the role of resonances in the strange scattering processes, we now turn our attention to the charm sector. The structure and the production mechanisms of the charmed baryons are investigated in chapters 5 and 6. In this chapter, we study the production rates of charmed baryons for the  $\pi^- p \rightarrow D^{*-} Y_c$ , where  $Y_c$  is the ground or excited states of charmed baryons, using a quark-diquark model.

### 5.1 Motivation

In the standard quark model, baryons and mesons are described as a three-quark state ( $qqq$ ) and a quark-antiquark state ( $q\bar{q}$ ), respectively. For baryons there are two independent internal motions of modes,  $\rho$  and  $\lambda$  ones. They are degenerate in the light flavor sector, and obviously split in the presence of one heavy quark exhibiting a different spectrum. In the strange sector, the so-called isotope shift is already observed as seen in the inversion of the mass ordering in  $\Sigma(1775)$ - $\Lambda(1830)$ . When we come to the charm sector, it may also be important to examine the structure of baryons systematically. Quark models [121, 122] exist for the study of the structures of charmed baryons.

Let us consider the reaction mechanism  $\pi N \rightarrow VB$ , where  $V$  stands for a charmed vector meson ( $D^*$ ) and  $B$  denotes a charmed baryon in ground or excited states ( $\Lambda_c, \Sigma_c \dots$ ). In Fig. 5.1, the corresponding  $t$ -channel process is drawn in which a charmed reggeon is exchanged. It couples with a light quark in the initial nucleon and transforms into a charm quark forming a charmed baryon in the final state.

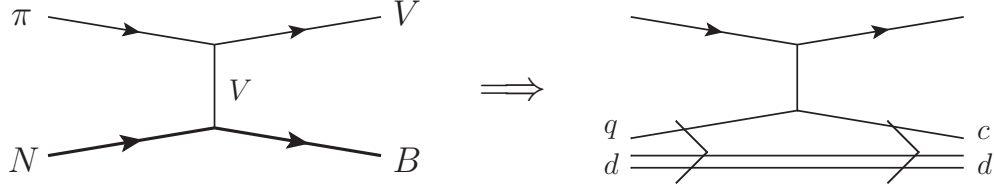


FIGURE 5.1:  $t$ -channel process for the  $\pi N \rightarrow VB$ , where  $V = K^*, D^*$  (left panel). Quark-diquark structure (right panel).

In this chapter, we aim to compute the production rates of various charmed baryons, up to the orbital excitations of  $d$ -wave ( $l = 2$ ), compared to ground state production, using a quark-diquark model [62]. In doing that, one assumption is made: we consider only vector ( $V = D^*$  or  $K^*$ ) reggeon exchanges assuming that they dominate. It is known that at high energies the cross section shows a forward peak. Thus we compute the differential cross sections only at the forward angle.

## 5.2 Quark-diquark model

Baryons can be described as a two-body system of a quark and a diquark. Then a heavy quark and a light diquark constitute a charmed baryon which is schematically drawn in the Jacobi coordinates in the left panel of Fig. 5.2. Here the  $\boldsymbol{\rho}$ ,  $\boldsymbol{\lambda}$ , and  $\mathbf{R}_{\text{cm}}$  coordinates are defined by

$$\boldsymbol{\rho} = \frac{\mathbf{r}_1 - \mathbf{r}_2}{\sqrt{2}}, \quad \boldsymbol{\lambda} = \frac{\mathbf{r}_1 + \mathbf{r}_2 - 2\mathbf{r}_3}{\sqrt{6}}, \quad \mathbf{R}_{\text{cm}} = \frac{m(\mathbf{r}_1 + \mathbf{r}_2) + m_Q \mathbf{r}_3}{2m + m_Q}, \quad (5.1)$$

assuming that the masses of two light quarks are the same. The  $\boldsymbol{\rho}$  and  $\boldsymbol{\lambda}$  coordinates are antisymmetric and symmetric, respectively, under the exchange of  $\mathbf{r}_1$  and  $\mathbf{r}_2$ .

A quark model Hamiltonian with spin-spin interactions can be expressed as

$$H_0 = \frac{1}{2m}(\mathbf{p}_1^2 + \mathbf{p}_2^2) + \frac{1}{2m_Q}\mathbf{p}_3^2 - \frac{1}{2M_{\text{tot}}}\mathbf{P}^2 + V_{\text{conf}}(HO) + V_{\text{CS}} + \dots \quad (5.2)$$

With the definitions

$$M = 2m + m_Q, \quad m_\rho = m, \quad m_\lambda = \frac{3mm_Q}{2m + m_Q}, \quad (5.3)$$

we obtain the momentum conjugate to the above three coordinates

$$\mathbf{p}_\rho = m_\rho \dot{\boldsymbol{\rho}}, \quad \mathbf{p}_\lambda = m_\lambda \dot{\boldsymbol{\lambda}}, \quad \mathbf{P}_{\text{cm}} = M \dot{\mathbf{R}}_{\text{cm}}. \quad (5.4)$$

Finally, in terms of these, the oscillator Hamiltonian reads

$$H_0 = \left( \frac{p_\rho^2}{2m_\rho} + \frac{3}{2}K\rho^2 \right) + \left( \frac{p_\lambda^2}{2m_\lambda} + \frac{3}{2}K\lambda^2 \right) + \frac{P_{\text{cm}}^2}{2M}. \quad (5.5)$$

Since the last term does not affect on the intrinsic spectrum of the baryon, only the first two terms play an important role. It turns out that  $\lambda$  mode acts more collectively. Since  $m_\rho < m_\lambda$  and

$$\begin{aligned} \omega_\rho &= \sqrt{\frac{3K}{m_\rho}} = \sqrt{\frac{3K}{m}}, \\ \omega_\lambda &= \sqrt{\frac{3K}{m_\lambda}} = \sqrt{\frac{K(2m + m')}{mm'}}, \end{aligned} \quad (5.6)$$

we get  $\omega_\rho > \omega_\lambda$ .

The color-magnetic (spin dependent) interaction in Eq. (5.2) has the following form

$$V_{\text{CS}} = - \sum_{ij} \frac{\alpha}{m_i m_j} \frac{\lambda^a(i)}{2} \frac{\lambda^a(j)}{2} \boldsymbol{\sigma}(i) \cdot \boldsymbol{\sigma}(j). \quad (5.7)$$

The interaction is proportional to the inverse masses of the quarks. Thus it is found that the diquark prefers to correlate strongly with light quark pairs, while the combination of containing at least one heavy quark is suppressed.

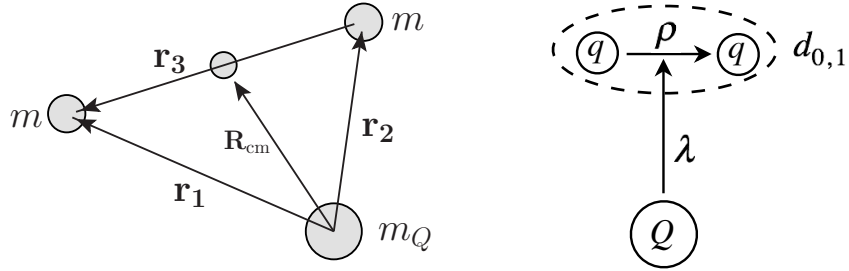


FIGURE 5.2: Jacobi coordinates (left panel).  $\lambda$  and  $\rho$  coordinates of a three-quark system (right panel).

In right panel of Fig. 5.2, the relative motion of the quark and the diquark is depicted by the  $\lambda$  coordinate. The  $\rho$  mode is also implicit in this scheme. Due to the spin-spin interaction, the pair of  ${}^3S_0^\rho$  quarks ( $d^0$ ) is expected to have a lower mass than that of  ${}^3S_1^\rho$  quarks ( $d^1$ ). Even though there can be internal excitations of diquarks and mixing of the  $\lambda$  and  $\rho$  modes, we focus on the  $\lambda$  motions of (orbitally) ground state diquarks of the two kinds,  $d^0$  and  $d^1$ , because the reaction mechanism shown in Fig. 5.2 excites the  $\lambda$  mode dominantly.

The quark-diquark wave functions of the  $\lambda$  modes are summarized in Appendix D. We have then made a tentative assignment of these states with the nominal ones listed in PDG when available [103] as shown in Table 5.1. We have also made arbitrary assignment for the unknown states to fill the corresponding ones by simply guessing their masses. The latter are shown in Table 5.1 with a \* symbol.

### 5.3 Amplitudes

To obtain the production rates of various charmed baryons, the baryon matrix elements should be computed. To do that, we introduce the following two interaction Lagrangians,

$$\mathcal{L}_{\pi VV} = f \epsilon_{\mu\nu\alpha\beta} \partial^\mu \pi \partial^\nu V^\alpha V^\beta, \quad (5.8)$$

$$\mathcal{L}_{Vqc} = g \bar{c} \gamma^\mu q V_\mu, \quad (5.9)$$

where  $f$  and  $g$  denotes the coupling constants, and  $q$  and  $c$  the spinors of the light ( $q = u, d$ ) and charm quarks, respectively.

First, the matrix element of the  $\pi VV$  coupling of Eq. (5.8), reads

$$\langle V(k_V) | \mathcal{L}_{\pi VV} | \pi(k_\pi) V(q) \rangle \sim 2f \epsilon_{\mu 0 \alpha \beta} k_\pi^\mu k_V^0 e^\alpha e^\beta \rightarrow 2f k_V^0 \vec{k}_\pi \times \vec{e} \cdot \vec{e}, \quad (5.10)$$

where  $k_\pi$ ,  $k_V$ , and  $q$  are the momenta of the initial pion, the final  $V$ , and the exchanged  $V$  meson, respectively.  $e^{\alpha, \beta}$  are the polarization vectors of either the final or the intermediate vector mesons. Here we assume that the reaction energy is not too large since the produced energy is limited to the range of  $s/s_0 \lesssim 2$ .

Next, we turn to the baryon matrix element of the  $Vqc$  coupling of Eq. (5.9),

$$\begin{aligned} \langle \mathcal{L}_{Vqc} \rangle &= \langle g \bar{c} \gamma^\mu V_\mu q \rangle \\ &= g \varphi_f^\dagger \left( 1, -\frac{\boldsymbol{\sigma} \cdot \mathbf{p}_f}{m_c + E_c} \right) \begin{pmatrix} V^0 & -\boldsymbol{\sigma} \cdot \mathbf{V} \\ \boldsymbol{\sigma} \cdot \mathbf{V} & -V^0 \end{pmatrix} \begin{pmatrix} 1 \\ \frac{\boldsymbol{\sigma} \cdot \mathbf{p}_i}{m_q + E_q} \end{pmatrix} \varphi_i, \end{aligned} \quad (5.11)$$

where  $\varphi_{i,f}$  stand for the two component spinors for the initial light quark and the final charm quark, respectively. Only the spatial component of the  $V$  meson is taken into account, because it solely survives when contracted with the  $\pi VV$  vertex. Thus we get

$$\begin{aligned} \langle \mathcal{L}_{Vqc} \rangle &\sim -g \varphi_f^\dagger \left[ \frac{1}{m_q + E_q} (\boldsymbol{\sigma} \cdot \mathbf{V}) (\boldsymbol{\sigma} \cdot \mathbf{p}_i) + \frac{1}{m_c + E_c} (\boldsymbol{\sigma} \cdot \mathbf{p}_f) (\boldsymbol{\sigma} \cdot \mathbf{V}) \right] \varphi_i \\ &= -g \varphi_f^\dagger \left[ \left( \frac{\mathbf{p}_f}{m_c + E_c} + \frac{\mathbf{p}_i}{m_q + E_q} \right) \cdot \mathbf{V} + i \boldsymbol{\sigma} \times \left( \frac{\mathbf{p}_f}{m_c + E_c} - \frac{\mathbf{p}_i}{m_q + E_q} \right) \cdot \mathbf{V} \right] \varphi_i \end{aligned} \quad (5.12)$$

Finally, combining the matrix elements Eqs. (5.10) and (5.12), we can express the scattering amplitude as

$$t_{fi} \sim 2fgk_V^0 \mathbf{k}_\pi \times \mathbf{e} \cdot \mathbf{J}_{fi} G_V(t), \quad (5.13)$$

where the baryon transition current  $\mathbf{J}_{fi}$  reads

$$\mathbf{J}_{fi} = \int d^3x \varphi_f^\dagger \left[ \frac{\mathbf{p}_f}{m_c + E_c} + \frac{\mathbf{p}_i}{m_q + E_q} + i\boldsymbol{\sigma} \times \left( \frac{\mathbf{p}_f}{m_c + E_c} - \frac{\mathbf{p}_i}{m_q + E_q} \right) \right] \varphi_i e^{i\mathbf{q}_{eff} \cdot \mathbf{x}} \quad (5.14)$$

and the Regge propagator  $G_V(t)$  is expressed as

$$G_V(t) = \left( \frac{s}{s_0} \right)^{\alpha_V(t)-1} \Gamma(1 - \alpha_V(t)). \quad (5.15)$$

Here we have defined the effective momentum transfer

$$\mathbf{q}_{eff} = \frac{m_d}{m_d + m_q} \mathbf{P}_N - \frac{m_d}{m_d + m_c} \mathbf{P}_B, \quad (5.16)$$

which takes into account the recoil of the center of mass motion due to the change in the masses of  $q$  and  $c$  quarks [123].

Finally, we obtain a rather concise formula for the amplitude

$$t_{fi} \sim \left( \frac{P_B}{2(m_c + m_d)} - 1 \right) k_V^0 k_\pi \langle f | \mathbf{e}_\perp \cdot \boldsymbol{\sigma} e^{i\mathbf{q}_{eff} \cdot \mathbf{x}} | i \rangle G_V(t). \quad (5.17)$$

Here  $\mathbf{e}_\perp$  denotes the transverse vector, and hence the transverse spin induces the transition, as expected for the vector ( $J^P = 1^-$ ) exchange process.

## 5.4 Production rates

We have computed the transition amplitudes  $t_{fi}$  from the nucleon  $i \sim N$  to various charmed baryons  $f \sim B$ . For charmed baryons, we consider all possible states including the ground,  $p$ -wave and  $d$ -wave excitations. The production rates are computed by

$$\mathcal{R} \sim \frac{1}{\text{Flux}} \times \sum_{fi} |t_{fi}|^2 \times \text{Phase space}. \quad (5.18)$$

Using the results of the amplitudes as shown in Appendix D, we find

$$\mathcal{R}(B(J^P)) = \frac{1}{4|\mathbf{p}|\sqrt{s}} \gamma^2 K^2 C |I_L|^2 \frac{q}{4\pi\sqrt{s}}. \quad (5.19)$$

In this expression,  $C$  is the geometric factor of the matrix element  $\langle f | \mathbf{e}_\perp \cdot \boldsymbol{\sigma} e^{i\mathbf{q}_{eff} \cdot \mathbf{x}} | i \rangle$  determined by the spin, angular momentum and total spin of the baryon, while  $I_L (L = 0, 1, 2)$  contains dynamical information of the baryon wave function.  $K$  is the kinematic factor

$$K = k_V^0 k_\pi \left( \frac{P_B}{2(m_c + m_d)} - 1 \right) G_V(t) \quad (5.20)$$

and  $\gamma$  the following isospin overlap factor

$$\begin{aligned} \gamma &= \frac{1}{\sqrt{2}} \quad \text{for } \Lambda \text{ baryons,} \\ &= \frac{1}{\sqrt{6}} \quad \text{for } \Sigma \text{ baryons,} \end{aligned} \quad (5.21)$$

$l = 0$	$\Lambda(\frac{1}{2}^+)$	$\Sigma(\frac{1}{2}^+)$	$\Sigma(\frac{3}{2}^+)$	
$M$ [MeV]	1116	1192	1385	
	2286	2455	2520	
$C$	1	1/9	8/9	
$\mathcal{R}(B_s)$	1	0.04	0.210	
$\mathcal{R}(B_c)$	1	0.03	0.17	
$l = 1$	$\Lambda(\frac{1}{2}^-)$	$\Lambda(\frac{3}{2}^-)$	$\Sigma(\frac{1}{2}^-)$	$\Sigma(\frac{3}{2}^-)$
$M$ [MeV]	1405	1520	1670	1690
	2595	2625	2750	2800
$C$	1/3	2/3	1/27	2/27
$\mathcal{R}(B_s)$	0.07	0.11	0.002	0.003
$\mathcal{R}(B_c)$	0.93	1.75	0.02	0.04
	$\Sigma'(\frac{1}{2}^-)$	$\Sigma'(\frac{3}{2}^-)$	$\Sigma'(\frac{5}{2}^-)$	
	1750	1750	1775	
	2750	2820	2820	
	2/27	56/135	2/5	
	0.003	0.01	0.01	
	0.05	0.21	0.21	
$l = 2$	$\Lambda(\frac{3}{2}^+)$	$\Lambda(\frac{5}{2}^+)$	$\Sigma(\frac{3}{2}^+)$	$\Sigma(\frac{5}{2}^+)$
$M$ [MeV]	1890	1820	1840	1915
	2940	2880	1840	3000*
$C$	2/5	3/5	2/45	3/45
$\mathcal{R}(B_s)$	0.02	0.04	0.003	0.001
$\mathcal{R}(B_c)$	0.49	0.86	0.01	0.02
	$\Sigma'(\frac{1}{2}^+)$	$\Sigma'(\frac{3}{2}^+)$	$\Sigma'(\frac{5}{2}^+)$	$\Sigma'(\frac{7}{2}^+)$
	1880	2000*	2000*	2000*
	3000*	3000*	3000*	3000*
	2/45	8/45	38/105	32/105
	0.001	0.001	0.001	0.001
	0.01	0.05	0.11	0.09

TABLE 5.1: Baryon masses  $M$  [MeV], spin-dependent coefficients  $C$  and the ratios of production rates  $\mathcal{R}$  given in Eq. (5.19). The second and third rows are the ratios  $\mathcal{R}$  for the strange and charmed baryons, respectively, which are normalized to the ground state  $\Lambda$ . They are computed at  $k_\pi^{Lab} = 4.2$  GeV for the strange, and at  $k_\pi^{Lab} = 20$  GeV for the charmed baryons.

By using the baryon wave functions as summarized in Appendix D, the geometric factors  $C$  and the production rates  $\mathcal{R}$  are computed. In Table 5.1, results are shown for both charm and strangeness productions at the pion momentum in the laboratory frame,  $k_\pi^{Lab} = 20$  GeV for charm production and  $k_\pi^{Lab} = 4.2$  GeV for strangeness production. These momenta correspond to  $s/s_{th} = 2$  for both cases. The wave functions of strange



baryons are obtained by replacing the charm quark by a strange quark. The rates  $\mathcal{R}$  presented in the Table 5.1 are normalized by that of the lowest  $\Lambda$  baryon.

## 5.5 Summary

We conclude that the  $\Lambda$  baryons are more produced than the  $\Sigma$ 's for both the strange and charm reactions when comparing the states which have the same quantum numbers. This is a consequence of SU(6) symmetry of the quark-diquark baryons. The charmed resonances turn out to exhibit higher rates of productions than the strangeness ones, except for the  $\Sigma(1/2^+)$  and  $\Sigma(3/2^+)$  when comparing the corresponding states. The  $\Lambda_c$  resonances are similarly or even more produced than the ground state  $\Lambda_c(2286)$ . This is owing to the large overlap of the wave functions when the momentum transfer is large, typically around 1 GeV for charm production. Meanwhile, in the case of the strange production, the  $\Lambda_s$  resonances are much suppressed compared to the ground state  $\Lambda_s(1116)$ .

In our calculation, we assumed that vector (V) reggeon exchange is dominant. But pseudoscalar (P) reggeon exchange also can be considered by replacing the transverse spin by the longitudinal spin,  $e_\perp \cdot \sigma \rightarrow e_\parallel \cdot \sigma$ . Note that the amplitudes of the  $V$  and  $P$  reggeon exchanges do not interfere each other due to the spin selection rule.

## Chapter 6

# Pion-induced $K^{*0}\Lambda$ and $D^{*-}\Lambda_c^+$ productions

The aim of this chapter is to investigate both the  $\pi^-p \rightarrow K^{*0}\Lambda$  and  $\pi^-p \rightarrow D^{*-}\Lambda_c^+$  processes based on an effective Lagrangian method and a Regge approach. The total and differential cross sections for the  $K^*$  production are calculated and those for the  $D^*$  one are estimated.

### 6.1 Motivation

In 2012, a new proposal was submitted at the J-PARC (Japan Proton Accelerator Research Complex) facility to investigate the charmed baryons via the pion-induced reactions at a high-momentum beam line [61]. There has been only one attempt at Brookhaven National Laboratory (BNL) in 1985 to search for the charm productions associated with the mechanism  $\pi^-p \rightarrow D^{*-}B_c$ , where  $B_c$  stands for a charmed baryon in ground or excited states ( $B_c = \Lambda_c^+, \Sigma_c^+, \dots$ ) [124]. No evidence was found for these reactions, but only an upper limit (95% confidence level) is estimated, namely  $7\text{-}nb$ .

On the theoretical side, the differential cross sections  $d\sigma/dt$  for the strange and charm productions, i.e.  $\pi^-p \rightarrow K^{*0}\Lambda$  and  $\pi^-p \rightarrow D^{*-}\Lambda_c^+$ , were calculated as a function of  $s/s_{\text{th}}$  by using a simple Regge model [62] as shown in Fig. 6.1.  $s/s_{\text{th}}$  is the threshold value of  $s$ :  $s_{\text{th}}(\text{strange}) = (m_{K^*} + m_\Lambda)^2$  and  $s_{\text{th}}(\text{charm}) = (m_{D^*} + m_{\Lambda_c})^2$  and the unit of the cross sections is arbitrary [au]. We simply considered only vector reggeon exchange for a rough estimation of the relative strength. The Kaidalov's prescription is employed,

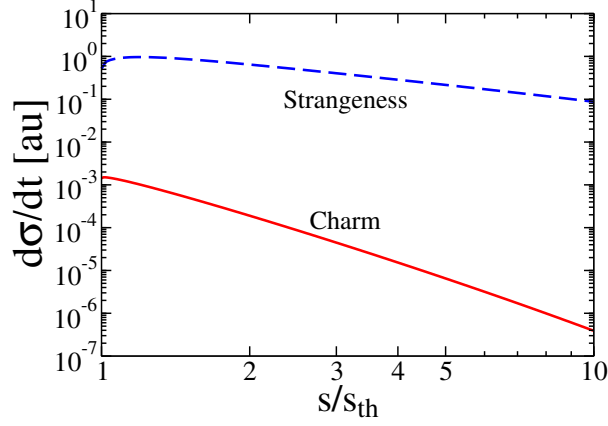


FIGURE 6.1: Forward differential cross sections  $d\sigma/dt(\theta = 0)$  as a function of  $s/s_{\text{th}}$  Ref. [62].

which is based on the quark-gluon string model (QGSM) [125–128],

$$\frac{d\sigma}{dt} = \frac{\text{factor}}{64\pi(p_{\text{cm}})^2 s} \Gamma^2(1 - \alpha_V(t)) \left(\frac{s}{\bar{s}}\right)^2 \left(\frac{s}{s_0}\right)^{2\alpha_V(t)-2}. \quad (6.1)$$

Here  $p_{\text{cm}}$  is the relative momentum of the initial particle in the center-of-mass frame and  $\bar{s}$  is a universal scale parameter. At this moment, the role of  $\bar{s}$  is not important. The other scale parameter  $s_0$  depends on flavors of the reggeon, and is determined by the QGSM [125],

$$s_0(\text{strange}) = 1.66 \text{ GeV}^2, \quad s_0(\text{charm}) = 4.75 \text{ GeV}^2. \quad (6.2)$$

The detailed form of Regge trajectories is referred to the Appendix E. The point here is to examine the forward cross section  $d\sigma/dt(\theta = 0)$  for strange and charm productions, which seems to be plausible since a Regge model is designed to work best in the forward angle region. The ratio of the charm to strange production turns out to be  $10^{-3}$  near the threshold and  $10^{-5}$  at high energy  $s/s_{\text{th}} \sim 10$ . The J-PARC experiment is expected to measure the total cross section most efficiently at  $s/s_{\text{th}} \sim 2$ . According to our results in Fig. 6.1, the rate of charm production is smaller than strange production by a factor about  $10^{-4}$  at this point. Thus, if one uses the data of the total cross sections for the  $K^*$  production, which is of the order of  $10 \text{ } [\mu\text{b}]$  [129, 130], the value for the  $D^*$  production is expected to be of the order of  $1 \text{ } [n\text{b}]$ , using this simple Regge model.

In this chapter, we want to further elaborate the study of Ref. [62] on these two processes, employing both an effective Lagrangian method and a Regge approach, placing emphasis on the latter. In Ref. [126], the  $\pi^- p \rightarrow D^- \Lambda_c^+$  reaction is studied with the QGSM, relying only on the  $D^*$  reggeon. However, in this work, we consider the contribution of the  $D$  and  $\Lambda_c$  reggeons as well as that of the  $D^*$  reggeon using the same model. As we will show later, the  $D^*$  reggeon plays a crucial role in describing the  $\pi^- p \rightarrow D^{*-} \Lambda_c^+$  reaction.

## 6.2 Formalism (Effective Lagrangian method)

In this section, we explain the general framework of an effective Lagrangian approach to study both the  $\pi^-p \rightarrow K^{*0}\Lambda$  and  $\pi^-p \rightarrow D^{*-}\Lambda_c^+$  reactions. The effective Lagrangian method is known to be successful in describing hadron productions near the low energy region.

### 6.2.1 Effective Lagrangians

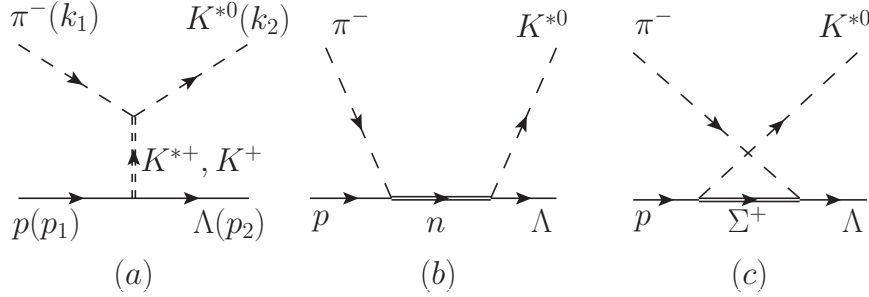


FIGURE 6.2: Tree-level diagrams for the  $\pi^-p \rightarrow K^{*0}\Lambda$ .

We first start with the  $\pi^-p \rightarrow K^{*0}\Lambda$  reaction. The relevant tree-level diagrams are depicted in Fig. 6.2 in which  $k_1$  and  $p_1$  stand for the momenta of the initial  $\pi$  and proton, respectively.  $k_2$  and  $p_2$  denote those of the final  $K^*$  and  $\Lambda$ , respectively. In this model, we consider (a) the  $t$ -channel process ( $K$  and  $K^*$  exchanges); (b) the  $s$ -channel one (the nucleon exchange); and (c) the  $u$ -channel one ( $\Sigma$  exchange).

The invariant Feynman amplitudes are calculated from the following Lagrangians:

$$\begin{aligned}\mathcal{L}_{\pi K K^*} &= -ig_{\pi K K^*}(\bar{K}\partial^\mu \boldsymbol{\tau} \cdot \boldsymbol{\pi} K_\mu^* - \bar{K}_\mu^* \partial^\mu \boldsymbol{\tau} \cdot \boldsymbol{\pi} K), \\ \mathcal{L}_{\pi K^* K^*} &= g_{\pi K^* K^*} \epsilon^{\mu\nu\alpha\beta} \partial_\mu \bar{K}_\nu^* \boldsymbol{\tau} \cdot \boldsymbol{\pi} \partial_\alpha K_\beta^*,\end{aligned}\tag{6.3}$$

for the  $K^*$  meson and pseudoscalar-octet-meson interactions. To determine the coupling constant  $g_{\pi K K^*}$ , the experimental data of the decay width  $\Gamma(K^* \rightarrow K\pi)$  [1] is used. From the above Lagrangian  $\mathcal{L}_{\pi K K^*}$ , the decay width can be expressed kinematically as

$$\Gamma(K^* \rightarrow K\pi) = g_{K^* K \pi}^2 \frac{k_\pi^3}{8\pi M_{K^*}^2},\tag{6.4}$$

where  $k_\pi$  is the three-momentum of the decaying particle

$$k_\pi = \frac{\sqrt{[M_{K^*}^2 - (M_K + M_\pi)^2][M_{K^*}^2 - (M_K - M_\pi)^2]}}{2M_{K^*}},\tag{6.5}$$

so that one can easily obtain  $g_{\pi K K^*} = 6.56$ . Using the hidden local gauge symmetry [131] and SU(3) flavor symmetry (Appendix F), we get the  $\pi K^* K^*$  coupling constant as  $g_{\pi K^* K^*} = 7.45 \text{ GeV}^{-1}$ .

The interaction between the  $K^*$  vector meson and the baryon octet is represented by the following effective Lagrangian:

$$\mathcal{L}_{K^* N Y} = -g_{K^* N Y} \bar{N} \left[ \gamma_\mu Y - \frac{\kappa_{K^* N Y}}{2M_N} \sigma_{\mu\nu} Y \partial^\nu \right] K^{*\mu} + \text{H.c.}, \quad (6.6)$$

where  $Y$  designates  $\Lambda$  or  $\tau \cdot \Sigma$ . We take the values of the coupling constants  $g_{K^* N Y}$  and  $\kappa_{K^* N Y}$  from the Nijmegen soft-core model (NSC97a) [78].

For the pseudoscalar meson and baryon octet vertices, two types of couplings are possible: the pseudoscalar (PS) or the pseudovector (PV) couplings. The former one corresponds to

$$\begin{aligned} \mathcal{L}_{\pi N N}^{\text{PS}} &= -ig_{\pi N N} \bar{N} \gamma_5 \tau \cdot \pi N, \\ \mathcal{L}_{\pi \Sigma \Lambda}^{\text{PS}} &= -ig_{\pi \Sigma \Lambda} \bar{\Lambda} \gamma_5 \pi \cdot \Sigma + \text{H.c.}, \\ \mathcal{L}_{K N \Lambda}^{\text{PS}} &= -ig_{K N \Lambda} \bar{N} \gamma_5 \Lambda K + \text{H.c.}, \end{aligned} \quad (6.7)$$

and the latter one reads

$$\begin{aligned} \mathcal{L}_{\pi N N}^{\text{PV}} &= \frac{g_{\pi N N}}{2M_N} \bar{N} \gamma_\mu \gamma_5 \partial^\mu \tau \cdot \pi N, \\ \mathcal{L}_{\pi \Sigma \Lambda}^{\text{PV}} &= \frac{g_{\pi \Sigma \Lambda}}{M_\Lambda + M_\Sigma} \bar{\Lambda} \gamma_\mu \gamma_5 \partial^\mu \pi \cdot \Sigma + \text{H.c.}, \\ \mathcal{L}_{K N \Lambda}^{\text{PV}} &= \frac{g_{K N \Lambda}}{M_N + M_\Lambda} \bar{N} \gamma_\mu \gamma_5 \Lambda \partial^\mu K + \text{H.c.} \end{aligned} \quad (6.8)$$

Note that the  $t$ -channel process is equivalent each other because only at this case the relevant baryons are on their mass shell. In other words, only  $\mathcal{L}_{K N \Lambda}^{\text{PS}}$  and  $\mathcal{L}_{K N \Lambda}^{\text{PV}}$  are equivalent each other. But the  $s$ - and  $u$ -channel processes do not yield the same result in two types. In the next section, we compare two different results according to the types of Lagrangians. The coupling constants  $g_{\pi N N}$ ,  $g_{\pi \Sigma \Lambda}$ , and  $g_{K N \Lambda}$  are again taken from the Nijmegen potential [78].

We tabulate all the relevant coupling constants in Table 6.1.

$g_{\pi K K^*}$	$g_{\pi K^* K^*}$	$g_{\pi N N}$	$g_{\pi \Sigma \Lambda}$	$g_{K N \Lambda}$	$g_{K^* N \Lambda}$	$\kappa_{K^* N \Lambda}$	$g_{K^* N \Sigma}$	$\kappa_{K^* N \Sigma}$
6.56	$7.45 \text{ GeV}^{-1}$	13.3	11.9	-13.4	-4.26	2.91	-2.46	-0.529

TABLE 6.1: The relevant coupling constants used in the  $\pi^- p \rightarrow K^{*0} \Lambda$ .

### 6.2.2 Scattering amplitudes

The scattering amplitude for the  $\pi N \rightarrow K^* \Lambda$  can be expressed as

$$\mathcal{M} = \varepsilon_\mu^* \bar{u}_\Lambda \mathcal{M}^\mu u_N, \quad (6.9)$$

where  $u_N$  and  $u_\Lambda$  stand for the Dirac spinors for the incoming nucleon and for the outgoing  $\Lambda$ , respectively, and  $\varepsilon_\mu$  denotes the polarization vector of the outgoing  $K^*$  meson.

For  $t$ -channel exchange, the amplitudes are obtained as follows:

$$\begin{aligned} \mathcal{M}_K^\mu(\text{PS}) &= I_K \frac{-ig_{\pi K K^*}}{t - M_K^2} g_{KN\Lambda} \gamma_5 k_1^\mu, \\ \mathcal{M}_K^\mu(\text{PV}) &= I_K \frac{ig_{\pi K K^*}}{t - M_K^2} \frac{g_{KN\Lambda}}{M_N + M_\Lambda} \gamma^\nu \gamma_5 k_1^\mu (k_2 - k_1)_\nu, \\ \mathcal{M}_{K^*}^\mu &= I_{K^*} \frac{g_{\pi K^* K} g_{K^* N \Lambda}}{t - M_{K^*}^2} \epsilon^{\mu\nu\alpha\beta} \left[ \gamma_\nu - \frac{i\kappa_{K^* N \Lambda}}{M_N + M_\Lambda} \sigma_{\nu\lambda} (k_2 - k_1)^\lambda \right] k_{2\alpha} k_{1\beta} \end{aligned} \quad (6.10)$$

and for  $s$ - and  $u$ -channel exchanges, we get

$$\begin{aligned} \mathcal{M}_N^\mu(\text{PS}) &= I_N \frac{ig_{K^* N \Lambda} g_{\pi N N}}{s - M_N^2} \left[ \gamma^\mu - \frac{i\kappa_{K^* N \Lambda} k_{2\nu}}{M_N + M_\Lambda} \sigma^{\mu\nu} \right] (\not{k}_1 + \not{p}_1 + M_N) \gamma_5, \\ \mathcal{M}_N^\mu(\text{PV}) &= I_N \frac{ig_{K^* N \Lambda} g_{\pi N N}}{s - M_N^2} \frac{g_{\pi N N}}{2M_N} \left[ \gamma^\mu - \frac{i\kappa_{K^* N \Lambda} k_{2\nu}}{M_N + M_\Lambda} \sigma^{\mu\nu} \right] (\not{k}_1 + \not{p}_1 + M_N) \gamma^\alpha \gamma_5 k_{1\alpha}, \\ \mathcal{M}_\Sigma^\mu(\text{PS}) &= I_\Sigma \frac{ig_{K^* N \Sigma} g_{\pi \Sigma \Lambda}}{u - M_\Sigma^2} \gamma_5 (\not{p}_2 - \not{k}_1 + M_\Sigma) \left[ \gamma^\mu - \frac{i\kappa_{K^* N \Sigma} k_{2\nu}}{M_N + M_\Sigma} \sigma^{\mu\nu} \right], \\ \mathcal{M}_\Sigma^\mu(\text{PV}) &= I_\Sigma \frac{ig_{K^* N \Sigma} g_{\pi \Sigma \Lambda}}{u - M_\Sigma^2} \frac{g_{\pi \Sigma \Lambda}}{M_\Sigma + M_\Lambda} \gamma^\alpha \gamma_5 (\not{p}_2 - \not{k}_1 + M_\Sigma) \left[ \gamma^\mu - \frac{i\kappa_{K^* N \Sigma} k_{2\nu}}{M_N + M_\Sigma} \sigma^{\mu\nu} \right] \end{aligned} \quad (6.11)$$

### 6.2.3 Form factors

We choose the following form of form factor

$$F(q, M) = \frac{\Lambda^4}{\Lambda^4 + (q^2 - M^2)^2}, \quad (6.12)$$

which is also used in the photoproduction process as discussed in chapters 3 and 4. Here  $q$  and  $M$  denote the transfer momentum and the mass of the exchanged particle, respectively. Note that we employ another type of form factor when investigating the Regge model. The cutoff mass  $\Lambda$  is usually fitted to reproduce the experimental data. The final form of the scattering amplitude is written as

$$\mathcal{M}(\pi^- p \rightarrow K^{*0} \Lambda) = \mathcal{M}_K \cdot F_K + \mathcal{M}_{K^*} \cdot F_{K^*} + \mathcal{M}_N \cdot F_N + \mathcal{M}_\Sigma \cdot F_\Sigma. \quad (6.13)$$

The isospin factor  $I$  turns out to be the same for all the channels,  $I_K = I_{K^*} = I_N = I_\Sigma = \sqrt{2}$ .

#### 6.2.4 Charm production

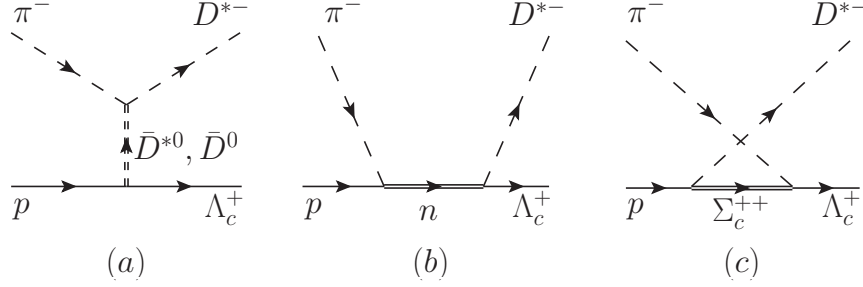


FIGURE 6.3: Tree-level diagrams for the  $\pi^- p \rightarrow D^{*-}\Lambda_c^+$ .

Now we turn to the charm production reaction  $\pi^- p \rightarrow D^{*-}\Lambda_c^+$ . The amplitude for this process is obtained just by replacing the strange mesons and the hyperons by the charmed ones. The relevant Feynman diagrams are shown in Fig. 6.3. In principle, the coupling constants for the charmed hadrons should be different from those for the strange hadrons. In the present calculation, however, we use intentionally the same coupling constants for the corresponding vertices. This might be considered to be a good assumption if strange and charm quarks are sufficiently heavy. One exception is the coupling constant  $g_{\pi D^* D^*}$ . The dimensionful constant  $g_{\pi K^* K^*}$  is related to the dimensionless one  $\bar{g}_{\pi K^* K^*}$  as  $g_{\pi K^* K^*} = \bar{g}_{\pi K^* K^*}/M_{K^*}$ . On the other hand, we normalize the dimensionful constant for the  $\pi D^* D^*$  vertex to be  $g_{\pi D^* D^*} = \bar{g}_{\pi K^* K^*}/M_{D^*}$ , which means that  $g_{\pi D^* D^*} = M_{K^*}/M_{D^*} \cdot g_{\pi K^* K^*}$ . Typically, the coupling constants in the strange and heavy sectors differ by a factor of order one; for instance  $g_{\pi K K^*} \sim g_{\pi D D^*}/2$ , while other relations are unknown. This is the main source of the possible uncertainty in our present study. Keeping this in our mind, we expect that the present prescription allows us to make a comparison between the strange and charm productions.

The form of the scattering amplitude is similar to that of the strange production amplitude

$$\mathcal{M}(\pi^- p \rightarrow D^{*-}\Lambda_c^+) = \mathcal{M}_D \cdot F_D + \mathcal{M}_{D^*} \cdot F_{D^*} + \mathcal{M}_N \cdot F_N + \mathcal{M}_{\Sigma_c} \cdot F_{\Sigma_c}. \quad (6.14)$$

### 6.3 Results (Effective Lagrangian method)

We present our numerical results in this section. To determine the cutoff parameters, the experimental data of the total and differential cross sections for the  $\pi^- p \rightarrow K^{*0}\Lambda$  [129,

[130, 132, 133] are used. In general, the cutoff mass  $\Lambda$  depends on the reaction channel,  $K$ -,  $K^*$ -,  $N$ -, and  $\Sigma$ -exchanges. At this moment, to minimize the number of parameters for a rough estimation of the production rate, two different values are employed, for the meson exchanges and baryon exchanges, separately. With the same coupling constants and cutoff masses, the total and differential cross sections for the  $\pi^- p \rightarrow D^{*-}\Lambda_c^+$  are predicted and compared to those for the  $\pi^- p \rightarrow K^{*0}\Lambda$ . The determined cutoff masses are listed in Table 6.2.

channel	$\Lambda_K$	$\Lambda_{K^*}$	$\Lambda_N$	$\Lambda_\Sigma$
$\pi^- p \rightarrow K^{*0}\Lambda$	0.55	0.55	0.60	0.60
channel	$\Lambda_D$	$\Lambda_{D^*}$	$\Lambda_N$	$\Lambda_{\Sigma_c}$
$\pi^- p \rightarrow D^{*-}\Lambda_c^+$	0.55	0.55	0.60	0.60

TABLE 6.2: Cutoff masses [GeV] to each channel for the  $\pi^- p \rightarrow K^{*0}\Lambda$  and the  $\pi^- p \rightarrow D^{*-}\Lambda_c^+$ .

### 6.3.1 Total cross sections

We first depict the contributions of each channel to the total cross section for the  $\pi^- p \rightarrow K^{*0}\Lambda$ . In the previous section, it is mentioned that there can be two types of couplings: pseudoscalar (PS) and pseudovector (PV) ones. Figures. 6.4 and 6.5 correspond to the results of the former and latter cases, respectively. It is drawn as a function of  $s/s_{\text{th}}$ , where  $s_{\text{th}}$  is the threshold value of  $s$ , i.e.  $s_{\text{th}} = (m_{K^*} + m_\Lambda)^2 = 4.05 \text{ GeV}^2$ .

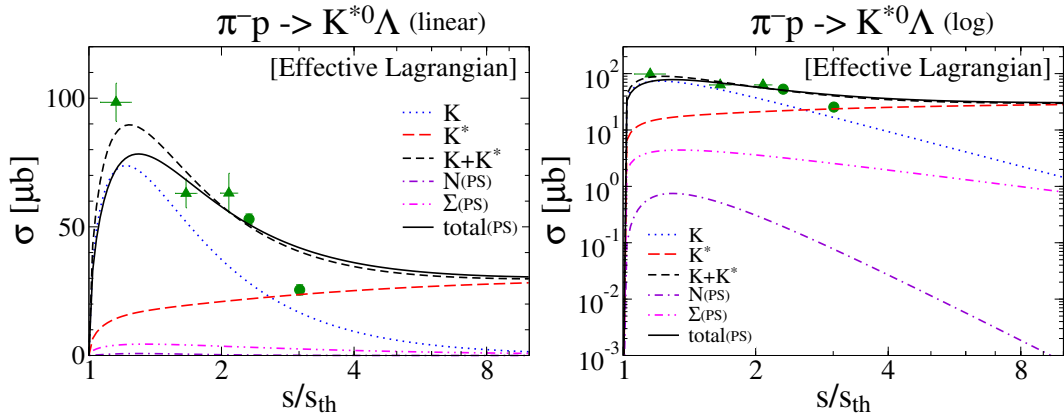


FIGURE 6.4: Total cross section for the  $\pi^- p \rightarrow K^{*0}\Lambda$  based on the effective Lagrangian method with the PS Lagrangian. The data are taken from Ref. [129] (triangles) and Ref. [130] (circles).

In both cases, it is found that the  $t$ -channel process makes the most dominant contribution to the total cross section.  $K$  exchange plays a decisive role in explaining the experimental data in the low energy region, whereas  $K^*$  exchange governs its behavior in the high energy region. This is so since the contribution of  $K$  exchange falls off as



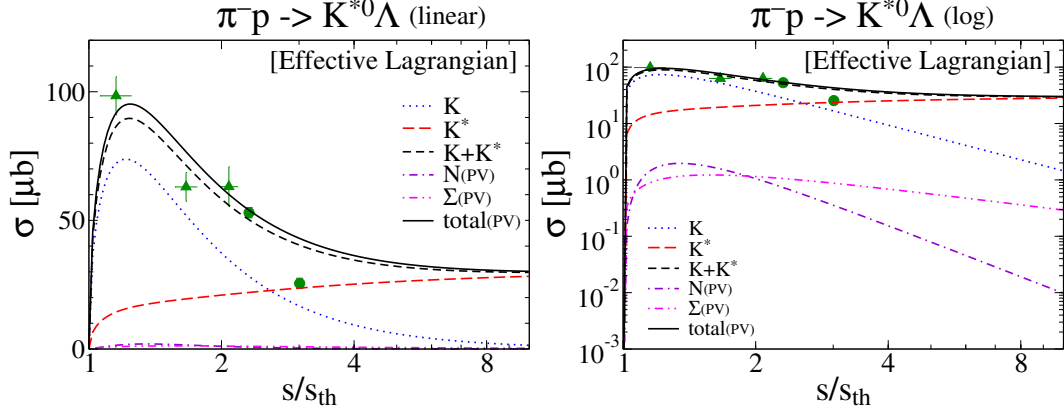


FIGURE 6.5: Total cross section for the  $\pi^- p \rightarrow K^{*0}\Lambda$  based on the effective Lagrangian method with the PV Lagrangian. The data are taken from Ref. [129] (triangles) and Ref. [130] (circles).

$s$  increases, while the effect of  $K^*$  exchange becomes larger with  $s$  increasing. But, in the end, it gets constant when  $s$  is large enough. The reason of this pattern of behavior comes from the fact that the cross section is proportional to  $J - 1$ ,  $\sigma \sim s^{J-1}$ , where  $J$  denotes the spin of an exchange particle in the  $t$  channel. This relation is derived by combining a single term of the  $t$ -channel partial-wave analysis and the optical theorem (Eq. 2.15). There is no interference between  $K$  and  $K^*$  exchanges as explained in Ref [62] in detail. Moreover, since the Lagrangian  $\mathcal{L}_{K\Lambda}^{\text{PS}}$  (Eq. (6.7)) is equivalent to  $\mathcal{L}_{K\Lambda}^{\text{PV}}$  (Eq. (6.8)), the contribution of  $K + K^*$  exchange is the same for both the PS and PV types.

On the other hand, baryon exchanges give almost marginal contribution at any energies. One noticeable feature is that the phase between this baryon exchanges and meson exchanges are different each other. In the case of the pseudoscalar (PS) type, the phase is destructive at lower energies and becomes constructive from  $s/s_{\text{th}} \sim 2$  (Fig. 6.4). In the case of the pseudovector (PV) type, it is always constructive over the whole energy region (Fig. 6.5).

The result of the total cross section matches the experimental data [129, 130] only in the relatively low energy region ( $s/s_{\text{th}} \lesssim 2.1$ ) and begins to deviate from the data as  $s$  increases. It seems to be reasonable because the effective Lagrangian method is based on the Born approximation and thus is constructed to describe mainly the lower energy region near threshold.

### 6.3.2 Differential cross sections $d\sigma/d\Omega$

In Figs. 6.6 and 6.7, the results of the differential cross sections  $d\sigma/d\Omega$  for the  $\pi^- p \rightarrow K^{*0}\Lambda$  are drawn as functions of  $\cos\theta$ .  $\theta$  is the scattering angle between the incoming

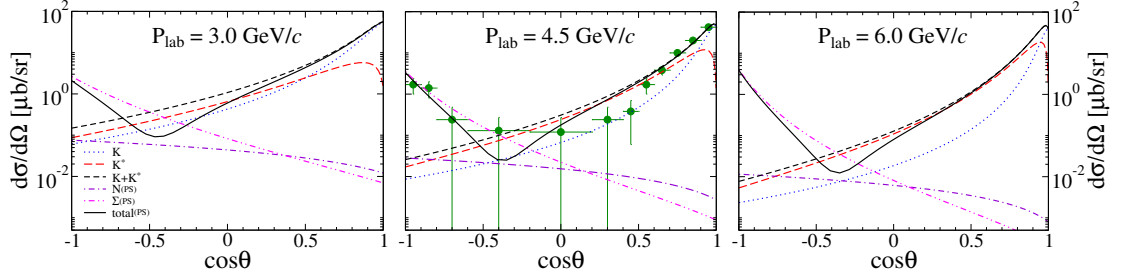


FIGURE 6.6: Differential cross sections  $d\sigma/d\Omega$  for the  $\pi^-p \rightarrow K^{*0}\Lambda$  as functions of  $\cos\theta$  based on the effective Lagrangian method with the PS Lagrangian. The data are taken from Ref. [130].

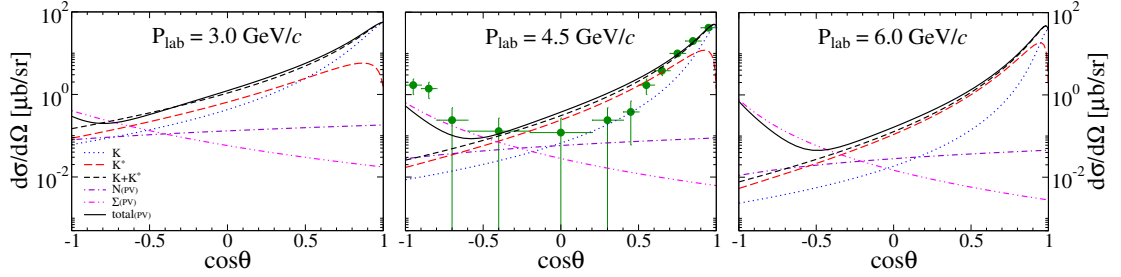


FIGURE 6.7: Differential cross sections  $d\sigma/d\Omega$  for the  $\pi^-p \rightarrow K^{*0}\Lambda$  as functions of  $\cos\theta$  based on the effective Lagrangian method with the PV Lagrangian. The data are taken from Ref. [130].

$\pi$  and the outgoing  $K^*$  meson in the center-of-mass frame. Similarly to the previous subsection, two types of results are illustrated separately.

$K$  and  $K^*$  exchanges are mostly dominant, especially in the forward angle region. When they reach near  $\cos\theta \sim 1$ , the contribution of  $K^*$  exchange is sharply reduced. But that of  $K$  exchange keeps its rising behavior over the whole angle region.  $s$ -channel exchange is known to exhibit the flatness in angle distribution. This is reflected in the PV type more precisely rather than in the PS one as seen in the  $N$  exchange. A relativistic effect may shift it slightly. On the other hand,  $\Sigma$  exchange in the  $u$  channel becomes important at backward angles though the magnitude is much smaller than that of  $t$ -channel exchange.

Because of these different characters of each contribution, the dip structure appears in the range of  $-0.6 \leq \cos\theta \leq -0.2$  and  $-0.8 \leq \cos\theta \leq -0.4$  for the PS and PV types, respectively. As  $P_{\text{lab}}$  increases, this tendency becomes stronger for both cases, and in the former case the differential cross section is much deeper than the latter case. This dip structure is not enough to describe the flatness of the experimental data [130] between the intermediate angles  $-0.5 \leq \cos\theta \leq 0$ . Only the very forward angle region is well reproduced by using the effective Lagrangian approach.

### 6.3.3 Differential cross sections $d\sigma/dt$

We show the results of the differential cross sections  $d\sigma/dt$  for the  $\pi^-p \rightarrow K^{*0}\Lambda$  in Fig. 6.8. Only the PV type is considered here and will be applied to the Regge formula in the next section since it seems to describe the total cross section better rather than the PS type. They are drawn as functions of  $-t' = t_{\max} - t$ , where the minimum and maximum values of  $t$  are expressed kinematically as

$$t_{\min}^{\max} = M_\pi^2 + M_{K^*}^2 - \frac{1}{2s} \left[ s - (M_N^2 - M_\pi^2) \right] \left[ s - (M_\Lambda^2 - M_{K^*}^2) \right] \mp \sqrt{[s - (M_N + M_\pi)^2][s - (M_N - M_\pi)^2]} \sqrt{[s - (M_\Lambda + M_{K^*})^2][s - (M_\Lambda - M_{K^*})^2]}, \quad (6.15)$$

respectively. For each of fixed energies,  $t$  varies between  $t_{\min}$  and  $t_{\max}$  (or  $-t'$  varies between 0 and  $t_{\max} - t_{\min}$ ). The differential cross section is defined in terms of the Feynman amplitude  $\mathcal{M}$  as

$$\frac{d\sigma}{dt} = \frac{1}{64\pi(p_{\text{cm}})^2 s} \frac{1}{2} \sum_{s_i, s_f, \lambda_f} |\mathcal{M}|^2, \quad (6.16)$$

where  $s_i$  and  $s_f$  designate the spins of the nucleon and the  $\Lambda$ , respectively.  $\lambda_f$  stands for the polarization label of  $K^*$  meson and the  $p_{\text{cm}}$  the momentum of pion in the center-of-mass frame.

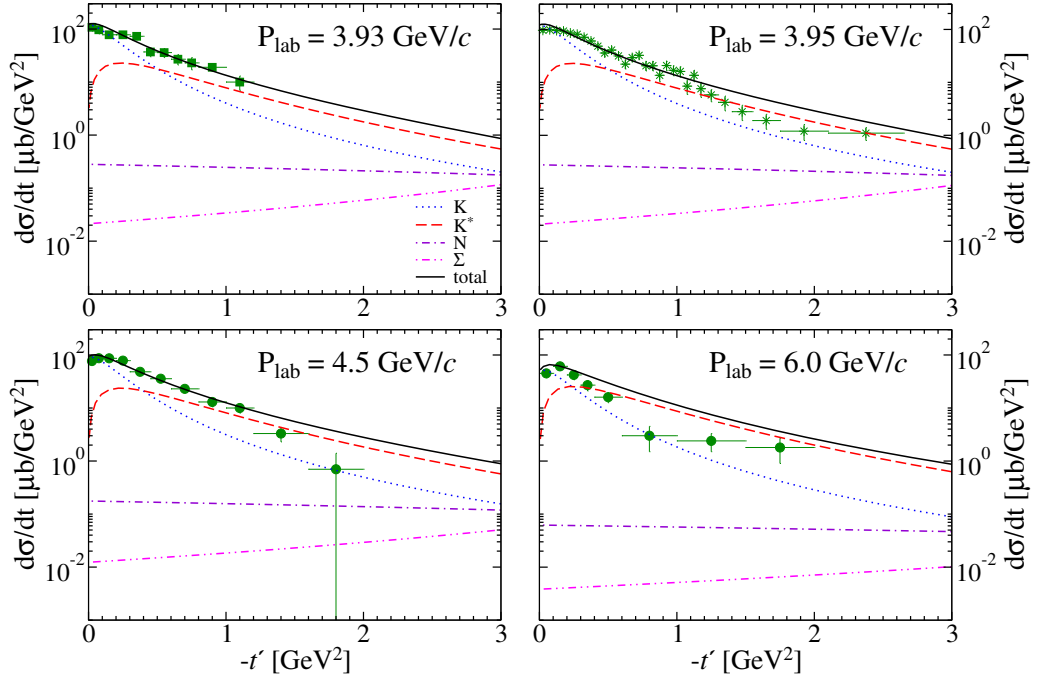


FIGURE 6.8: Differential cross sections  $d\sigma/dt$  for the  $\pi^-p \rightarrow K^{*0}\Lambda$  as functions of  $t'$  based on the effective Lagrangian method with the PV Lagrangian. The data are taken from Ref. [132] (squares), Ref. [133] (stars), and Ref. [130] (circles).

The contributions of  $t$ -channel exchanges decrease as  $-t'$  increases, as expected.  $K$  exchange governs  $d\sigma/dt$  near  $-t' \approx 0$ , whereas  $K^*$  exchange becomes the main contribution to  $d\sigma/dt$ . This feature does not change in general, even though  $P_{\text{lab}}$  increases. The  $s$ - and  $u$ -channel effects are almost negligible. The results from the effective Lagrangian approach are in good agreement with the experimental data between  $-t' = 0$  and  $-t' = 1.2 \text{ GeV}^2$ , and they start to deviate from the data as  $-t'$  increases. Note that the effective Lagrangian method can only explain the data in the smaller  $-t'$  region when  $P_{\text{lab}} = 6.0 \text{ GeV}/c$ .

### 6.3.4 Charm production

We now turn to the charm production, again based on the effective Lagrangian method. In the left panel of Fig. 6.9, the results of the total cross section for the  $\pi^- p \rightarrow D^{*-}\Lambda_c^+$  reaction are drawn as a function of  $s/s_{\text{th}}$ . Note that  $s_{\text{th}}$  is different from the case of strange production, i.e.  $s_{\text{th}} = (m_{D^*} + m_{\Lambda_c})^2 = 18.4 \text{ GeV}^2$ . In contrast with the  $K^*\Lambda$  production, the effect of  $D$  exchange is very much suppressed in the  $D^*\Lambda_c$  production, while  $D^*$  exchange dominates the process. As mentioned in the case of the strange production, the total cross section for the  $\pi N \rightarrow D^*\Lambda_c$  reaction is proportional to  $s^{J-1}$  when  $s$  is large, so that  $D^*$  exchange dictates the total cross section at higher energies. All other contributions including  $D$  exchange have some effects on it only in the vicinity of threshold.

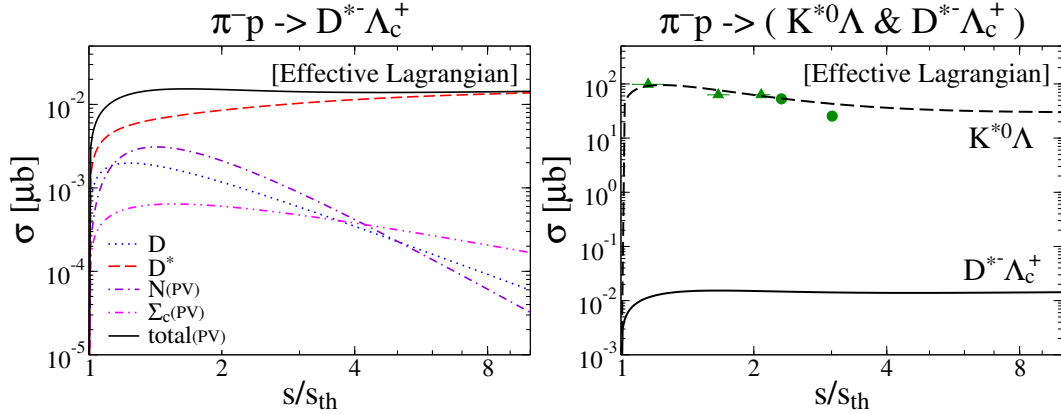


FIGURE 6.9: Total cross section for the  $\pi^- p \rightarrow D^{*-}\Lambda_c^+$  based on the effective Lagrangian method using PV Lagrangian (left panel). Comparison of the total cross section for the  $\pi^- p \rightarrow D^{*-}\Lambda_c^+$  with that for the  $\pi^- p \rightarrow K^{*0}\Lambda$  (right panel). The data are taken from Ref. [129] (triangles) and Ref. [130] (circles).

The result of the total cross section for the  $\pi^- p \rightarrow D^{*-}\Lambda_c^+$  reaction is compared with that for the  $\pi^- p \rightarrow K^{*0}\Lambda$  in the right panel of Fig. 6.9. The total cross section for the charm production is about  $10^4$  times smaller than that for the strange one near the threshold region. When  $s/s_{\text{th}}$  reaches around 10, the total cross section for the  $D^*\Lambda_c$

production becomes approximately  $10^3$  times smaller than that for the  $K^*\Lambda$  production. The reason for this smallness mainly comes from the form factors.

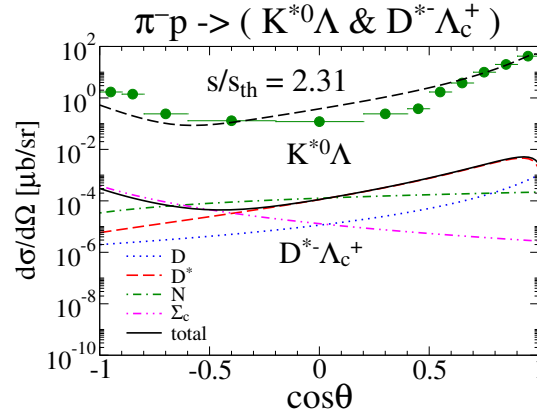


FIGURE 6.10: Comparison of the differential cross section for the  $\pi^-p \rightarrow D^{*-}\Lambda_c^+$  with that for the  $\pi^-p \rightarrow K^{*0}\Lambda$  based on the effective Lagrangian method using PV Lagrangian. The data are taken from Ref. [130].

The difference in the differential cross section  $d\sigma/d\Omega$  is also analyzed in Fig 6.10. As expected from the data of the total cross section,  $D^*$  exchange is dominant, particularly in the range of  $0 \leq \cos\theta \leq 1$ . In the backward region,  $\Sigma_c$  exchange governs the charm process.

## 6.4 Formalism (Regge approach)

Having studied the effective Lagrangian method so far, we now switch to another model to examine the same strange and charm productions. Spurred on the finding that the effective Lagrangian method explains the experimental data only near low energy regions, we will introduce a Regge approach, which is known to explain high energy scattering quite well with unitarity preserved.

### 6.4.1 Regge propagators and trajectories

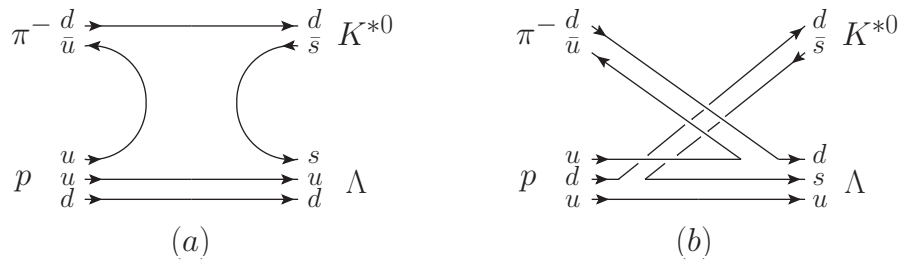


FIGURE 6.11: (a) Planar and (b) non-planar diagrams for the  $\pi^-p \rightarrow K^{*0}\Lambda$ .

We first consider the  $\pi^- p \rightarrow K^{*0}\Lambda$ . The relevant diagrams are drawn in Fig. 6.11 by the quark lines. In the Regge theory, the planar diagram is described by reggeon exchange in the  $t$  channel, whereas the non-planar one corresponds to reggeon exchange in the  $u$  channel. In our process, the reggeons in the  $t$  channel are dictated by the  $K$  and  $K^*$  trajectories, whereas the  $\Sigma$ -baryon trajectory leads to the reggeon in the  $u$  channel as displayed in Fig. 6.11.

In the case of  $t$ -channel exchange, the Regge amplitudes are derived by replacing the Feynman propagator  $P^F$  by the Regge propagator  $P^R$  [65] as follows:

$$\begin{aligned} P_K^F = \frac{1}{t - M_K^2} &\Rightarrow P_K^R(s, t) = \left( \frac{1}{e^{-i\pi\alpha_K(t)}} \right) \left( \frac{s}{s_K} \right)^{\alpha_K(t)} \Gamma[-\alpha_K(t)] \alpha'_K, \\ P_{K^*}^F = \frac{1}{t - M_{K^*}^2} &\Rightarrow P_{K^*}^R(s, t) = \left( \frac{1}{e^{-i\pi\alpha_{K^*}(t)}} \right) \left( \frac{s}{s_{K^*}} \right)^{\alpha_{K^*}(t)-1} \Gamma[1 - \alpha_{K^*}(t)] \alpha'_{K^*}, \end{aligned} \quad (6.17)$$

where  $\alpha_K(t)$  and  $\alpha_{K^*}(t)$  denote the Regge trajectories for the  $K$  and  $K^*$  mesons, respectively.  $s_K$  and  $s_{K^*}$  stand for the energy scale parameters. The Regge trajectories for  $K$  and  $K^*$  are taken from Ref. [134], respectively, as  $\alpha_K(t) = -0.151 + 0.617t$ ,  $\alpha_{K^*}(t) = 0.414 + 0.707t$ . The energy scale parameters are determined by using the QGSM [125–128]:  $s_K = 1.752$  and  $s_{K^*} = 1.662$ . In Appendix E, more details are explained.

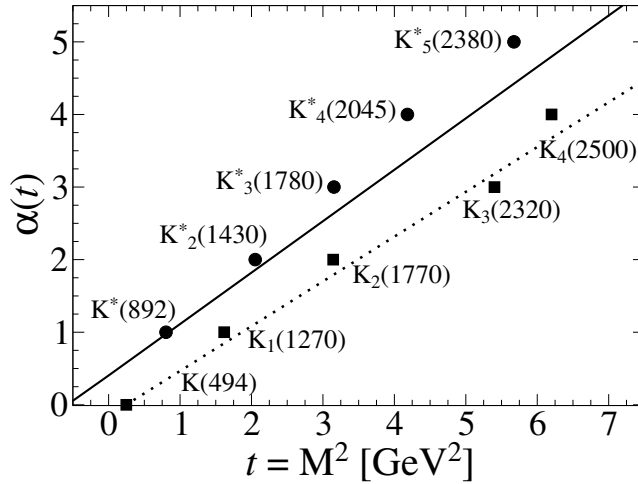


FIGURE 6.12:  $K$  and  $K^*$  meson trajectories.

In general, a Regge propagator is expressed in terms of a linear combination of the two different signatures. However, when a Regge trajectory for a hadron with odd spins is approximately the same as that for a hadron with even spins, that is, two trajectories are almost degenerate, one of the signature is canceled out. As depicted in Fig. 6.12, which are taken from Ref. [134], both the  $K$  trajectory and the  $K^*$  one are almost degenerate, respectively. Thus the Regge propagator can have either the signature 1 or  $e^{-i\pi\alpha_{K(K^*)}}$  as shown in Eq.(6.17) [20, 23]. Since we have these two different signatures, there are

four different ways of selecting the signatures for both the  $K$  and  $K^*$  Regge propagators. We will examine each case in the next section.

Within the framework of a Regge approach, the differential cross section  $d\sigma/dt$  must comply with the following form when  $t$  approaches to zero

$$\frac{d\sigma}{dt}(s \rightarrow \infty, t \rightarrow 0) \propto s^{2\alpha(t)-2}. \quad (6.18)$$

In the case of  $u$ -channel exchange, we similarly replace the Feynman propagator by the Regge propagator as done in the  $t$  channel

$$P_{\Sigma}^F = \frac{1}{u - M_{\Sigma}^2} \Rightarrow P_{\Sigma}^R(s, u) = \left( \frac{1}{e^{-i\pi\alpha_{\Sigma}(u)}} \right) \left( \frac{s}{s_{\Sigma}} \right)^{\alpha_{\Sigma}(u) - \frac{1}{2}} \Gamma \left[ \frac{1}{2} - \alpha_{\Sigma}(u) \right] \alpha'_{\Sigma}(u). \quad (6.19)$$

As for the  $\Sigma$  trajectory, it is not easy to find some tendency like the  $K$  and  $K^*$  trajectories. In Fig. 6.13, we depict two trajectories for  $\Sigma$ s, assuming that the quantum numbers for some unknown resonances are fixed [67]. In the present calculation, the solid trajectory is taken into account, for which  $\alpha_{\Sigma}(u) = -0.79 + 0.87u$  [67], since it contains the lowest-lying  $\Sigma(1190)$ . Based on this trajectory, we are able to determine the scale parameter to be  $s_{\Sigma} = 1.569$ . We also assume that the  $\Sigma$  trajectory is degenerated and two different signatures 1 and  $e^{-i\pi\alpha_{\Sigma}(u)}$  are considered as we did for the mesonic cases.

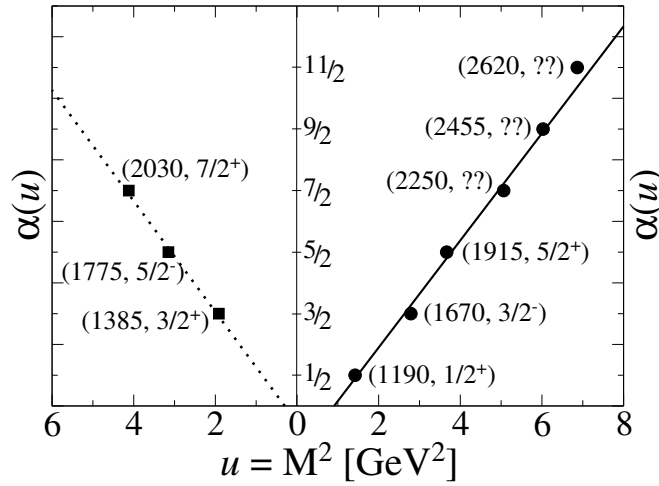


FIGURE 6.13:  $\Sigma$  trajectory [67].

The differential cross section  $d\sigma/du$  should obey the following condition when  $u$  approaches zero asymptotically

$$\frac{d\sigma}{du}(s \rightarrow \infty, u \rightarrow 0) \propto s^{2\alpha(u)-2}. \quad (6.20)$$

### 6.4.2 Regge amplitudes and form factors

The key point of our model is to interpolate between the low and high energy regions just by substituting the Regge propagator  $P^R$  for the Feynman propagator  $P^F$  from the Feynman amplitude  $\mathcal{M}$  defined in Eqs. (6.10) and (6.11)

$$\begin{aligned} T_K(s, t) &= \mathcal{M}_K(s, t) \frac{P_K^R(s, t)}{P_K^F(t)}, \\ T_{K^*}(s, t) &= \mathcal{M}_{K^*}(s, t) \frac{P_{K^*}^R(s, t)}{P_{K^*}^F(t)}, \\ T_\Sigma(s, u) &= \mathcal{M}_\Sigma(s, u) \frac{P_\Sigma^R(s, u)}{P_\Sigma^F(u)}. \end{aligned} \quad (6.21)$$

By doing that, we keep the structure at low energies which comes from the effective Lagrangians, and the asymptotic behavior (Eqs. (6.18) and (6.20)) is also conserved at high energies. To prove the latter point, analytical calculations are essentially required and done carefully. It is found that, in the limit of  $s \rightarrow \infty$ , one has  $\mathcal{M}_K \propto s^0$ ,  $\mathcal{M}_{K^*} \propto s^1$ , and  $\mathcal{M}_\Sigma \propto s^{\frac{1}{2}}$ . The explicit forms are given in Appendix G. In this section, we use the PV type because it fits the data of the total cross section better rather than the PS type (see Figs. 6.4 and 6.5 for comparison).

In the previous section, when dealing with the effective Lagrangians, we take account of the form factor which satisfies  $F(q, M) = 1$  provided the relevant particle is on mass shell  $q^2 = M^2$  (see Eq. (6.12)). Here we consider another type of form factor  $C(q)$ , which is only a function of the transfer momentum and is independent of the particle mass

$$C(q) = \frac{a}{1 - q^2/\Lambda^2}, \quad (6.22)$$

where  $a$  and  $\Lambda$  denote a dimensionless constant and a cutoff mass in units of GeV, respectively.

The final form of the scattering amplitude for this strange process is given by

$$T(\pi^- p \rightarrow K^{*0}\Lambda) = T_K \cdot C_K + T_{K^*} \cdot C_{K^*} + T_\Sigma \cdot C_\Sigma. \quad (6.23)$$

Note that, since the Regge approach is not applicable to the  $s$  channel,  $N$  exchange is excluded here.



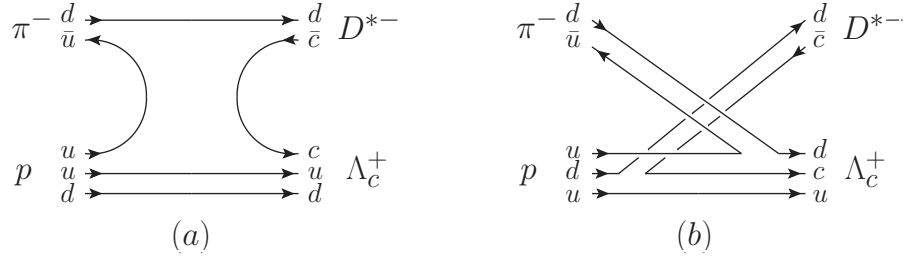


FIGURE 6.14: Planar and non-planar diagrams for the  $\pi^- p \rightarrow D^{*-} \Lambda_c^+$  in the left and right panels, respectively.

### 6.4.3 Charm production

Replacing the  $s$  quarks in Fig. 6.11 with  $c$  quarks, we can display the quark diagrams for the  $\pi^- p \rightarrow D^{*-} \Lambda_c^+$  process (Fig. 6.14). We can derive the Regge amplitudes for the charm production in a similar way directly by using the expressions for the  $\pi^- p \rightarrow K^{*0} \Lambda$  process:

$$\begin{aligned}
 T_D(s, t) &= \mathcal{M}_D(s, t) \left( \frac{s}{s_D} \right)^{\alpha_D(t)} \Gamma[-\alpha_D(t)] \frac{\alpha'_D}{P_D^F(t)}, \\
 T_{D^*}(s, t) &= \mathcal{M}_{D^*}(s, t) \left( \frac{s}{s_{D^*}} \right)^{\alpha_{D^*}(t)-1} \Gamma[1 - \alpha_{D^*}(t)] \frac{\alpha'_{D^*}}{P_{D^*}^F(t)}, \\
 T_{\Sigma_c}(s, u) &= \mathcal{M}_{\Sigma_c}(s, u) \left( \frac{s}{s_{\Sigma_c}} \right)^{\alpha_{\Sigma_c}(u)-\frac{1}{2}} \Gamma\left[\frac{1}{2} - \alpha_{\Sigma_c}(u)\right] \frac{\alpha'_{\Sigma_c}}{P_{\Sigma_c}^F(u)}. \quad (6.24)
 \end{aligned}$$

The final form of the scattering amplitude is expressed as

$$T(\pi^- p \rightarrow D^{*-} \Lambda_c^+) = T_D \cdot C_D + T_{D^*} \cdot C_{D^*} + T_{\Sigma_c} \cdot C_{\Sigma_c}. \quad (6.25)$$

We can now directly compare the magnitude of the charm production with that of the strange one. We consider the same signatures as in the strange production for both the  $t$ - and  $u$ -channels, the values of which will be determined in the next section.

## 6.5 Results (Regge approach)

We are now in a position to discuss the numerical results from the Regge approach. The Regge amplitudes behave typically as  $T \sim s^{\alpha(0)}$  as  $s$  becomes very large, which in general are in accordance with the experimental data. Thus, the intercepts  $\alpha(0)$  play a decisive role in explaining the experimental data at high energies. On the other hand, the magnitude of the total cross section is determined by the coupling constants and form factors.

### 6.5.1 Form factors and phases

Before showing final results, we should fit free parameters, the dimensionless constant  $a$  and the cutoff mass  $\Lambda$  in the form factor  $C(q)$ , and the phases, either a constant or rotating one.

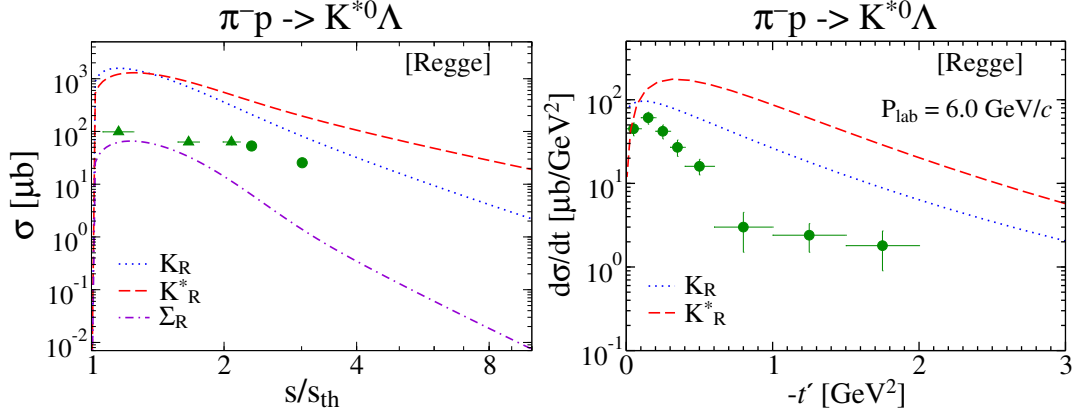


FIGURE 6.15: Total cross sections for the  $\pi^- p \rightarrow K^{*0}\Lambda$  based on the Regge approach without form factors. The data are taken from Ref. [129] (triangles) and Ref. [130] (circles).

Figure 6.15 draws the  $s$  and  $t$  dependence on the total and differential sections, respectively, without considering the form factors. It is notable that the total cross section is comparable in relative magnitude to that of the effective Lagrangian method (see Figs. 6.4 and 6.5 for comparison). Taking a look at the slope of each channel, it is implied that  $K^*$  reggeon would play an important role by comparing its slope with that of the experimental data. The  $t$  dependence is even more interesting. The slope seems to be similar each other, but near small  $t$  region the curve of  $K^*$  exchange rapidly decreases, which is also shown in the experimental data. This fact also indicates that the contribution of  $K^*$  exchange could be dominant.

To reduce the ambiguity, the same values of cutoff masses are employed, which turns out to be almost the same as the ones used in the effective Lagrangian method. The dimensionless constant  $a$  is fitted to the experimental data. It controls the absolute value of the cross sections. The free parameters contained in the form factors are listed in Table 6.3.

channel	$a_K$	$a_{K^*}$	$a_\Sigma$	$\Lambda_K$	$\Lambda_{K^*}$	$\Lambda_\Sigma$
$\pi^- p \rightarrow K^{*0}\Lambda$	0.6	0.9	1.6	0.55	0.55	0.55
channel	$a_D$	$a_{D^*}$	$a_{\Sigma_c}$	$\Lambda_D$	$\Lambda_{D^*}$	$\Lambda_{\Sigma_c}$
$\pi^- p \rightarrow D^{*-}\Lambda_c^+$	0.6	0.9	1.6	0.55	0.55	0.55

TABLE 6.3: Free parameters in form factors to each channel for the  $\pi^- p \rightarrow K^{*0}\Lambda$  and the  $\pi^- p \rightarrow D^{*-}\Lambda_c^+$ .

It should be noted that the cutoff masses are related to the size of relevant hadrons. Since we have determined the cutoff masses by fitting to the strange production, those for the charmed production ought to be different. In Appendix H, the size of a charmed baryon is calculated in comparison with the nucleon which is given by  $0.5\text{ fm}$ . It turns out to be  $0.512\text{ fm}$ . Therefore, since the cutoff mass is in inverse proportion to the size of a relevant hadron, the cutoff mass for the charmed production might be  $0.55\text{ GeV} \cdot 0.5/0.512 = 0.537\text{ GeV}$ . However, this change does not affect the general result when employing  $0.55\text{ GeV}$ .

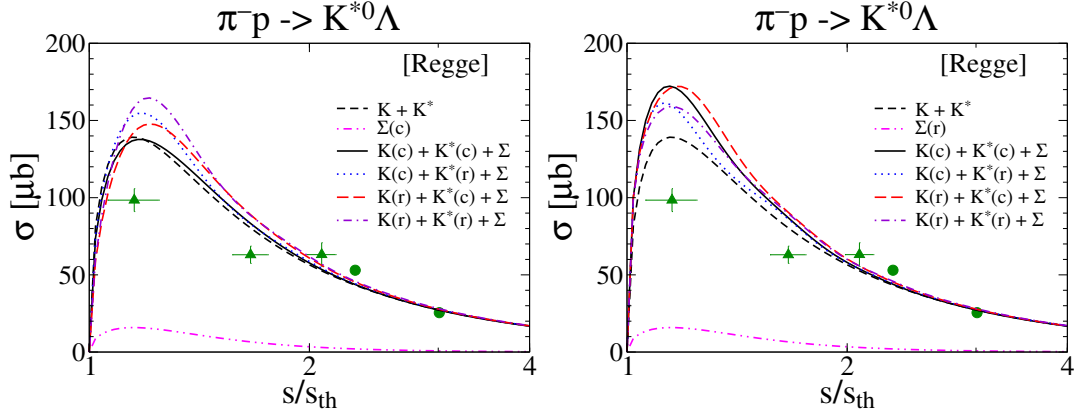


FIGURE 6.16: Total cross sections for the  $\pi^- p \rightarrow K^{*0}\Lambda$  based on the Regge approach according to the phases for each channel. The data are taken from Ref. [129] (triangles) and Ref. [130] (circles).

There are all eight possibilities for the phases. We have examined each case in Fig. 6.16.  $c$  and  $r$  in the parentheses denote the constant or rotating phases, respectively, for each channel. Whatever phase we use, the contribution of  $K + K^*$  exchange is the same since there is no interference between them [62]. But when  $\Sigma$  exchange is included, all different results appear. Only the low energy region ( $1 \leq s/s_{\text{th}} \leq 2$ ) is affected by the change of the phase, and within 20% we have similar absolute values. We choose the signature factor 1 in common for all the Regge propagators.

### 6.5.2 Total cross sections

In Fig. 6.17, each contribution to the total cross section is illustrated.  $K^*$  reggeon exchange governs its dependence on  $s$ . The contribution of  $K$  reggeon exchange is smaller than that of  $K^*$  reggeon exchange and the gap gets larger as  $s$  increases. The reason is clear from the value of  $\alpha_K(t)$  mentioned previously: the corresponding intercept is smaller than that for the  $K^*$  trajectory. We have seen in Figs. 6.4 and 6.5 that the contribution of  $K^*$  exchange in the effective Lagrangian method rises slowly as  $s$  increases, which results in deviation from the experimental data. On the other hand,  $K^*$  reggeon exchange exhibits the  $s$  dependence of the total cross section correctly, so that it

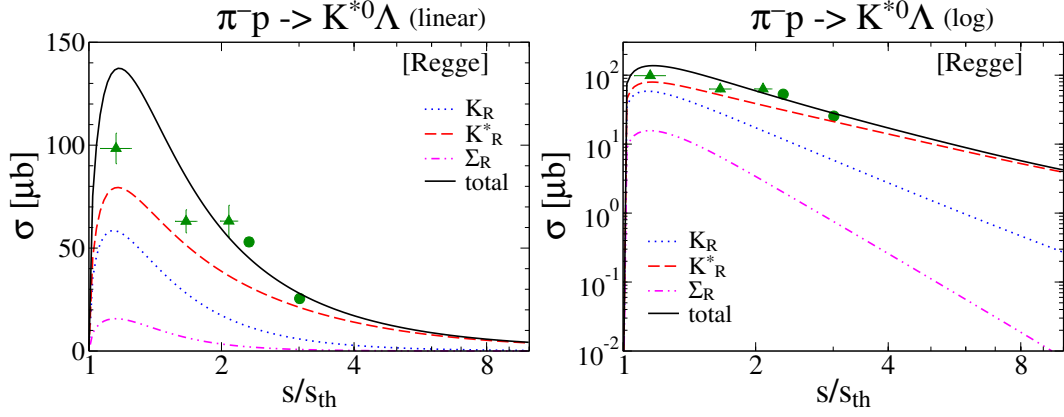


FIGURE 6.17: Total cross sections for the  $\pi^- p \rightarrow K^{*0}\Lambda$  based on the Regge approach. The data are taken from Ref. [129] (triangles) and Ref. [130] (circles).

describes the experimental data much better than  $K^*$  exchange in the effective Lagrangian method at higher values of  $s$ .  $\Sigma$  reggeon exchange in the  $u$  channel makes some effects only on the threshold region and falls off more rapidly than  $t$ -channel exchange. This can be understood from the behavior of the  $u$ -channel Regge amplitude:  $T_\Sigma \sim s^{-0.79}$ .

### 6.5.3 Differential cross sections $d\sigma/d\Omega$

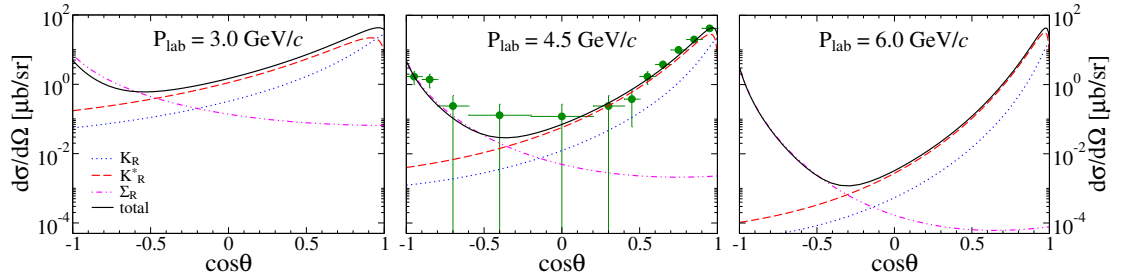


FIGURE 6.18: Differential cross sections  $d\sigma/d\Omega$  for the  $\pi^- p \rightarrow K^{*0}\Lambda$  as functions of  $\cos\theta$  based on the Regge approach. The data are taken from Ref. [130].

Figure 6.18 depicts the results of the differential cross section  $d\sigma/d\Omega$  for the  $\pi^- p \rightarrow K^{*0}\Lambda$ . The  $K^*$  reggeon in the  $t$  channel makes a dominant contribution to the differential cross section in the forward region, whereas the  $\Sigma$  reggeon in the  $u$  channel enhances it at the backward angles. The effect of  $K$  reggeon exchange is important to describe the experimental data at the very forward angle. We already have found that the results from the effective Lagrangian method deviate from the experimental data except for the forward region. However, the Regge approach correctly describes the experimental data at  $P_{\text{lab}} = 4.5 \text{ GeV}/c$  over the whole angles. Moreover, on the whole, it elucidates the flatness of the differential cross section between  $\cos\theta = -0.7$  and  $\cos\theta = 0.3$ , which was never explained in the effective Lagrangian method.

### 6.5.4 Differential cross sections $d\sigma/dt$

In Fig. 6.19, we draw the results of the  $\pi^-p \rightarrow K^{*0}\Lambda$  differential cross section  $d\sigma/dt$  as functions of  $-t'$  at four different values of  $P_{\text{lab}}$ . The most dominant contribution comes from  $K^*$  reggeon exchange.  $K$  reggeon exchange plays a crucial role in explaining the data at the very forward angle together with  $K^*$  reggeon exchange. A similar feature can be also found in the case of  $K\Lambda$  photoproduction [20]. The effect of  $\Sigma$  reggeon exchange turns out to be tiny. Though the general tendency of the results from the Regge approach looks apparently similar to that of the effective Lagrangian ones, they are in fact different each other. The results from the Regge approach fall off faster than those from the effective Lagrangian method, as  $-t'$  increases. The results from the Regge approach are in better agreement with the experimental data in comparison with those from the effective Lagrangian method.

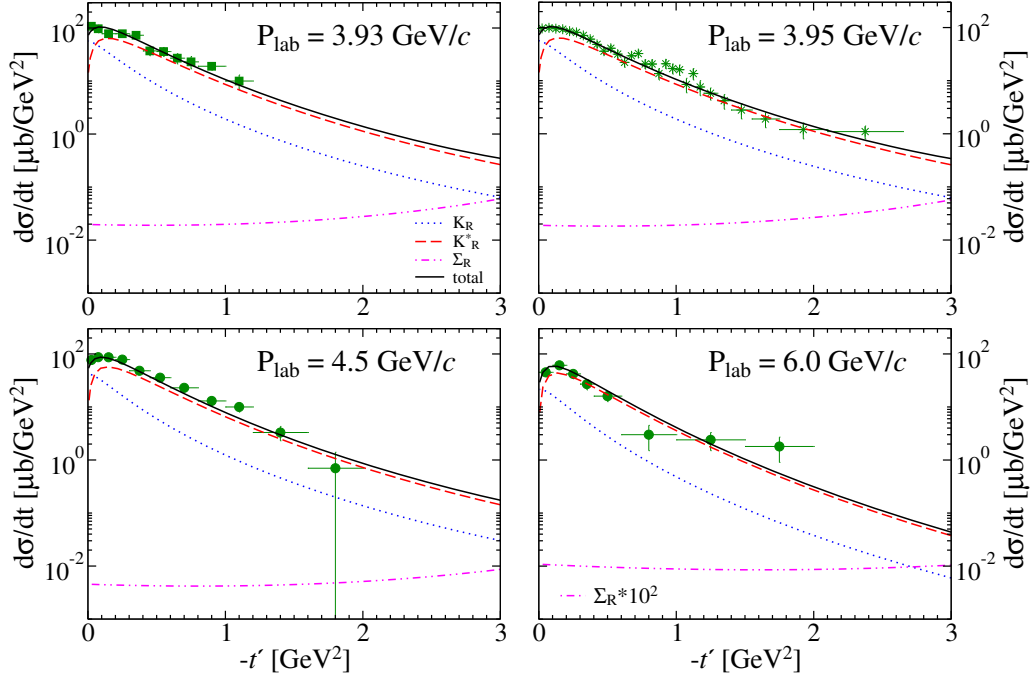


FIGURE 6.19: Differential cross sections  $d\sigma/dt$  for the  $\pi^-p \rightarrow K^{*0}\Lambda$  as functions of  $t'$  based on the Regge approach. The data are taken from Ref. [132] (squares), Ref. [133] (stars), and Ref. [130] (circles).

### 6.5.5 Charm production

We now discuss the results of the charm production. In the left panel of Fig. 6.20, we draw each contribution to the total cross section of the  $\pi^-p \rightarrow D^{*-}\Lambda_c^+$ .  $D^*$  reggeon exchange dictates the  $s$  dependence of the total cross section. The effect  $D$  reggeon and  $\Sigma_c$  reggeon exchanges is smaller than that of  $D^*$  reggeon exchange.

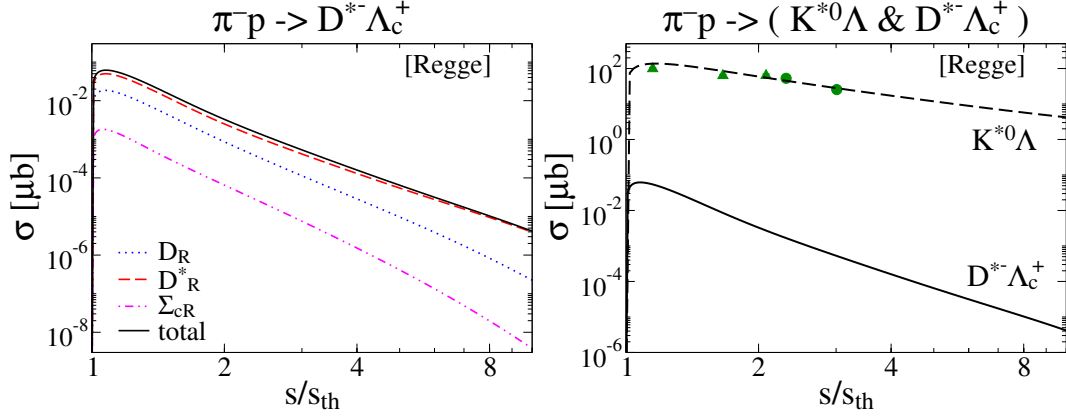


FIGURE 6.20: Total cross section for the  $\pi^- p \rightarrow D^{*-} \Lambda_c^+$  based on the Regge approach (left panel). Comparison of the the total cross section for the  $\pi^- p \rightarrow D^{*-} \Lambda_c^+$  with that for the  $\pi^- p \rightarrow K^{*0} \Lambda$  (right panel). The data are taken from Ref. [129] (triangles) and Ref. [130] (circles).

In the right panel of Fig. 6.20, we find that the total cross section of the charm production is approximately  $10^3 - 10^6$  times smaller than that of the strange production depending on the energy range. The resulting production rate for  $D^* \Lambda_c$  at  $s/s_{\text{th}} \sim 2$ , which is the expected maximum energy J-PARC Collaboration can produce, is suppressed by about factor  $10^4$  in comparison with the strange production. This implies that the production cross section of  $D^* \Lambda_c$  is around  $3 \text{ nb}$  at that energy.

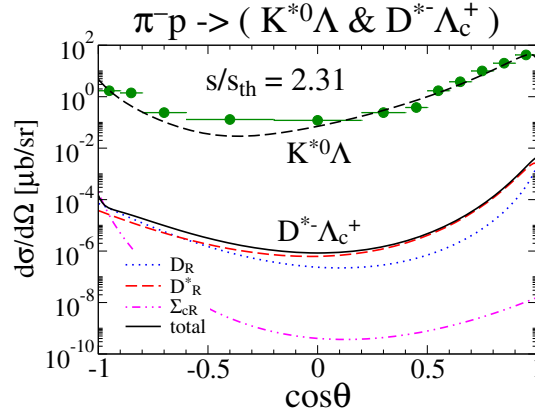


FIGURE 6.21: Comparison of the differential cross section for the  $\pi^- p \rightarrow D^{*-} \Lambda_c^+$  with that for the  $\pi^- p \rightarrow K^{*0} \Lambda$  based on the Regge approach. The data are taken from Ref. [130].

In Fig. 6.21, the differential cross section  $d\sigma/d\Omega$  is also compared for both strange and charm productions.  $D^*$  reggeon exchange plays an crucial role through the whole angle region, even at the backward angles. This is unexpected since  $u$ -channel exchange usually comes into play backward angle regions. The form factor results in the rising behavior in the  $t$  channel at backward angles.

### 6.5.6 Comparison with another model

So far, we have employed a minimal formulation for the Regge approach (except for the form factor). In the literature, a phenomenological form factor is additionally introduced to describe a better  $t$ -dependence, which exhibits a model dependence for the estimation of the charm production. To discuss it briefly, we take a model of Grishina *et al.* [135] as an example, where an additional  $t$ -dependent form factor is included. Their formula for the total cross section takes the following form [135, 136]

$$\sigma = \int C \frac{g_{\pi K^* K^*}^2 g_{K^* N \Lambda}^2}{64\pi(p_{\text{cm}})^2 s} \exp(2R^2 t) \left( \frac{s}{s_{\text{th}}} \right)^{2\alpha_{K^*}(t)} dt, \quad (6.26)$$

where  $R^2 = 2.13 \text{ GeV}^{-2}$  [135] and a dimensionless factor  $C$  is chosen to reproduce the experimental data for the strange production. The Regge trajectory  $\alpha_{K^*}$  is taken from Ref. [134]. The results are drawn in Fig. 6.22 in which the solid curves correspond to the results from the present work, whereas the dashed ones are obtained based on Eq. (6.26). The slope obtained from Eq. (6.26) for the strange production seems to be slightly less steeper than the present one. However, when it comes to the charm production, the situation becomes very interesting. While the total cross section is strongly suppressed near the threshold region than that of the present work, it turns larger than that, as  $s$  increases. Considering the fact that Ref. [124] has experimentally measured only a upper limit  $\sigma \sim 7 \text{ nb}$  at the pion momentum  $P_{\text{lab}} = 13 \text{ GeV}/c$  for the charm production, we find that the result derived from Ref. [135] is within this upper limit, while our result slightly overestimates it:  $\sigma = 2.3 \text{ nb}$  from Eq. (6.26) and  $\sigma = 24 \text{ nb}$  from the present work.

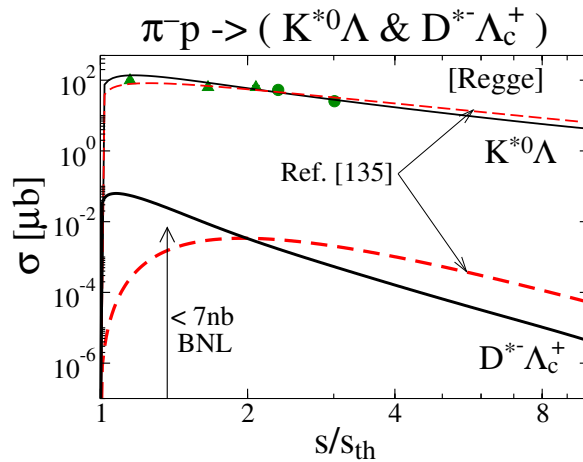


FIGURE 6.22: Total cross section for the  $\pi^- p \rightarrow D^{*-}\Lambda_c^+$  (thicker curve) is compared with that for the  $\pi^- p \rightarrow K^{*0}\Lambda$  (thinner one).

## 6.6 Normalization factor

In this section, we employ the prescription motivated by Totiv *et al* [137]. Regge model generally explains the  $s$  dependence of the total cross section at high energies, whereas its magnitude cannot be determined. To solve this problem, they introduced a normalization factor to the Regge amplitude.

### 6.6.1 Formalism

The normalization factor is inserted into the Regge amplitude as follows:

$$\begin{aligned} T_K(s, t) &= \mathcal{M}_K(s, t) \mathcal{N}_K(s, t) \frac{P_K^R(s, t)}{P_K^F(t)}, \\ T_{K^*}(s, t) &= \mathcal{M}_{K^*}(s, t) \mathcal{N}_{K^*}(s, t) \frac{P_{K^*}^R(s, t)}{P_{K^*}^F(t)}, \\ T_\Sigma(s, u) &= \mathcal{M}_\Sigma(s, u) \mathcal{N}_\Sigma(s, u) \frac{P_\Sigma^R(s, u)}{P_\Sigma^F(u)}, \end{aligned} \quad (6.27)$$

where the corresponding normalization factor  $\mathcal{N}$  is defined by [137]

$$\mathcal{N}(s, t) = \frac{A^\infty(s)}{A(s, t)}, \quad A^2(s, t) = \sum_{s_i, s_f, \lambda_f} |\mathcal{M}'(s, t)|^2, \quad (6.28)$$

for the  $t$  channel and

$$\mathcal{N}(s, u) = \frac{A^\infty(s)}{A(s, u)}, \quad A^2(s, u) = \sum_{s_i, s_f, \lambda_f} |\mathcal{M}'(s, u)|^2, \quad (6.29)$$

for the  $u$  channel.

Here,  $\mathcal{M}'$  is the reduced amplitude that excludes the isospin factor, the coupling constants, and the Feynman propagator

$$\begin{aligned} \mathcal{M}_K(s, t) &= \mathcal{M}'_K(s, t) I_K g_{\pi K K^*} g_{K N \Lambda} P_K^F(t), \\ \mathcal{M}_{K^*}(s, t) &= \mathcal{M}'_{K^*}(s, t) I_{K^*} g_{\pi K^* K^*} g_{K^* N \Lambda} P_{K^*}^F(t), \\ \mathcal{M}_\Sigma(s, u) &= \mathcal{M}'_\Sigma(s, u) I_\Sigma g_{K^* N \Sigma} g_{\pi \Sigma \Lambda} P_\Sigma^F(u). \end{aligned} \quad (6.30)$$

$A^\infty(s)$  represents the dominant term for the  $A(s, t)$  when  $s$  is large enough. This method removes the extra  $s$  and  $t$  dependence coming from the Lagrangians, whereas it keeps the ratios of  $K$  and  $K^*$  Regge amplitudes as dictated by the coupling constants,  $g_{\pi K K^*}$ ,  $g_{\pi K^* K^*}$ , and so on.



For the  $K$  reggon, the dominant term is expressed as

$$A_K^\infty = \frac{1}{\sqrt{2}M_{K^*}}(M_{K^*}^2 - M_\pi^2)(M_\Lambda - M_N), \quad (6.31)$$

and

$$A_{K^*}^\infty(s, t) = \sqrt{-2s^2t}, \quad (6.32)$$

for the  $K^*$  reggeon.

We still have a further problem. The asymptotic behavior of the differential cross section given by Eq. (6.18) is not completely satisfied, since the  $t$  dependence is not suppressed, even though  $t \rightarrow 0$ . To deal with this problem, let us introduce additionally a form factor  $C(t)$  defined by

$$C(t) = \frac{0.6}{1 - t/\Lambda^2}, \quad (6.33)$$

into  $A_{K^*}^\infty(s, t)$ , so that we have

$$A_{K^*}^\infty(s, t) = \sqrt{-2s^2t} C(t). \quad (6.34)$$

Then, we are able to restore the correct asymptotic behavior of  $d\sigma/dt$  in Eq. (6.18) phenomenologically. The form factor  $C(t)$  is exactly the same as that used in the previous section and the corresponding cutoff mass is chosen as  $\Lambda = 1.0 \text{ GeV}$ . As will be shown in the next subsection, it improves much the  $t$  dependence of the differential cross section  $d\sigma/dt$ , keeping the  $s$  dependence of the total cross section more or less satisfied.

For the  $\Sigma$  reggeon, the dominant term reads

$$\begin{aligned} A_\Sigma^\infty(s) = & \sqrt{2s} \frac{M_\Lambda}{M_\Sigma + M_\Lambda} \left[ M_\Sigma^2 (M_N^2/M_{K^*}^2 + 2) + 6 \frac{\kappa_{K^*N\Sigma}}{M_\Sigma + M_N} M_N M_\Sigma^2 \right. \\ & \left. + \frac{\kappa_{K^*N\Sigma}^2}{(M_\Sigma + M_N)^2} M_\Sigma^2 (2M_N^2 + M_{K^*}^2) \right]^{\frac{1}{2}}. \end{aligned} \quad (6.35)$$

The normalization factors satisfy the following condition

$$\lim_{s \rightarrow \infty} \mathcal{N}_K(s, t) = \lim_{s \rightarrow \infty} \mathcal{N}_{K^*}(s, t) = \lim_{s \rightarrow \infty} \mathcal{N}_\Sigma(s, u) = 1. \quad (6.36)$$

### 6.6.2 Results

In Fig. 6.23, each contribution to the total cross section for the  $\pi^- p \rightarrow K^{*0}\Lambda$  and the  $\pi^- p \rightarrow D^{*-}\Lambda_c^+$  is shown in the left and right panel, respectively. A striking difference of this model from ours comes for the charm production. Whereas  $K^*$  (vector) reggeon

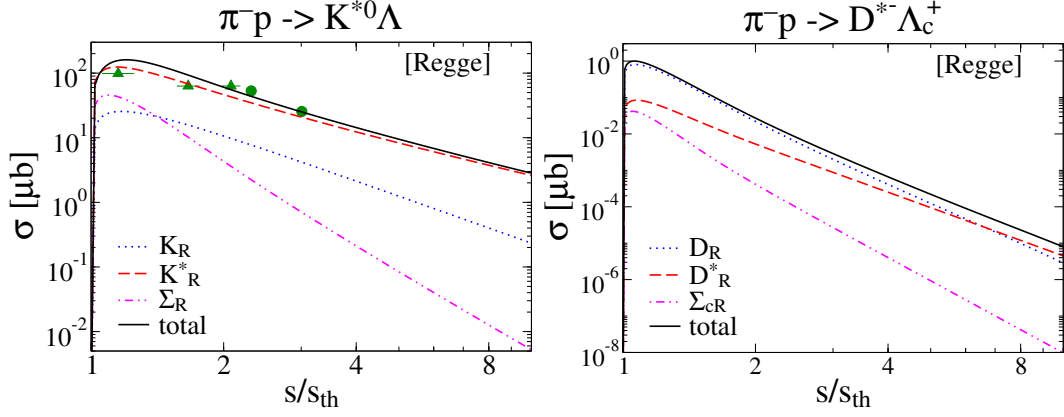


FIGURE 6.23: Total cross sections for the  $\pi^-p \rightarrow K^{*0}\Lambda$  (left panel) and for the  $\pi^-p \rightarrow D^{*-}\Lambda_c^+$  (right panel) based on the Regge approach using the Titov's prescription. The data are taken from Ref. [129] (triangles) and Ref. [130] (circles).

exchange dominates the whole energy region in the strange process,  $D$  (pseudoscalar) reggeon exchange, in general, has larger values than  $D^*$  (vector) reggeon one. It implies that the dominant (leading order) term in the normalization factor does not reflect a consistent result concerning the relative strength.

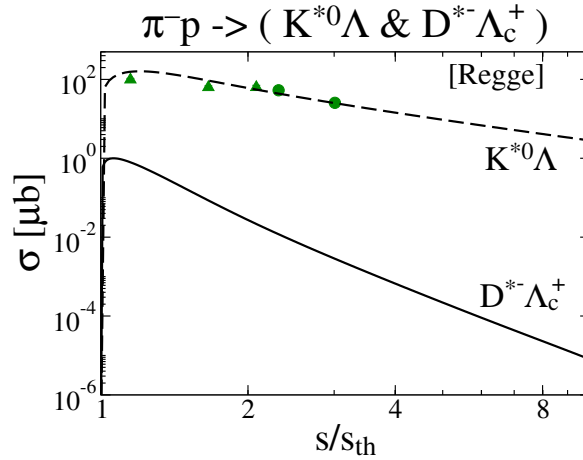


FIGURE 6.24: Comparison of the total cross section for the  $\pi^-p \rightarrow D^{*-}\Lambda_c^+$  with that for the  $\pi^-p \rightarrow K^{*0}\Lambda$  using the Titov's prescription. The data are taken from Ref. [129] (triangles) and Ref. [130] (circles).

In Fig. 6.24, the difference in the total cross section is depicted. At threshold it turns out to be a factor of  $10^2$  and as  $s$  increases, the gap becomes large. When it reaches  $s/s_{\text{th}} = 10$ , the difference is nearly a factor of  $10^5$ .

## 6.7 Summary

In this chapter, we aimed at describing both the strange and charm productions by the pion beam, based on both an effective Lagrangian method and a Regge approach.

We started with the effective Lagrangian method to describe the  $\pi N \rightarrow K^*\Lambda$  and  $\pi N \rightarrow D^*\Lambda_c$  reactions. The coupling constants were determined either by using the experimental data or by employing those from a nucleon-nucleon potential. The cutoff masses of the form factors were fixed to reproduce the experimental data. However, in order to reduce the ambiguity of the effective Lagrangian method, we used the same values of the cut-off masses for each case of meson exchange and baryon exchange.

We were able to explain the total cross section for the  $\pi^-p \rightarrow K^{*0}\Lambda$  in lower energy regions within the framework of the effective Lagrangian method. However, the results from the effective Lagrangian method start to deviate from the data, as the square of the total energy  $s$  increases. The magnitude of the total cross section for the  $\pi p^- \rightarrow D^{*-}\Lambda_c^+$  was approximately 1000 times smaller than that for the  $\pi N \rightarrow K^*\Lambda$ . As expected, the  $t$  channel contributes to the differential cross section in the forward direction, whereas the  $u$  channel does to that in the backward direction. The differential cross section  $d\sigma/dt$  for the  $\pi^-p \rightarrow K^{*0}\Lambda$  tends to decrease, as  $-t'$  increases. The results of  $d\sigma/dt$  were in agreement with the experimental data only at lower  $P_{\text{lab}}$ .

We constructed the Regge propagators for  $K^-$ ,  $K^{*-}$ , and  $\Sigma$ -reggeons. Since the corresponding trajectories are degenerate, we were able to consider the signature either to be 1 or to be a complex phase. We selected 1 as the signatures for all three Regge propagators. Compared with the results from the effective Lagrangian method, the Regge approach describes the experimental data much better, in particular, in higher energy regions. The total cross section for the  $\pi^-p \rightarrow D^{*-}\Lambda_c^+$  turns out to  $10^3$ - $10^6$  times smaller than that for the  $\pi^-p \rightarrow K^{*0}\Lambda$  depending on the range of production energy.

## Chapter 7

# Summary

In this thesis, we have studied strange and charm hadron productions with the aid of an effective Lagrangian method and a Regge approach.

In chapter 2, we explained the general framework of two theoretical models, the effective Lagrangian and Regge models. They are known to describe the reactions at low and high energy regions, respectively.

In chapter 3, we started with the photoproduction  $\gamma N \rightarrow K^* \Sigma$ , in which two different final states,  $\gamma p \rightarrow K^{*0} \Sigma^+$  and  $\gamma p \rightarrow K^{*+} \Sigma^0$ , are considered. An effective Lagrangian method is employed at the tree-level Born approximation.  $K$  and  $\kappa$  exchanges in the  $t$  channel,  $N$ - and  $\Delta$ -pole exchanges in the  $s$  channel, and  $\Sigma$  and  $\Sigma^*$  exchanges in the  $u$  channel are regarded as the background contribution. Additionally,  $K^*$  and  $\Lambda$  exchanges are included only in the  $K^{*+} \Sigma^0$  channel because of charge conservation. The contact term is required for the  $K^{*+} \Sigma^0$  channel too, to preserve gauge invariance. It was found that the  $\Delta$ -pole and  $K$  exchanges make a dominant contribution to the cross sections of the CBELSA/TAPS and CLAS data rather than other exchanges for both channels. Various  $N^*$  and  $\Delta^*$  resonances listed in PDG are also taken into account in addition to the background contribution. They are  $D_{13}(2080)$ ,  $S_{11}(2090)$ ,  $G_{17}(2190)$ ,  $D_{15}(2200)$ ,  $S_{31}(2150)$ ,  $G_{37}(2200)$ , and  $F_{37}(2390)$  in the  $s$  channel, which lie near the threshold of  $K^* \Sigma$  production. The resonance transition magnetic moments are derived by the helicity amplitudes given by the PDG or by the SU(6) quark model. The other parameters, strong coupling constants, are derived by using the SU(6) quark model. It has turned out that all the resonance contributions make almost negligible effects on the cross sections due to their small couplings. On the other hand, the spin observables are affected by the resonance terms unlike by the background ones.

In chapter 4, we continued to study the photoproduction,  $\gamma N \rightarrow K^* \Lambda$ , using effective Lagrangians. The different charged states in the final state,  $\gamma p \rightarrow K^{*+} \Lambda$  and  $\gamma n \rightarrow K^{*0} \Lambda$ , were considered. Concerning the background terms, the  $t$ -channel mesons ( $K$  and  $\kappa$ ),  $s$ -channel nucleon, and  $u$ -channel hyperons ( $\Lambda$ ,  $\Sigma$ , and  $\Sigma^*$ ) are included in common for both channels.  $K^*$  exchange and the contact term are possible only for the  $K^{*+} \Lambda$  channel. The four PDG resonances  $N(2000) 5/2^+$ ,  $N(2060) 5/2^-$ ,  $N(2120) 3/2^-$ , and  $N(2190) 7/2^-$  are also considered besides the background terms. Contrary to the  $K^* \Sigma$  photoproduction, some resonances play important roles in explaining the CLAS data such as  $N(2120) 3/2^-$  and  $N(2190) 7/2^-$  for the  $K^{*+} \Lambda$  channel. But for the  $K^{*0} \Lambda$  channel, the effects of  $N^*$  resonances are almost marginal. Since the values of the strong coupling constants are the same for both channels, this different feature mainly comes from the electromagnetic couplings.

In chapter 5, we moved on to the charm production reactions. Based on the process  $\pi^- p \rightarrow D^{*-} \Lambda_c^+$ , the production rates of various ground and excited charmed baryons ( $\Lambda_c^{*+}$ ,  $\Sigma_c^+$ ,  $\Sigma_c^{*+}$ , ...) were predicted in comparison with the ground state  $\Lambda_c^+$ . All possible states including the ground,  $p$ -wave, and  $d$ -wave excitations are considered with the aid of a quark-diquark model. We assumed that  $t$ -channel  $D^*$  reggeon exchange governs this process for the high energy reaction ( $k_\pi^{\text{Lab}} = 20 \text{ GeV}$ ). This method was also applied to the strange production reaction  $\pi^- p \rightarrow K^{*0} \Lambda$  at  $k_\pi^{\text{Lab}} = 4.2 \text{ GeV}$ . It has turned out that the production rates of  $\Lambda$  baryons are larger than those of  $\Sigma$  baryons, which is a consequence of the SU(6) symmetry of quark-diquark baryons. Moreover, some excited  $\Lambda_c^*$ 's are comparable in rate to the ground state  $\Lambda_c$  or even larger. This will give a good opportunity for the study of excited states.

In chapter 6, we examined the differences in the total and differential cross sections for the  $\pi^- p \rightarrow D^{*-} \Lambda_c^+$  and the  $\pi^- p \rightarrow K^{*0} \Lambda$  reactions. For each of the two theoretical methods, effective Lagrangians and a Regge approach, the production rates are compared and discussed. When employing effective Lagrangians,  $K$  (pseudoscalar) and  $K^*$  (vector) exchanges are important in low and high energies, respectively, for the strange production because of the property of the cross section,  $\sigma \sim s^{J-1}$ , in the  $t$  channel. For the charm production, the role of  $D$  (pseudoscalar) exchange is relatively smaller but the importance of  $D^*$  (vector) exchange at high energies is unchanged. For both reactions, baryon exchanges give small contributions. However, the dominant vector-meson exchange eventually violates the unitarity. Thus, a Regge model is taken into account to describe the high energy region. The Regge parameters are fixed by using QGSM (Quark-Gluon String Model). We have found that  $K^*(D^*)$  reggeon governs the whole energy region for the strange (charm) production. It is due to the intercept of Regge trajectory, which is related to the Regge amplitude as  $T \sim s^{\alpha(0)}$ . It should be noted that the  $K$  reggeon exchange also plays a crucial role in describing the forward angle

region together with the  $K^*$  reggeon one. The magnitude of the total cross section for the  $\pi^- p \rightarrow D^{*-} \Lambda_c^+$  was smaller than that for the  $\pi^- p \rightarrow K^{*0} \Lambda$  by a factor of about  $10^4$  near threshold and about  $10^6$  at  $s/s_{\text{th}} = 10$ .

Both photon- and pion-induced reactions are the commonly used scattering processes. We have made a systematic study of strange and charmed productions of them. The recent CLAS data of cross sections for the  $K^* \Sigma$  and  $K^* \Lambda$  photoproductions are well described with the inclusion of  $N^*$  and  $\Delta^*$  resonances. Our achievement will be the basis for the future investigation of other unknown reactions such as  $K^* \Lambda^*$  and  $K^* \Sigma^*$  photoproductions. The pion-induced charm production reaction is one of the major experimental issues in J-PARC. As shown by using the quark-diquark model, this process is useful to disentangle the structure of charmed baryons. To predict the production rates of charmed hadrons, our Regge approach seems to be useful since it is designed to interpolate between the low and high energy regions. We want to study more the microscopic dynamics of hadrons through various production reactions such as  $D^{*-} \Sigma_c^+$ ,  $D^{*-} \Lambda_c^{*+}$ ,  $D^{*-} \Sigma_c^{*+}$ ,  $D^- \Lambda_c^+$ ,  $D^- \Sigma_c^+$ , and  $J/\psi X$  pion-induced productions.

# Appendix A

## Notation and kinematics

### A.1 Notation

The Bjorken-Drell convention is used for the metric and the  $\gamma$ -matrices. We used two types of spinors in the numerical calculation.

#### A.1.1 Metric

The metric in the Minkowski space is defined as

$$g_{\mu\nu} = g^{\mu\nu} = \begin{pmatrix} 1 & 0 & 0 & 0 \\ 0 & -1 & 0 & 0 \\ 0 & 0 & -1 & 0 \\ 0 & 0 & 0 & -1 \end{pmatrix}. \quad (\text{A.1})$$

The space-time four-vector  $x^\mu \equiv (x^0, x^1, x^2, x^3) = (t, x, y, z)$  is contravariant and thus the covariant four-vector  $x_\mu$  is given as

$$x_\mu = g_{\mu\nu}x^\nu = (t, -x, -y, -z). \quad (\text{A.2})$$

Note that the derivative operator is

$$\partial_\mu = \frac{\partial}{\partial x^\mu} = \left( \frac{\partial}{\partial t}, \nabla \right), \quad \partial^\mu = \frac{\partial}{\partial x_\mu} = \left( \frac{\partial}{\partial t}, -\nabla \right). \quad (\text{A.3})$$

Based on these notations, we can express the scalar-product of two four-vectors as

$$a^\mu b_\mu = g_{\mu\nu}a^\mu b^\nu = a^0 b^0 - \mathbf{a} \cdot \mathbf{b},$$

$$\begin{aligned}
a^\mu \partial_\mu &= a^0 \frac{\partial}{\partial t} + \mathbf{a} \cdot \nabla, \\
\partial^\mu \partial_\mu &= \frac{\partial^2}{\partial t^2} - \nabla \cdot \nabla.
\end{aligned} \tag{A.4}$$

### A.1.2 Pauli and Dirac matrices

The general form of the Pauli matrices is given as

$$\sigma^1 = \begin{pmatrix} 0 & 1 \\ 1 & 0 \end{pmatrix}, \quad \sigma^2 = \begin{pmatrix} 0 & -i \\ i & 0 \end{pmatrix}, \quad \sigma^3 = \begin{pmatrix} 1 & 0 \\ 0 & -1 \end{pmatrix}, \tag{A.5}$$

with the properties

$$\begin{aligned}
\text{tr}(\sigma^i) &= 0, \\
\text{tr}(\sigma^i \sigma^j) &= 2\delta^{ij}, \\
(\sigma^i)^\dagger &= \sigma^i, \\
\sigma^i \sigma^j &= \delta^{ij} + i\epsilon^{ijk} \sigma^k, \\
(\boldsymbol{\sigma} \cdot \mathbf{a})(\boldsymbol{\sigma} \cdot \mathbf{b}) &= \mathbf{a} \cdot \mathbf{b} + i\boldsymbol{\sigma} \cdot (\mathbf{a} \times \mathbf{b}).
\end{aligned} \tag{A.6}$$

The Dirac  $\gamma$ -matrices are represented by the Pauli matrices and the unit  $2 \times 2$  matrix

$$\gamma^0 = \begin{pmatrix} 1 & 0 \\ 0 & -1 \end{pmatrix}, \quad \gamma^i = \begin{pmatrix} 0 & \sigma^i \\ -\sigma^i & 0 \end{pmatrix}, \quad \gamma^5 = i\gamma^0\gamma^1\gamma^2\gamma^3 = \begin{pmatrix} 0 & 1 \\ 1 & 0 \end{pmatrix}. \tag{A.7}$$

They obey the following relations

$$\begin{aligned}
\{\gamma^\mu, \gamma^\nu\} &= 2g^{\mu\nu}, \\
(\gamma^\mu)^\dagger &= \gamma^0 \gamma^\mu \gamma^0, \\
\{\gamma^\mu, \gamma^5\} &= 0, \\
(\gamma^5)^\dagger &= \gamma^5, \\
(\gamma^5)^2 &= 1,
\end{aligned} \tag{A.8}$$

and have the following trace properties

$$\begin{aligned}
\text{tr}(\text{any odd \# of } \gamma\text{'s}) &= 0, \\
\text{tr}(\gamma^\mu \gamma^\nu) &= 4g^{\mu\nu}, \\
\text{tr}(\gamma^\mu \gamma^\nu \gamma^\alpha \gamma^\beta) &= 4(g^{\mu\nu} g^{\alpha\beta} - g^{\mu\alpha} g^{\nu\beta} - g^{\mu\beta} g^{\nu\alpha}), \\
\text{tr}(\gamma^5) &= 0, \\
\text{tr}(\gamma^\mu \gamma^\nu \gamma^5) &= 0, \\
\text{tr}(\gamma^\mu \gamma^\nu \gamma^\alpha \gamma^\beta \gamma^5) &= -4i\epsilon^{\mu\nu\alpha\beta}.
\end{aligned} \tag{A.9}$$



Also note that the following identities

$$\begin{aligned}\epsilon^{\mu\nu\alpha\beta}\epsilon_{\mu\nu\alpha\beta} &= -24, \\ \epsilon^{\mu\nu\alpha\beta}\epsilon_{\mu\nu\alpha\delta} &= -6\delta^\beta_\delta, \\ \epsilon^{\mu\nu\alpha\beta}\epsilon_{\mu\nu\delta\gamma} &= -2(\delta^\alpha_\delta\delta^\beta_\gamma - \delta^\alpha_\gamma\delta^\beta_\delta),\end{aligned}\tag{A.10}$$

which are derived from the last form of Eq. A.9.

### A.1.3 Spinors

#### A.1.3.1 Bjorken-Drell representation

$$u(p, s_z = +\frac{1}{2}) = \frac{1}{\sqrt{2M_p}} \begin{pmatrix} \sqrt{E_p + M_p} \\ 0 \\ \frac{p_z}{\sqrt{E_p + M_p}} \\ \frac{p_x + ip_y}{\sqrt{E_p + M_p}} \end{pmatrix}, u(p, s_z = -\frac{1}{2}) = \frac{1}{\sqrt{2M_p}} \begin{pmatrix} 0 \\ \sqrt{E_p + M_p} \\ \frac{p_x + ip_y}{\sqrt{E_p + M_p}} \\ -\frac{p_z}{\sqrt{E_p + M_p}} \end{pmatrix}.\tag{A.11}$$

$$\begin{aligned}\bar{u}(\mathbf{p}, s)u(\mathbf{p}, s') &= \delta_{s,s'}, \\ u^\dagger(\mathbf{p}, s)u(\mathbf{p}, s') &= \frac{E_p}{M_p}\delta_{s,s'}.\end{aligned}\tag{A.12}$$

#### A.1.3.2 Helicity based representation

$$\begin{aligned}u(\mathbf{p}, s) &= \sqrt{\frac{E_p + M_p}{2M_p}} \begin{pmatrix} 1 \\ \frac{2\sigma \cdot \mathbf{p}}{E_p + M_p} \end{pmatrix}, \frac{2\sigma \cdot \mathbf{p}}{2|\mathbf{p}|}|\lambda\rangle = \lambda|\lambda\rangle, \\ &= \sqrt{\frac{E_p + M_p}{2M_p}} \begin{pmatrix} 1 \\ \frac{2\lambda|\mathbf{p}|}{E_p + M_p} \end{pmatrix}.\end{aligned}\tag{A.13}$$

$$u(p, s_z = +\frac{1}{2}) = \frac{1}{\sqrt{2M_p}} \begin{pmatrix} \sqrt{E_p + M_p} \\ 0 \\ \frac{|\mathbf{p}|}{\sqrt{E_p + M_p}} \\ 0 \end{pmatrix}, u(p, s_z = -\frac{1}{2}) = \frac{1}{\sqrt{2M_p}} \begin{pmatrix} 0 \\ \sqrt{E_p + M_p} \\ 0 \\ \frac{-|\mathbf{p}|}{\sqrt{E_p + M_p}} \end{pmatrix}.\tag{A.14}$$

$$\begin{aligned}\bar{u}(\mathbf{p}, s)u(\mathbf{p}, s') &= \delta_{s,s'}, \\ u^\dagger(\mathbf{p}, s)u(\mathbf{p}, s') &= \frac{E_p}{M_p}\delta_{s,s'}.\end{aligned}\tag{A.15}$$

## A.2 Kinematics

### A.2.1 Mandelstam variables

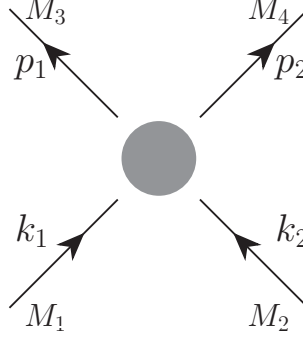


FIGURE A.1: Mandelstam variables in the two-body process.

A scattering amplitude can be expressed in terms of the Lorentz-invariant Mandelstam variables

$$\begin{aligned} s &= (k_1 + k_2)^2 = (p_1 + p_2)^2, \\ t &= (k_1 - p_1)^2 = (k_2 - p_2)^2, \\ u &= (k_1 - p_2)^2 = (k_2 - p_1)^2, \end{aligned} \tag{A.16}$$

$$\begin{aligned} s &= (k_1 + k_2)^2 = M_1^2 + M_2^2 + 2|\vec{k}|^2 + 2E_1E_2, \\ &= (p_1 + p_2)^2 = M_3^2 + M_4^2 + 2|\vec{p}|^2 + 2E_3E_4, \end{aligned} \tag{A.17}$$

$$\begin{aligned} t &= (k_1 - p_1)^2 = M_1^2 + M_3^2 - 2(E_1E_3 - |\vec{k}||\vec{p}|\cos\theta), \\ &= (k_2 - p_2)^2 = M_2^2 + M_4^2 - 2(E_2E_4 - |\vec{k}||\vec{p}|\cos\theta), \end{aligned} \tag{A.18}$$

$$\begin{aligned} u &= (k_1 - p_2)^2 = M_1^2 + M_4^2 - 2(E_1E_4 + |\vec{k}||\vec{p}|\cos\theta), \\ &= (k_2 - p_1)^2 = M_2^2 + M_3^2 - 2(E_2E_3 + |\vec{k}||\vec{p}|\cos\theta), \end{aligned} \tag{A.19}$$

where  $\theta$  is the scattering angle in the COM frame and

$$s + t + u = \sum_i M_i^2. \tag{A.20}$$

### A.2.2 Energy and momentum in two-body process

Combining the definitions  $E_1^2 - |\vec{k}|^2 = M_1^2$ ,  $E_2^2 - |\vec{k}|^2 = M_2^2$ , and  $E_1 + E_2 = E_{\text{cm}} = \sqrt{s}$ , one can easily derive each energy of initial particles in the center of mass (COM) frame

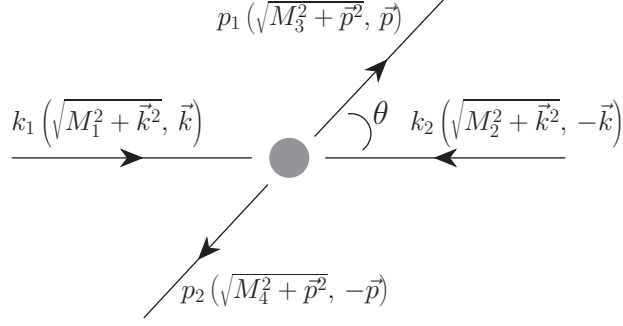


FIGURE A.2: center of mass frame.

(Fig. A.2) as

$$E_1 = \frac{1}{2\sqrt{s}}(s + M_1^2 - M_2^2), \quad E_2 = \frac{1}{2\sqrt{s}}(s + M_2^2 - M_1^2), \quad (\text{A.21})$$

and similarly,

$$E_3 = \frac{1}{2\sqrt{s}}(s + M_3^2 - M_4^2), \quad E_4 = \frac{1}{2\sqrt{s}}(s + M_4^2 - M_3^2). \quad (\text{A.22})$$

The three-momenta of the initial and final particles in the COM frame are

$$\begin{aligned} |\vec{k}| &= k_{\text{cm}} = \frac{1}{2\sqrt{s}} \sqrt{(s - (M_1 + M_2)^2)(s - (M_1 - M_2)^2)}, \\ |\vec{p}| &= p_{\text{cm}} = \frac{1}{2\sqrt{s}} \sqrt{(s - (M_3 + M_4)^2)(s - (M_3 - M_4)^2)}. \end{aligned} \quad (\text{A.23})$$



FIGURE A.3: laboratory frame.

In the laboratory (LAB) frame (Fig. A.3),

$$\begin{aligned} s &= (E_{\text{lab}} + M_2)^2 - \vec{k}_{\text{lab}}^2 \\ &= (E_{\text{lab}}^2 - \vec{k}_{\text{lab}}^2) + M_2^2 + 2E_{\text{lab}}M_2 \\ &= M_1^2 + M_2^2 + 2E_{\text{lab}}M_2, \end{aligned} \quad (\text{A.24})$$

that is,

$$E_{\text{lab}}(k_1) = \frac{1}{2M_2}(s - M_1^2 - M_2^2), \quad E_{\text{lab}}(k_2) = M_2. \quad (\text{A.25})$$

Using this relation, one can derive the three-momentum of the particle 1

$$k_{\text{lab}} = \frac{1}{2M_2} \sqrt{(s - (M_1 + M_2)^2)(s - (M_1 - M_2)^2)}, \quad (\text{A.26})$$

and using Eqs. (A.23) and (A.26), we obtain

$$k_{\text{cm}} = k_{\text{lab}} \frac{M_2}{\sqrt{s}}. \quad (\text{A.27})$$

## Appendix B

# Propagators and helicity amplitudes

In chapters 3 and 4, when dealing with the resonance parameters, resonance propagators and photon helicity amplitudes, we used the following forms.

### B.1 Resonance propagators

The resonance field for a spin-3/2 is treated as the Rarita-Schwinger field [79, 80], and the corresponding propagator with momentum  $p$  and mass  $M$  is written as

$$\Delta_{\alpha\beta}(p, M) = \frac{\not{p} + M}{p^2 - M^2} \left[ -g_{\alpha\beta} + \frac{1}{3}\gamma_\alpha\gamma_\beta + \frac{1}{3M}(\gamma_\alpha p_\beta - \gamma_\beta p_\alpha) + \frac{2}{3M^2}p_\alpha p_\beta \right] \quad (\text{B.1})$$

The propagators for spins-5/2 and -7/2 resonances are given by [91–94],

$$\begin{aligned} \Delta_{\beta\alpha}(R, p) &= (\not{p} + M_R) \left[ -g_{\beta\alpha} + \frac{1}{3}\gamma_\beta\gamma_\alpha + \frac{1}{3M_R}(\gamma_\beta p_\alpha - \gamma_\alpha p_\beta) + \frac{2}{3M_R^2}p_\beta p_\alpha \right], \\ \Delta_{\beta_1\beta_2;\alpha_1\alpha_2}(R, p) &= (\not{p} + M_R) \left[ \frac{1}{2}(\bar{g}_{\beta_1\alpha_1}\bar{g}_{\beta_2\alpha_2} + \bar{g}_{\beta_1\alpha_2}\bar{g}_{\beta_2\alpha_1}) - \frac{1}{5}\bar{g}_{\beta_1\beta_2}\bar{g}_{\alpha_1\alpha_2} \right. \\ &\quad \left. - \frac{1}{10}(\bar{\gamma}_{\beta_1}\bar{\gamma}_{\alpha_1}\bar{g}_{\beta_2\alpha_2} + \bar{\gamma}_{\beta_1}\bar{\gamma}_{\alpha_2}\bar{g}_{\beta_2\alpha_1} + \bar{\gamma}_{\beta_2}\bar{\gamma}_{\alpha_1}\bar{g}_{\beta_1\alpha_2} + \bar{\gamma}_{\beta_2}\bar{\gamma}_{\alpha_2}\bar{g}_{\beta_1\alpha_1}) \right], \\ \Delta_{\beta_1\beta_2\beta_3;\alpha_1\alpha_2\alpha_3}(R, p) &= (\not{p} + M_R) \frac{1}{36} \sum_{P(\alpha), P(\beta)} \left[ -\bar{g}_{\beta_1\alpha_1}\bar{g}_{\beta_2\alpha_2}\bar{g}_{\beta_3\alpha_3} + \frac{3}{7}\bar{g}_{\beta_1\alpha_1}\bar{g}_{\beta_2\beta_3}\bar{g}_{\alpha_2\alpha_3} \right. \\ &\quad \left. + \frac{3}{7}\bar{\gamma}_{\beta_1}\bar{\gamma}_{\alpha_1}\bar{g}_{\beta_2\alpha_2}\bar{g}_{\beta_3\alpha_3} - \frac{3}{35}\bar{\gamma}_{\beta_1}\bar{\gamma}_{\alpha_1}\bar{g}_{\beta_2\beta_3}\bar{g}_{\alpha_2\alpha_3} \right], \end{aligned} \quad (\text{B.2})$$

where the summation runs over all possible permutations of  $\alpha_i$ 's and  $\beta_i$ 's. Here the following notations are used for convenience:

$$\bar{g}_{\alpha\beta} \equiv g_{\alpha\beta} - \frac{p_\alpha p_\beta}{M^2}, \quad \bar{\gamma}_\alpha \equiv \gamma_\alpha - \frac{p_\alpha}{M^2} \not{p}, \quad (\text{B.3})$$

and the mass of the resonance in the  $N^*$  propagator is replaced as  $M \rightarrow M - i\Gamma/2$  with its decay width  $\Gamma$ .

In principle, off-shell parameters may appear in resonance propagators and vertices. However, in our numerical calculation, it turns out that such off-shell effects are negligible since resonances come into play near the on-mass shell region [29], which has been verified numerically.

## B.2 Photon helicity amplitudes

From the effective Lagrangians  $\mathcal{L}_{\gamma NR}$  of electromagnetic vertices expressed in chapters 3 and 4, the helicity amplitudes are obtained using the following relations

$$A_{1/2} \left( \frac{1^\pm}{2} \right) = \mp \frac{eh_1}{2M_N} \sqrt{\frac{p_\gamma M_R}{M_N}}, \quad (\text{B.4})$$

for spin-1/2 resonances,

$$\begin{aligned} A_{1/2} \left( \frac{3^\pm}{2} \right) &= \mp \frac{e\sqrt{6}}{12} \sqrt{\frac{p_\gamma}{M_N M_R}} \left[ h_1 + \frac{h_2}{4M_N^2} M_R (M_R \mp M_N) \right] \\ A_{3/2} \left( \frac{3^\pm}{2} \right) &= \mp \frac{e\sqrt{2}}{4M_N} \sqrt{\frac{p_\gamma M_R}{M_N}} \left[ h_1 \mp \frac{h_2}{4M_N} (M_R \mp M_N) \right], \end{aligned} \quad (\text{B.5})$$

for spin-3/2 resonances,

$$\begin{aligned} A_{1/2} \left( \frac{5^\pm}{2} \right) &= \pm \frac{e}{4\sqrt{10}} \frac{p_\gamma}{M_N} \sqrt{\frac{p_\gamma}{M_N M_R}} \left[ h_1 + \frac{h_2}{4M_N^2} M_R (M_R \pm M_N) \right] \\ A_{3/2} \left( \frac{5^\pm}{2} \right) &= \pm \frac{e}{4\sqrt{5}} \frac{p_\gamma}{M_N^2} \sqrt{\frac{p_\gamma M_R}{M_N}} \left[ h_1 \pm \frac{h_2}{4M_N} (M_R \pm M_N) \right], \end{aligned} \quad (\text{B.6})$$

for spin-5/2 resonances, and

$$\begin{aligned} A_{1/2} \left( \frac{7^\pm}{2} \right) &= \mp \frac{e\sqrt{70}}{280} \frac{p_\gamma^2}{M_N^2} \sqrt{\frac{p_\gamma}{M_N M_R}} \left[ h_1 + \frac{h_2}{4M_N^2} M_R (M_R \mp M_N) \right] \\ A_{3/2} \left( \frac{7^\pm}{2} \right) &= \mp \frac{e\sqrt{42}}{168} \frac{p_\gamma^2}{M_N^3} \sqrt{\frac{p_\gamma M_R}{M_N}} \left[ h_1 \mp \frac{h_2}{4M_N} (M_R \mp M_N) \right] \end{aligned} \quad (\text{B.7})$$

for spin-7/2 resonances.

The helicity amplitudes, in which the transition magnetic moments  $h_{1,2}$  are included, can be expressed as follows:

$$\Gamma(R \rightarrow N\gamma) = \frac{p_\gamma^2}{\pi} \frac{2M_N}{(2j+1)M_R} [|A_{1/2}|^2 + |A_{3/2}|^2], \quad (\text{B.8})$$

where the three-momentum of decaying particle is  $p_\gamma = (M_R^2 - M_N^2)/(2M_R)$ .

## Appendix C

### Spin observables

In chapters 3 and 4, we exhibited the results of various spin observables. They can be expanded in terms of the helicity amplitudes in the COM frame. Since the  $\gamma N \rightarrow K^* Y$  process is studied, the corresponding helicity amplitudes are decomposed as [120]

$$\begin{aligned}
 H_{1,\lambda_V} &\equiv \left\langle \lambda_V, \lambda_f = +\frac{1}{2} \left| T \right| \lambda_\gamma = 1, \lambda_i = -\frac{1}{2} \right\rangle, \\
 H_{2,\lambda_V} &\equiv \left\langle \lambda_V, \lambda_f = +\frac{1}{2} \left| T \right| \lambda_\gamma = 1, \lambda_i = +\frac{1}{2} \right\rangle, \\
 H_{3,\lambda_V} &\equiv \left\langle \lambda_V, \lambda_f = -\frac{1}{2} \left| T \right| \lambda_\gamma = 1, \lambda_i = -\frac{1}{2} \right\rangle, \\
 H_{4,\lambda_V} &\equiv \left\langle \lambda_V, \lambda_f = -\frac{1}{2} \left| T \right| \lambda_\gamma = 1, \lambda_i = +\frac{1}{2} \right\rangle,
 \end{aligned} \tag{C.1}$$

where  $\lambda_\gamma$ ,  $\lambda_V$ , and  $\lambda_{i,f}$  stand for the helicities of the photon, vector meson V, target nucleon, and recoil hyperon Y, respectively. Note that parity invariance makes the following relation

$$\left\langle \lambda_V, \lambda_f \left| T \right| \lambda_\gamma, \lambda_i \right\rangle = (-1)^{\lambda_f - \lambda_i} \left\langle -\lambda_V, -\lambda_f \left| T \right| -\lambda_\gamma, -\lambda_i \right\rangle. \tag{C.2}$$

The  $6 \times 4$  matrix  $\mathcal{F}$  in helicity space is given by

$$\mathcal{F} \equiv \begin{pmatrix} H_{2,1} & H_{1,1} & H_{3,-1} & -H_{4,-1} \\ H_{4,1} & H_{3,1} & -H_{1,-1} & H_{2,-1} \\ H_{2,0} & H_{1,0} & -H_{3,0} & H_{4,0} \\ H_{4,0} & H_{3,0} & H_{1,0} & -H_{2,0} \\ H_{2,-1} & H_{1,-1} & H_{3,1} & -H_{4,1} \\ H_{4,-1} & H_{3,-1} & -H_{1,1} & H_{2,1} \end{pmatrix}.$$



The general form of spin observable  $\bar{\Omega}$  is expressed as

$$\bar{\Omega} = \frac{\text{Tr}[\mathcal{F}A_\gamma A_N \mathcal{F}^\dagger B_V B_Y]}{\text{Tr}[\mathcal{F}\mathcal{F}^\dagger]}, \quad (\text{C.3})$$

from which we can construct any of spin observables. Here  $A_\gamma$ ,  $A_N$ ,  $B_V$ , and  $B_Y$  are given in terms of the elements of the corresponding density matrices.

The cross section intensity is defined by

$$\mathcal{I}(\theta) = \frac{1}{4} \text{Tr}(\mathcal{F}\mathcal{F}^\dagger) = \frac{1}{2} \sum_{i=1}^4 \sum_{a=\pm 1,0} |H_{i,a}|^2. \quad (\text{C.4})$$

## C.1 Single polarization observables

The polarized beam asymmetry  $\Sigma_x$ , target asymmetry  $T_y$ , recoil asymmetry  $P_y$ , and vector-meson asymmetry  $V_i$  are defined by

$$\begin{aligned} \Sigma_x &= \frac{\text{Tr}[\mathcal{F}\sigma_\gamma^x \mathcal{F}^\dagger]}{\text{Tr}[\mathcal{F}\mathcal{F}^\dagger]}, \\ T_y &= \frac{\text{Tr}[\mathcal{F}\sigma_N^y \mathcal{F}^\dagger]}{\text{Tr}[\mathcal{F}\mathcal{F}^\dagger]}, \\ P_y &= \frac{\text{Tr}[\mathcal{F}\mathcal{F}^\dagger \sigma_Y^y]}{\text{Tr}[\mathcal{F}\mathcal{F}^\dagger]}, \\ V_i &= \frac{\text{Tr}[\mathcal{F}\mathcal{F}^\dagger \Omega_j^V]}{\text{Tr}[\mathcal{F}\mathcal{F}^\dagger]}, \end{aligned} \quad (\text{C.5})$$

where

$$\Omega_j^V = \sqrt{\frac{3}{2}}(S_x, S_y, S_z), \quad \frac{1}{\sqrt{6}}(S_{xx} - S_{yy}), \quad \frac{1}{\sqrt{2}}S_{zz}, \quad \sqrt{\frac{2}{3}}(S_{xy}, S_{yz}, S_{zx}), \quad (\text{C.6})$$

with the following notation

$$S_x = \frac{1}{\sqrt{2}} \begin{pmatrix} 0 & 1 & 0 \\ 1 & 0 & 1 \\ 0 & 1 & 0 \end{pmatrix}, \quad S_y = \frac{1}{\sqrt{2}} \begin{pmatrix} 0 & -i & 0 \\ i & 0 & -i \\ 0 & i & 0 \end{pmatrix}, \quad S_z = \begin{pmatrix} 1 & 0 & 0 \\ 0 & 0 & 0 \\ 0 & 0 & -1 \end{pmatrix}. \quad (\text{C.7})$$

They have the property

$$S_{jk} = \frac{3}{2}(S_j S_k + S_k S_j) - 2\delta_{jk} 1_3, \quad \text{Tr} \Omega_j^V \Omega_k^V = 3\delta_{jk}. \quad (\text{C.8})$$

Finally, with all these ingredients, we can express the nonvanishing single polarization observables as

$$\begin{aligned}
\Sigma_x \cdot \mathcal{I}(\theta) &= -\text{Re}\{H_{4,1}^* H_{1,-1} - H_{4,0}^* H_{1,0} + H_{4,-1}^* H_{1,1} \\
&\quad - H_{3,1}^* H_{2,-1} + H_{3,0}^* H_{2,0} - H_{3,-1}^* H_{2,1}\}, \\
T_y \cdot \mathcal{I}(\theta) &= -\text{Im}\{H_{4,-1}^* H_{3,-1} - H_{4,0}^* H_{3,0} + H_{4,1}^* H_{3,1} \\
&\quad + H_{2,-1}^* H_{1,-1} + H_{2,0}^* H_{1,0} + H_{2,1}^* H_{1,1}\}, \\
P_{y'} \cdot \mathcal{I}(\theta) &= -\text{Im}\{H_{4,-1}^* H_{2,-1} + H_{4,0}^* H_{2,0} + H_{4,1}^* H_{2,1} \\
&\quad + H_{3,-1}^* H_{1,-1} + H_{3,0}^* H_{1,0} + H_{3,1}^* H_{1,1}\}, \\
V_{y'} \cdot \mathcal{I}(\theta) &= -\frac{\sqrt{3}}{2} \text{Im}\{H_{4,0}^* (H_{4,1} - H_{4,-1}) + H_{3,0}^* (H_{3,1} - H_{3,-1}) \\
&\quad + H_{2,0}^* (H_{2,1} - H_{2,-1}) + H_{1,0}^* (H_{1,1} - H_{1,-1})\}, \\
V_{x'x'y'y'} \cdot \mathcal{I}(\theta) &= \frac{\sqrt{3}}{2} \text{Re}\{H_{4,-1}^* H_{4,1} + H_{3,-1}^* H_{3,1} + H_{2,-1}^* H_{2,1} + H_{1,-1}^* H_{1,1}\}, \\
V_{z'z'} \cdot \mathcal{I}(\theta) &= \frac{1}{2\sqrt{2}} \{|H_{4,-1}|^2 - 2|H_{4,0}|^2 + |H_{4,1}|^2 + |H_{3,-1}|^2 - 2|H_{3,0}|^2 + |H_{3,1}|^2 \\
&\quad + |H_{2,-1}|^2 - 2|H_{2,0}|^2 + |H_{2,1}|^2 + |H_{1,-1}|^2 - 2|H_{1,0}|^2 + |H_{1,1}|^2\}, \\
V_{z'x'} \cdot \mathcal{I}(\theta) &= -\frac{\sqrt{3}}{2} \text{Re}\{H_{4,0}^* (H_{4,1} - H_{4,-1}) + H_{3,0}^* (H_{3,1} - H_{3,-1}) \\
&\quad + H_{2,0}^* (H_{2,1} - H_{2,-1}) + H_{1,0}^* (H_{1,1} - H_{1,-1})\}. \tag{C.9}
\end{aligned}$$

## C.2 Double polarization observables

It is even more interesting to polarize simultaneously two of the four components. One example is the beam-target (BT) asymmetry  $C_{ij}^{\text{BT}}$  which is defined by

$$C_{ij}^{\text{BT}} = \frac{\text{Tr}[\mathcal{F} \sigma_\gamma^i \sigma_N^j \mathcal{F}^\dagger]}{\text{Tr}[\mathcal{F} \mathcal{F}^\dagger]}. \tag{C.10}$$

In total, six double polarization observables are possible, and among which we display some of the nonvanishing ones. The beam-target (BT) asymmetries  $C_{ij}^{\text{BT}}$  are

$$\begin{aligned}
C_{zz}^{\text{BT}} \cdot \mathcal{I}(\theta) &= \frac{1}{2} \{|H_{4,-1}|^2 + 2|H_{4,0}|^2 + |H_{4,1}|^2 - |H_{3,-1}|^2 - |H_{3,0}|^2 - |H_{3,1}|^2 \\
&\quad + |H_{2,-1}|^2 + |H_{2,0}|^2 + |H_{2,1}|^2 - |H_{1,-1}|^2 - |H_{1,0}|^2 - |H_{1,1}|^2\}, \\
C_{yx}^{\text{BT}} \cdot \mathcal{I}(\theta) &= -\text{Im}\{H_{4,-1}^* H_{2,1} - H_{4,0}^* H_{2,0} + H_{4,1}^* H_{2,-1} \\
&\quad - H_{3,-1}^* H_{1,1} + H_{3,0}^* H_{1,0} - H_{3,1}^* H_{1,-1}\}, \\
C_{yz}^{\text{BT}} \cdot \mathcal{I}(\theta) &= +\text{Im}\{H_{4,-1}^* H_{1,1} - H_{4,0}^* H_{1,0} + H_{4,1}^* H_{1,-1} \\
&\quad + H_{3,-1}^* H_{2,1} - H_{3,0}^* H_{2,0} + H_{3,1}^* H_{2,-1}\}, \\
C_{zx}^{\text{BT}} \cdot \mathcal{I}(\theta) &= +\text{Re}\{H_{4,-1}^* H_{3,-1} + H_{4,0}^* H_{3,0} + H_{4,1}^* H_{3,1} \\
&\quad + H_{2,-1}^* H_{1,-1} - H_{2,0}^* H_{1,0} + H_{2,1}^* H_{1,1}\}. \tag{C.11}
\end{aligned}$$

The beam-recoil (BR) asymmetries  $C_{ij}^{\text{BR}}$  are

$$\begin{aligned}
C_{zz}^{\text{BR}} \cdot \mathcal{I}(\theta) &= -\frac{1}{2} \{ |H_{4,-1}|^2 + |H_{4,0}|^2 + |H_{4,1}|^2 + |H_{3,-1}|^2 + |H_{3,0}|^2 + |H_{3,1}|^2 \\
&\quad - |H_{2,-1}|^2 - |H_{2,0}|^2 - |H_{2,1}|^2 - |H_{1,-1}|^2 - |H_{1,0}|^2 - |H_{1,1}|^2 \}, \\
C_{yy'}^{\text{BR}} \cdot \mathcal{I}(\theta) &= \text{Im} \{ H_{4,-1}^* H_{3,1} - H_{4,0}^* H_{3,0} + H_{4,1}^* H_{3,-1} \\
&\quad - H_{2,-1}^* H_{1,1} + H_{2,0}^* H_{1,0} - H_{2,1}^* H_{1,-1} \}, \\
C_{yz'}^{\text{BR}} \cdot \mathcal{I}(\theta) &= +\text{Im} \{ H_{4,-1}^* H_{1,1} - H_{4,0}^* H_{1,0} + H_{4,1}^* H_{1,-1} \\
&\quad - H_{3,-1}^* H_{2,1} + H_{3,0}^* H_{2,0} - H_{3,1}^* H_{2,-1} \}, \\
C_{zx'}^{\text{BR}} \cdot \mathcal{I}(\theta) &= -\text{Re} \{ H_{4,-1}^* H_{2,-1} + H_{4,0}^* H_{2,0} + H_{4,1}^* H_{2,1} \\
&\quad + H_{3,-1}^* H_{1,-1} + H_{3,0}^* H_{1,0} + H_{3,1}^* H_{1,1} \}.
\end{aligned} \tag{C.12}$$

The target-recoil (TR) asymmetries  $C_{ij}^{\text{TR}}$  are

$$\begin{aligned}
C_{zz'}^{\text{TR}} \cdot \mathcal{I}(\theta) &= -\frac{1}{2} \{ |H_{4,-1}|^2 + |H_{4,0}|^2 + |H_{4,1}|^2 - |H_{3,-1}|^2 - |H_{3,0}|^2 - |H_{3,1}|^2 \\
&\quad - |H_{2,-1}|^2 - |H_{2,0}|^2 - |H_{2,1}|^2 + |H_{1,-1}|^2 + |H_{1,0}|^2 + |H_{1,1}|^2 \}, \\
C_{xx'}^{\text{TR}} \cdot \mathcal{I}(\theta) &= \text{Re} \{ H_{4,-1}^* H_{1,-1} + H_{4,0}^* H_{1,0} + H_{4,1}^* H_{1,1} \\
&\quad + H_{3,-1}^* H_{2,-1} + H_{3,0}^* H_{2,0} + H_{3,1}^* H_{2,1} \}, \\
C_{xz'}^{\text{TR}} \cdot \mathcal{I}(\theta) &= -\text{Re} \{ H_{4,-1}^* H_{3,-1} + H_{4,0}^* H_{3,0} + H_{4,1}^* H_{3,1} \\
&\quad - H_{2,-1}^* H_{1,-1} - H_{2,0}^* H_{1,0} - H_{2,1}^* H_{1,1} \}, \\
C_{zx'}^{\text{TR}} \cdot \mathcal{I}(\theta) &= \text{Re} \{ H_{4,-1}^* H_{2,-1} + H_{4,0}^* H_{2,0} + H_{4,1}^* H_{2,1} \\
&\quad - H_{3,-1}^* H_{1,-1} - H_{3,0}^* H_{1,0} - H_{3,1}^* H_{1,1} \}.
\end{aligned} \tag{C.13}$$

The beam-vector-meson (BV) asymmetries  $C_{ij}^{\text{BV}}$  are

$$\begin{aligned}
C_{zz'}^{\text{BV}} \cdot \mathcal{I}(\theta) &= -\frac{1}{2} \sqrt{\frac{3}{2}} \{ |H_{4,-1}|^2 - |H_{4,1}|^2 + |H_{3,-1}|^2 - |H_{3,1}|^2 \\
&\quad + |H_{2,-1}|^2 - |H_{2,1}|^2 + |H_{1,-1}|^2 - |H_{1,1}|^2 \}, \\
C_{yy'}^{\text{BV}} \cdot \mathcal{I}(\theta) &= -\frac{\sqrt{3}}{2} \text{Im} \{ H_{4,-1}^* H_{1,0} + H_{4,0}^* (H_{1,-1} + H_{1,1}) + H_{4,1}^* H_{1,0} \\
&\quad - H_{3,-1}^* H_{2,0} + H_{3,0}^* (H_{2,-1} + H_{2,1}) - H_{3,1}^* H_{2,0} \}, \\
C_{yz'}^{\text{BV}} \cdot \mathcal{I}(\theta) &= -\frac{\sqrt{3}}{2} \text{Im} \{ H_{4,-1}^* H_{1,1} - H_{4,1}^* H_{1,-1} - H_{3,-1}^* H_{2,1} + H_{3,1}^* H_{2,-1} \}, \\
C_{zx'}^{\text{BV}} \cdot \mathcal{I}(\theta) &= \frac{\sqrt{3}}{2} \text{Re} \{ H_{4,0}^* (H_{4,-1} + H_{4,1}) + H_{3,0}^* (H_{3,-1} + H_{3,1}) \\
&\quad + H_{2,0}^* (H_{2,-1} + H_{2,1}) + H_{1,0}^* (H_{1,-1} + H_{1,1}) \}.
\end{aligned} \tag{C.14}$$

The target-vector-meson asymmetries  $C_{ij}^{\text{TV}}$  are

$$\begin{aligned}
C_{zz'}^{\text{TV}} \cdot \mathcal{I}(\theta) &= -\frac{1}{2} \sqrt{\frac{3}{2}} \{ |H_{4,-1}|^2 - |H_{4,1}|^2 - |H_{3,-1}|^2 + |H_{3,1}|^2 \\
&\quad + |H_{2,-1}|^2 - |H_{2,1}|^2 - |H_{1,-1}|^2 + |H_{1,1}|^2 \}, \\
C_{xx'}^{\text{TV}} \cdot \mathcal{I}(\theta) &= -\frac{\sqrt{3}}{2} \text{Re} \{ H_{4,0}^* (H_{3,-1} + H_{3,1}) + H_{3,0}^* (H_{4,-1} + H_{4,1}) \\
&\quad + H_{2,0}^* (H_{1,-1} + H_{1,1}) + H_{1,0}^* (H_{2,-1} + H_{2,1}) \},
\end{aligned}$$

$$\begin{aligned}
C_{xz'}^{TV} \cdot \mathcal{I}(\theta) &= -\frac{\sqrt{3}}{2} \text{Re}\{H_{4,-1}^* H_{3,-1} - H_{4,1}^* H_{3,1} + H_{2,-1}^* H_{1,-1} - H_{2,1}^* H_{1,1}\}, \\
C_{zx'}^{TV} \cdot \mathcal{I}(\theta) &= -\frac{\sqrt{3}}{2} \text{Re}\{H_{4,0}^* (H_{4,-1} + H_{4,1}) - H_{3,0}^* (H_{3,-1} + H_{3,1}) \\
&\quad + H_{2,0}^* (H_{2,-1} + H_{2,1}) - H_{1,0}^* (H_{1,-1} + H_{1,1})\}. \tag{C.15}
\end{aligned}$$

The recoil-vector-meson asymmetries  $C_{ij}^{\text{RV}}$  are

$$\begin{aligned}
C_{z'z'}^{RV} \cdot \mathcal{I}(\theta) &= -\frac{1}{2} \sqrt{\frac{3}{2}} \{ |H_{4,-1}|^2 - |H_{4,1}|^2 + |H_{3,-1}|^2 - |H_{3,1}|^2 \\
&\quad - |H_{2,-1}|^2 + |H_{2,1}|^2 - |H_{1,-1}|^2 + |H_{1,1}|^2 \}, \\
C_{x'x'}^{RV} \cdot \mathcal{I}(\theta) &= -\frac{\sqrt{3}}{2} \text{Re}\{H_{4,0}^* (H_{2,-1} + H_{2,1}) + H_{3,0}^* (H_{1,-1} + H_{1,1}) \\
&\quad + H_{2,0}^* (H_{4,-1} + H_{4,1}) + H_{1,0}^* (H_{3,-1} + H_{3,1})\}, \\
C_{x'z'}^{RV} \cdot \mathcal{I}(\theta) &= \sqrt{\frac{3}{2}} \text{Re}\{H_{4,-1}^* H_{2,-1} - H_{4,1}^* H_{2,1} + H_{3,-1}^* H_{1,-1} - H_{3,1}^* H_{1,1}\}, \\
C_{z'x'}^{RV} \cdot \mathcal{I}(\theta) &= \frac{\sqrt{3}}{2} \text{Re}\{H_{4,0}^* (H_{4,-1} + H_{4,1}) + H_{3,0}^* (H_{3,-1} + H_{3,1}) \\
&\quad - H_{2,0}^* (H_{2,-1} + H_{2,1}) - H_{1,0}^* (H_{1,-1} + H_{1,1})\}. \tag{C.16}
\end{aligned}$$

## Appendix D

# Baryon wave functions

### D.1 Three quark system

#### D.1.1 Spin ( $2^3 = 8 = 4(S) + 2(\rho) + 2(\lambda)$ )

Three spin- $\frac{1}{2}$  quarks cause a total spin  $S = \frac{3}{2}$  or  $S = \frac{1}{2}$ .

The  $S = \frac{3}{2}$  states are symmetric under the exchange of any two spins.

$$4(S) \begin{cases} \chi_{\frac{3}{2}, \frac{3}{2}}^3 &= \alpha(1)\alpha(2)\alpha(3), \\ \chi_{\frac{3}{2}, \frac{1}{2}}^3 &= \frac{1}{\sqrt{3}}(\alpha\alpha\beta + \alpha\beta\alpha + \beta\alpha\alpha), \\ \chi_{\frac{3}{2}, -\frac{1}{2}}^3 &= \frac{1}{\sqrt{3}}(\alpha\beta\beta + \beta\alpha\beta + \beta\beta\alpha), \\ \chi_{\frac{3}{2}, -\frac{3}{2}}^3 &= \beta\beta\beta. \end{cases} \quad (\text{D.1})$$

When considering the case of total spin  $S = \frac{1}{2}$ , there are two types of mixed symmetric states,  $\chi_{\frac{1}{2}}^\rho$  and  $\chi_{\frac{1}{2}}^\lambda$ .

$$\begin{aligned} \chi_{\frac{1}{2}, \frac{1}{2}}^\rho &= \sum_{m_s} \left( 0 m \frac{1}{2} m_s \middle| \frac{1}{2} \frac{1}{2} \right) \left| 0 m \right\rangle \left| \frac{1}{2} m_s \right\rangle \\ &= \left( 0 0 \frac{1}{2} \frac{1}{2} \middle| \frac{1}{2} \frac{1}{2} \right) \left| 0 0 \right\rangle \left| \frac{1}{2} \frac{1}{2} \right\rangle = \frac{1}{\sqrt{2}}(\alpha\beta - \beta\alpha)\alpha. \end{aligned} \quad (\text{D.2})$$

$$\begin{aligned} \chi_{\frac{1}{2}, \frac{1}{2}}^\lambda &= \sum_{m_s} \left( 1 m \frac{1}{2} m_s \middle| \frac{1}{2} \frac{1}{2} \right) \left| 1 m \right\rangle \left| \frac{1}{2} m_s \right\rangle \\ &= \left( 1 1 \frac{1}{2} \frac{1}{2} \middle| \frac{1}{2} \frac{1}{2} \right) \left| 1 1 \right\rangle \left| \frac{1}{2} \frac{1}{2} \right\rangle + \left( 1 0 \frac{1}{2} \frac{1}{2} \middle| \frac{1}{2} \frac{1}{2} \right) \left| 1 0 \right\rangle \left| \frac{1}{2} \frac{1}{2} \right\rangle \\ &= \frac{2}{\sqrt{6}}\alpha\alpha\beta - \frac{1}{\sqrt{3}}\frac{1}{\sqrt{2}}(\alpha\beta + \beta\alpha)\alpha = \frac{1}{\sqrt{6}}(2\alpha\alpha\beta - \alpha\beta\alpha - \beta\alpha\alpha). \end{aligned} \quad (\text{D.3})$$

$$\begin{aligned}
\chi_{\frac{1}{2}, -\frac{1}{2}}^\rho &= \sum_{m_s} \left( 0 m \frac{1}{2} m_s \middle| \frac{1}{2} \frac{-1}{2} \right) \left| 0 m \right\rangle \left| \frac{1}{2} m_s \right\rangle \\
&= \left( 0 0 \frac{1}{2} \frac{-1}{2} \middle| \frac{1}{2} \frac{-1}{2} \right) \left| 0 0 \right\rangle \left| \frac{1}{2} \frac{-1}{2} \right\rangle = \frac{1}{\sqrt{2}} (\alpha\beta - \beta\alpha)\beta. \quad (D.4)
\end{aligned}$$

$$\begin{aligned}
\chi_{\frac{1}{2}, -\frac{1}{2}}^\lambda &= \sum_{m_s} \left( 1 m \frac{1}{2} m_s \middle| \frac{1}{2} \frac{-1}{2} \right) \left| 1 m \right\rangle \left| \frac{1}{2} m_s \right\rangle \\
&= \left( 1 - 1 \frac{1}{2} \frac{1}{2} \middle| \frac{1}{2} \frac{-1}{2} \right) \left| 1 - 1 \right\rangle \left| \frac{1}{2} \frac{1}{2} \right\rangle + \left( 1 0 \frac{1}{2} \frac{-1}{2} \middle| \frac{1}{2} \frac{-1}{2} \right) \left| 1 0 \right\rangle \left| \frac{1}{2} \frac{-1}{2} \right\rangle \\
&= -\frac{2}{\sqrt{6}} \beta\beta\alpha + \frac{1}{\sqrt{3}} \frac{1}{\sqrt{2}} (\alpha\beta + \beta\alpha)\beta = \frac{1}{\sqrt{6}} (-2\beta\beta\alpha + \alpha\beta\beta + \beta\alpha\beta). \quad (D.5)
\end{aligned}$$

### D.1.2 Flavor ( $3^3 = 27 = 10(S) + 8(\rho) + 8(\lambda) + 1(A)$ )

$$10(S) = \left\{ \begin{array}{l} 3 : uuu, ddd, sss, \\ 6 : \psi^S(udd) = \frac{1}{\sqrt{3}}[udd + dud + ddu], \\ \quad \psi^S(uss) = \frac{1}{\sqrt{3}}[uss + sus + ssu], \\ \quad \psi^S(duu) = \frac{1}{\sqrt{3}}[duu + udu + uud], \\ \quad \psi^S(dss) = \frac{1}{\sqrt{3}}[dss + dsd + ssd], \\ \quad \psi^S(suu) = \frac{1}{\sqrt{3}}[suu + usu + uus], \\ \quad \psi^S(sdd) = \frac{1}{\sqrt{3}}[sdd + dsd + dds], \\ 1 : uds. \end{array} \right. \quad (D.6)$$

8  $\rho$ -type is antisymmetric in 1 and 2, and 8  $\lambda$ -type is symmetric in 1 and 2.

### D.1.3 Spin $\times$ Flavor wave functions ( $2^3 \times 3^3 = 6^3 = 216$ )

<hr/> <hr/>	
56 ( $S$ )	
$4_{10} : \chi^S \phi^S$	$2_8 : (\chi^\rho \phi^\rho + \chi^\rho \phi^\rho)/\sqrt{2}$
<hr/>	
20 ( $A$ )	
$4_1 : \chi^S \phi^A$	$2_8 : (\chi^\rho \phi^\lambda - \chi^\lambda \phi^\rho)/\sqrt{2}$
<hr/>	
70 ( $\rho$ )	
$2_{10} : \chi^\rho \phi^S$	$4_8 : \chi^S \phi^\rho$
$2_8 : (\chi^\rho \phi^\lambda + \chi^\lambda \phi^\rho)/\sqrt{2}$	$2_1 : \chi^\rho \phi^A$
<hr/>	
70 ( $\lambda$ )	
$2_{10} : \chi^\lambda \phi^S$	$4_8 : \chi^S \phi^\lambda$
$2_8 : (\chi^\rho \phi^\rho - \chi^\lambda \phi^\lambda)/\sqrt{2}$	$2_1 : \chi^\lambda \phi^A$
<hr/> <hr/>	

TABLE D.1: Spin-flavor wave functions of a baryon.

$$4_{10} + 2_8 = 56(S),$$

$$\begin{aligned}
{}^4_1 + {}^2_8 &= 20(A), \\
{}^2_{10} + {}^4_8 + {}^2_8 + {}^2_1 &= 70(\rho), \\
{}^2_{10} + {}^4_8 + {}^2_8 + {}^2_1 &= 70(\lambda).
\end{aligned}
\tag{D.7}$$

## D.2 Two body system

When one of the three quarks in a baryon is heavy enough, the dynamics is governed by the other light quarks.

$$\text{Spin : } \quad 2 \times 2 = 1(A) + 3(S), \tag{D.8}$$

$$\text{Flavor : } \quad 3 \times 3 = \bar{3}(A) + 6(S). \tag{D.9}$$

For the ground and  $p$ -wave excited states, the following is possible  $qq$  states

$$\text{ground : } \quad \bar{3}^1 S_0, \quad 6^3 S_1, \tag{D.10}$$

$$\text{p - wave : } \quad \bar{3}^1 \lambda_1, \quad 6^3 \lambda_{0,1,2}, \quad \bar{3}^3 \lambda_{0,1,2}, \quad 6^1 \rho_1. \tag{D.11}$$

## D.3 Matrix elements

Let us calculate the matrix elements  $\langle f | \vec{e}_\perp \cdot \vec{\sigma} e^{i\vec{q}_{eff} \cdot \vec{x}} | i \rangle$  for baryons  $B$  with various spin and parity  $J^P$ . For forward scattering, due to helicity conservation, it is sufficient to consider only one helicity flip transition for a given  $J$  (remember that only transverse polarization transfer is possible),

$$i \rightarrow f = J_z(N) \rightarrow (J_z(B), h) = 1/2 \rightarrow (-1/2, 1) \tag{D.12}$$

for  $J = 1/2$  and  $3/2$ , and

$$J_z(N) \rightarrow (J_z(B), h) = -1/2 \rightarrow (-3/2, 1) \tag{D.13}$$

for  $J = 3/2$ . Here  $h$  denotes the helicity of the vector meson  $V$ . Other amplitudes are related to these elements by time reversal.

The total cross section is then proportional to the sum of squared amplitudes over possible spin states. For  $J = 1/2$

$$\begin{aligned}
\sigma &\sim |\langle -1/2, +1 | t | +1/2 \rangle|^2 + |\langle +1/2, -1 | t | -1/2 \rangle|^2 \\
&= 2 |\langle -1/2, +1 | t | +1/2 \rangle|^2
\end{aligned}
\tag{D.14}$$

and for  $J = 3/2$  and  $5/2$

$$\sigma \sim 2 \left( |\langle -1/2, +1 | t | +1/2 \rangle|^2 + |\langle +3/2, -1 | t | +1/2 \rangle|^2 \right). \quad (\text{D.15})$$

### D.3.1 $N(1/2^+) \rightarrow$ **ground state baryons**

First we consider the transition to  $\Lambda(1/2^+)$  (of both charm and strangeness)

$$\langle \psi_{000} \chi_{-1/2}^\rho V(+1) | \vec{e}_\perp \cdot \vec{\sigma} e^{i\vec{q}_{eff} \cdot \vec{x}} | \psi_{000} \chi_{+1/2}^\rho \rangle, \quad (\text{D.16})$$

where the baryon orbital wave functions  $\psi_{nlm}$  are given in this Appendix. Note that since the diquark behaves as a spectator in the reaction (Fig. 5.1), the good diquark component of  $\chi^\rho$  for the nucleon is taken. The spectroscopic (overlap) factor of the good diquark component in the nucleon is tabulated in below where isospin factor is included also. Choosing the  $V$  polarization as  $\vec{e}_\perp$ , we have

$$\langle \psi_{000} \chi_{-1/2}^\rho | \sqrt{2} \sigma_- e^{i\vec{q}_{eff} \cdot \vec{x}} | \psi_{000} \chi_{+1/2}^\rho \rangle = \langle \chi_{-1/2}^\rho | \sigma_- | \chi_{+1/2}^\rho \rangle \langle \psi_{000} | \sqrt{2} e^{i\vec{q}_{eff} \cdot \vec{x}} | \psi_{000} \rangle \quad (\text{D.17})$$

where the spin and orbital parts are separated and  $\sigma_-$  is the spin lowering matrix given as

$$\sigma_- = \begin{pmatrix} 0 & 0 \\ 1 & 0 \end{pmatrix}. \quad (\text{D.18})$$

The spin matrix elements are easily computed as

$$\begin{aligned} \langle \chi_{-1/2}^\rho | \sigma_- | \chi_{+1/2}^\rho \rangle &= 1, \\ \langle \chi_{-1/2}^\lambda | \sigma_- | \chi_{+1/2}^\lambda \rangle &= -\frac{1}{3}, \\ \langle \chi_{-1/2}^S | \sigma_- | \chi_{+1/2}^\lambda \rangle &= \frac{\sqrt{2}}{3}, \\ \langle \chi_{-3/2}^S | \sigma_- | \chi_{+1/2}^\lambda \rangle &= -\sqrt{\frac{2}{3}}, \end{aligned} \quad (\text{D.19})$$

where we have shown all relevant matrix elements in the following calculations. Therefore, the remaining is the elementary integral over the radial distance  $r$  with Gaussian functions. We find

$$\Lambda(1/2^+) : \langle \psi_{000} \chi_{-1/2}^\rho | \sqrt{2} \sigma_- e^{i\vec{q}_{eff} \cdot \vec{x}} | \psi_{000} \chi_{+1/2}^\rho \rangle = I_0, \quad (\text{D.20})$$



where the radial integral  $I_0$  is given by

$$I_0 = \langle \psi_{000} | \sqrt{2} e^{i\vec{q}_{eff} \cdot \vec{x}} | \psi_{000} \rangle = \sqrt{2} \left( \frac{\alpha' \alpha}{A^2} \right)^{3/2} e^{-q_{eff}^2/(4A^2)},$$

$$A^2 = \frac{\alpha^2 + \alpha'^2}{2}. \quad (\text{D.21})$$

The oscillator parameters are  $\alpha$  and  $\alpha'$  are for the initial and final state baryons, respectively.

Similarly, we calculate the transitions to the ground state  $\Sigma$ 's, picking up the  $\chi^\lambda$  part for the nucleon wave function. Only the difference is the spin matrix element which are computed by making Clebsh-Gordan decompositions. Results are

$$\begin{aligned} \Sigma(1/2^+) : \quad \langle \psi_{000} \chi_{-1/2}^\lambda | \sqrt{2} \sigma_- e^{i\vec{q}_{eff} \cdot \vec{x}} | \psi_{000} \chi_{+1/2}^\lambda \rangle &= -\frac{1}{3} I_0, \\ \Sigma(3/2^+) : \quad \langle \psi_{000} \chi_{-1/2}^S | \sqrt{2} \sigma_- e^{i\vec{q}_{eff} \cdot \vec{x}} | \psi_{000} \chi_{+1/2}^\lambda \rangle &= \frac{\sqrt{2}}{3} I_0, \\ \langle \psi_{000} \chi_{-3/2}^S | \sqrt{2} \sigma_- e^{i\vec{q}_{eff} \cdot \vec{x}} | \psi_{000} \chi_{-1/2}^\lambda \rangle &= -\sqrt{\frac{2}{3}} I_0, \end{aligned} \quad (\text{D.22})$$

where two independent matrix elements for  $\Sigma(3/2^+)$  are shown.

### D.3.2 $N(1/2^+) \rightarrow p$ -wave baryons

Let us first consider the transition to  $\Lambda(1/2^-)$ . The relevant matrix element is given as

$$\langle [\psi_{01}, \chi^\rho]_{-1/2}^{1/2} | \sqrt{2} \sigma_- e^{i\vec{q}_{eff} \cdot \vec{x}} | \psi_{000} \chi_{+1/2}^\rho \rangle = \sqrt{\frac{1}{3}} \langle \chi_{-1/2}^\rho | \sigma_- | \chi_{+1/2}^\rho \rangle \langle \psi_{010} | \sqrt{2} e^{i\vec{q}_{eff} \cdot \vec{x}} | \psi_{000} \rangle \quad (\text{D.23})$$

where the factor  $\sqrt{1/3}$  is the Clebsh-Gordan coefficients in the state  $[\psi_{01}, \chi^\rho]_{-1/2}^{1/2}$ . The radial part is computed as

$$\langle \psi_{010} | \sqrt{2} e^{i\vec{q}_{eff} \cdot \vec{x}} | \psi_{000} \rangle = \frac{(\alpha' \alpha)^{3/2} \alpha' q_{eff}}{A^5} e^{-q_{eff}^2/(4A^2)} \equiv I_1 \quad (\text{D.24})$$

and so

$$\Lambda(1/2^-) : \quad \langle [\psi_{01}, \chi^\rho]_{-1/2}^{1/2} | \sqrt{2} \sigma_- e^{i\vec{q}_{eff} \cdot \vec{x}} | \psi_{000} \chi_{+1/2}^\rho \rangle = \sqrt{\frac{1}{3}} I_1. \quad (\text{D.25})$$

Other matrix elements can be computed similarly:

$$\begin{aligned}
\Lambda(3/2^-) : \quad & \langle [\psi_{01}, \chi^\rho]_{-1/2}^{3/2} | \sqrt{2} \sigma_- e^{i\vec{q}_{eff} \cdot \vec{x}} | \psi_{000} \chi_{+1/2}^\rho \rangle = \sqrt{\frac{2}{3}} I_1, \\
& \langle [\psi_{01}, \chi^\rho]_{-3/2}^{3/2} | \sqrt{2} \sigma_- e^{i\vec{q}_{eff} \cdot \vec{x}} | \psi_{000} \chi_{-1/2}^\rho \rangle = 0, \\
\Sigma(1/2^-) : \quad & \langle [\psi_{01}, \chi^\lambda]_{-1/2}^{3/2} | \sqrt{2} \sigma_- e^{i\vec{q}_{eff} \cdot \vec{x}} | \psi_{000} \chi_{+1/2}^\lambda \rangle = \frac{1}{3\sqrt{3}} I_1, \\
\Sigma(3/2^-) : \quad & \langle [\psi_{01}, \chi^\lambda]_{-1/2}^{3/2} | \sqrt{2} \sigma_- e^{i\vec{q}_{eff} \cdot \vec{x}} | \psi_{000} \chi_{+1/2}^\lambda \rangle = -\frac{1}{3} \sqrt{\frac{2}{3}} I_1, \\
& \langle [\psi_{01}, \chi^\lambda]_{-3/2}^{3/2} | \sqrt{2} \sigma_- e^{i\vec{q}_{eff} \cdot \vec{x}} | \psi_{000} \chi_{-1/2}^\lambda \rangle = 0, \\
\Sigma'(1/2^-) : \quad & \langle [\psi_{01}, \chi^S]_{-1/2}^{1/2} | \sqrt{2} \sigma_- e^{i\vec{q}_{eff} \cdot \vec{x}} | \psi_{000} \chi_{+1/2}^\lambda \rangle = -\frac{1}{3} \sqrt{\frac{2}{3}} I_1, \\
\Sigma'(3/2^-) : \quad & \langle [\psi_{01}, \chi^S]_{-1/2}^{3/2} | \sqrt{2} \sigma_- e^{i\vec{q}_{eff} \cdot \vec{x}} | \psi_{000} \chi_{+1/2}^\lambda \rangle = \frac{1}{3} \sqrt{\frac{2}{15}} I_1, \\
& \langle [\psi_{01}, \chi^S]_{-3/2}^{3/2} | \sqrt{2} \sigma_- e^{i\vec{q}_{eff} \cdot \vec{x}} | \psi_{000} \chi_{-1/2}^\lambda \rangle = \sqrt{\frac{2}{5}} I_1, \\
\Sigma'(5/2^-) : \quad & \langle [\psi_{01}, \chi^S]_{-1/2}^{5/2} | \sqrt{2} \sigma_- e^{i\vec{q}_{eff} \cdot \vec{x}} | \psi_{000} \chi_{+1/2}^\lambda \rangle = -\sqrt{\frac{2}{15}} I_1, \\
& \langle [\psi_{01}, \chi^S]_{-3/2}^{5/2} | \sqrt{2} \sigma_- e^{i\vec{q}_{eff} \cdot \vec{x}} | \psi_{000} \chi_{-1/2}^\lambda \rangle = -\sqrt{\frac{4}{15}} I_1. \quad (D.26)
\end{aligned}$$

### D.3.3 $N(1/2^+) \rightarrow d\text{-wave baryons}$

Computations go in completely similar manner as before, except for the radial matrix element

$$\langle \psi_{020} | \sqrt{2} e^{i\vec{q}_{eff} \cdot \vec{x}} | \psi_{000} \rangle = \frac{1}{2} \sqrt{\frac{2}{3}} \frac{(\alpha\alpha')^{3/2}}{A^3} \left( \frac{\alpha' q}{A^2} \right)^2 e^{-q_{eff}^2/(4A^2)} \equiv I_2. \quad (D.27)$$

The results are

$$\begin{aligned}
\Lambda(3/2^+) : \quad & \langle [\psi_{02}, \chi^\rho]_{-1/2}^{3/2} | \sqrt{2} \sigma_- e^{i\vec{q}_{eff} \cdot \vec{x}} | \psi_{000} \chi_{+1/2}^\rho \rangle = -\sqrt{\frac{2}{5}} I_2, \\
& \langle [\psi_{02}, \chi^\rho]_{-3/2}^{3/2} | \sqrt{2} \sigma_- e^{i\vec{q}_{eff} \cdot \vec{x}} | \psi_{000} \chi_{-1/2}^\rho \rangle = 0, \\
\Lambda(5/2^+) : \quad & \langle [\psi_{02}, \chi^\rho]_{-1/2}^{5/2} | \sqrt{2} \sigma_- e^{i\vec{q}_{eff} \cdot \vec{x}} | \psi_{000} \chi_{+1/2}^\rho \rangle = \sqrt{\frac{3}{5}} I_2, \\
& \langle [\psi_{02}, \chi^\rho]_{-3/2}^{5/2} | \sqrt{2} \sigma_- e^{i\vec{q}_{eff} \cdot \vec{x}} | \psi_{000} \chi_{-1/2}^\rho \rangle = 0, \\
\Sigma(3/2^+) : \quad & \langle [\psi_{02}, \chi^\lambda]_{-1/2}^{3/2} | \sqrt{2} \sigma_- e^{i\vec{q}_{eff} \cdot \vec{x}} | \psi_{000} \chi_{+1/2}^\lambda \rangle = \sqrt{\frac{3}{5}} I_2, \\
& \langle [\psi_{02}, \chi^\lambda]_{-3/2}^{3/2} | \sqrt{2} \sigma_- e^{i\vec{q}_{eff} \cdot \vec{x}} | \psi_{000} \chi_{-1/2}^\lambda \rangle = 0, \\
\Sigma(5/2^+) : \quad & \langle [\psi_{02}, \chi^\lambda]_{-1/2}^{5/2} | \sqrt{2} \sigma_- e^{i\vec{q}_{eff} \cdot \vec{x}} | \psi_{000} \chi_{+1/2}^\lambda \rangle = \sqrt{\frac{3}{5}} I_2, \\
& \langle [\psi_{02}, \chi^\lambda]_{-3/2}^{5/2} | \sqrt{2} \sigma_- e^{i\vec{q}_{eff} \cdot \vec{x}} | \psi_{000} \chi_{-1/2}^\lambda \rangle = 0, \\
\Sigma'(1/2^+) : \quad & \langle [\psi_{02}, \chi^S]_{-1/2}^{1/2} | \sqrt{2} \sigma_- e^{i\vec{q}_{eff} \cdot \vec{x}} | \psi_{000} \chi_{+1/2}^\lambda \rangle = \sqrt{\frac{3}{5}} I_2, \\
\Sigma'(3/2^+) : \quad & \langle [\psi_{02}, \chi^S]_{-1/2}^{3/2} | \sqrt{2} \sigma_- e^{i\vec{q}_{eff} \cdot \vec{x}} | \psi_{000} \chi_{+1/2}^\lambda \rangle = \sqrt{\frac{3}{5}} I_2, \\
& \langle [\psi_{02}, \chi^S]_{-3/2}^{3/2} | \sqrt{2} \sigma_- e^{i\vec{q}_{eff} \cdot \vec{x}} | \psi_{000} \chi_{-1/2}^\lambda \rangle = 0, \\
\Sigma'(5/2^+) : \quad & \langle [\psi_{02}, \chi^S]_{-1/2}^{5/2} | \sqrt{2} \sigma_- e^{i\vec{q}_{eff} \cdot \vec{x}} | \psi_{000} \chi_{+1/2}^\lambda \rangle = \sqrt{\frac{3}{5}} I_2, \\
& \langle [\psi_{02}, \chi^S]_{-3/2}^{5/2} | \sqrt{2} \sigma_- e^{i\vec{q}_{eff} \cdot \vec{x}} | \psi_{000} \chi_{-1/2}^\lambda \rangle = 0, \\
\Sigma'(7/2^+) : \quad & \langle [\psi_{02}, \chi^S]_{-1/2}^{7/2} | \sqrt{2} \sigma_- e^{i\vec{q}_{eff} \cdot \vec{x}} | \psi_{000} \chi_{+1/2}^\lambda \rangle = \sqrt{\frac{3}{5}} I_2, \\
& \langle [\psi_{02}, \chi^S]_{-3/2}^{7/2} | \sqrt{2} \sigma_- e^{i\vec{q}_{eff} \cdot \vec{x}} | \psi_{000} \chi_{-1/2}^\lambda \rangle = 0. \tag{D.28}
\end{aligned}$$

## D.4 Baryon wave functions

We summarize the baryon wave functions used in the present calculations [138]. They are constructed by a quark and a diquark, and are expressed as products of isospin, spin and orbital wave functions. Here we show explicitly spin and orbital parts. For orbital wave functions, we employ harmonic oscillator functions as given in Appendix D.

For spin wave functions, using the notation for angular momentum coupling  $[L_1, L_2]^{L_{tot}}$  we employ the three functions

$$\begin{aligned}
\chi_m^\rho &= [d^0, \chi]_m^{1/2}, \\
\chi_m^\lambda &= [d^1, \chi]_m^{1/2}, \\
\chi_m^S &= [d^1, \chi]_m^{3/2}, \tag{D.29}
\end{aligned}$$

where  $d^S$  denotes the diquark spin function, and  $\chi$  the two component spinor for a single quark. For the ground baryons we have three states

$$\begin{aligned}\Lambda(1/2^+, m) &= \psi_{000}(\vec{x})\chi_m^\rho, \\ \Sigma(1/2^+, m) &= \psi_{000}(\vec{x})\chi_m^\lambda, \\ \Sigma(3/2^+, m) &= \psi_{000}(\vec{x})\chi_m^S.\end{aligned}\tag{D.30}$$

For the first excited states of negative parity there are seven states ( $\psi_{nlm} \rightarrow \psi_{nl} = \psi_{01}$ )

$$\begin{aligned}\Lambda(1/2^-, m) &= [\psi_{01}(\vec{x}), \chi_m^\rho]^{1/2}, \\ \Lambda(3/2^-, m) &= [\psi_{01}(\vec{x}), \chi_m^\rho]^{3/2}, \\ \Sigma(1/2^-, m) &= [\psi_{01}(\vec{x}), \chi_m^\lambda]^{1/2}, \\ \Sigma(3/2^-, m) &= [\psi_{01}(\vec{x}), \chi_m^\lambda]^{3/2}, \\ \Sigma'(1/2^-, m) &= [\psi_{01}(\vec{x}), \chi_m^S]^{1/2}, \\ \Sigma'(3/2^-, m) &= [\psi_{01}(\vec{x}), \chi_m^S]^{3/2}, \\ \Sigma'(5/2^-, m) &= [\psi_{01}(\vec{x}), \chi_m^S]^{5/2}.\end{aligned}\tag{D.31}$$

Similarly, we obtain the wave functions for the  $l = 2$  excited baryons.

Finally, the nucleon wave function is given by

$$N = \psi_{000} \frac{1}{\sqrt{2}} \left( \chi^\rho \phi^\rho + \chi^\lambda \phi^\lambda \right), \tag{D.32}$$

where  $\phi^\rho$  and  $\phi^\lambda$  are the isospin 1/2 wave functions of the nucleon with three quarks.

## D.5 Harmonic oscillator wave functions

We summarize some of the harmonic oscillator wave functions for low lying states. Including the angular and radial parts, they are given by

$$\psi_{nlm}(\vec{x}) = Y_{lm}(\hat{x}) R_{nl}(r), \tag{D.33}$$

where  $R_{nl}(r)$  are

$$\begin{aligned}
R_{00}(r) &= \frac{\alpha^{3/2}}{\pi^{1/4}} 2e^{-(\alpha^2/2)r^2}, \\
R_{01}(r) &= \frac{\alpha^{3/2}}{\pi^{1/4}} \left(\frac{8}{3}\right)^{1/2} \alpha r e^{-(\alpha^2/2)r^2}, \\
R_{10}(r) &= \frac{\alpha^{3/2}}{\pi^{1/4}} (2 \cdot 3)^{1/2} \left(1 - \frac{2}{3}(\alpha r)^2\right) e^{-(\alpha^2/2)r^2}, \\
R_{02}(r) &= \frac{\alpha^{3/2}}{\pi^{1/4}} \left(\frac{16}{5 \cdot 3}\right)^{1/2} (\alpha r)^2 e^{-(\alpha^2/2)r^2}.
\end{aligned} \tag{D.34}$$

The oscillator parameter  $\alpha$  is related to the frequency  $\omega$  by

$$\alpha = \sqrt{m\omega} = (km)^{1/4}, \tag{D.35}$$

where  $k$  is the spring constant.

# Appendix E

## Regge parameters

### E.1 Regge trajectories

For meson trajectories, we use the so called “square-root” trajectory [134]

$$\alpha(t) = \alpha(0) + \gamma[\sqrt{T} - \sqrt{T-t}], \quad (\text{E.1})$$

where  $\gamma$  is an universal slope and  $T$  a scale parameter. Equation (E.1) can be approximated to a linear form

$$\alpha(t) = \alpha(0) + \alpha' t, \quad (\text{E.2})$$

in a high energy limit with the slope  $\alpha' = \gamma/2\sqrt{T}$ .

In the case of the  $\rho$  trajectory, the intercept is chosen to be  $\alpha_\rho(0) = 0.55$  from many evidences as explained in detail in Ref. [134]. Other parameters are determined by using the relation between the mass and the spin of  $\rho$  and  $\rho_3$ :  $\alpha_\rho(M_\rho^2) = 1$  with  $M_\rho = 769.0 \pm 0.9$  MeV and  $\alpha_\rho(M_{\rho_3}^2) = 3$  with  $M_{\rho_3} = 1688.8 \pm 2.1$  MeV, which is given as [134]

$$\gamma = 3.65 \pm 0.05 \text{ GeV}^{-1}, \sqrt{T}_\rho = 2.46 \pm 0.03 \text{ GeV}. \quad (\text{E.3})$$

The universal parameter  $\gamma$  is applicable to all the trajectories.

In the case of the  $K^*$  trajectory, a similar relation is used to get the intercept and the slope of the  $K^*$  reggeon:  $\alpha_{K^*}(M_{K^*}^2) = 1$  with  $M_{K^*0} = 896.1 \pm 0.3$  MeV and  $\alpha_{K^*}(M_{K_3^*}^2) = 3$  with  $M_{K_3^*0} = 1776 \pm 7$  MeV. Their numerical values are given as [134]

$$\alpha_{K^*}(0) = 0.414 \pm 0.006, \sqrt{T}_{K^*} = 2.58 \pm 0.03 \text{ GeV}. \quad (\text{E.4})$$

We finally extract the  $\phi$  trajectory from the following relations [125, 134]

$$2\alpha_{\bar{s}q}(0) = \alpha_{\bar{q}q}(0) + \alpha_{\bar{s}s}(0), \quad (\text{E.5})$$

$$2/\alpha'_{\bar{s}q} = 1/\alpha'_{\bar{q}q} + 1/\alpha'_{\bar{s}s}, \quad (\text{E.6})$$

where  $\alpha_{\bar{q}q}(t)$ ,  $\alpha_{\bar{s}q}(t)$ , and  $\alpha_{\bar{s}s}(t)$  are the trajectories corresponding to  $\rho$ ,  $K^*$ , and  $\phi$  mesons, respectively. We display all the numerical values of the related Regge trajectories in Table E.1, including the cases of pseudoscalar reggeons and the corresponding charm trajectories [134].

For the baryon trajectories, we use similar relations as Eqs. (E.5) and (E.6) [137]:

$$2\alpha_{ds}(0) = \alpha_{\bar{d}d}(0) + \alpha_{\bar{s}s}(0), \quad (\text{E.7})$$

$$2/\alpha'_{ds} = 1/\alpha'_{\bar{d}d} + 1/\alpha'_{\bar{s}s}, \quad (\text{E.8})$$

where  $d$  denotes a  $uu$  diquark, and  $\alpha_{ds}(u)$  is the  $\Sigma$  trajectory taken from Ref. [67]

$$\alpha_{ds}(u) \simeq \alpha_{\Sigma}(u) \simeq -0.79 + 0.87u. \quad (\text{E.9})$$

Since we know the value of  $\alpha_{\bar{s}s}(u)$  from the above,  $\alpha_{\bar{d}d}(u)$  can be easily obtained. We use this to get the  $\Sigma_c$  trajectory,  $\alpha_{dc}(u)$ . Another input parameter is the  $J/\psi$  trajectory,  $\alpha_{\bar{c}c}(u)$ , taken from Ref. [134]. In Table E.2, We summarize all the values of the baryon trajectories.

$\pi^- p \rightarrow K^{*0} \Lambda$				$\pi^- p \rightarrow D^{*-} \Lambda_c^+$			
	$\alpha(0)$	$\sqrt{T} [\text{GeV}]$	$\alpha' [\text{GeV}^{-2}]$		$\alpha(0)$	$\sqrt{T} [\text{GeV}]$	$\alpha' [\text{GeV}^{-2}]$
$\bar{q}q(\rho)$	0.55	2.46	0.742	$\bar{q}q(\rho)$	0.55	2.46	0.742
$\bar{s}q(K^*)$	0.414	2.58	0.707	$\bar{c}q(D^*)$	-1.02	3.91	0.467
$\bar{s}s(\phi)$	0.27	2.70	0.675	$\bar{c}c(J/\psi)$	-2.60	5.36	0.340
$\bar{q}q(\pi)$	-0.0118	2.82	0.647	$\bar{q}q(\pi)$	-0.0118	2.82	0.647
$\bar{s}q(K)$	-0.151	2.96	0.617	$\bar{c}q(D)$	-1.61105	4.16	0.439
$\bar{s}s(\eta_s)$	-0.291	3.10	0.606	$\bar{c}c(\eta_c)$	-3.2103	5.49	0.332

TABLE E.1: Mason trajectories from Ref. [134].

$\pi^- p \rightarrow K^{*0} \Lambda$				$\pi^- p \rightarrow D^{*-} \Lambda_c^+$			
	$\alpha(0)$	$\alpha' [\text{GeV}^{-2}]$			$\alpha(0)$	$\alpha' [\text{GeV}^{-2}]$	
$ds(\Sigma)$	-0.79	0.87	Ref. [67]	$\bar{d}d$	-1.85	1.22	
$\bar{s}s(\phi)$	0.27	0.675	Ref. [134]	$\bar{c}c(J/\psi)$	-2.60	0.340	Ref. [134]
$\bar{d}d$	-1.85	1.22		$dc(\Sigma_c)$	-2.23	0.532	

TABLE E.2: Baryon trajectories.

Let us check whether the baryon trajectories satisfy the correct relations between the mass and the spin:  $\alpha(M^2) = J$ . For reference, we calculate the bottom part also. We obtain the trajectories as  $\alpha(M_\Sigma^2) = 0.442$ ,  $\alpha(M_{\Sigma_c}^2) = 0.971$ , and  $\alpha(M_{\Sigma_b}^2) = 0.484$  [1]. Note that there is some uncertainty in the charm sector, compared with the others. However, we take it as a good approximation.

## E.2 Regge energy scale parameters

The energy scale parameters  $s^{\pi N}$ ,  $s^{K^* \Lambda}$ , and  $s^{D^* \Lambda_c}$  are computed from

$$s^{ab} = \left( \sum_i m_{i\perp} \right)_a \left( \sum_j m_{j\perp} \right)_b, \quad (\text{E.10})$$

where  $m_i$  is the transverse mass of the constituent quark  $i$  with  $m_q \simeq 0.5$  GeV,  $m_s \simeq 0.6$  GeV, and  $m_c \simeq 1.6$  GeV [126]. From these values, we can deduce the energy scale parameters [126, 137]

$$(s_K^{\pi N:K^* \Lambda})^{2\alpha_K(0)} = (s^{\pi N})^{\alpha_\pi(0)} \times (s^{K^* \Lambda})^{\alpha_{\eta s}(0)}, \quad (\text{E.11})$$

$$(s_{K^*}^{\pi N:K^* \Lambda})^{2(\alpha_{K^*}(0)-1)} = (s^{\pi N})^{\alpha_\rho(0)-1} \times (s^{K^* \Lambda})^{\alpha_\phi(0)-1}, \quad (\text{E.12})$$

$$(s_\Sigma^{\pi N:K^* \Lambda})^{2(\alpha_{ds}(0)-\frac{1}{2})} = (s^{\pi N})^{\alpha_{\bar{d}d}(0)} \times (s^{K^* \Lambda})^{\alpha_{\bar{s}s}(0)-1}, \quad (\text{E.13})$$

$$(s_D^{\pi N:D^* \Lambda_c})^{2\alpha_D(0)} = (s^{\pi N})^{\alpha_\pi(0)} \times (s^{D^* \Lambda_c})^{\alpha_{\eta c}(0)}, \quad (\text{E.14})$$

$$(s_{D^*}^{\pi N:D^* \Lambda_c})^{2(\alpha_{D^*}(0)-1)} = (s^{\pi N})^{\alpha_\rho(0)-1} \times (s^{D^* \Lambda_c})^{\alpha_{J/\psi}(0)-1}, \quad (\text{E.15})$$

$$(s_{\Sigma_c}^{\pi N:D^* \Lambda_c})^{2(\alpha_{dc}(0)-\frac{1}{2})} = (s^{\pi N})^{\alpha_{\bar{d}d}(0)} \times (s^{D^* \Lambda_c})^{\alpha_{\bar{c}c}(0)-1}. \quad (\text{E.16})$$

In Table E.3, we summarize all the related values.

$s^{\pi N}$	$s^{K^* \Lambda}$	$s^{D^* \Lambda_c}$	$s_K^{\pi N:K^* \Lambda}$	$s_{K^*}^{\pi N:K^* \Lambda}$	$s_\Sigma^{\pi N:K^* \Lambda}$	$s_D^{\pi N:D^* \Lambda_c}$	$s_{D^*}^{\pi N:D^* \Lambda_c}$	$s_{\Sigma_c}^{\pi N:D^* \Lambda_c}$
1.5	1.76	5.46	1.752	1.662	1.569	5.434	4.748	3.513

TABLE E.3: The energy scale parameters



## Appendix F

# Isospin Factors

### F.1 $\Delta$ vertex

The isospin structures of the  $\Delta$  vertices in Eq. (3.13) are given as follows, respectively:

$$\bar{\Delta}I^0N, \quad \bar{\Delta}\mathbf{I} \cdot \boldsymbol{\Sigma}K^*, \quad (\text{F.1})$$

where  $I$  stands for the isospin transition ( $3/2 \rightarrow 1/2$ ) matrices

$$I^- = \frac{1}{\sqrt{6}} \begin{pmatrix} 0 & 0 \\ 0 & 0 \\ \sqrt{2} & 0 \\ 0 & \sqrt{6} \end{pmatrix}, \quad I^0 = \frac{1}{\sqrt{6}} \begin{pmatrix} 0 & 0 \\ 2 & 0 \\ 0 & 2 \\ 0 & 0 \end{pmatrix}, \quad I^+ = \frac{1}{\sqrt{6}} \begin{pmatrix} \sqrt{6} & 0 \\ 0 & \sqrt{2} \\ 0 & 0 \\ 0 & 0 \end{pmatrix}. \quad (\text{F.2})$$

Thus the  $\Delta$  and nucleon vertex is expressed as

$$\begin{aligned} \bar{\Delta}I^0N &= \sqrt{\frac{2}{3}}(\bar{\Delta}^{++}, \bar{\Delta}^+, \bar{\Delta}^0, \bar{\Delta}^-) \begin{pmatrix} 0 & 0 \\ 1 & 0 \\ 0 & 1 \\ 0 & 0 \end{pmatrix} \begin{pmatrix} p \\ n \end{pmatrix} \\ &= \sqrt{\frac{2}{3}}(\bar{\Delta}^+p + \bar{\Delta}^0n). \end{aligned} \quad (\text{F.3})$$

The  $\Delta\Sigma K^*$  vertex has the form

$$\mathbf{I} \cdot \boldsymbol{\Sigma} = -I^{(+)}\Sigma^+ + I^{(-)}\Sigma^- + I^{(0)}\Sigma^0 = \frac{1}{\sqrt{3}} \begin{pmatrix} -\sqrt{3}\Sigma^+ & 0 \\ \sqrt{2}\Sigma^0 & -\Sigma^+ \\ \Sigma^- & \sqrt{2}\Sigma^0 \\ 0 & \sqrt{3}\Sigma^- \end{pmatrix}, \quad (\text{F.4})$$

$$\begin{aligned} \bar{\Delta}\mathbf{I} \cdot \boldsymbol{\Sigma}K^* &= \frac{1}{\sqrt{3}}(\bar{\Delta}^{++}, \bar{\Delta}^+, \bar{\Delta}^0, \bar{\Delta}^-) \begin{pmatrix} -\sqrt{3}\Sigma^+ & 0 \\ \sqrt{2}\Sigma^0 & -\Sigma^+ \\ \Sigma^- & \sqrt{2}\Sigma^0 \\ 0 & \sqrt{3}\Sigma^- \end{pmatrix} \begin{pmatrix} K^{*+} \\ K^{*0} \end{pmatrix} \\ &= \frac{1}{\sqrt{3}}(-\sqrt{3}\bar{\Delta}^{++}\Sigma^+K^{*+} + \sqrt{2}\bar{\Delta}^{+}\Sigma^0K^{*+} - \bar{\Delta}^{+}\Sigma^+K^{*0} \\ &\quad + \bar{\Delta}^0\Sigma^-K^{*+} + \sqrt{2}\bar{\Delta}^0\Sigma^0K^{*0} + \sqrt{3}\bar{\Delta}^-\Sigma^-K^{*0}). \end{aligned} \quad (\text{F.5})$$

## F.2 VVP vertex

The isospin structure of the  $VVP$  vertex in Eq. (6.3) is expressed as

$$P = \begin{bmatrix} \frac{1}{\sqrt{6}}\eta + \frac{1}{\sqrt{2}}\boldsymbol{\tau} \cdot \boldsymbol{\pi} & K \\ \bar{K} & -\frac{2}{\sqrt{6}}\eta \end{bmatrix} = \begin{bmatrix} \frac{1}{\sqrt{6}}\eta + \frac{1}{\sqrt{2}}\pi^0 & \pi^+ & K^+ \\ \pi^- & \frac{1}{\sqrt{6}}\eta - \frac{1}{\sqrt{2}}\pi^0 & K^0 \\ K^- & \bar{K}^0 & -\frac{2}{\sqrt{6}}\eta \end{bmatrix}, \quad (\text{F.6})$$

$$V = \begin{bmatrix} \frac{1}{\sqrt{2}}\omega + \frac{1}{\sqrt{2}}\boldsymbol{\tau} \cdot \boldsymbol{\rho} & K^* \\ \bar{K}^* & -\phi \end{bmatrix} = \begin{bmatrix} \frac{1}{\sqrt{2}}\omega + \frac{1}{\sqrt{2}}\rho^0 & \rho^+ & K^{*+} \\ \rho^- & \frac{1}{\sqrt{2}}\omega - \frac{1}{\sqrt{2}}\rho^0 & K^{*0} \\ K^{*-} & \bar{K}^{*0} & -\phi \end{bmatrix}, \quad (\text{F.7})$$

$$\mathcal{L}_{VVP} = g_{VVP}\epsilon^{\mu\nu\alpha\beta}\text{Tr}(\partial_\mu V_\nu \partial_\alpha V_\beta P), \quad (\text{F.8})$$

$$\begin{aligned} \text{Tr}[VVP] &= \frac{1}{\sqrt{2}}\bar{K}^*\boldsymbol{\tau} \cdot \boldsymbol{\pi}K^* - \frac{1}{\sqrt{6}}\bar{K}^*K^*\eta + \frac{1}{\sqrt{2}}\bar{K}^*\boldsymbol{\tau} \cdot \boldsymbol{\rho}K + \frac{1}{\sqrt{2}}\bar{K}^*K\omega \\ &\quad - \bar{K}^*K\phi + \sqrt{2}\boldsymbol{\rho} \cdot \boldsymbol{\pi}w + \frac{1}{\sqrt{6}}\boldsymbol{\rho} \cdot \boldsymbol{\rho}\eta + \frac{1}{\sqrt{6}}\omega\omega\eta - \frac{2}{\sqrt{6}}\phi\phi\eta. \end{aligned} \quad (\text{F.9})$$

## Appendix G

# Structures of Feynman Amplitudes

The analytical calculations for the amplitudes of the  $\pi^- p \rightarrow K^{*0} \Lambda$  reaction is expressed.

### G.1 $K$ amplitude

$$\mathcal{M}'_K = \bar{u}_\Lambda \gamma_5 u_N \varepsilon_\mu^* k_1^\mu. \quad (\text{G.1})$$

$$\begin{aligned} \sum_{s_i, s_f, \lambda_f} |\mathcal{M}'_K|^2 &= \sum_{s_i, s_f, \lambda_f} (\bar{u}_\Lambda \gamma_5 u_N) (-\bar{u}_N \gamma_5 u_\Lambda) \varepsilon_\mu^* \varepsilon_\nu k_1^\mu k_1^\nu \\ &= -\text{Tr} \left( \sum_{s_f} u_\Lambda \bar{u}_\Lambda \right) \gamma_5 \left( \sum_{s_i} u_N \bar{u}_N \right) \gamma_5 \left( \sum_{\lambda_f} \varepsilon_\mu^* \varepsilon_\nu \right) k_1^\mu k_1^\nu \\ &= -\text{Tr} (\not{p}_2 + M_\Lambda) \gamma_5 (\not{p}_1 + M_N) \gamma_5 \left[ -g_{\mu\nu} + \frac{1}{M_{K^*}^2} k_{2\mu} k_{2\nu} \right] k_1^\mu k_1^\nu \\ &= \text{Tr} (\not{p}_2 + M_\Lambda) (\not{p}_1 - M_N) \left[ -g_{\mu\nu} + \frac{1}{M_{K^*}^2} k_{2\mu} k_{2\nu} \right] k_1^\mu k_1^\nu \\ = A_K^2(t) &= \frac{1}{2M_{K^*}^2} (M_{K^*}^2 - M_\pi^2)^2 (M_\Lambda - M_N)^2, \\ &\quad -t \left[ (M_\Lambda - M_N)^2 \left( 1 + \frac{M_\pi^2}{M_{K^*}^2} \right) + \frac{1}{2M_{K^*}^2} (M_{K^*}^2 - M_\pi^2)^2 \right] \\ &\quad + t^2 \left[ 1 + \frac{M_\pi^2}{M_{K^*}^2} + \frac{1}{2M_{K^*}^2} (M_\Lambda - M_N)^2 \right] - t^3 \frac{1}{2M_{K^*}^2} \\ &= \sum_{x=0}^3 a_x t^x. \quad (\text{G.2}) \end{aligned}$$

The dominant term is expressed as

$$A_K^\infty = \frac{1}{\sqrt{2}M_{K^*}}(M_{K^*}^2 - M_\pi^2)(M_\Lambda - M_N). \quad (\text{G.3})$$

## G.2 $K^*$ amplitude

$$\begin{aligned} \mathcal{M}'_{K^*} &= \epsilon^{\mu\nu\alpha\beta} \bar{u}_\Lambda \left[ \gamma_\nu - \frac{i\kappa_{K^*N\Lambda}}{M_N + M_\Lambda} \sigma_{\nu\lambda} (k_2 - k_1)^\lambda \right] u_N k_{1\alpha} k_{2\beta} \varepsilon_\mu^* \\ &= \epsilon^{\mu\nu\alpha\beta} \bar{u}_\Lambda \left[ (1 + \kappa_{K^*N\Lambda}) \gamma_\nu - \kappa_{K^*N\Lambda} \frac{(p_1 + p_2)_\nu}{M_N + M_\Lambda} \right] u_N k_{1\alpha} k_{2\beta} \varepsilon_\mu^*. \end{aligned} \quad (\text{G.4})$$

$$\begin{aligned} &\sum_{s_i, s_f, \lambda_f} |\mathcal{M}'_{K^*}|^2 \\ &= \sum_{s_i, s_f, \lambda_f} \epsilon^{\mu\nu\alpha\beta} \epsilon^{\mu'\nu'\alpha'\beta'} \bar{u}_\Lambda \left[ (1 + \kappa_{K^*N\Lambda}) \gamma_\nu - \kappa_{K^*N\Lambda} \frac{(p_1 + p_2)_\nu}{M_N + M_\Lambda} \right] u_N \\ &\quad \times \bar{u}_\Lambda \left[ (1 + \kappa_{K^*N\Lambda}) \gamma_{\nu'} - \kappa_{K^*N\Lambda} \frac{(p_1 + p_2)_{\nu'}}{M_N + M_\Lambda} \right] u_\Lambda \\ &\quad \times (k_{1\alpha} k_{2\beta} \varepsilon_\mu^*) (k_{1\alpha'} k_{2\beta'} \varepsilon_{\mu'}^*) \\ &= \epsilon^{\mu\nu\alpha\beta} \epsilon^{\mu'\nu'\alpha'\beta'} \text{Tr} \left( \sum_{s_f} u_\Lambda \bar{u}_\Lambda \right) \left[ (1 + \kappa_{K^*N\Lambda}) \gamma_\nu - \kappa_{K^*N\Lambda} \frac{(p_1 + p_2)_\nu}{M_N + M_\Lambda} \right] \\ &\quad \times \left( \sum_{s_i} u_N \bar{u}_N \right) \left[ (1 + \kappa_{K^*N\Lambda}) \gamma_{\nu'} - \kappa_{K^*N\Lambda} \frac{(p_1 + p_2)_{\nu'}}{M_N + M_\Lambda} \right] \left( \sum_{\lambda_f} \varepsilon_\mu^* \varepsilon_{\mu'}^* \right) \\ &\quad \times (k_{1\alpha} k_{1\alpha'} k_{2\beta} k_{2\beta'}) \\ &= \epsilon^{\mu\nu\alpha\beta} \epsilon^{\mu'\nu'\alpha'\beta'} \text{Tr} (\not{p}_2 + M_\Lambda) \left[ (1 + \kappa_{K^*N\Lambda}) \gamma_\nu - \kappa_{K^*N\Lambda} \frac{(p_1 + p_2)_\nu}{M_N + M_\Lambda} \right] \\ &\quad \times (\not{p}_1 + M_N) \left[ (1 + \kappa_{K^*N\Lambda}) \gamma_{\nu'} - \kappa_{K^*N\Lambda} \frac{(p_1 + p_2)_{\nu'}}{M_N + M_\Lambda} \right] \\ &\quad \times \left[ -g_{\mu\mu'} + \frac{1}{M_{K^*}^2} k_{2\mu} k_{2\mu'} \right] (k_{1\alpha} k_{1\alpha'} k_{2\beta} k_{2\beta'}) \\ &= A_{K^*}^2(s, t) \\ &= -2s^2 t + 2s^2 t^2 \frac{\kappa_{K^*N\Lambda}^2}{(M_N + M_\Lambda)^2} \\ &\quad - 2s(M_{K^*}^2 - M_\pi^2)(M_\Lambda^2 - M_N^2) + 2st(M_\pi^2 + M_N^2 + M_{K^*}^2 + M_\Lambda^2) \\ &\quad + 2st\kappa_{K^*N\Lambda}^2(M_{K^*}^2 - M_\pi^2) \frac{M_\Lambda - M_N}{M_\Lambda + M_N} \\ &\quad - 2st^2 - 2st^2 \frac{\kappa_{K^*N\Lambda}^2}{(M_\Lambda + M_N)^2} (M_\pi^2 + M_N^2 + M_{K^*}^2 + M_\Lambda^2) + 2st^3 \frac{\kappa_{K^*N\Lambda}^2}{(M_\Lambda + M_N)^2} \\ &\quad - t \left[ (1 + \kappa_{K^*N\Lambda})^2 \left( 2M_N^2 M_\Lambda^2 + M_{K^*}^2 (2M_\Lambda^2 - 4M_N M_\Lambda + M_{K^*}^2) \right. \right. \\ &\quad \left. \left. - M_\pi^2 (4M_N M_\Lambda - 2M_N^2 - M_\pi^2) \right) - 4\kappa_{K^*N\Lambda} (1 + \kappa_{K^*N\Lambda}) (M_\Lambda^2 - M_{K^*}^2) (M_N^2 - M_\pi^2) \right. \\ &\quad \left. + \frac{2\kappa_{K^*N\Lambda}^2}{(M_\Lambda + M_N)^2} \left( M_N^2 M_\Lambda^2 (M_\Lambda + M_N)^2 - 2M_\pi^2 (M_\Lambda^2 - M_{K^*}^2) (M_\Lambda^2 + M_N M_\Lambda) \right) \right] \end{aligned}$$

$$\begin{aligned}
& -M_{K^*}^2 M_N^2 (2M_N M_\Lambda + 2M_N^2 + M_{K^*}^2) + 2M_\pi^2 M_{K^*}^2 M_N^2 - M_\pi^4 M_\Lambda^2 \Big) \Big] \\
& + t^2 \left[ (1 + \kappa_{K^* N \Lambda})^2 \left( (M_\Lambda - M_N)^2 + 2(M_{K^*}^2 + M_\pi^2) \right) \right. \\
& \quad \left. + \frac{2\kappa_{K^* N \Lambda}^2}{(M_\Lambda + M_N)^2} (M_\Lambda^2 - M_{K^*}^2)(M_N^2 - M_\pi^2) \right] - t^3 (1 + \kappa_{K^* N \Lambda})^2 \\
& + \left[ (1 + \kappa_{K^* N \Lambda})^2 \left( 2M_{K^*}^2 M_N^2 (M_\Lambda^2 - M_N^2) + M_{K^*}^4 (M_\Lambda^2 - 2M_N M_\Lambda - M_N^2) \right. \right. \\
& \quad \left. \left. - 2M_\pi^2 (M_\Lambda^4 - M_N^2 M_\Lambda^2 - 2M_{K^*}^2 M_N M_\Lambda) - M_\pi^4 (M_\Lambda^2 + 2M_N M_\Lambda - M_N^2) \right) \right. \\
& \quad \left. - 2\kappa_{K^* N \Lambda} (2 + \kappa_{K^* N \Lambda}) \left( (M_\Lambda^2 - M_N^2)(M_{K^*}^2 M_N^2 - M_\pi^2 M_\Lambda^2) \right. \right. \\
& \quad \left. \left. + (M_\Lambda^2 + M_N^2) M_\pi^2 M_{K^*}^2 - (M_{K^*}^4 M_N^2 + M_\pi^4 M_\Lambda^2) \right) \right] \\
& = s^2 \sum_{x=1}^2 a_x t^x + s \sum_{x=0}^3 a_x t^x + \sum_{x=0}^3 t^x. \tag{G.5}
\end{aligned}$$

The dominant term is

$$A_{K^*}^\infty(s, t) = \sqrt{-2s^2 t}. \tag{G.6}$$

### G.3 $\Sigma$ amplitude

$$\mathcal{M}'_\Sigma = \bar{u}_\Lambda \gamma_5 (\not{p}_2 - \not{k}_1 + M_\Sigma) \left[ \gamma^\mu - \frac{i\kappa_{K^* N \Sigma}}{M_N + M_\Sigma} \sigma^{\mu\nu} k_{2\nu} \right] \varepsilon_\mu^* u_N. \tag{G.7}$$

$$\begin{aligned}
& \sum_{s_i, s_f, \lambda_f} |\mathcal{M}'_\Sigma|^2 \\
& = \sum_{s_i, s_f, \lambda_f} \bar{u}_\Sigma \gamma_5 (\not{p}_2 - \not{k}_1 + M_\Sigma) \left[ \gamma^\mu + \frac{\kappa_{K^* N \Sigma} k_{2\nu}}{2(M_N + M_\Sigma)} (\gamma^\mu \gamma^\nu - \gamma^\nu \gamma^\mu) \right] u_N \\
& \quad \times \bar{u}_N \left[ \gamma^{\mu'} + \frac{\kappa_{K^* N \Sigma} k_{2\nu'}}{2(M_N + M_\Sigma)} (\gamma^{\nu'} \gamma^{\mu'} - \gamma^{\mu'} \gamma^{\nu'}) \right] (\not{p}_2 - \not{k}_1 + M_\Sigma) (-\gamma_5) u_\Sigma (\varepsilon_\mu^* \varepsilon_{\mu'}) \\
& = -\text{Tr} \left( \sum_{s_f} u_\Sigma \bar{u}_\Sigma \right) \gamma_5 (\not{p}_2 - \not{k}_1 + M_\Sigma) \left[ \gamma^\mu + \frac{\kappa_{K^* N \Sigma} k_{2\nu}}{2(M_N + M_\Sigma)} (\gamma^\mu \gamma^\nu - \gamma^\nu \gamma^\mu) \right] \\
& \quad \times \left( \sum_{s_i} u_N \bar{u}_N \right) \left[ \gamma^{\mu'} + \frac{\kappa_{K^* N \Sigma} k_{2\nu'}}{2(M_N + M_\Sigma)} (\gamma^{\nu'} \gamma^{\mu'} - \gamma^{\mu'} \gamma^{\nu'}) \right] (\not{p}_2 - \not{k}_1 + M_\Sigma) \gamma_5 \\
& \quad \times \left( \sum_{\lambda_f} \varepsilon_\mu^* \varepsilon_{\mu'} \right) \\
& = -\text{Tr} (\not{p}_2 + M_\Sigma) \gamma_5 (\not{p}_2 - \not{k}_1 + M_\Sigma) \left[ \gamma^\mu + \frac{\kappa_{K^* N \Sigma} k_{2\nu}}{2(M_N + M_\Sigma)} (\gamma^\mu \gamma^\nu - \gamma^\nu \gamma^\mu) \right] \\
& \quad \times (\not{p}_1 + M_N) \left[ \gamma^{\mu'} + \frac{\kappa_{K^* N \Sigma} k_{2\nu'}}{2(M_N + M_\Sigma)} (\gamma^{\nu'} \gamma^{\mu'} - \gamma^{\mu'} \gamma^{\nu'}) \right] (\not{p}_2 - \not{k}_1 + M_\Sigma) \gamma_5
\end{aligned}$$

$$\begin{aligned}
& \times \left[ -g_{\mu\mu'} + \frac{1}{M_{K^*}^2} k_{2\mu} k_{2\mu'} \right] \\
& = A_{\Sigma}^2(s, u) \\
& = s \sum_{x=0}^2 a_x u^x + \sum_{x=0}^3 u^x.
\end{aligned} \tag{G.8}$$

The dominant term is

$$\begin{aligned}
A_{\Sigma}^{\infty}(s) &= \sqrt{2s} \frac{M_{\Lambda}}{M_{\Sigma} + M_{\Lambda}} \left[ M_{\Sigma}^2 (M_N^2 / M_{K^*}^2 + 2) + 6 \frac{\kappa_{K^* N \Sigma}}{M_{\Sigma} + M_N} M_N M_{\Sigma}^2 \right. \\
&\quad \left. + \frac{\kappa_{K^* N \Sigma}^2}{(M_{\Sigma} + M_N)^2} M_{\Sigma}^2 (2M_N^2 + M_{K^*}^2) \right]^{\frac{1}{2}}.
\end{aligned} \tag{G.9}$$

## Appendix H

### Size of a charmed baryon

Let us estimate the size of a charmed baryon compared with the nucleon. The size of a baryon can be obtained from the square root of an average of distance of COM (center of mass), which is defined by

$$\sqrt{\langle R^2 \rangle} = \sqrt{\frac{1}{3} \sum_{i=1}^3 (\mathbf{x}_i - \mathbf{R}_{\text{cm}})^2}, \quad (\text{H.1})$$

where the coordinate  $\mathbf{x}_i$  is depicted in Fig. [H.1](#).

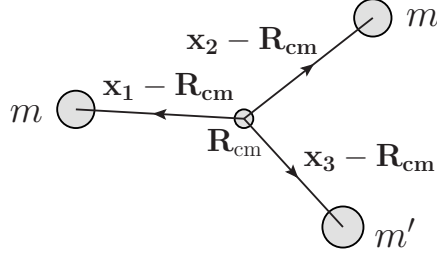


FIGURE H.1: Relative coordinates for a three-body system.

We can express it in terms of the  $\boldsymbol{\rho}$  and  $\boldsymbol{\lambda}$  coordinates as

$$\begin{aligned} \mathbf{x}_1 - \mathbf{R}_{\text{cm}} &= \frac{m'}{2m + m'} \boldsymbol{\lambda} + \frac{1}{2} \boldsymbol{\rho}, \\ \mathbf{x}_2 - \mathbf{R}_{\text{cm}} &= \frac{m'}{2m + m'} \boldsymbol{\lambda} - \frac{1}{2} \boldsymbol{\rho}, \\ \mathbf{x}_3 - \mathbf{R}_{\text{cm}} &= -\frac{2m}{2m + m'} \boldsymbol{\lambda}, \end{aligned} \quad (\text{H.2})$$

and

$$\langle R^2 \rangle = \frac{1}{3} \left[ \frac{2m'^2 + 4m^2}{(2m + m')^2} \langle \boldsymbol{\lambda}^2 \rangle + \frac{1}{2} \langle \boldsymbol{\rho}^2 \rangle \right]. \quad (\text{H.3})$$

The  $\langle \lambda^2 \rangle$  and the  $\langle \rho^2 \rangle$  are calculated by using the harmonic oscillator wave function defined in Eq. (D.33) for the lowest states,

$$\begin{aligned}
 \langle \lambda^2 \rangle &= \int d^3\lambda \lambda^2 \psi_{000}^*(\lambda) \psi_{000}(\lambda) \\
 &= \frac{4\alpha_\lambda^3}{\sqrt{\pi}} \int d\lambda \lambda^4 e^{-\alpha_\lambda^2 \lambda^2} \int d\Omega Y_{00}^*(\hat{\lambda}) Y_{00}(\hat{\lambda}) \\
 &= \frac{3}{2} \frac{1}{\alpha_\lambda^2}, \\
 \langle \rho^2 \rangle &= \frac{3}{2} \frac{1}{\alpha_\rho^2}.
 \end{aligned} \tag{H.4}$$

Thus Eq. (H.3) is changed to

$$\langle R^2 \rangle = \left[ \frac{m'^2 + 2m^2}{(2m + m')^2} \frac{1}{\alpha_\lambda^2} + \frac{1}{4\alpha_\rho^2} \right]. \tag{H.5}$$

The oscillator paramter  $\alpha$  is defined by

$$\begin{aligned}
 \alpha_\rho^2 &= m_\rho \omega_\rho = m_\rho \sqrt{\frac{3K}{m_\rho}} = \sqrt{3m_\rho K} = \sqrt{3mK}, \\
 \alpha_\lambda^2 &= m_\lambda \omega_\lambda = m_\lambda \sqrt{\frac{3K}{m_\lambda}} = \sqrt{3m_\lambda K} = 3\sqrt{\frac{mm'K}{2m + m'}}.
 \end{aligned} \tag{H.6}$$

To calculate the spring constant  $K$ , let us consider the case of the nucleon. The quark core size of the nucleon is well known as around  $0.5 \text{ fm}$  experimentally. The constituent light-quark mass is chosen as  $m' = m \simeq 0.35 \text{ GeV}$ . Then Eq. (H.5) reduces to

$$\langle R^2 \rangle = \frac{1}{3\alpha_\lambda^2} + \frac{1}{4\alpha_\rho^2} = \frac{7}{12} \frac{1}{\sqrt{3mK}} = (0.5 \text{ fm})^2 = (2.5 \text{ GeV}^{-1})^2 \tag{H.7}$$

and  $K$  is obtained as

$$K = 0.0083 \text{ GeV}^3. \tag{H.8}$$

In the case of a charmed baryon, the constituent heavy-quark mass is given by  $m' = m_Q \simeq 1.5 \text{ GeV}$  and Eq. (H.5) becomes

$$\langle R^2 \rangle = \sqrt{\frac{1}{m_Q K}} \left[ \frac{1}{3m_Q^{\frac{1}{2}}} \frac{m_Q^2 + 2m^2}{(2m + m_Q)^{\frac{3}{2}}} + \frac{1}{4\sqrt{3}} \right] = (2.56 \text{ GeV}^{-1})^2 = (0.512 \text{ fm})^2. \tag{H.9}$$

Finally, it is found that the size of a charmed baryon is  $0.512 \text{ fm}$ , which is slightly larger than the size of the nucleon.



# Bibliography

- [1] K. A. Olive *et al.* [Particle Data Group], Chin. Phys. C **38**, 090001 (2014).
- [2] M. Ablikim *et al.* [BESIII Collaboration], Phys. Rev. Lett. **110**, 022001 (2013).
- [3] S. Capstick, Phys. Rev. D **46**, 2864 (1992).
- [4] S. Capstick and W. Roberts, Phys. Rev. D **49**, 4570 (1994).
- [5] S. Capstick and W. Roberts, Phys. Rev. D **58**, 074011 (1998).
- [6] S. Capstick and W. Roberts, Prog. Part. Nucl. Phys. **45**, S241 (2000).
- [7] R. Bijker, F. Iachello, and A. Leviatan, Annals Phys. **284**, 89 (2000).
- [8] K. Hicks *et al.* [LEPS Collaboration], Phys. Rev. C **76**, 042201 (2007).
- [9] M. E. McCracken *et al.* [CLAS Collaboration], Phys. Rev. C **81**, 025201 (2010).
- [10] S. A. Pereira *et al.* [CLAS Collaboration], Phys. Lett. B **688**, 289 (2010).
- [11] B. Dey *et al.* [CLAS Collaboration], Phys. Rev. C **82**, 025202 (2010).
- [12] P. Aguar-Bartolome *et al.* [A2 Collaboration], Phys. Rev. C **88**, 044601 (2013).
- [13] J. W. C. McNabb *et al.* [CLAS Collaboration], Phys. Rev. C **69**, 042201 (2004).
- [14] R. Bradford *et al.* [CLAS Collaboration], Phys. Rev. C **73**, 035202 (2006).
- [15] S. Janssen, J. Ryckebusch, D. Debruyne and, T. Van Cauteren, Phys. Rev. C **66**, 035202 (2002).
- [16] S. Janssen, J. Ryckebusch, D. Debruyne, and T. Van Cauteren, Phys. Rev. C **65**, 015201 (2002).
- [17] T. Mart, Phys. Rev. C **82**, 025209 (2010).
- [18] T. Mart, Phys. Rev. C **83**, 048203 (2011).
- [19] T. Mart, Phys. Rev. C **90**, 065202 (2014).

- [20] M. Guidal, J. M. Laget, and M. Vanderhaeghen, Nucl. Phys. A **627**, 645 (1997).
- [21] L. De Cruz, D. G. Ireland, P. Vancraeyveld, and J. Ryckebusch, Phys. Lett. B **694**, 33 (2010).
- [22] B. G. Yu, T. K. Choi, and W. Kim, Phys. Lett. B **701**, 332 (2011).
- [23] T. Corthals, J. Ryckebusch, and T. Van Cauteren, Phys. Rev. C **73**, 045207 (2006).
- [24] T. Corthals, D. G. Ireland, T. Van Cauteren, and J. Ryckebusch, Phys. Rev. C **75**, 045204 (2007).
- [25] L. De Cruz, J. Ryckebusch, T. Vrancx, and P. Vancraeyveld, Phys. Rev. C **86**, 015212 (2012).
- [26] W. T. Chiang, F. Tabakin, T. S. H. Lee, and B. Saghai, Phys. Lett. B **517**, 101 (2001).
- [27] V. Shklyar, H. Lenske, and U. Mosel, Phys. Rev. C **72**, 015210 (2005).
- [28] X. Cao, V. Shklyar, and H. Lenske, Phys. Rev. C **88**, 055204 (2013).
- [29] S. I. Nam, A. Hosaka, and H.-Ch. Kim, Phys. Rev. D **71**, 114012 (2005).
- [30] S. i. Nam, K. S. Choi, A. Hosaka, and H. C. Kim, Phys. Rev. D **75**, 014027 (2007).
- [31] J. J. Xie and J. Nieves, Phys. Rev. C **82**, 045205 (2010).
- [32] J. He and X. R. Chen, Phys. Rev. C **86**, 035204 (2012).
- [33] J. J. Xie, E. Wang, and J. Nieves, Phys. Rev. C **89**, 015203 (2014).
- [34] H. Toki, C. Garcia-Recio, and J. Nieves, Phys. Rev. D **77**, 034001 (2008).
- [35] S. i. Nam and C. W. Kao, Phys. Rev. C **81**, 055206 (2010).
- [36] J. He, Nucl. Phys. A **927**, 24 (2014).
- [37] E. Wang, J. J. Xie, and J. Nieves, Phys. Rev. C **90**, 065203 (2014).
- [38] N. Muramatsu, J. Y. Chen, W. C. Chang, D. S. Ahn, J. K. Ahn, H. Akimune, Y. Asano, and S. Date *et al.*, Phys. Rev. Lett. **103**, 012001 (2009).
- [39] H. Kohri *et al.* [LEPS Collaboration], Phys. Rev. Lett. **104**, 172001 (2010).
- [40] M. Niiyama, H. Fujimura, D. S. Ahn, J. K. Ahn, S. Ajimura, H. C. Bhang, T. H. Chang, and W. C. Chang *et al.*, Phys. Rev. C **78**, 035202 (2008).
- [41] K. Hicks [LEPS Collaboration], Chin. Phys. C **34**, 1275 (2010).

- [42] K. Moriya *et al.* [CLAS Collaboration], Phys. Rev. C **88**, 045201 (2013) [Phys. Rev. C **88**, 049902 (2013)].
- [43] S. H. Kim, S. i. Nam, A. Hosaka, and H.-Ch. Kim, Phys. Rev. D **88**, 054012 (2013).
- [44] S. H. Kim, A. Hosaka, and H. C. Kim, Phys. Rev. D **90**, 014021 (2014).
- [45] S. K. Choi *et al.* [Belle Collaboration], Phys. Rev. Lett. **91**, 262001 (2003).
- [46] B. Aubert *et al.* [BaBar Collaboration], Phys. Rev. D **71**, 071103 (2005).
- [47] B. Aubert *et al.* [BaBar Collaboration], Phys. Rev. Lett. **95**, 142001 (2005).
- [48] K. Abe *et al.* [Belle Collaboration], Phys. Rev. Lett. **98**, 082001 (2007).
- [49] S. K. Choi *et al.* [Belle Collaboration], Phys. Rev. Lett. **100**, 142001 (2008).
- [50] A. Bondar *et al.* [Belle Collaboration], Phys. Rev. Lett. **108**, 122001 (2012).
- [51] M. Ablikim *et al.* [BESIII Collaboration], Phys. Rev. Lett. **110**, 252001 (2013).
- [52] Z. Q. Liu *et al.* [Belle Collaboration], Phys. Rev. Lett. **110**, 252002 (2013).
- [53] R. Aaij *et al.* [LHCb Collaboration], Phys. Rev. Lett. **110**, 222001 (2013).
- [54] R. Aaij *et al.* [LHCb Collaboration], Phys. Rev. Lett. **112**, 222002 (2014).
- [55] E. S. Swanson, Phys. Rept. **429**, 243 (2006).
- [56] N. Brambilla, S. Eidelman, B. K. Heltsley, R. Vogt, G. T. Bodwin, E. Eichten, A. D. Frawley, and A. B. Meyer *et al.*, Eur. Phys. J. C **71**, 1534 (2011).
- [57] D. Diakonov, V. Petrov and M. V. Polyakov, Z. Phys. A **359**, 305 (1997).
- [58] T. Nakano *et al.* [LEPS Collaboration], Phys. Rev. Lett. **91**, 012002 (2003).
- [59] A. Aktas *et al.* [H1 Collaboration], Phys. Lett. B **588**, 17 (2004).
- [60] R. Aaij *et al.* [LHCb Collaboration], Phys. Rev. Lett. **115**, 072001 (2015).
- [61] Charmed Baryon Spectroscopy via the  $(\pi^-, D^{*-})$  reaction (2012). (Available at: [http://www.j-parc.jp/researcher/Hadron/en/Proposal\\_e.html#1301](http://www.j-parc.jp/researcher/Hadron/en/Proposal_e.html#1301)). J-PARC P50 proposal.
- [62] S. H. Kim, A. Hosaka, H.-Ch. Kim, H. Noumi, and K. Shirotori, Prog. Theor. Exp. Phys. **2014**, 103D01 (2014).
- [63] V. Gribov, Strong Interactions of Hadrons at High Energies (Cambridge University Press, UK, 2012).

- [64] O. I. Dahl, L. M. Hardy, R. I. Hess, J. Kirz, D. H. Miller, and J. A. Schwartz, Phys. Rev. **163**, 1430 (1967) [Phys. Rev. **183**, 1520 (1969)].
- [65] A. Donnachie, H. G. Dosch, P. V. Landshoff, and O. Nachtmann, Pomeron Physics and QCD (Cambridge University Press, UK, 2002).
- [66] M. Froissart, Phys. Rev. **123**, 1053 (1961).
- [67] J. K. Storrow, Phys. Rep. **103**, 317 (1984).
- [68] W. Tang *et al.* [CLAS Collaboration], Phys. Rev. C **87**, 065204 (2013).
- [69] S. H. Hwang *et al.* (LEPS Collaboration), Phys. Rev. Lett. **108**, 092001 (2012).
- [70] M. Nanova *et al.* (CBELSA/TAPS Collaboration), Eur. Phys. J. A **35**, 333 (2008).
- [71] I. Hleiqawi and K. Hicks, arXiv:nucl-ex/0512039.
- [72] I. Hleiqawi *et al.* (CLAS Collaboration), Phys. Rev. C **75**, 042201 (2007); C **76**, 039905(E) (2007).
- [73] Y. Oh and H. Kim, Phys. Rev. C **74**, 015208 (2006).
- [74] Q. Zhao, J. S. Al-Khalili, and C. Bennhold, Phys. Rev. C **64**, 052201 (2001).
- [75] S. H. Kim, A. Hosaka, S. i. Nam, and H.-Ch. Kim, JPS Conf. Proc. **1**, 013044 (2014).
- [76] K. Nakamura *et al.* [Particle Data Group], J. Phys. G **37**, 075021 (2010).
- [77] D. Black, M. Harada, and J. Schechter, Phys. Rev. Lett. **88**, 181603 (2002).
- [78] V. G. J. Stoks and Th. A. Rijken, Phys. Rev. C **59**, 3009 (1999); Th. A. Rijken, V. G. J. Stoks, and Y. Yamamoto, *ibid.* **59**, 21 (1999).
- [79] W. Rarita and J. Schwinger, Phys. Rev. **60**, 61 (1941).
- [80] B. J. Read, Nucl. Phys. B **52**, 565 (1973).
- [81] S. Taylor *et al.* [CLAS Collaboration], Phys. Rev. C **71**, 054609 (2005) [Phys. Rev. C **72**, 039902 (2005)].
- [82] Y. Oh and H. Kim, Phys. Rev. C **73**, 065202 (2006).
- [83] R. Machleidt, K. Holinde, and C. Elster, Phys. Rep. **149**, 1 (1987).
- [84] V. V. Molchanov *et al.* (SELEX Collaboration), Phys. Lett. B **590**, 161 (2004).
- [85] R. H. Hackman, N. G. Deshpande, D. A. Dicus, and V. L. Teplitz, Phys. Rev. D **18**, 2537 (1978).

- [86] J. W. Darewych, M. Horbatsch, and R. Koniuk, Phys. Rev. D **28**, 1125 (1983).
- [87] C. L. Schat, C. Gobbi, and N. N. Scoccola, Phys. Lett. B **356**, 1 (1995).
- [88] A. Abada, H. Weigel, and H. Reinhardt, Phys. Lett. B **366**, 26 (1996).
- [89] G. Wagner, A. J. Buchmann, and A. Faessler, Phys. Rev. C **58**, 1745 (1998).
- [90] H.-Ch. Kim, M. Polyakov, M. Praszalowicz, G.-S. Yang, and K. Goeke, Phys. Rev. D **71**, 094023 (2005).
- [91] S. J. Chang, Phys. Rev. **161**, 1308 (1967).
- [92] J. G. Rushbrooke, Phys. Rev. **143**, 1345 (1966).
- [93] R. E. Behrends and C. Fronsdal, Phys. Rev. **106**, 345 (1957).
- [94] Y. Oh, EPJ Web Conf. **20**, 02008 (2012).
- [95] K. Ohta, Phys. Rev. C **40**, 1335 (1989).
- [96] H. Haberzettl, Phys. Rev. C **56**, 2041 (1997).
- [97] H. Haberzettl, C. Bennhold, T. Mart, and T. Feuster, Phys. Rev. C **58**, R40 (1998).
- [98] R. M. Davidson and R. Workman, Phys. Rev. C **63**, 025210 (2001).
- [99] H. Haberzettl, K. Nakayama, and S. Krewald, Phys. Rev. C **74**, 045202 (2006).
- [100] A. I. Titov and T. S. H. Lee, Phys. Rev. C **66**, 015204 (2002).
- [101] R. Bradford *et al.* [CLAS Collaboration], Phys. Rev. C **75**, 035205 (2007).
- [102] S. i. Nam, Phys. Rev. C **81**, 015201 (2010).
- [103] J. Beringer *et al.* [Particle Data Group], Phys. Rev. D **86**, 010001 (2012).
- [104] A. V. Anisovich, R. Beck, E. Klempt, V. A. Nikonov, A. V. Sarantsev, and U. Thoma, Eur. Phys. J. A **48**, 15 (2012).
- [105] G. Höhler, F. Kaiser, R. Koch, and E. Pietarinen, “*Handbook Of Pion Nucleon Scattering*,” pp. 440 (Physics Data, No. 12-1 (1979)).
- [106] A. V. Anisovich, E. Klempt, V. A. Nikonov, A. V. Sarantsev, and U. Thoma, Phys. Lett. B **711**, 167 (2012).
- [107] A. V. Anisovich, E. Klempt, V. A. Nikonov, A. V. Sarantsev, H. Schmieden, and U. Thoma, Phys. Lett. B **711**, 162 (2012).

- [108] N. Awaji, H. Hayashii, S. Iwata, R. Kajikawa, K. Makino, A. Miyamoto, H. Ozaki, and A. Sugiyama *et al.*, DPNU-29-81, (1981).
- [109] K. Fujii, H. Hayashii, S. Iwata, R. Kajikawa, A. Miyamoto, T. Nakanishi, Y. Ohashi, and S. Okumi *et al.*, Nucl. Phys. B **197**, 365 (1982).
- [110] S. H. Kim, S. i. Nam, Y. Oh, and H.-Ch. Kim, Phys. Rev. D **84**, 114023 (2011).
- [111] S. Ozaki, H. Nagahiro, and A. Hosaka, Phys. Rev. C **81**, 035206 (2010).
- [112] L. Guo and D. P. Weygand [CLAS Collaboration], arXiv:hep-ex/0601010.
- [113] K. Hicks, D. Keller, and W. Tang, AIP Conf. Proc. **1374**, 177 (2011).
- [114] A. V. Anisovich, V. Burkert, E. Klempt, V. A. Nikonov, A. V. Sarantsev, and U. Thoma, Eur. Phys. J. A **49**, 67 (2013).
- [115] M. Chretien and R. E. Peierls, Proc. Roy. Soc. Lond. A **223**, 468 (1954).
- [116] P. Mattione, PoS Hadron **2013**, 096 (2013).
- [117] P. Mattione [CLAS Collaboration], Int. J. Mod. Phys. Conf. Ser. **26**, 1460101 (2014).
- [118] C. G. Fasano, F. Tabakin, and B. Saghai, Phys. Rev. C **46**, 2430 (1992).
- [119] M. Pichowsky, C. Savkli, and F. Tabakin, Phys. Rev. C **53**, 593 (1996).
- [120] A. I. Titov, Y. Oh, S. N. Yang, and T. Morii, Phys. Rev. C **58**, 2429 (1998).
- [121] L. A. Copley, N. Isgur, and G. Karl, Phys. Rev. D **20**, 768 (1979) [Erratum-ibid. D **23**, 817 (1981)].
- [122] W. Roberts and M. Pervin, Int. J. Mod. Phys. A **23**, 2817 (2008).
- [123] K. Itonaga, T. Motoba, and H. Bando, Prog. Theor. Phys. **84**, 291 (1990).
- [124] J. H. Christenson, E. Hummel, G. A. Kreiter, J. Sculli, and P. Yamin, Phys. Rev. Lett. **55**, 154 (1985).
- [125] A. B. Kaidalov, Z. Phys. C **12**, 63 (1982).
- [126] K. G. Boreskov and A. B. Kaidalov, Sov. J. Nucl. Phys. **37**, 100 (1983); [Yad. Fiz. **37**, 174 (1983)].
- [127] A. B. Kaidalov and O. I. Piskunova, Sov. J. Nucl. Phys. **43**, 994 (1986); [Yad. Fiz. **43**, 1545 (1986)].
- [128] A. B. Kaidalov and P. E. Volkovitsky, Z. Phys. C **63**, 517 (1994).

- [129] O. I. Dahl, L. M. Hardy, R. I. Hess, J. Kirz, and D. H. Miller, Phys. Rev. **163**, 1377 (1967).
- [130] D. J. Crennell, H. A. Gordon, K. -W. Lai, and J. M. Scarr, Phys. Rev. D **6**, 1220 (1972).
- [131] M. Bando, T. Kugo, and K. Yamawaki, Phys. Rept. **164**, 217 (1988).
- [132] D. Yaffe, M. Abramovich, V. Chaloupka, A. Ferrando, M. Korkea-Aho, M. J. Losty, L. Montanet, E. Paul *et al.*, Nucl. Phys. B **75**, 365, (1974).
- [133] M. Aguilar-Benitez *et al.*, Z. Physik. C, Particles and Fields **6**, 195 (1980).
- [134] M. M. Brisudova, L. Burakovsky, and J. T. Goldman, Phys. Rev. D **61**, 054013 (2000).
- [135] V. Y. Grishina, L. A. Kondratyuk, W. Cassing, M. Mirazita, and P. Rossi, Eur. Phys. J. A **25**, 141 (2005).
- [136] H. Noumi, PoS Hadron **2013**, 031 (2013).
- [137] A. I. Titov and B. Kampfer, Phys. Rev. C **78**, 025201 (2008).
- [138] A. Hosaka and H. Toki, "Quarks, baryons and chiral symmetry", World Scientific, 2001.